



HAL
open science

Contribution to the development of a traceable stereovision system for the 3D scanning of large and complex parts

Safouane El Ghazouali

► To cite this version:

Safouane El Ghazouali. Contribution to the development of a traceable stereovision system for the 3D scanning of large and complex parts. Informatique. HESAM Université, 2022. Français. NNT : 2022HESAC025 . tel-03994528

HAL Id: tel-03994528

<https://theses.hal.science/tel-03994528>

Submitted on 17 Feb 2023

HAL is a multi-disciplinary open access archive for the deposit and dissemination of scientific research documents, whether they are published or not. The documents may come from teaching and research institutions in France or abroad, or from public or private research centers.

L'archive ouverte pluridisciplinaire **HAL**, est destinée au dépôt et à la diffusion de documents scientifiques de niveau recherche, publiés ou non, émanant des établissements d'enseignement et de recherche français ou étrangers, des laboratoires publics ou privés.

ÉCOLE DOCTORALE SMI
Laboratoire commun de métrologie LCM

THÈSE

présentée par : **Safouane EL GHAZOUALI**

soutenue le : **24 Novembre 2022**

pour obtenir le grade de : **Docteur d'HESAM Université**

préparée au : **Conservatoire national des arts et métiers**

Discipline : **61**

Spécialité : **Informatique et traitement d'images**

**Contribution au développement d'un système
de stéréovision traçable pour la mesure 3D de
pièces complexes de grands volumes**

*Contribution to the development of a traceable
stereovision system for the 3D scanning of large and
complex parts*

THÈSE dirigée par :

Hichem NOUIRA, IGR. HDR., LCM

et co-encadrée par :

Alain VISSIERE, IGR., LCM

Jury

M. Marc PIERRROT-DESEILLIGNY, Directeur de recherche, ENSG

M. Nabil ANWER, PU, Université Paris-Saclay, IUT Cachan

M. Yassine EL HILLALI, PU, Polytechnique Haut de France

Mme. Anne-Françoise OBATON, Directrice de recherche, LNE-CNAM (LCM)

M. Mohamed Lamjed BOUAZIZI, PU, PSAU University

M. Romain BRAULT, Responsable R&D IGR., CETIM

Président

Rapporteur

Rapporteur

Examinatrice

Examinateur

Examinateur

**T
H
È
S
E**

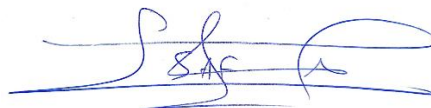
Affidavit

Je soussigné, **Safouane El Ghazouali**, déclare par la présente que le travail présenté dans ce manuscrit est mon propre travail, réalisé sous la direction scientifique de **Hichem NOUIRA** et le co-encadrement de **Alain VISSIERE**, dans le respect des principes d'honnêteté, d'intégrité et de responsabilité inhérents à la mission de recherche. Les travaux de recherche et la rédaction de ce manuscrit ont été réalisés dans le respect de la charte nationale de déontologie des métiers de la recherche.

Ce travail n'a pas été précédemment soumis en France ou à l'étranger dans une version identique ou similaire à un organisme examinateur.

Fait à Paris, le 16/08/2022

Signature



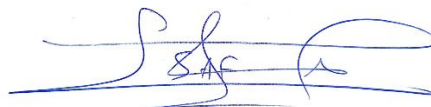
Affidavit

I, undersigned, **Safouane El Ghazouali**, hereby declare that the work presented in this manuscript is my own work, carried out under the scientific direction of **Hichem NOUIRA** and the co-supervision **Alain VISSIERE**, in accordance with the principles of honesty, integrity and responsibility inherent to the research mission. The research work and the writing of this manuscript have been carried out in compliance with the French charter for Research Integrity.

This work has not been submitted previously either in France or abroad in the same or in a similar version to any other examination body.

Paris, 16/08/2022

Signature



Abstract

This thesis deals with the development of a 3D vision system integrated into an industrial robot for contactless 3D scanning of mechanical parts in the aeronautic domain. Unlike tactile probing coordinate measurement machines (CMMs), 3D vision systems integrated with industrial robot leads to scan large mechanical parts in a short time, in quite harsh environments. All scanning operations, initially performed on canonical parts, have recently been extended to complex surfaces while catching the new industrial needs in terms of in-line measurement, as specified in the roadmap dedicated to industry of future (or Industry 4.0). Therefore, the quality assurance of multi-camera scanning systems and their traceability to the SI meter definition represents a challenging objective of the European project 17IND03-LaVA. The full measurement system combining one camera-projector system and one industrial robot allows in-line 3D scanning of mechanical large volume parts with complex shapes.

One 3D vision system based on the principle of structured light has been developed and calibrated in-house. The calibration of 3D vision systems is a crucial step prior to any 3D scanning operations. It enables to identify the requested internal, external and distortion parameters used for collecting a dense and accurate measured datasets of a mechanical part. In this context, calibration techniques of 3D vision systems have been studied and one novel optimisation method is proposed to improve the calibration accuracy. A synthetic and experimental evaluation was conducted to prove the efficiency of the optimisation method where the convergence has been proven to be faster. The calibration of the developed 3D vision system is carried out with a traceable ceramic checkerboard measured with a traceable optical CMM (Micro-Vu Excel) at LNE.

Finally, a specific large volume part (quite similar to that of aeronautics) with a complex shape is developed, measured by the traceable CMM machine, and used for the evaluation of the developed 3D vision system. A local scanning strategy is adopted to cover the whole surface of the large volume part. It consists of independently scanning several areas of the part and then aligning the measurement in one coordinate system using a validated registration technique. Afterwards, a reliable and accurate measurement results, 3D data processing and fusion algorithms were investigated and applied. The returned results have shown a maximum fitting residual of 150 μm .

Keywords: 3D Metrology; Point cloud; Calibration; Large volume parts; Complex surface; Machine Learning; Optimisation; Registration; Vision systems; Robotic

Résumé

Ce travail de thèse est destiné à contribuer au développement d'un système de vision 3D, couplé à un système de déplacement, pour la mesure sans contact de pièces mécaniques complexes. Contrairement aux machines de mesures 3D tactiles, les systèmes de vision 3D permettent de fournir un nuage de point dense en un temps quasi réel. Les opérations de mesure 3D, initialement réalisées sur des pièces simples, ont été étendues à des surfaces complexes pour répondre aux nouveaux besoins industriels en matière d'automatisation de la mesure en ligne, selon les besoins de l'industrie du futur (ou Industrie 4.0). Dans le cadre du projet EMPIR 17IND03-LaVA avec cette thèse, le LNE a contribué à la mise en œuvre d'un système de mesure multi-caméras (de photogrammétrie/lumière structurée) traçable à la définition SI du mètre. La combinaison du système de cameras-projecteur avec un robot industriel constitue le système de mesure complet destiné à des opérations de scanning 3D en ligne sur des pièces mécaniques complexes de grands volumes.

L'étalonnage des systèmes de vision 3D basé sur le principe de lumière structurée, réalisé dans le cadre de mon projet de thèse, représente une étape cruciale pour aboutir à des mesures traçables. Il permet aussi d'obtenir des informations nécessaires à la triangulation. Dans ce contexte, les techniques d'étalonnage ont été étudiées, et une nouvelle méthode d'optimisation permettant d'améliorer l'exactitude de l'étalonnage a été proposée. Ensuite, l'étalonnage du système de vision 3D est réalisé par l'intermédiaire d'un étalon matériel mesuré avec une machine optique traçable (Micro-Vu Excel), permettant de raccorder notre système de vision à la chaîne de traçabilité SI du mètre.

Enfin, une pièce mécanique complexe de grand volume, similaire à celles utilisées dans l'aéronautique, a été développée et étalonnée sur une machine de mesure traçable. Cette étalon est utilisé pour l'évaluation des performances métrologiques du système de vision 3D. Une stratégie de scan a également été proposée pour couvrir toute la surface de la pièce. Cela implique de numériser plusieurs zones de la pièce individuellement et de fusionner les mesures dans un même référentiel à l'aide de techniques d'alignement. Des algorithmes de traitement et de fusion de données 3D ont été implémentés. Le résultat de mesure obtenu en terme de résidus ($150 \mu\text{m}$) est très encourageant.

Mots clés : Métrologie 3D; Nuage de points; Etalonnage; Pièces de grand volume; Surface complexe; Apprentissage automatique; Robotique

Contents

Abstract	iii
Résumé	iv
Contents	v
List of appendix	xi
Nomenclature	xii
Introduction	1
Context	2
Organization of the thesis manuscript	3
Contributions	4
C H A P T E R . I Overview, design and development of a 3D scanning system	5
I.1. Introduction	6
I.2. Choice of the scanning method	7
I.2.1. State of the art on the advantages and drawbacks of the existing methods	7
I.2.2. Analysis of the state of art	9
I.3. Structured lighting (SL) techniques	9
I.3.1. SL: general concept	9
I.3.2. SL: codification strategies	10
I.4. Design and conception of an optical 3D measurement system	13
I.4.1. Introduction	13
I.4.2. Design of the traceable 3D scanner	14
I.4.3. Resolution of the traceable 3D scanner	16
I.4.4. Protocol for 3D scanning of large volume parts (LVPs)	19
I.5. Conclusion	26
C H A P T E R . II Camera model and sensor calibration	27
II.1. Introduction	28
II.2. Modelling and calibration of a single camera	28
II.2.1. How does a camera work?	28
II.2.2. Perspective projection fundamentals	29
II.2.3. Lens distortion model	32
II.2.4. Camera calibration	35
II.3. Modelling and calibration of stereo vision systems	46
II.3.1. Stereo vision model	47
II.3.2. Calibration of stereo systems	49
II.3.3. Inverse camera/projector calibration	49

II.4.	Conclusion.....	52
C H A P T E R . III	Optimised calibration of camera-based systems	54
III.1.	Introduction	55
III.2.	Novel optimisation method for a camera-based system	56
III.2.1.	Polynomial approximation	56
III.2.2.	Particle swarm optimisation	58
III.2.3.	Full implemented calibration flowchart	60
III.3.	Optimisation for stereo systems	61
III.3.1.	Polynomial regression of the extrinsic parameters.....	62
III.3.2.	Weighted sum of the estimated polynomials.....	62
III.3.3.	Multiobjective function minimization.....	63
III.4.	Synthetic evaluation of the proposed optimisation.....	65
III.4.1.	Simulation of the calibration process	65
III.4.2.	Simulation results and analysis	66
III.5.	Experimental validation of a single camera	70
III.5.1.	Experimental setup	70
III.5.2.	Traceability establishment through CMM measurements.....	71
III.5.3.	Calibration of an industrial camera	74
III.5.4.	Time complexity analysis.....	77
III.5.5.	Comparison of results and discussion	78
III.6.	Experimental validation of the SL scanner.....	80
III.6.1.	Pose optimisation.....	80
III.6.2.	Coordinate measuring system based on multilateration	82
III.6.3.	Comparison of the transformations between robot poses.....	86
III.7.	Conclusion.....	88
C H A P T E R . IV	Quality control of large and complex parts.....	91
IV.1.	Approach for data acquisition using the calibrated scanner	92
IV.1.1.	Single view: triangulation.....	92
IV.1.2.	Multiple views: point-cloud registration	93
IV.2.	Evaluation method of the 3D scanner.....	93
IV.2.1.	Single view: repeatability and trueness	93
IV.2.2.	Multiple views: point-cloud registration	93
IV.3.	Measurement protocol on proposed material standard.....	94
IV.3.1.	Suggested material standard.....	94
IV.3.1.1.	Large volume standard (LVS).....	94
IV.3.1.2.	Secondary artefacts.....	95

IV.3.1.3.	Large volume standard with the secondary artefacts.....	96
IV.3.1.4.	Reflectivity effect on 3D scanning	97
IV.3.2.	SL scanning protocol.....	97
IV.3.2.1.	SL scanner	97
IV.3.2.2.	Probe-contact CMM	97
IV.4.	Evaluation: single view scanning	99
IV.4.1.	Flatness.....	99
IV.4.2.	Semi-sphere	102
IV.4.3.	Semi-cylinder	103
IV.5.	Evaluation: multiple view scanning	105
IV.5.1.	Pairwise registration	107
IV.5.2.	Groupwise registration	112
IV.6.	Proposed pipeline for point-cloud registration.....	113
IV.6.1.	Tracking-based registration using industrial robot.....	113
IV.6.2.	Global registration pipeline	114
IV.6.3.	Synthetic evaluation of the proposed pipeline.....	115
IV.6.4.	Experimental evaluation of the proposed pipeline (3D scanning of the LVS) and analysis of the returned results	118
IV.7.	Conclusion.....	122
Conclusion and perspectives		124

List of Figures

Figure 1 <i>Measurement machine classification according to [Elha14]</i>	1
Figure 2 <i>Example of large volume parts from automotive and aeronautical industries [Elha14]</i>	2
Figure I.1 <i>Selection criteria of scanning methods</i>	6
Figure I.2 <i>configuration of structured light system inspired by [LiLi14]</i>	10
Figure I.3 <i>Classification of coding strategies for structured light scanners [Geng11]</i>	11
Figure I.4 <i>Example of 4 bits binary coding [TaML14]</i>	12
Figure I.5 <i>Portable 3D scanners: (a) Gocator SL scanner (costs around 15k €), (b) EINSscan pro 2X (~6k €), Fixed 3D scanners: (c) GOM Atos core (>33k €), (d) David scanner retails (~4k €)</i>	13
Figure I.6 <i>Design of the 3D scanner: (a) industrial cameras; (b) projector; (c) Camera rotational frame; (d) Projector rotational frame; (e) aluminium mounting frame; (f) Scanner-robot fixing part; (g) Laser rangefinder targets</i>	15
Figure I.7 <i>Effect of the distance d_2 on the spatial resolution</i>	16
Figure I.8 <i>Effect of projector orientation on the spatial resolution</i>	17
Figure I.9 <i>(a) Camera fixing frame for rotation along the vertical axis (b) Projector fixing frames for rotation along the horizontal axis</i>	18
Figure I.10 <i>(a) parallel configuration of the 3D scanner elements (b) angular configuration of the cameras with respect to the projection surface</i>	18
Figure I.11 <i>specification of the selected industrial robot KAWASAKI RS03N</i>	19
Figure I.12 <i>Addition of a 7th axis to the robot</i>	20
Figure I.13 <i>Scanning procedure of large volume part</i>	21
Figure I.14 <i>Illustration of the transformation from the robot end-effector to the robot base</i>	23
Figure I.15 <i>(a) Design of laser rangefinder, (b) spherical glass target [GuTW20a]</i>	24
Figure I.16 <i>General overview of the developed 3D scanning system</i>	25
Figure II.1 <i>Light recoding using an industrial camera Ximea [Xime00]</i>	29
Figure II.2 <i>Perspective projection modelling inspired form [MCHD07]</i>	30
Figure II.3 <i>Tangential and radial distortion effect on an ideal position of a pixel [LZHT13]</i>	33
Figure II.4 <i>Radial distortion: positive distortion called "pincushion", negative distortion called "barrel" (inspired from [Unde20])</i>	33
Figure II.5 <i>Illustration of tangential distortions: (a) decentring and non-parallelism error of the camera assembly (b) effect of tangential distortion of the image [Sinh00]</i>	34
Figure II.6 <i>Flowchart of the suggested calibration protocol based on Zh-method</i>	36
Figure II.7 <i>Example of robot-based camera calibration</i>	37
Figure II.8 <i>Example of the used calibration grids (a) Square grid 8x10 (b) Checkerboard 6x8 (c) Circle grid 5x7 (where \times are the points of interest)</i>	38
Figure II.9 <i>Ceramic chrome coating with a checkerboard pattern</i>	40
Figure II.10 <i>Projection of the incoming light (reflected on the 3D scene) on the image sensor</i>	44
Figure II.11 <i>(a) single camera capture, (b) advantage of using stereo vision inspired from [FSLY20]</i>	47
Figure II.12 <i>Triangulation configuration : (a) Cameras separated by a distance b called baseline and located such as the optical axes 1 and 2 are parallel (b) $[R T]$ transformation between $C1$ and $C2$ [Yama00]</i>	48
Figure II.13 <i>Example of pixel coding using Gray-code pattern. Where black is identified by 0 and white by 1. The green point can be identified by the string [1000111101] [JoGr10]</i>	51
Figure II.14 <i>Illustration of Gray-code steps for the calibration of camera-projector systems</i>	52
Figure III.1 <i>Evolution of the reprojection error RE_i vs. the orientations α and β for the case of a single camera system</i>	56
Figure III.2 <i>Illustration of the k-fold cross-validation principle</i>	57
Figure III.3 <i>Evolution of the MAE vs. the polynomial degree when applying the k-fold cross-validation method (CI is the confidence interval)</i>	58
Figure III.4 <i>Full flowchart of the proposed methodology for machine vision calibration. RE is the average reprojection error and ϵ is the threshold</i>	60
Figure III.5 <i>Illustration of plane-based calibration of an active stereo system</i>	61
Figure III.6 <i>Flowchart of the proposed positioning optimisation method [EGVL22]</i>	64

Figure III.7 Illustration of the proposed virtual checkerboard simulation: (a) without effect, (b) using anti-aliasing, (c) adding the depth of field effect	65
Figure III.8 Simulated views for image acquisition in the checkerboard coordinate frame (only rotations are applied and presented in this figure).....	66
Figure III.9 Visualization of selected feature points in the checkerboard seen by to the camera with regard of the set of optimal poses returned by the ML-approach.....	67
Figure III.10 Comparison of reprojection errors estimated using ML-approach CW and R-method.....	67
Figure III.11 Evolution of the pinhole camera parameters returned by ML-approach, CW- (Calibration Wizard) and R-method (R: Rojtberg): (a) & (b) is the focal length, (c) & (d) are the principal point coordinates, (e) & (f) are the coefficients of radial distortion and (g) & (h) are the extrinsic parameter. Note : the initial points for k_1 and k_2 are not illustrated since they present high values of errors	69
Figure III.12 Calibration process of single camera using the ML-approach: (a) 3D scanning system; (b) Connection cables to the terminal computer; (c) Checkerboard calibration grid; (d) Industrial 6-axis KAWASAKI robot; (e) 7th motion axis.	71
Figure III.13 (a) Traceable optical Micro-Vu Excel CMM, (b) Ceramic calibration grid printed with checkerboard pattern	72
Figure III.14 Detailed full traceability pyramid adopted for the calibration of cameras	72
Figure III.15 (a) CMM 2D reconstruction of the checkerboard where H1 is the first horizontal line and V1 the first vertical line; (b) the checkerboard to be calibrated; (c) Least-square fitting of the line H1; (c) Least-square fitting of the line V1	73
Figure III.16 Example of the process of extracting points for vertical line using black-to-white threshold of 125	74
Figure III.17 Minimal objective function's particle value vs. the PSO iterations	75
Figure III.18 Estimated optimal extrinsic parameters from camera perspective	75
Figure III.19 Samples of resulting optimal poses returned by the ML-approach.....	76
Figure III.20 Bar chart of reprojection errors estimated for each identified best pose using the ML-approach. Each bar represents the average reprojection error calculated for the image of the ceramic calibration grid. ..	76
Figure III.21 Error distribution of the estimated 2D coordinates of the traceable ceramic calibration grid.	78
Figure III.22 Repeatability test of the norm vector across 20 tests	79
Figure III.23 Visualisation of the calibration process using a single pose	81
Figure III.24 Estimated camera and projector reprojection errors when applying the ML-approach [EGVL22]	81
Figure III.25 Photograph of the experimental setup	82
Figure III.26 Experimental results of the multilateration with self-calibration	84
Figure III.27 Uncertainties on position of both the heads and the targets.....	84
Figure III.28 Reproducibility of the interpoint distances of the targets mounted on the SL system	85
Figure III.29 Illustration of the motion of targets on the SL scanner.....	86
Figure III.30 Difference between the transformations obtained by the calibration of the SL scanner and the ones obtained by the external coordinate measuring system.	87
Figure IV.1 Steps of 3D reconstruction of an elementary surface	92
Figure IV.2 Evaluation method of a fully reconstructed mechanical part	94
Figure IV.3 CAD of the designed large volume standard	94
Figure IV.4 CAD of the designed secondary artefacts	95
Figure IV.5 CAD model of the LVS equipped with secondary artefacts	96
Figure IV.6 Point-cloud generation process using Zeiss probe-contact CMM (a) process of probe scanning (b) definition of the coordinates frame of the mechanical part, (c) definition of the scanning points and the path ...	98
Figure IV.7 Measured datasets with the traceable tactile Zeiss CMM: the LVS and the semi sphere, semi-cylinder and stepped pyramidal shapes.	99
Figure IV.8 Visualization of the least square fitting of a point-cloud to a plane	101
Figure IV.9 Repeatability test of flatness across 70 tests.....	101
Figure IV.10 Visualization of the least square fitting of a point-cloud to a sphere	102
Figure IV.11 Repeatability test of the sphericity parameter across 70 tests	103
Figure IV.12 Visualization of the least squares fitting of a point-cloud to a cylinder	104
Figure IV.13 Repeatability test of the cylindricity across 70 tests	105
Figure IV.14 Example of a point-cloud registration for a complex part.....	106

Figure IV.15 <i>illustration of pairwise registration process</i>	107
Figure IV.16 <i>Estimation of normal distributions at each voxel of SL point-cloud</i>	108
Figure IV.17 <i>Visualization of point-clouds registration using NDT, ICP and CPD for semi-sphere and semi-cylinder</i>	111
Figure IV.18 <i>Visualization of pose graph optimisation of multiple point-clouds</i>	112
Figure IV.19 <i>Illustration of the transformations between the different coordinate frames</i>	114
Figure IV.20 <i>Flowchart of the proposed point-cloud registration pipeline</i>	115
Figure IV.21 <i>Illustration of view sampling on a complex part</i>	116
Figure IV.22 <i>Flowchart of the synthetic evaluation of the registration pipeline. Where T_{GT} ground truth transformation, T_{est} is the estimated one and view is the simulated position of the scanner with respect to the CAD</i>	117
Figure IV.23 <i>Obtained RMSE, MAE and PV values (in mm) and their associated uncertainties</i>	118
Figure IV.24 <i>End-effector positioning of the industrial robot to scan an edge of the large volume part</i>	119
Figure IV.25 <i>Obtained 3D reconstruction of the large volume part using the proposed registration pipeline. Each colour defines a point-cloud generated from a specific pose of the SL scanner</i>	119
Figure IV.26 <i>RMSE evolution of the ICP registration (a) ICP with correspondence distance of 2 mm, (b) ICP with correspondence distance set to 1 mm</i>	120
Figure IV.27 <i>Comparison of CMM and SL fitting of the large volume part. (a) SL point-cloud, (b) Distance error distribution of SL point-cloud to the CAD model, (c) CMM point-cloud, (d) Distance error distribution of CMM point-cloud to the CAD model</i>	121
Figure A.1 <i>3D reconstruction using drone photogrammetry [Dron00]</i>	167
Figure A.2 <i>Principal of laser triangulation [MSTM15]</i>	169
Figure A.3 <i>Coloured stripe coding for 3D reconstruction using structured light systems</i>	170
Figure A.4 <i>Example of De Bruijn sequence projected on a freeform</i>	171
Figure A.5 <i>Grid indexing codification strategy [Geng11]</i>	172
Figure A.6 <i>Example of 4 bits binary coding [KiRL08]</i>	172
Figure A.7 <i>3D reconstruction using Gray-coding strategy [Geng11]</i>	173
Figure A.8 <i>3D reconstruction using phase shifting encoding strategy [BeLZ16]</i>	173
Figure A.9 <i>Example of three-phase-shifting of a sinusoidal pattern for a projector with a resolution of 1024×768 pixels</i>	174
Figure A.10 <i>Step of camera-projector calibration using phase-shifting projection</i>	175
Figure C.1 <i>rotation angles</i>	178
Figure D.1 <i>Visualization of particles motion in PSO</i>	180

List of appendix

Résumé substantiel en français	152
Appendix A: Overview of camera-based 3D scanners	167
Passive and active photogrammetry.....	167
A.1. Passive 3D scanning.....	167
A.2. Active 3D scanning	168
Stripe indexing	169
De Bruijn Sequences	170
Grid Indexing: 2D Spatial Grid Patterns.....	171
Gray-code Patterns	172
Gray-Level Patterns	173
Phase Shift	173
Phase shift-based: calibration	174
Appendix B: Non-linear optimisation using Levenberg-Marquardt.....	176
B.1. Model establishing	176
B.2. Jacobian function.....	177
Appendix C: Representations of rotations	178
C.1. Euler rotation angles.....	178
C.2. Rotation matrix.....	178
C.3. Rodriguez rotations	179
Appendix D: Particle Swarm Optimisation (PSO).....	180
D.1. Application of PSO on multivariate polynomial.....	180
Appendix E: Tsai calibration method.....	182

Nomenclature

3D: Three dimensional
BFGS : Broyden–Fletcher–Goldfarb–Shanno algorithm
CAD : Computer-aided design
CCD : Charged coupled device
CI : Confidence interval
CMM : Coordinate-measuring machine
CMOS : Complementary Metal Oxide Semiconductor
CNAM : Conservatoire national des arts et métiers
CPD : Coherent Point Drift
CW : Calibration Wizard
DLP : Digital light processing
DLT : Direct linear transform
FoV : Field of view
GMM : Gaussian mixture model
GPD : Gaussian probability distribution
HSV : Hue Saturation and Value, Voir
ICP : Iterative closest point
IDE : integrated development environment
IFR : International Federation of Robotics
 L_2 : Least squares
LCM : Laboratoire commun de métrologie
LM : Levenberg–Marquardt
LVM : Large volume metrology
LVP : Large volume part
MAE : Mean absolute error
ML : Machine learning
NDT : Normal distribution transform
PV : Peak to valley
PSO : Particle swarm optimisation
RF : Radio Frequency
RGB : Red green blue
RMSE : Root-mean-square error
SL : Structure from motion
SL : Structured lighting
SVD : Singular-value decomposition

Introduction

In a permanent concern of quality control, the need for 3D scanning of mechanical parts has been growing during the last twenty years. Although many 3D scanners are marketed, improvements must be made, particularly regarding the metrological traceability and the estimation of measurement uncertainties. According to the VIM (International Vocabulary of Metrology), traceability is defined as the "property of a measurement result whereby the result can be related to a reference through a documented unbroken chain of calibrations, each contributing to the measurement uncertainty" [Inte12]. Currently, the traceability of industrial vision systems is not ensured enough and there are still some challenges and issues to be solved in Large Volume Metrology (LVM). LVM is defined as the ability to measure size, location, orientation and form of large dimension objects, assemblies or large working-volume machines. LVM is a critical requirement in industries such as aerospace, automotive, shipbuilding, civil engineering and energy, especially in the quality control of mechanical parts.

This thesis deals with the 3D scanning of large volume parts with complex shapes, located in the large-scale metrology as shown in Figure 1.

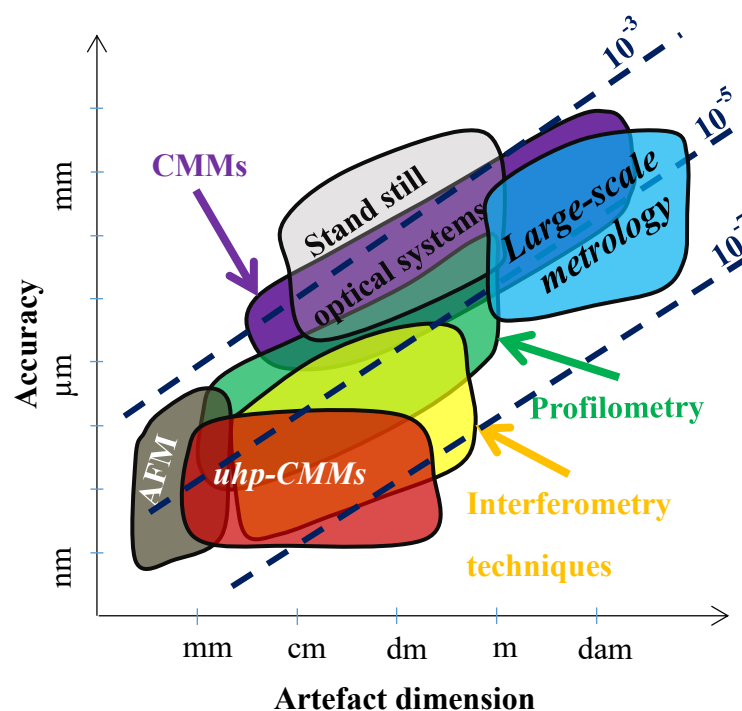


Figure 1 Measurement machine classification according to [Elha14]

Context

The LCM (LNE-CNAM) is developing a research axis on 3D scanning by machine vision as well as the associated data processing methods. It takes part of the European project LaVA-17IND03 (Large Volume Metrology Applications), launched in 2018 under the coordination of the National Physical Laboratory (NPL). A number of partners are involved in this project funded by the EMPIR-EURAMET program: NPL (UK), CNAM (FR), LNE (FR), GUM (PO), INRIM (IT), VTT (FI), IK4TEKNIKER (SP), SAAB (SW), FIDIA (IT), ISI-CAS (CZ), FIDIA (IT), WZL (GE), AACHEN UNIVERSITY (GE), MAPVISION (FI), and RI-SE (SE).

The LaVA project aims to develop measurement systems to scan large complex parts with a measurement uncertainty below 200 μm . LNE-CNAM, project partner, is focusing on the development of a low-cost three-dimensional measurement system for the characterization of large-volume complex parts. The most common examples of large volume parts are from the aeronautical, railway and shipbuilding fields (Figure 2).



Figure 2 *Example of large volume parts from automotive and aeronautical industries [Elha14]*

The inspection of mechanical sub-assemblies such as airframes or aircraft sections requires the use of flexible, accurate, real-time and traceable measurement systems located close to the production line to improve the manufacturing cycle process. For example, aircraft parts, such as airplane wings, require the use of non-contact 3D scanners, because the measurement time with contact sensors is often very important due to their large dimensions, and consequently the manufacturing cycle is not optimal [Whee19].

Traditionally, the inspection of mechanical parts relied on the use of tactile probes integrated into CMMs. The advantage of tactile CMMs lies mainly in their low measurement uncertainty. However, there are two disadvantages: (1) the measurement cycle is very long to scan large volume parts, (2) the measurement volume is limited by the structure of CMMs. Recently, several studies on optical 3D measurement techniques have been launched in order to overcome this issue. These studies have often led to the development of new contactless 3D scanning

techniques (photogrammetry, laser triangulation, stereoscopic vision) [AMRA19, HuFF20, ONTD18]. This type of technologies allows to acquire large cloud of points in short time. To scan large dimensions objects, a local scanning approach is usually adopted. Thanks to industrial robots, several scans can be performed on elementary zones of a large volume part and the collected datasets are merged into one coordinate system. Therefore, the thesis topic is focused on the development of a traceable and contactless 3D scanning system for large volume mechanical parts, which can be used for online metrology.

Organization of the thesis manuscript

This document is organised as the following:

- Chapter 1 presents the state of the art of contactless 3D scanners focusing on camera-based reconstruction techniques and their advantages compared to other methods. The concept of the developed structured lighting based on cameras and projector is also detailed. The 3D scanning strategy that includes the use of an industrial robot is introduced and techniques for aligning the collected datasets are discussed.
- Chapter 2 deals with the modelling and calibration methodology of a camera as well as a stereo system (camera-camera / camera-projector). The geometrical model of cameras, also called “pinhole model”, is detailed. Existing camera calibration and stereo cameras calibration techniques are discussed while Zhang calibration is well emphasised due to its accuracy and robustness.
- Chapter 3 presents a novel optimisation approach of the Zhang’s calibration method. The optimisation aims to improve the quality of the calibration for both single camera and stereo systems. The theory models are presented, then evaluated on synthetic data (by simulating a virtual scene) and successfully tested/applied on experimental data collected on a traceable ceramic checkerboard.
- In chapter 4, a designed large volume mechanical part and eight secondary artefacts, that have been used to assess the performance of the SL (structured light) scanner, are presented. Form errors are identified and a repeatability test for some secondary artefacts such as plan, sphere and cylinder are performed and evaluated. Both pairwise and groupwise point-clouds registration techniques are applied and the returned results are compared. A registration pipeline is proposed for the SL point-clouds and evaluated through a synthetic and experimental validation.

- Finally, a general conclusion of the thesis is given and a number of perspectives are suggested in order to improve the developed 3D scanning system.

Contributions

The thesis topic deals with the development of a traceable 3D scanner and associated data processing algorithms. Since tactile probes are limited in term of applications, measurement speed and density of data, one contactless system is proposed to guarantee the best compromise between scanning speed, accuracy and density. In this context, camera-based systems are best suited to reach the objective.

Therefore, the main contributions are:

- Study of camera-based 3D scanning systems (choice of technology and calibration methods):
 - camera calibration methods,
 - identification of the internal, external and distortion parameters,
 - exploitation of the identified parameters,
 - estimation of calibration uncertainties.
- Development of a 3D traceable scanner combining industrial cameras, industrial robot and tracking sensors (telemeters).
- Development, design and manufacturing of one large volume material standard with a geometry similar to parts in aeronautics. The traceability of the large volume material standards to the SI definition of the metre was established through measurements on the traceable Zeiss CMM at LNE.
- Development of a robust post-acquisition algorithm for data post-processing by exploiting intrinsic surface parameters such as shape variation and/or data from tracking sensors. Data fusion is an essential step to generate a global point cloud representative of the part.

CHAPTER . I Overview, design and development of a 3D scanning system

This chapter deals with 3D scanning methods proposed in the literature. A comparison between camera-based scanners is detailed in section I.2. In section I.3, a focus on structured lighting techniques and the 3D reconstruction using coded structured lights is given. Finally, section I.4 details the developed 3D vision system for scanning large volume and complex mechanical parts.

CHAPTER . I Overview, design and development of a 3D scanning system.....	5
I.1. Introduction	6
I.2. Choice of the scanning method	7
I.2.1. State of the art on the advantage and drawbacks of the existing methods	7
I.2.2. Analysis of the state of art	9
I.3. Structured lighting techniques	9
I.3.1. SL: general concept	9
I.3.2. SL codification strategies	10
I.4. Design and conception of an optical 3D measurement system	13
I.4.1. Introduction	13
I.4.2. Design of the traceable 3D scanner	14
I.4.3. Resolution of the traceable 3D scanner	16
I.4.4. Protocol for 3D scanning of LVPs	19
I.5. Conclusion.....	26

I.1. Introduction

Contactless 3D scanning methods have recently grown in popularity and are increasingly adopted in almost all industries, especially in projects involving R&D. The process of recovering 3D information of objects through camera recording is called photogrammetry. There are two categories of photogrammetry techniques [BGBM13, ElBB95]: **passive photogrammetry techniques** such as SfM (structure from motion) and stereovision as well as **active photogrammetry technique** such as laser scanners and structured light (SL). There are several brands and models in each category that all fulfil 3D scanning demands [BBPP21, DHAN18, ReBF10, SZPY12]. The capabilities, uses, and prices of 3D scanners vary greatly.

According to [BeBa14, Cara20, ChZh95, HeLe21, JHPS21], it seems critical to choose the appropriate 3D **scanning method** with respect to the target application. For example in quality control of mechanical parts, usually laser scanner and SL systems are used [BiJa04, PLMG20]. The selection of one contactless scanning technique depends on a number of criteria as shown in Figure I.1: (1) the accuracy of the 3D scan; (2) the real-time aspect to scan moving or static objects for example; (3) the scanning speed which is the ability to generate a point cloud within few seconds; (4) the density of the point-cloud; (5) the effect of environment condition such as lighting; (6) safety constraints as an important factor; and finally (7) the cost.

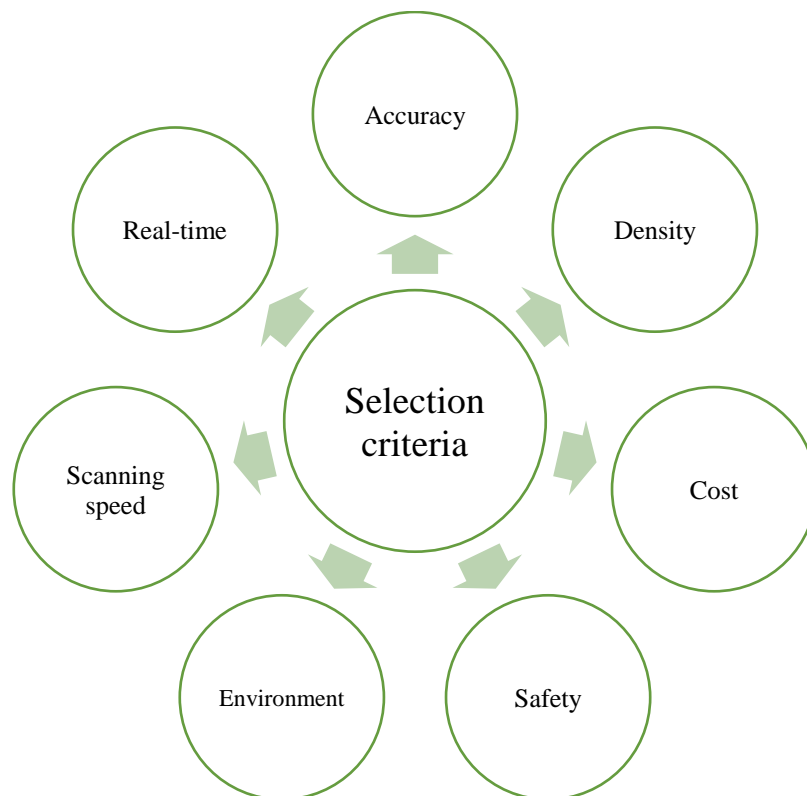


Figure I.1 Selection criteria of scanning methods

I.2. Choice of the scanning method

I.2.1. State of the art on the advantages and drawbacks of the existing methods

The choice of the scanning method depends on the target application. Here, the objective is to perform a *3D reconstruction* by collecting a dense and accurate point-cloud resulting from the scan of a given large volume part (LVP). This conceivably could be done by scanning the fixed surface elementary zones (SEZ) and merging all the collected point-clouds into a single one leading to a global 3D representation of the LVP.

Table I.1 summarizes the advantages and drawbacks of each optical scanning method with regard to the developed application. The mainly focused points are related to the use simplicity (the implementation requires a less complex mechanical configuration), the scanning time required to fully scan a LVP without compromising the scanning accuracy and the density of the 3D reconstruction.

Table I.1 *Comparison between 3D scanning methods*

Technologies	Advantages	Drawbacks
Photogrammetry [HuFF20, Luhm10, NBSR20]	<ul style="list-style-type: none"> - Simple mechanical configuration - low-cost (200 €) - Spatial resolution > 1 mm for aerial mapping - Medium and large range measurement - Accurate up to 1 – 5 mm for aerial photogrammetry 	<ul style="list-style-type: none"> - Can only be adapted for surfaces that contain features or physical markers - High time consuming due to algorithm complexity - Highly dependent on the areal surface texture - Highly affected by ambient lighting
Passive stereovision [Naou06, USAN05]	<ul style="list-style-type: none"> - Simple mechanical configuration - Low-cost (200 €) - Spatial resolution > 1 mm - Accuracy of about 1 – 2 mm for mapping - Medium range measurement 	<ul style="list-style-type: none"> - Useless for uniform surfaces and objects without targets - Highly affected by ambient lighting - Low accuracy compared to laser triangulation and SL

Shape-from-X [ChBK04, NaNa94, OVBS17]	<ul style="list-style-type: none"> - Low-cost - Adopted in many 3D scanning applications such as archaeology and cartography 	<ul style="list-style-type: none"> - Depend on ambient lighting - Highly depends on scene characteristics - Low accuracy > 1 mm
Time of flight [AmHS09, CSCT10]	<ul style="list-style-type: none"> - Medium and large range measurement - High acquisition frequency - Independent of ambient light 	<ul style="list-style-type: none"> - Lower measurement accuracy compared to triangulation technique for close-range (few mm)
Laser triangulation [ScSa00, SMMR19]	<ul style="list-style-type: none"> - Simple mechanical configuration - Close-range measurement - Submillimetre spatial resolution - Allow 3D reconstruction of an object regardless of the texture - Accurate up to few μm for moving objects 	<ul style="list-style-type: none"> - Security constraints related to the use of the laser source - Limited range measurement and volumes (few cm^3) - Scanning time
Structured lighting (SL) [Geng11, SaPB04, Vill00]	<ul style="list-style-type: none"> - Simple mechanical configuration - Accuracy to the micrometre level - Could operate in real-time - Close-range measurement - Spatial resolution of pixel size (few micrometres) - 3D scanning of an object regardless of the texture - High scanning speed - High density 	<ul style="list-style-type: none"> - Noise due to the process of encoding-decoding - Less accurate for moving objects

I.2.2. Analysis of the state of art

Both photogrammetry and passive stereovision techniques [AMRA19, NBSR20, USAN05] are used for images that contain feature points. Feature points (also called key points) in image processing, are defined as the elements of information about the pixels in an image [LiXW21]. These elements of information could be an edge, texture, colour variation, curvature, area with certain properties, or physical markers [GMRD20, LiXW21, Roud04, Weij05]. Usually, the manufactured LVP has a uniform aspect of the surface. Therefore, photogrammetry and passive stereovision scanning methods are unusable since there are no feature points to be identified in the images. In addition, shape-from-X [OVBS17] and time of flight [CSCT10] cannot be used because they provide low accuracy 3D reconstructions (>1 mm). Alternatively, the laser triangulation technique is based on the projection of a laser beam aimed at the surface of the LVP and collected from the camera perspective. The latter technique uses the projection of a laser point or line to scan the object. This principle represents the main drawback, as the scanning time is quite high. Since the scanning time represents one fundamental criterion to be considered when scanning LVP, the SL technique could be the appropriate solution in terms of scanning speed, but also in terms of robustness, density and accuracy.

SL system is an active technique based on the projection of well-known patterns on the surface. The projection patterns would be deformed according to the shape of the object and then used to recover the 3D information. The simplest example is the projection of a line (fringe) on a sphere, which will deform the projection due to its rounded shape. On this topic, several projection patterns are presented in the literature [HuMa89, KiRL08, SaPB04, ZDKS17] such as phase-shifting, Gray-code, Segmented stripes, De Bruijn sequences ...etc.

I.3. Structured lighting (SL) techniques

I.3.1. SL: general concept

The SL method is based on the analysis of the deformation of well-known patterns projected on the object. The principle is similar to laser triangulation, except that a projector replaces the laser source as shown in Figure I.2. The baseline is defined as the distance D between the camera frame and the projector. 3D scanning using SL technique is based on triangulation principle, performed between the pixel point of the projector (u_p, v_p) and its projection (u_c, v_c) on the image plane. Here, the transformation T_{p-c} (camera to projector) and internal parameters of the scanner elements are considered known.

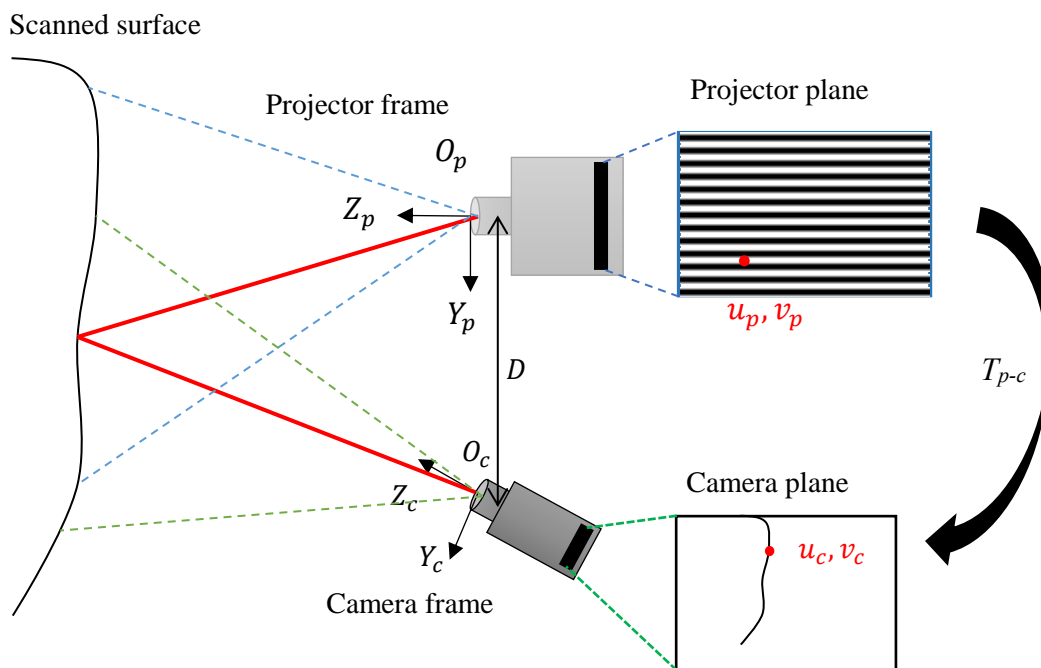


Figure I.2 configuration of structured light system inspired by [LiLi14]

The process of identification of the projected pixels on the image sensor is called a codification strategy [SaPB04]. Thus, codification consists of generating a well-known pattern through the projector and finding the correspondences between projector pixels and camera pixels [SaPB04].

I.3.2. SL: codification strategies

I.3.2.1. Existing codification strategies

In the literature [HKJK13, MRGO14, WiBP12], several codification strategies are proposed and classified into two main categories according to [Geng11]. The classification depends on the static or dynamic aspect of the scanned object:

- (1) **Multi-shot** techniques (Figure I.3) based on the projection of different patterns respectively while taking images. This is used to scan static objects, and usually leads to more accurate results [Geng11].
- (2) **Single-shot** techniques (Figure I.3) are rather based on the projection of a single pattern and mainly used to scan dynamic objects. Single-shot has been proposed with the main objective of scanning objects in real-time without the need for high accuracy. There are 3 types of single-shot techniques: (i) continuous patterns that consist of projecting endlessly coloured pattern; (ii) stripe indexing based on the codification of each singular projected stripe; (iii) grid indexing that consists of projecting a specific shape such as a grid or markers [TTAM18].

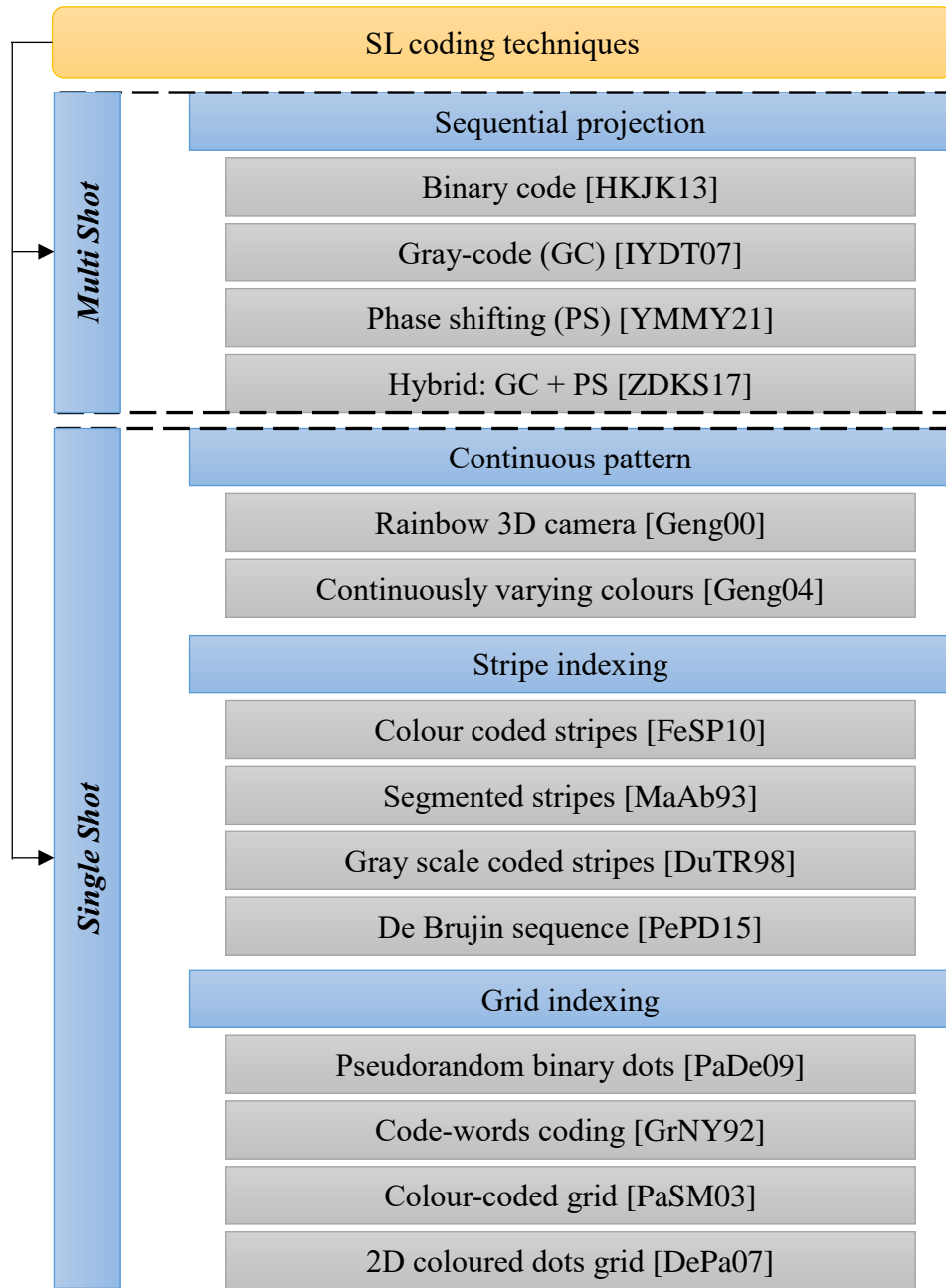


Figure I.3 Classification of coding strategies for structured light scanners [Geng11]

One of the most used single-shot techniques is strip indexing. It is based on the recognition of each projected pattern on the image plan by associating an index to each stripe, because the projected set of stripes does not necessarily correspond to the viewed ones. Coloured stripe indexing proposed by Chen [CZLF07] consists of the analyse of both the colour and the intensity of the projected pattern composed in the HSV colour space (Hue, Saturation, and Value). HSV is a model presented by [Smit78] such a non-linear transformation of RGB colour space from discrete values of colour to continuous is considered. Here, not only the colour is considered, but also the saturation and the brightness values are taken into account. This method

is used for 3D scanning in real time with the millimetre accuracy. Additional existing SL techniques have been proposed to achieve higher accuracy; however, they cannot perform real-time scanning. Phase-shifting [Kauf16] is a method based on the projection of a sinusoidal pattern with a varying intensity in the range of $[0, 255]$. The pattern is then shifted by one phase. For a three-step phase shifting projection, the shift is done by $\pi/3$ phase. This method uses the phase information calculated for each pixel, rather than the intensity values [YMMY21]. Each pixel of the projection pattern is identified using its own phase code, and can be located on the image plane.

I.3.2.2. Choice of codification strategy

In the context of this project, the LVP is considered physically fixed with respect to the developed 3D scanner. Hence, multi-shot techniques are selected in order to achieve the targeted accuracy. According to [ZDKS17], the multi-shot class could be split into two categories: *spatial* and *temporal*. Phase shifting is a *temporal* category that has been proposed to perform accurate 3D scanning in a short time. However, it fails when the scanned surface presents complex shapes and/or right angles. Those shapes complexity result of a phase shifting of more than 2π which causes errors in the estimation of the 3D coordinates [Kauf16]. On the other hand, Gray-code is a *spatial* category that relies on the analysis of pixel neighbourhood to provide 3D estimation of point coordinate. The *spatial* category is not optimised for real-time scanning, but mainly chosen to scan complex shapes [QCVG06].

For encoding binary patterns, the selection of Gray-codes is related to its robustness to image noise and interference between neighbouring pixels [Matt18]. The Gray-code [IYDT07] [KiRL08] uses two intensity values : black (intensity 0) and white (intensity 1) to form a sequence of projection patterns, so that each point of the object surface has a unique binary code. In general, n patterns can encode 2^n fringes. Figure I.4 shows an example of a simplified projection pattern of 4 *bits*. Once this pattern sequence is projected onto a static scene, there are 16 (2^4) unique areas encoded with unique bands. The 3D coordinates (X, Y, Z) could be calculated for the 16 points along each horizontal band, forming a complete 3D image frame.

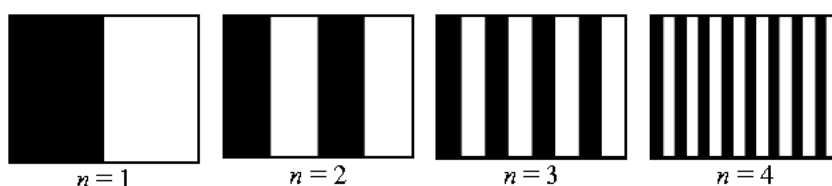


Figure I.4 Example of 4 bits binary coding [TaML14]

The choice of Gray-code is motivated by its capacity to scan inter-reflections [XuAl09]. Let's consider the following examples: if a point on the scene is in shadow, then it has zero intensity under any illumination pattern. However, due to inter-reflections from other surfaces, the pixel might store a large intensity value and thus be incorrectly decoded. The Gray-code is robust against those problems compared to phase-shifting.

I.4. Design and conception of an optical 3D measurement system

I.4.1. Introduction

Most commercial scanners (EINScan Pro [Eins00], HandySCAN 3D [Crea00], David Starter-kit [Davi00], Gocator [Lmig00], GOM Atos inspect [Atos00]) provide limited use for specific applications, and they are usually unusable for other use-cases and/or environments (Figure I.5). For example, some recent solutions integrate both a fixed 3D scanner and a rotating table for the repositioning of the scanned part [Davi00]. These systems are frequently used for small size parts and lead to a better registration result since multiple point of views are recorded [SeDP17]. For LVP scanning, the use of a rotating table requires complex mechanical configurations due to its large dimensions and its weight. In addition, the LVP could be deformed or damaged during the movement.

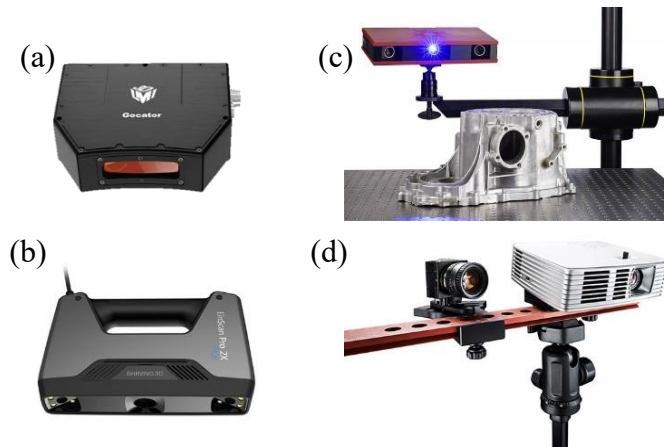


Figure I.5 **Portable** 3D scanners: (a) *Gocator SL scanner* (costs around 15k €), (b) *EINScan pro 2X* (~6k €), **Fixed** 3D scanners: (c) *GOM Atos core* (>33k €), (d) *David scanner* retails (~4k €)

Several studies have been conducted on the compactness and portability of 3D scanners, as they could be integrated in manufacturing processes to detect anomalies in real time. They are designed with specific mechanical configurations (camera/projector positions and orientations) and factory calibration strategies [VBRF21]. The principle of those 3D scanners is based on the exploitation of some predefined intrinsic and extrinsic parameters used to convert a set of

images to a 3D point-cloud. Those parameters are inaccessible and difficult to evaluate because the 3D scanners are factory calibrated. Therefore, the calibration traceability cannot be established, and, the requested high precision cannot be guaranteed and achieved. Consequently, a prototype of SL scanning system has been developed while providing a full traceable chain for LVP quality control to the SI metre definition.

The workflow of the 3D scanner development is described as following:

- (1) the developed system is composed of industrial optical components useful in industrial environment;
- (2) the 3D scanning of LVP with high accuracy;
- (3) the aimed scanning speed of ms;
- (4) the spatial resolution of 100 μm to collect dense scanning (high density point-cloud);
- (5) the system should be compact to be used in any displacement.

I.4.2. Design of the traceable 3D scanner

The designed 3D scanner integrates two industrial cameras (a) and one pattern projector (b) (Figure I.6). The use of two industrial cameras could guarantee better spatial redundancy [IfAw12] and more accurate results. Furthermore, the term ‘industrial’ is formally used for optical components that have been customized to endure severe conditions such as temperature variation and/or dust. One additional constraint regarding the selection of the proper optical components is related to the expected spatial resolution that depends on both the projector and the camera pixel resolutions. Cameras have typically a higher pixel resolution than projectors, which is a limiting factor for such SL systems [WSRK11]. Therefore, the pixel resolutions must be comparable to the used camera.

Several angular configurations can be adopted for the developed system illustrated in Figure I.6: the camera rotational frame (c) along the x-axis allows to match both cameras field of views (FoVs) such as the same scene is observed twice. Here, the two industrial cameras FoVs overlap can vary between 40 % (for parallel configuration) and 100% (when an angular configuration is adopted). One additional projector rotational frame (d) along the vertical z-axis allows to project the fringe in the cameras FoVs.

The selected cameras are XIMEA MQ013rg-e2 equipped with a digital lens LM8JCM_V of 8.5 mm focal length. This camera has a pixel resolution of 1280 \times 1024 pixels, and each pixel has a dimension of 5 \times 5 μm^2 with a frame rate of 60 per second (fps). The choice of the camera is motivated by its performance in several applications and environments [Xime00]. The chosen

projector is a DLP Lightcrafter 4500 for which the native pixel resolution is about 912×1140 pixels with a projection rate of 120 Hz [Dlp100]. The projector has been selected with respect to two constrains: (1) the dimensions of the projector allows it to be included in a compact and portable 3D scanner; (2) the pixel resolution of the projector is comparable to that of the camera to avoid interferences due to the difference between the resolutions. The cameras-projector assembly (cf. Figure I.6) is supported by a rigid supporting frame made of aluminium (e) to avoid mechanical deformation of the system during the scanning process. The system is set up on the end effector of an industrial robot using the fixing part (f). Additionally, 6 optical spheres (g) have been fixed on the supporting frame while tracking the poses of the 3D scanner in the measurement volume by the mean of four laser rangefinders.

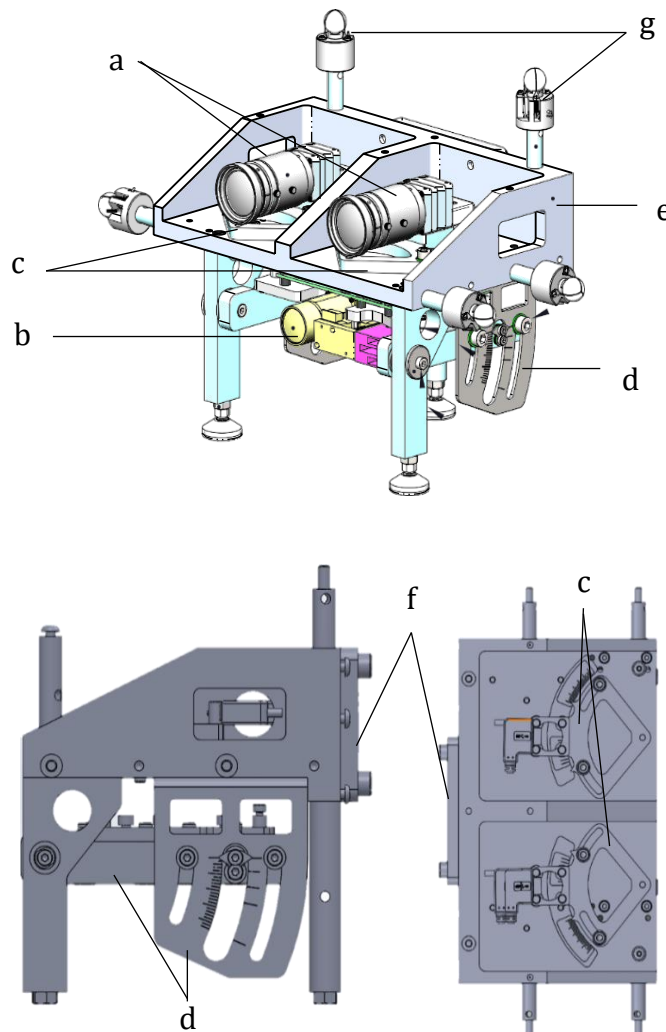


Figure I.6 Design of the 3D scanner: (a) industrial cameras; (b) projector; (c) Camera rotational frame; (d) Projector rotational frame; (e) aluminium mounting frame; (f) Scanner-robot fixing part; (g) Laser rangefinder targets

I.4.3. Resolution of the traceable 3D scanner

I.4.3.1. Spatial resolution of imaging sensors

A flat surface located at two scanning distances d_1 and d_2 from the camera perspective are considered as illustrated in Figure I.7. For the selected XIMEA MQ013rg-e2 camera, the pixel dimensions are $5 \times 5 \mu\text{m}^2$ and the focal length is $f = 8 \text{ mm}$. If the flat surface is placed at a distance $d_1 = f$, each pixel of the sensor covers a $5 \times 5 \mu\text{m}^2$ from the flat surface. When the object is moved away by a distance d_2 (eq.I.1) from the XIMEA MQ013rg-e2 (where k is a positive integer), the pixel covers a surface of $5k \times 5k \mu\text{m}^2$.

$$d_2 = f \times k \text{ (mm)} \quad \text{I.1}$$

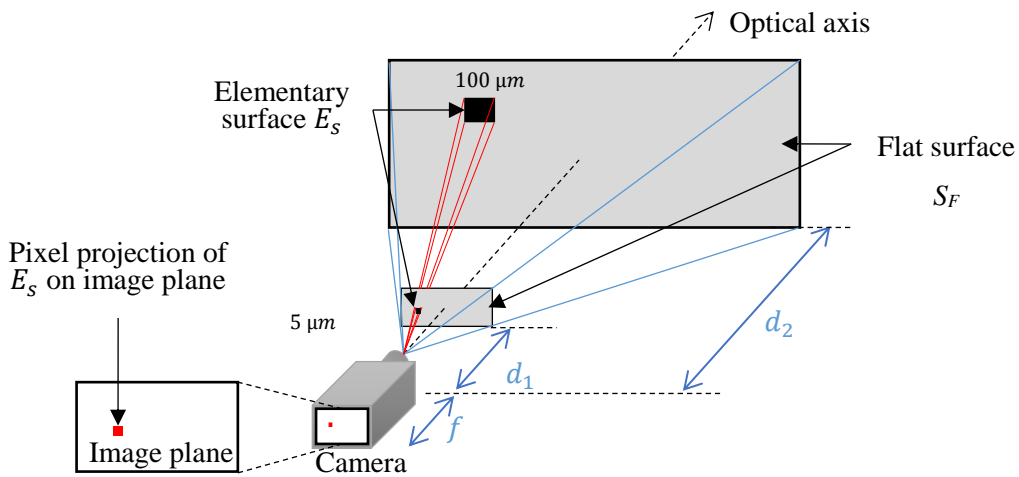


Figure I.7 Effect of the distance d_2 on the spatial resolution

The fixed distances between the components of the 3D scanner are selected as to have a compact system that could be easily integrate on the end-effector of an industrial robot. As the spatial resolution of the scanner is highly affected by the scanning distance (Figure I.7), the distance between both the 3D scanner and the flat surface is set to 170 mm, based on eq. I.1, where $k = 10$, as to ensure a maximum spatial resolution of $100 \mu\text{m}$.

I.4.3.2. Conceptual schematisation of the 3D scanner

Based on [Prin00], it seems well known that a large focal length value f leads to a high spatial resolution of the 3D scanner as shown in Figure I.8 where θ is the angle between the optical axis of the projector and that of the camera. In this figure, two orientations θ and θ' of the projector with respect to the camera are shown. The higher the angle θ , the nearer the camera is to the flat surface, resulting in low or high spatial resolution.

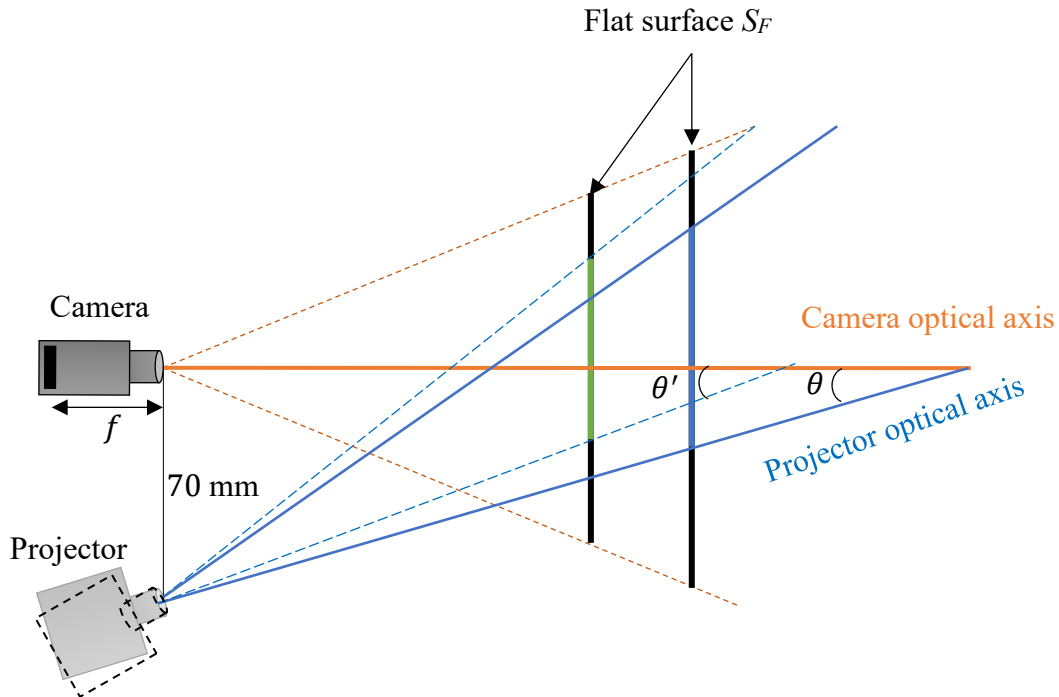


Figure I.8 Effect of projector orientation on the spatial resolution

Each camera is fixed on an angular positioning component (Figure I.9-a), to allow the study of the influence of the *overlapping area* on the performance of the 3D scanner. Furthermore, the projector is fixed on one supplementary rotational component (Figure I.9-b). Based on those rotational components, the multiple configurations that can be adopted by the elements of the 3D scanner are classified as parallel and angular configurations (also known as toed-in configuration) [Yama00, ZaPr97].

- The parallel configuration consists of placing both the cameras and the projector so that their optical axes are all parallel as shown in Figure I.10-a. The main goal of this configuration is to simplify the transformation from the projector to each camera since only translations are applied. However, the overlapping area between the projection zone and the camera FoV is rather small, and the scanning of a LVP could take several poses to generate the whole point-cloud of the surface.
- The angular configuration allows to change the overlapping area up to 100%. Thus, each camera is oriented to the projection zone so that a maximum of this projection is seen as shown in Figure I.10-b. In this configuration, the transformations between the scanner elements must all be estimated while performing an accurate 3D scanning.

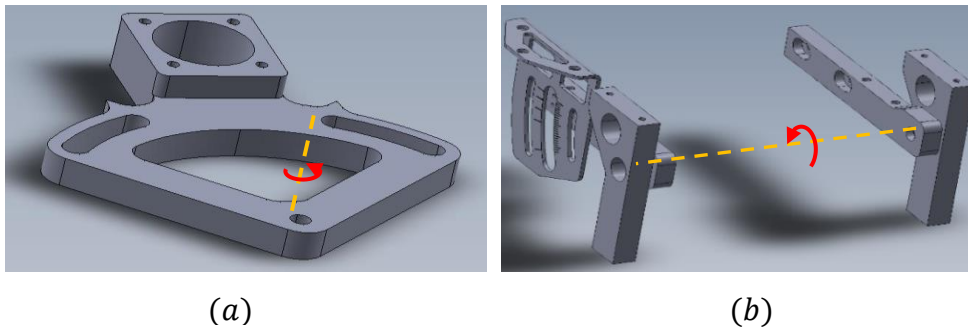


Figure I.9 (a) Camera fixing frame for rotation along the vertical axis (b) Projector fixing frames for rotation along the horizontal axis

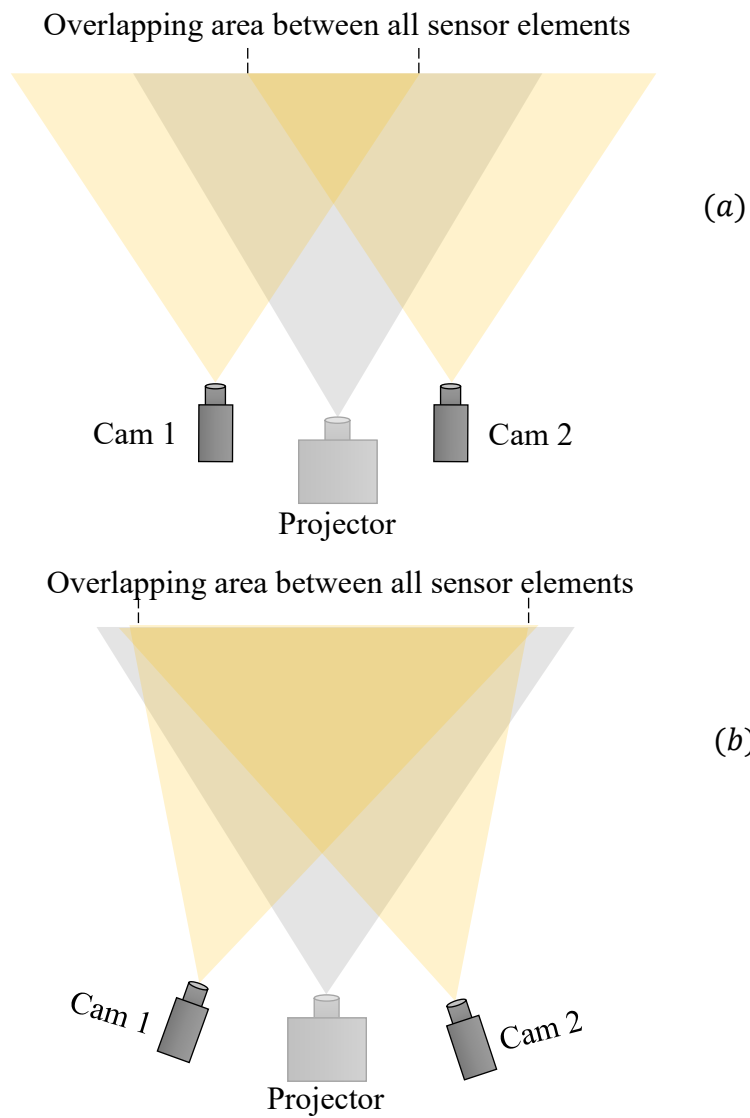


Figure I.10 (a) parallel configuration of the 3D scanner elements (b) angular configuration of the cameras with respect to the projection surface

The developed 3D scanner allows obtaining a 3D point-cloud for a surface size with an effective scanning area of $100 \times 70 \text{ mm}$. The scanning process of LVP requires to move the 3D scanner in the measurement space. In order to scan LVP over wide range, the portability of the 3D scanner should be considered. This could be achieved either manually or using a motion system such as an industrial robot, widely used in industry 4.0, especially for manufacturing and quality control applications [Cisz18].

I.4.4. Protocol for 3D scanning of large volume parts (LVPs)

The combination of multiple scans at different positions and orientations is necessary for covering the whole surface of a LVP. Therefore, a 6-axis industrial robot KAWASAKI RS03N is selected and equipped with the 3D scanner on the end-effector.

The adopted scanning procedure consists of subdividing the LVP into elementary surfaces to be scanned individually in static mode. Each elementary surface corresponds to a position and an orientation of the 3D scanner generated by the industrial KAWASAKI robot (Figure I.11).

RS03N

Maximum load	3 kg
Horizontal range	620 mm
Vertical range	967 mm
Repeatability	$\pm 0.02 \text{ mm}$
Maximum speed	6,000 mm/s



Figure I.11 Specification of the selected industrial robot KAWASAKI RS03N

The Kawasaki robot range is $967 \times 620 \times 620 \text{ mm}^3$. It has been enlarged by adding one 7th unidirectional motion axis of 1500 mm range allowing to scan LVP up to $2000 \times 600 \times 100 \text{ mm}^3$ (Figure I.12).

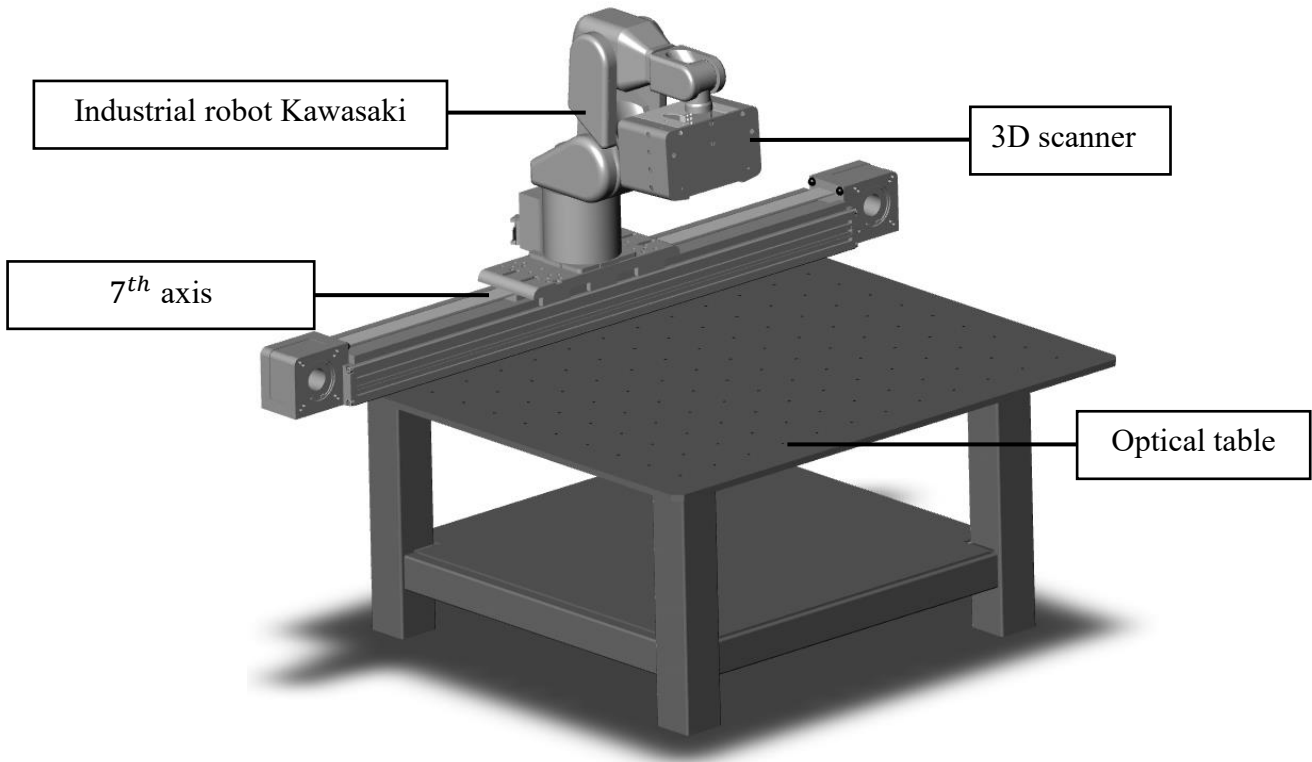
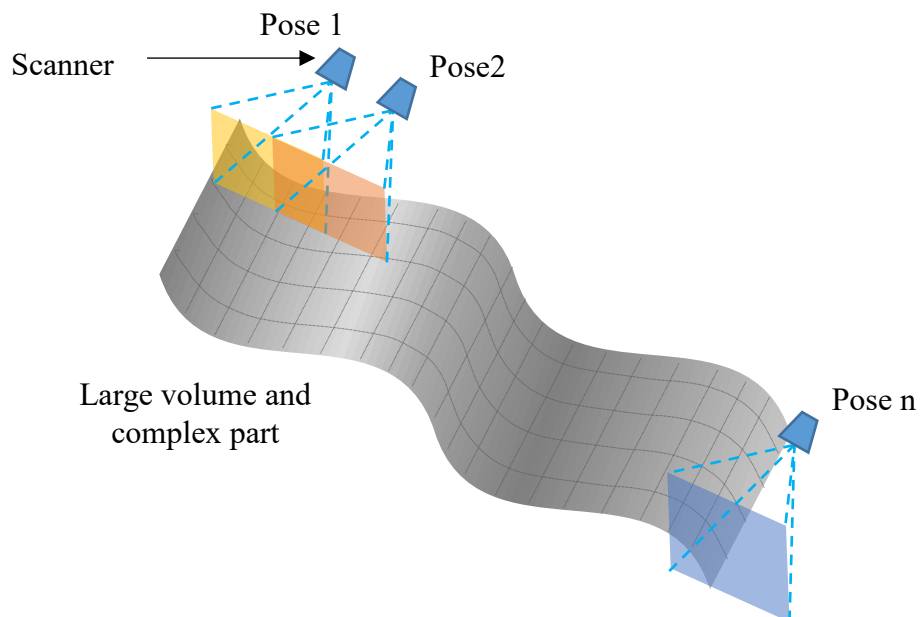


Figure I.12 Addition of a 7th axis to the robot

The suggested 3D scanning procedure to scan a LVP is illustrated in Figure I.13. The elementary surfaces are scanned in a successive way by the 3D scanner, and then the collected scans are merged together in one unique coordinate frame. One additional scanning condition with respect to [Liu06, Thom00, WYDL21] is the overlapping. It is fixed to approximately 60%, leading to an accurate estimation of the transformation between two scanner poses.



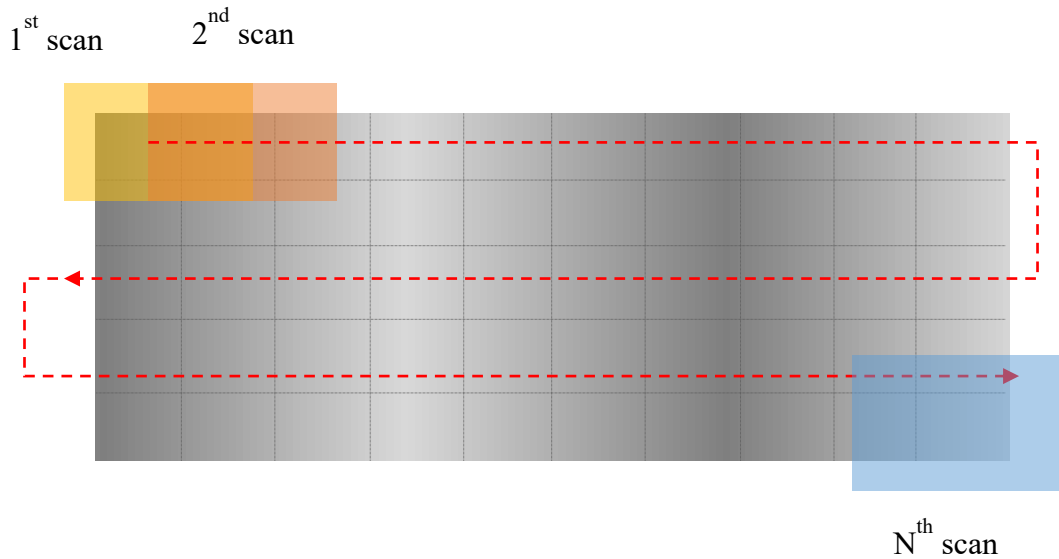


Figure I.13 Scanning procedure of large volume part

The knowledge of the 3D scanner poses allow to merge the point-clouds, when applying the point-cloud registration method.

I.4.4.1. Point-cloud registration

Registration is the process of overlaying multiple scans taken at different positions from different view angles for covering the fully scene [Bosc12, WYDL21]. Since the scans are initially generated in the camera frame, the knowledge of relative positions and orientations between views can be used for merging the 3D scans in the same frame.

The transformation between two scanner's poses should be estimated as to align two scans with a common overlapping area. There are two ways to register point clouds: (1) by *tracking the poses* of the scanner in the measurement space (2) or by using *feature based registration*.

- (1) Tracking-base systems such as industrial robots and displacement sensors including rangefinders, are usually used for an initial estimation of the transformation between two poses [JŠŠŠ15].
- (2) Feature based registration can be performed by manual matching, target-based matching, or feature-based matching [Bosc12].
 - The manual registration requires the user to manually select the features in both point-clouds and to match them. This method is time consuming and the registration accuracy is strongly affected by the user. If the points are inaccurately selected, the alignment result is highly affected [MTLP12].

- The target-based method consists of adding identifiable targets on the mechanical part, which can be easily recognizable in both point-clouds and aligned. This method requires at least three targets visible in the overlapping area from the perspective of the camera, and the physical targets need to be placed (usually glued) on the mechanical part which might affect the surface quality [LLSK06].
- The feature-based method is an automatic alignment performed by detecting and extracting 3D features from different datasets that can be used for alignment [RDHV07]. This method does not require any manual operation nor the use of physical markers to register the scans.

Since an industrial robot is used for the positioning of the 3D scanner, the tracking-based method is selected for point-clouds registration.

I.4.4.2. Proposed tracking-based registration

Tracking the poses of the 3D scanner can be carried out through the returned coordinates of the end-effector. The estimation of the transformation from the camera to the end-effector and from the end-effector to the robot base could be used to transform the 3D scans to the robot base. Let R_B be robot base coordinates frame, R_E the robot end-effector frames and R_{C1} and R_{C2} both cameras frames (Figure I.14).

- 1- From camera to end-effector: since the point-cloud is generated in the camera frame, the estimation of the transformation from the cameras to the end-effector noted T_{C1E} and T_{C2E} allows to transform the point-clouds from the camera frame to the robot end-effector. This transformation could be estimated using the CAD model of the 3D scanner. However, some geometric and non-geometric errors such as manufacturing and assembly errors, might cause a deviation from the CAD transformation.
- 2- From end-effector to robot base: once the transformations T_{C1E} and T_{C2E} are estimated, the initial alignment of the point-cloud could be performed using the coordinates of the robot end-effector. The selected KAWASAKI robot returns the Euler angles and translations of the transformation T_{EB} from the end-effector coordinates R_E to the robot base R_B . The estimated transformation T_{EB} is inaccurate due to positioning errors. Industrial robots are known to have a sub-millimetre repeatability (20 μm for the selected robot in this experience), but their accuracy is rather large (few millimetres) [DaGD04, PiPi18a]. According to [CaAn90, RaPR20, WCWM19], documents published by the International Federation of Robotics (IFR) and the IEEE Robotics and

Automation Society (IEEE/RAS) [DGLL20, JuKn90], geometric and non-geometric sources of error (thermal gradient, mechanical behaviour, vibration, etc.) are all causes of accuracy degradation.

The transformations T_{C1E} , T_{C2E} and T_{EB} could be used to register the returned scans with an error up to few millimetres (corresponding to the robot positioning error).

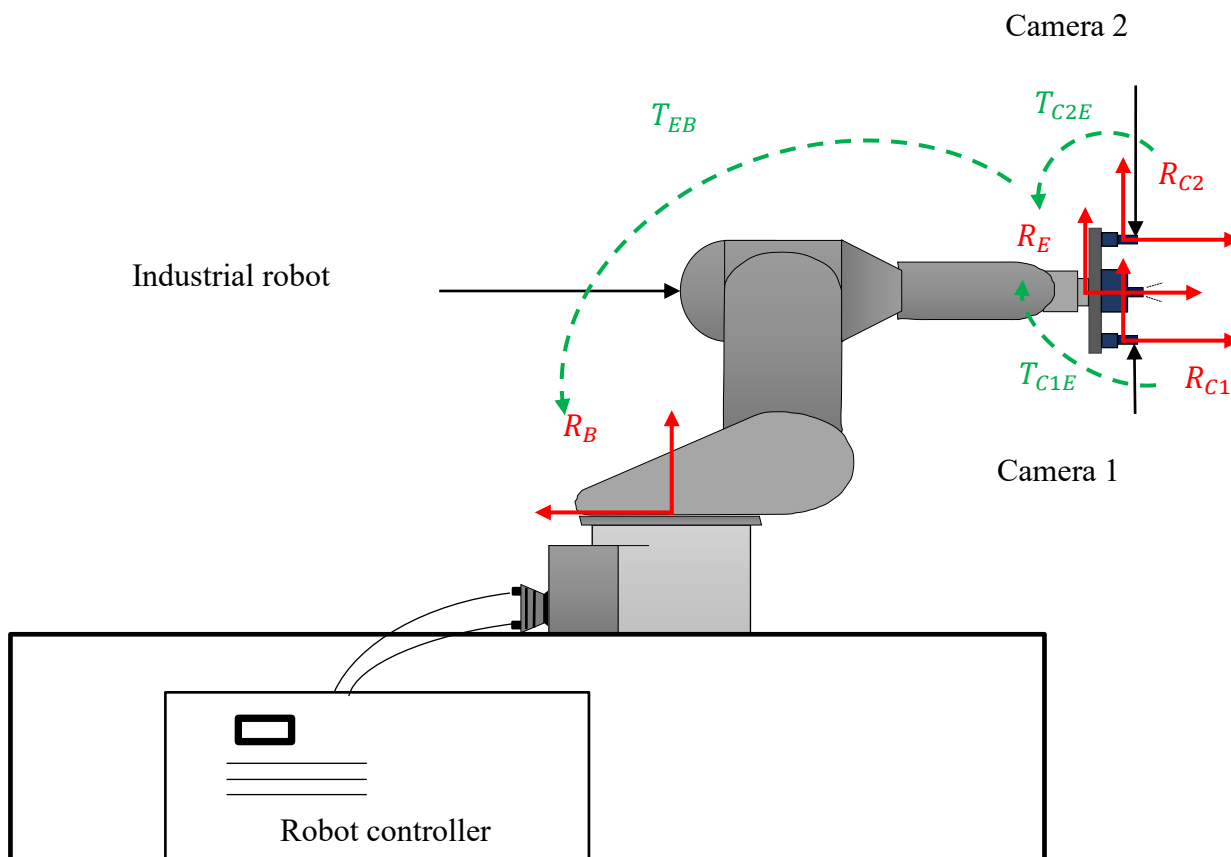


Figure I.14 Illustration of the transformation from the robot end-effector to the robot base

As robots are used in industries due to their good repeatability (0.02 mm), they are rather inaccurate when estimating the positions and orientation of the end-effector (2 mm) [DaGD04, PiPi18b]. Hence, an external tracking system can be used to accurately track the 3D scanner.

I.4.4.3. Scanner tracking using laser rangefinders

Laser rangefinders work on the principle of Time of Flight (ToF) technique [HaDu14]. The distance is determined by measuring the phase accumulated by a Radio Frequency (RF) wave that propagates in the air through a laser beam. This propagation in free space is performed by means of an optical beam that gets reflected on a target before converting it to an electric signal

by a photodetector. Thus, the position and orientation of the targets in the space of the rangefinders is determined thanks to the principle of multilateration [GuTW20a].

The laser rangefinder accuracy outperforms the robot accuracy, thus it could be used as an external tracking device. A spherical retro-reflective glass target has been added to the scanner to track the position of the 3D scanner using laser rangefinders. The laser rangefinders have an uncertainty of $4.3 \mu\text{m}$ for a distance of 7 m. Figure I.15 shows the CAD of the laser rangefinder developed at CNAM-LCM.

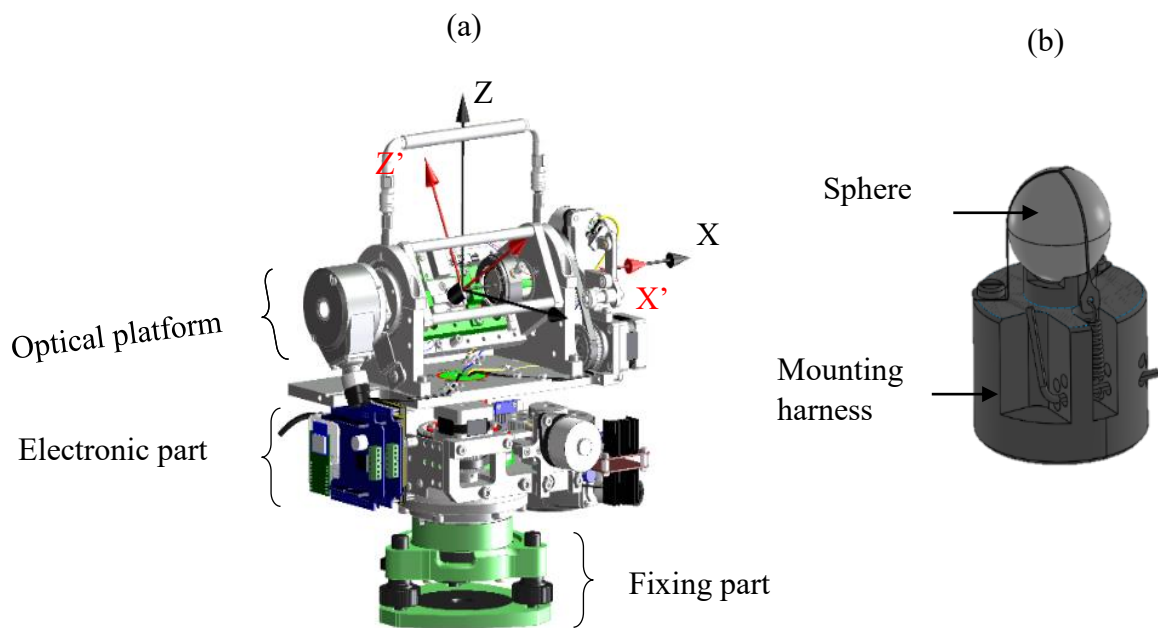


Figure I.15 (a) Design of laser rangefinder, (b) spherical glass target [GuTW20a]

Four laser rangefinders have been used to track the pose of the 3D scanner. Each laser rangefinder is fixed on a rigid mechanical structure (also called fixing plot (Figure I.16-a)). The tracker needs to be initially aligned with the optical spheres on the robot at each pose. Afterwards, the poses of the 3D scanner are estimated using the triangulation principle [WuHC06].

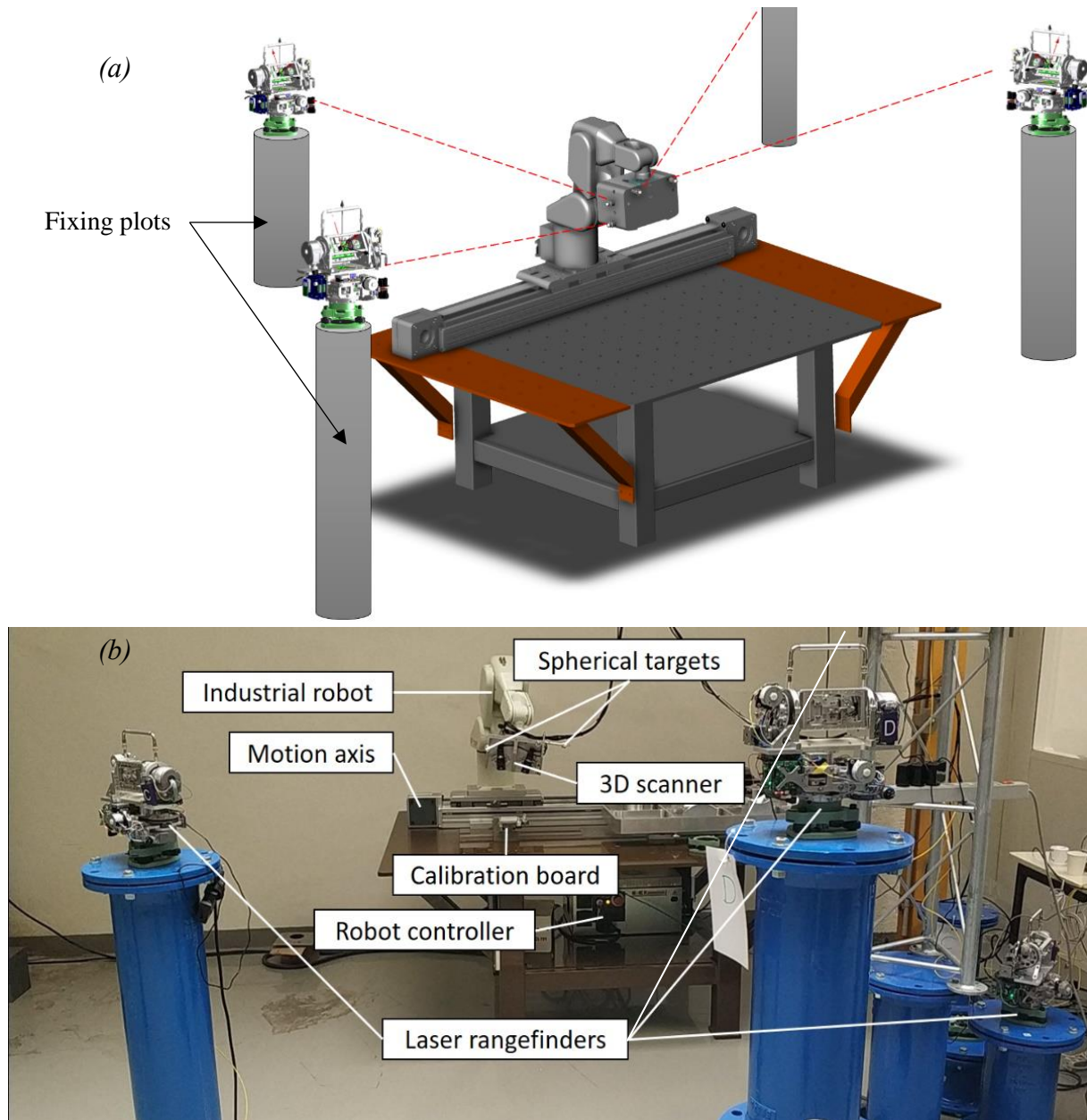


Figure I.16 General overview of the developed 3D scanning system

In order to estimate the 6 degrees of freedom (DoF) (3 rotations and 3 translations), at least 3 spheres need to be fixed on the 3D scanner. Nevertheless, at certain poses, a sphere could be hidden in the field of view of one of the rangefinders. Therefore, a 4th sphere was added in order to solve this issue. In addition, a supplementary fixing structure of the calibration board has been added on the optical table to perform the calibration of the 3D scanner without having to disassemble the system (Figure I.16-b).

I.5. Conclusion

This section provides an overview on camera scanning systems. A classification of structured light techniques is presented and investigated as to select the most appropriate scanning method for mechanical quality control. For the scanning of large volume mechanical parts, the active scanners category is considered due to its accuracy compared to the passive one. Active photogrammetry groups includes several methods such as interferometry, time of flight and SL. The accuracy of each method depends on the technology and the complexity of the post-processing software. A compromise between cost, accuracy and speed of scanning leads to the choice of structured light-based 3D scanning. Structured light is an active technique used to provide 3D information of close-range scenes by projecting a well-known pattern (such as vertical fringe or circle pattern) and analysing its deformation caused by the shape of the mechanical part.

One objective of this work concerns the development of an accurate scanning system for the scanning of large volume part. Two cameras and one fringe projector supported by rigid aluminium elements have been designed so that the system could be equipped on the end-effector of an industrial robot. The industrial robot serves as a positioning system to place the 3D scanner in the measurement space. For large volume parts, multiple areas are scanned individually, a registration is then applied to merge the scans into one coordinate system. The registration consists of estimating the transformations between successive 3D scans. Therefore, the tracking of the scanner pose during the measurement is required and could be performed using an external system. This step could be achieved with the returned robot data or by using an external tracking system. Since industrial robots have low accuracy, they can be used as manipulators while the tracking is accomplished using a laser rangefinder. Spherical targets have been setup on the 3D scanner so that it could be tracked by four laser rangefinders. The estimated uncertainty of these tracking systems is around $5\ \mu\text{m}$ for close-range applications, which improves the process of alignment/registration.

The 3D scanning of any mechanical part is based on the triangulation principle. Therefore, it requires the exploitation of a number of parameters: the internal configuration of the cameras and the projector as well as the rigid transformations between the scanner elements. The process involved in the estimation of cameras and projector parameters, called *geometric calibration*, will be detailed and discussed in the next chapter.

CHAPTER . II Camera model and sensor calibration

Calibration represents the process that lead to estimate the parameters required for accurate use of the 3D scanner with respect to the geometrical model of the imaging sensor. Therefore the calibration allows to establish the relationship between a point from the scene and its projection on the image plane. This chapter contains mainly two sections: (1) modelling and calibration of a single camera, (2) modelling and calibration of an active and passive stereo system.

CHAPTER . II Camera model and sensor calibration.....	27
II.1. Introduction	28
II.2. Modelling and calibration of a single camera	28
II.2.1. How does a camera work?.....	28
II.2.2. Perspective projection fundamentals.....	29
II.2.3. Lens distortion model.....	32
II.2.4. Camera calibration.....	35
II.3. Modelling and calibration of stereo vision systems	46
II.3.1. Stereo vision model	47
II.3.2. Calibration of stereo systems.....	49
II.3.3. Inverse camera/projector calibration	49
II.4. Conclusion.....	52

II.1. Introduction

During the past decades, the imaging technologies have gone further regarding the improvement of picture quality and acquisition frequency. In this chapter, a focus on the geometric aspect of optics is pointed as to understand the principle of 3D scanning.

The selected stereovision system involves the use of two optical devices (camera-camera or camera-projector) to 3D scan a LVP. The 3D scanning of LVP requires the knowledge about the relationship between points in the world coordinates frame and the pixels in the image plane. The relationship could be established through the geometric modelling of the imaging sensor. Several camera models have been proposed in the literature. In this chapter, both the selection of the appropriate model and the calibration procedure are detailed.

II.2. Modelling and calibration of a single camera

II.2.1. How does a camera work?

In computer vision, the two main categories of digital imaging sensors are: Charge Coupled Device (CCD) and Complementary Metal Oxide Semiconductor (CMOS) [Shug20]. Both technologies are based on the same acquisition principle, which consists of storing the light intensity on an element of the sensor called “pixel”. The difference between the technologies is the light intensity recording process. For CCD, the charge on each pixel is read out and later converted to intensity. For CMOS sensors, each pixel has its own analog-digital converter. CMOS are the most commonly used in industrial applications. This is due to their low power consumption, better integration on electronic systems and higher acquisition speed compared to CCD [Shug20].

Cameras apply the principle of light detection [Howc01, IhRM16]. It contains two main components: the camera body and the camera lenses (Figure II.1). Some of the light rays generated by the light source is absorbed by the LVP and the rest is reflected. Part of the reflected rays pass through the camera lenses. The camera lenses are used to converge lights to the imaging sensor. It is composed of an assembly of lenses and systems such as the diaphragm and the focal length adjusting system. Then, an image is produced at the imaging sensor. The imaging sensor is composed of multiple small elements called pixels structured in a 2D grid. Each pixel records light information such as the intensity, the colour, etc. The imaging sensor records 3D world object reflections in the form of light intensity.

In order to recover the 3D information (coordinates of the scanned points in the LVP) from an image, the knowledge of the geometrical transformation of light rays from its reflection on a surface to its arrival on the pixel is indispensable. In this context, the geometrical aspect of the optical system, named *geometrical optics*, is analysed. Geometrical optics is defined as the model of optics that describes the propagation of light without taking into account other phenomena such as interference, diffraction, etc. effects [Pedr08]. The closest model that defines these geometric properties of a camera is known as the perspective projection model (or perspective model).

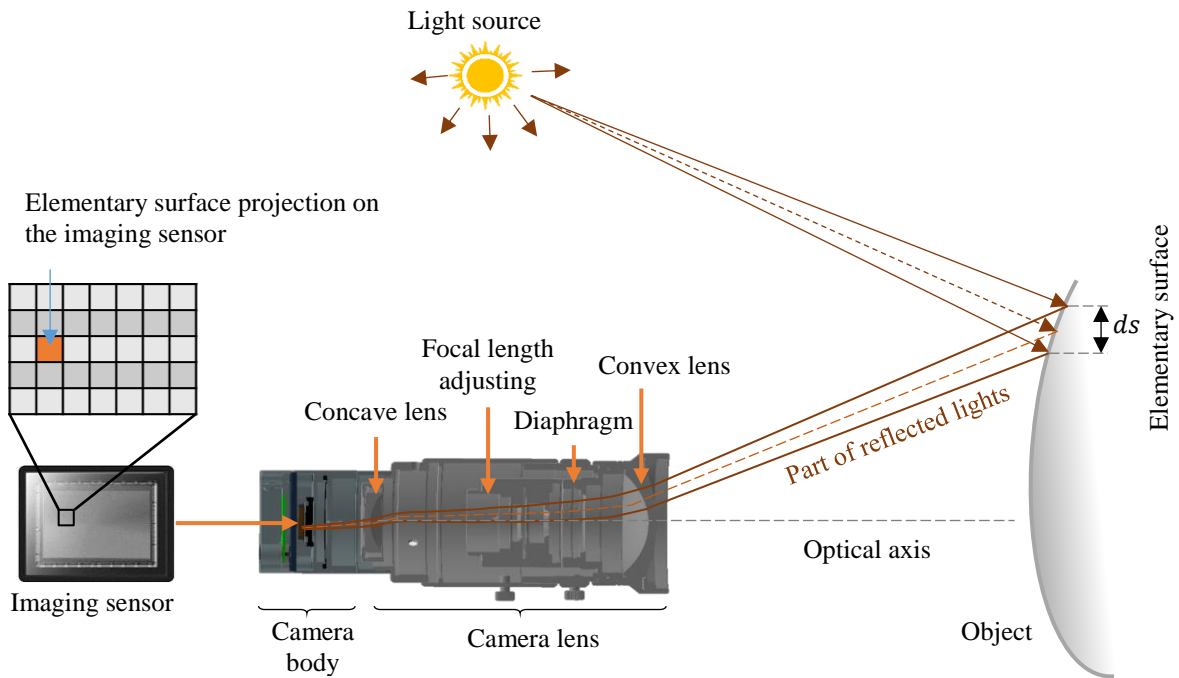


Figure II.1 Light recoding using an industrial camera Ximea [Xime00]

II.2.2. Perspective projection fundamentals

Considering the perspective model shown in Figure II.2, the projected point $M_i(X, Y, Z)$ from the real-world coordinates system on the image plane is $m_i(u, v)$ through the *optical centre* O (also named perspective centre). In geometrical optics, the optical axis is defined as the perpendicular line to the image plane passing through the optical centre O . It is considered as the unique axis of rotational symmetry for an imaging system [Stur14]. The orthogonal projection of O onto the image plane is called *principal point* C . The distance between O and the point C is defined as the *focal length* f .

The relationship between point $M_i(X, Y, Z)$ and its projection $m_i(u, v)$ is expressed by eq. II.1:

$$\frac{v}{Y} = \frac{u}{X} = \frac{f}{Z} \quad \Rightarrow \quad u = \frac{fX}{Z}; \quad v = \frac{fY}{Z} \quad \text{II.1}$$

In homogenous coordinates, the relation that defines the projection from the world frame to the image plane is expressed by eq. II.2:

$$\begin{pmatrix} u \\ v \\ 1 \end{pmatrix} = \begin{bmatrix} f & 0 & 0 & 0 \\ 0 & f & 0 & 0 \\ 0 & 0 & 1 & 0 \end{bmatrix} \begin{pmatrix} X \\ Y \\ Z \\ 1 \end{pmatrix} \quad \text{II.2}$$

The defined model corresponds to an ideal camera where the optical axis is assumed to cross the image plane in the centre of the image. Practically, imaging sensors have mechanical imperfections that cause geometrical deviations between the intersection of the optical axis, the image plane and the actual image centre. This geometrical deviation is called ‘‘principal point offset’’.

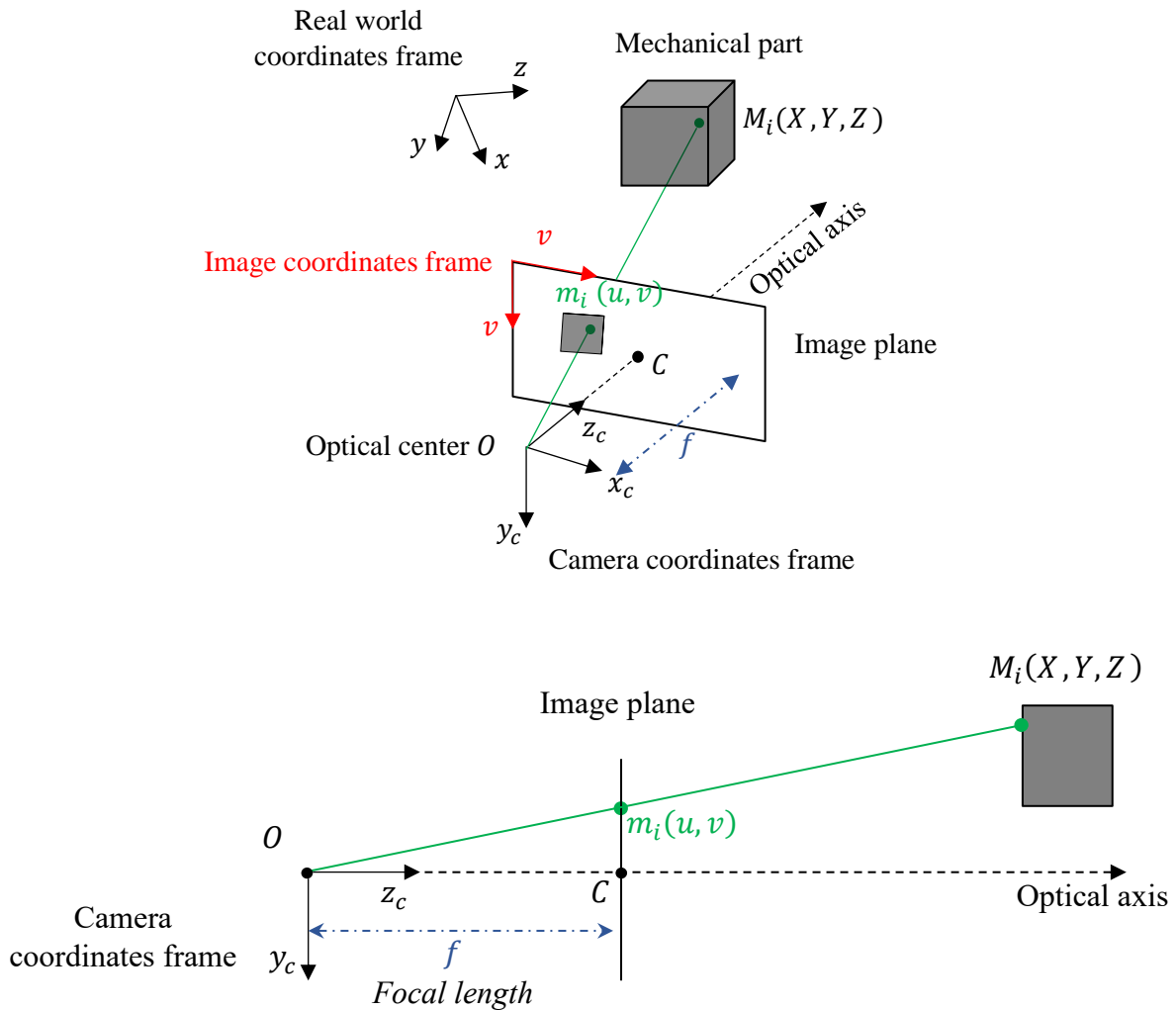


Figure II.2 Perspective projection modelling inspired form [MCHD07]

II.2.2.1. Model refinement: Principal point offset

The principal point is defined as the pixel coordinates of the point of intersection between the optical axis and the image plane [CIWF98]. Let (c_u, c_v) be the pixel coordinates of the principal point. The pinhole model is expressed in homogenous coordinates as (eq. II.3):

$$\begin{pmatrix} u \\ v \\ 1 \end{pmatrix} = \begin{bmatrix} f_u & 0 & c_u & 0 \\ 0 & f_v & c_v & 0 \\ 0 & 0 & 1 & 0 \end{bmatrix} \begin{pmatrix} X \\ Y \\ Z \\ 1 \end{pmatrix} = A \begin{pmatrix} X \\ Y \\ Z \\ 1 \end{pmatrix} \quad \text{II.3}$$

- c_u, c_v : Pixel coordinates of the principal point
- f_u, f_v : Focal length in pixel
- A : the camera matrix which contains the parameters of the camera

The pinhole model is given by (eq. II.4) when decomposing the A matrix as following:

$$\begin{aligned} \begin{pmatrix} u \\ v \\ 1 \end{pmatrix} &= \begin{bmatrix} f_u & 0 & c_u \\ 0 & f_v & c_v \\ 0 & 0 & 1 \end{bmatrix} [I \ 0] \begin{pmatrix} X \\ Y \\ Z \\ 1 \end{pmatrix} \\ &= K [I \ 0] P \end{aligned} \quad \text{II.4}$$

where K is referred to as the intrinsic matrix.

The obtained model assumes that the camera coordinates frame is a right-handed Cartesian coordinate system, meaning that the axis x_c, y_c and z_c are orthogonal. In practice, the angles between the axes might slightly diverge from 90° .

II.2.2.2. Model refinement: image skewness

The so-called image skewness allows to model the pixel layout that occurs from skewed image axes (theoretically supposed to be 90°) [Jori00][HaSa00]. Depending on the aimed accuracy, the skewness is mainly caused by the manufacturing errors of the imaging sensors. Let s be the skewness between the image axes, then the intrinsic matrix becomes:

$$K = \begin{bmatrix} f_u & s & c_u \\ 0 & f_v & c_v \\ 0 & 0 & 1 \end{bmatrix} \quad \text{II.5}$$

II.2.2.3. Model refinement: camera rotation and translation

Practically, a motion matrix from world coordinates to camera coordinates system must be defined in order to make the camera system coincide with the world system as $[R \ T]$, where R

is the rotation matrix and T is the translation vector. The full camera matrix is then expressed in eq. II.6 [HaSa00]:

$$\begin{pmatrix} u \\ v \\ 1 \end{pmatrix} = K[R \ T] \begin{pmatrix} X \\ Y \\ Z \\ 1 \end{pmatrix} \quad \text{II.6}$$

where:

$$R = \begin{pmatrix} r_1 & r_2 & r_3 \\ r_4 & r_5 & r_6 \\ r_7 & r_8 & r_9 \end{pmatrix} \quad T = \begin{pmatrix} t_x \\ t_y \\ t_z \end{pmatrix} \quad K = \begin{bmatrix} f_u & s & c_u \\ 0 & f_v & c_v \\ 0 & 0 & 1 \end{bmatrix}$$

$r_i, i \in [1,9]$ are the elements of the rotation matrix function of the Euler rotational angles (α, β, γ) along x, y and z axes respectively, and (t_x, t_y, t_z) are the translations from the world frame to the image coordinates frame.

II.2.3. Lens distortion model

The pinhole model describes a camera for which all the light pass though a single point and no lens. In practice, the optical lenses are used to converge light to the pixels on the imaging sensor. Those lenses have geometrical errors causing deviation of the reflected light called lens distortions [KZBŠ17, NiAg12, StLD18, TGMM17]. The lens distortion models were proposed by Conrady in 1919 [Conr19] and re-studied then re-modelled by Brown in 1971 [Brow00]. This model is widely adopted by the computer vision and photogrammetry communities.

Two types of distortion can be distinguished as specified in [PeKo02, Stew21]: the *radial distortion* related to the symmetry of the lens, and the *tangential distortion* related to the imaging sensor and parallelism of the optical lens's axes. Thus, the radial distortion is caused by the spherical shape errors of each lens [YMYW14], while the tangential distortion is caused by the decentring and non-orthogonality of the lenses with respect to the optical axis [DrLe16] [SwNa00]. The effect of both radial and tangential distortion on a projected point in the imaging sensor is illustrated in Figure II.3, where dt is the tangential error and dr is the radial error.

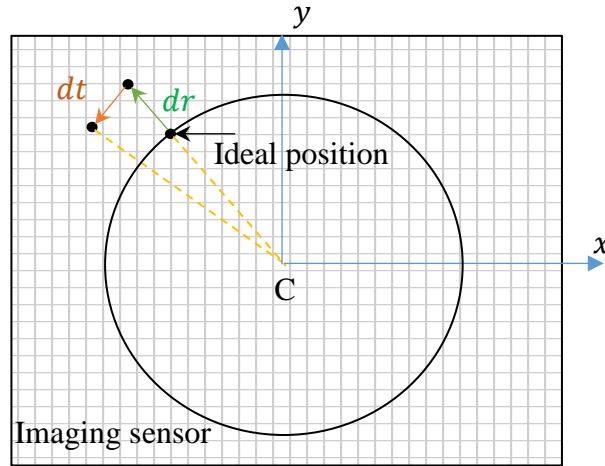


Figure II.3 Tangential and radial distortion effect on an ideal position of a pixel [LZHT13]

II.2.3.1. Radial distortion

In optics, the radial distortion can be classified in two different categories: the barrel distortion and the pin-cushion distortion (Figure II.4) [Mour16]. The barrel distortion corresponds to negative distortion values (Figure II.4.a). They are commonly seen in wide-angle lenses because the FoV is wider compared to the size of the imaging sensor. The more the points move away from the centre C of the image, the more the inward curvature of the lines becomes significant. However, unlike the first type of distortion, pincushion corresponds to positive values and lines are curved outward the image centre (Figure II.4.b).

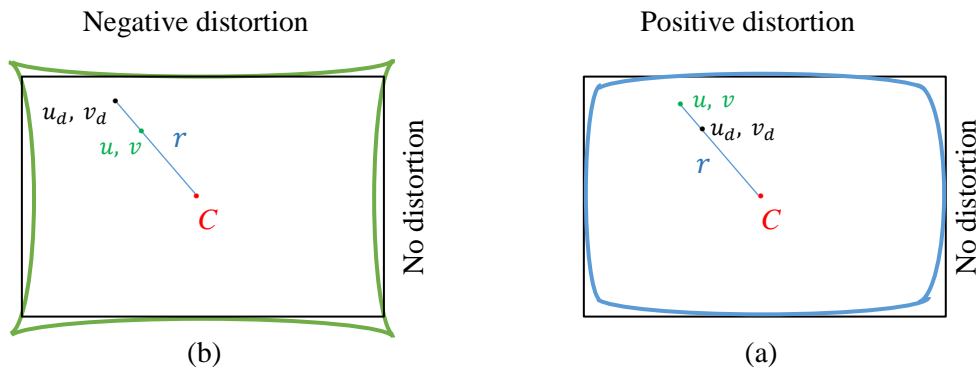


Figure II.4 Radial distortion: positive distortion called "pincushion", negative distortion called "barrel" (inspired from [Unde20])

The radial distortions are modelled by eq. II.7 [Unde20]:

$$\begin{aligned} u_d &= u(1 + k_0r^2 + k_1r^4 + k_2r^6) \\ v_d &= v(1 + k_0r^2 + k_1r^4 + k_2r^6) \end{aligned} \tag{II.7}$$

Where:

- u_d, v_d : distorted point
- u, v : undistorted pixel location
- k_0, k_1 and k_2 : coefficients of radial distortion
- $r^2 = u^2 + v^2$

Usually, the two coefficients of k_0 and k_1 are sufficient to correct the effects of radial distortion [WSZL08]. However, for the most distorted cases such as fisheye lenses (lenses with a very short focal length and therefore a large angle of view, up to 180 °), the third coefficient k_2 could be considered for a better correction of the image.

II.2.3.2. Tangential distortion

Tangential distortion occurs when the lens is not parallel to the imaging sensor [Brow00] [What00] (Figure II.5). They are also called decentring errors because the primary error source comes from the assembly of the camera and the lens.

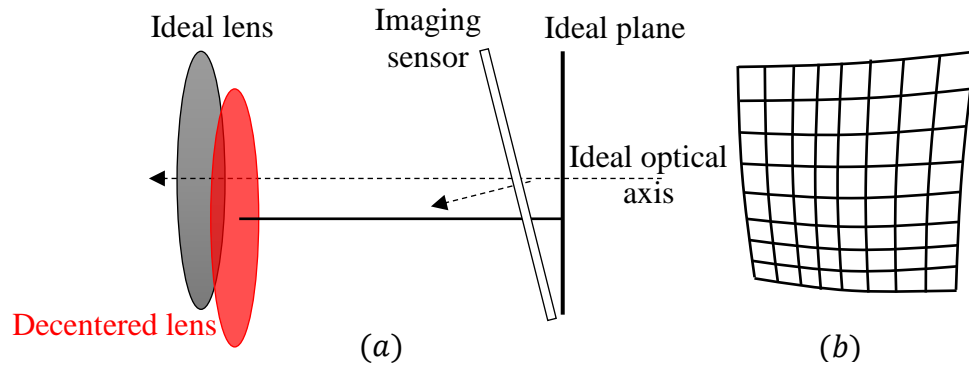


Figure II.5 *Illustration of tangential distortions: (a) decentring and non-parallelism error of the camera assembly (b) effect of tangential distortion of the image [Sinh00]*

The tangential distortions model is described in eq. II.8.

$$\begin{aligned} u_d &= u + [2p_1uv + p_2(r^2 + 2u^2)] \\ v_d &= v + [p_1(r^2 + 2v^2) + 2p_2uv] \end{aligned} \tag{II.8}$$

- u_d, v_d : distorted point
- u, v : undistorted pixel location
- p_1 and p_2 : coefficients of tangential distortion
- $r^2 = u^2 + v^2$

From both radial and tangential model, the global distortion model can be written as following (eq. II.9):

$$\begin{pmatrix} u_d \\ v_d \end{pmatrix} = (1 + k_1 r^2 + k_2 r^4 + k_3 r^6) \begin{pmatrix} u \\ v \end{pmatrix} + \begin{pmatrix} 2p_1 uv + p_2(r^2 + 2u^2) \\ p_1(r^2 + 2v^2) + 2p_2 uv \end{pmatrix} \quad \text{II.9}$$

II.2.4. Camera calibration

In machine vision, the used camera system requires a geometric calibration before performing any 3D scanning of a mechanical part. A geometric camera calibration is the process of estimating the camera parameters that are useful to generate an accurate image of the scene on the imaging sensor [HaZi04]. Those parameters are categorised into: (1) **intrinsic** camera parameters that describe the internal geometry of the camera such as the focal length f_u, f_v , the principal point pixel coordinates (c_u, c_v) and lens distortions coefficients k_0, k_1 , and (2) the **extrinsic** parameters that define the position and orientation of the camera with respect to the LVP coordinate frame [Burg16].

Fraser [Fras97] proposed a self-calibration method adopted for medium and large range applications such as city mapping and drone photogrammetry. The estimation of the internal parameters of the camera uses unstructured images of the scene instead of using a calibration target. The self-calibration is practical for applications that require a large FoV, since there is no need of calibration targets, however it is less accurate compared to Tsai and Zhang methods (Zh-method) [Tsai87a, Zhan00a]. Tsai and Zh-method proposed a geometric camera calibration method for close-range photogrammetry based on target observation. Using a known artefact named calibration grid, the perspective model parameters (also called pinhole parameters) could be estimated.

Tsai method [Tsai87a] is based on the observation of a 3D calibration grid printed with a pattern easily detectible from the camera perspective. Zhang [Zhan00a] simplifies this process by employing a 2D calibration grid instead. The camera parameters can be identified through multiple pictures taken on the 2D calibration grid.

The choice of the appropriate calibration method is fundamental when achieving accurate 3D scanning. Few comparative studies have been made to compare Zh-method and Tsai calibration [FCWC08, TiAS19]. Those comparative studies have shown a better convergence for the estimation of intrinsic parameters when using the Zh-method. Accordingly, this method is selected to calibrate the developed 3D scanner.

II.2.4.1. Zhang calibration method

The Zh-method, based on the pinhole model, is the commonly used method to calibrate cameras due to its flexibility and accuracy in estimating the intrinsic parameters [FCWC08, LWYC19, RiSa07]. The original Zh-method, based on the observation of a 2D calibration grid, includes six steps as shown in Figure II.6: (1) acquisition of a number of images on the 2D calibration grid under several poses, (2) feature points detection [Jian12, SáMS18a], (3) homography estimation using the Direct Linear Transform [Dubr09], (4) identification of the pinhole parameters using the Singular Value Decomposition [KILa80], (5) global refinement [Mitt00], and finally (6) calculation of the reprojection error. Those six steps are classified into three main stages: (1) pre-processing, (2) calibration and (3) verification.

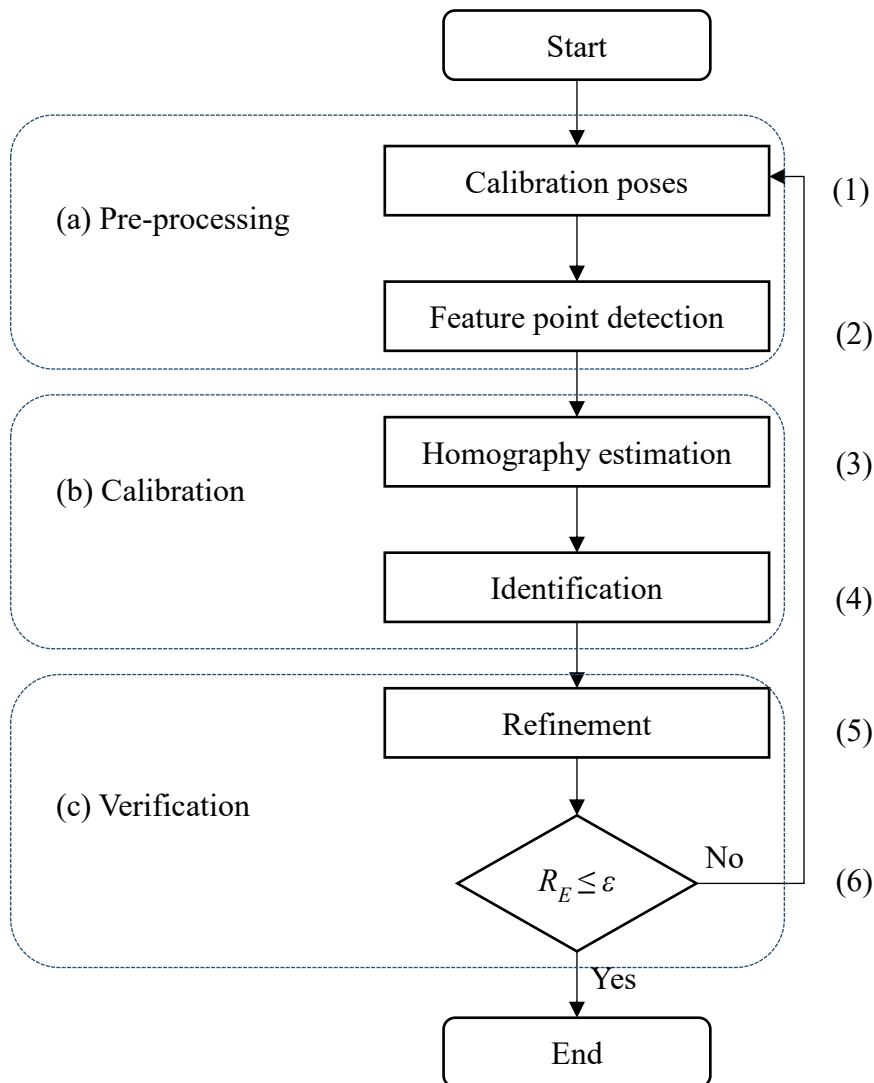


Figure II.6 Flowchart of the suggested calibration protocol based on Zh-method

(a) Pre-processing

The pre-processing stage involves the definition of the environment to calibrate the camera. First, the choice of the pattern impacts the accuracy since some patterns are more suitable for an accurate calibration. In literature, there are mainly two types of calibration grid patterns usually selected because of their detection simplicity in an image and their manufacturing easiness: checkerboard and circle board [BGTV14, MaWh00].

- Step 1: calibration poses

This step consists of selecting the calibration grid pattern and its positioning in the camera FoV. Hence, multiple positions and orientations of the calibration grid are set, and an image is taken at each pose. One condition is the number of the required control points and number of views that could be at least equal to 4, and 3 respectively according to Zhang. However, the more images taken, the better the calibration. The first step could be either manual or automated. Manual positioning is subjective and strongly depends on the operator, which affects the calibration quality. Automated calibration on the other hand is more precise and leads to a better calibration accuracy [FiSh05].

In this context, robots are widely used to calibrate cameras [Chec00, TaAh15, TaAh17], that allows to effectively compare the calibration result in terms of accuracy. This strategy is motivated by the positions of the artefact to the camera that are no longer random but rather controlled by the uncertainty of the robot. An illustration of the calibration process using a robot arm is shown in Figure II.7.

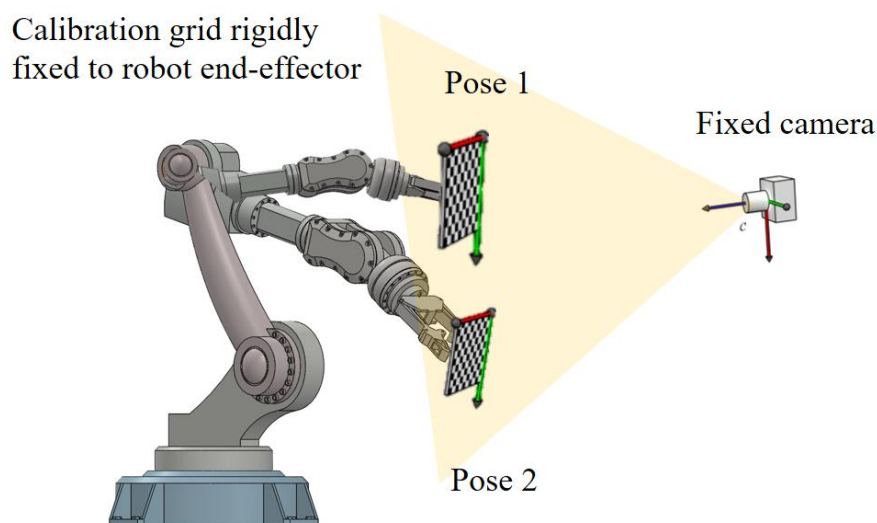


Figure II.7 Example of robot-based camera calibration

- Step 2: feature point detection

Feature points detection is the second step in the algorithm, implying the identification of control points, referred as the points of interest. It allows to relate the 2D calibration grid in the world coordinates to its projection into the image plane. Patterns such as square grid [Zhan00b] [WeCH92], checkerboard [LuMi02] and circle-board [Heik00][KaBr06], are used for camera calibration as they can be manufactured at high precision with laser and chrome printing machines. However, the feature points detection algorithm is different for each pattern. For the checkerboard and the square grid, the points of interest are the corners of each pattern, whereas for the circle-board, they are defined as circle centres (Figure II.8).

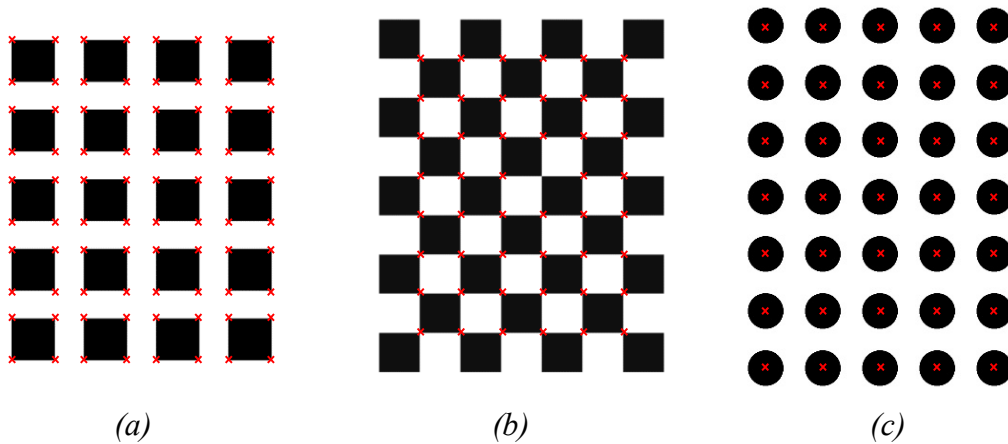


Figure II.8 Example of the used calibration grids (a) Square grid 8x10 (b) Checkerboard 6x8 (c) Circle grid 5x7 (where \times are the points of interest)

According to Malhon [MaWh00], a circle pattern can provide an inaccurate estimation of the distortion parameters caused by of the perspective bias and distortion bias. If the angle between the optical axis and the perpendicular axis to the surface are not perfectly parallel, the observed circle shape is elliptical, which influences the detection of the centre. Based on this observation, the checkerboard is favoured as the calibration pattern.

In computer vision systems, a method based on corner detection allows to extract specific features in images. A corner detection is defined in [MeNR90] as the intersection of two lines, thus, two different edge directions are distinguished in a local neighbourhood of the point. It is used in many fields such as video tracking, object recognition and camera calibration. In this context, Chris Harris and Mike Stephens [HaSt88] improved the algorithm of corners detector initially proposed in 1977 by Moravec's [Mora00]. The Harris corner detector is based on the calculation of variations produced by a window when moved in any direction. This method was

investigated in several comparative studies ([DNBD12] [WPXW17] [BaLu12]), which confirms both its robustness and accuracy. It applies the 2D grayscale image I , considered as a scalar function depending on the intensity variation in the local neighbourhood [SáMS18b]. One example is the high intensity variation in the pixels neighbourhood [SáMS18b] that could be modelled by an autocorrelation function (eq. II.10). Let (u, v) be the displacement around the position (x, y) , a corner is defined as the maximum variation of $\max[E(u, v)]$ regardless of the direction.

$$\max[E(u, v)] = \max \left[\sum_{x,y} w(x, y) [I(x + u, y + v) - I(x, y)]^2 \right] \quad \text{II.10}$$

- E : difference between the original and the moved windows
- u : window displacement in x direction
- v : window displacement in y direction
- $w(x, y)$: mask that ensures the use of the selected window at position (x, y) defined as rectangular or Gaussian function
- I : intensity of the image at the position (x, y)
- $I(x+u, y+v)$: intensity of displaced windows

Applying the Taylor series (representation of a function as infinite sum of the function's derivatives at a single point [Tayl20]), the difference between the original and the moved windows $E(u, v)$ is approximated by eqs. II.11–13:

$$I(x + u, y + v) \approx I(x, y) + uI_x + vI_y \quad \text{II.11}$$

$$E(u, v) \approx \sum_{x,y} w(x, y) [I(x, y) + uI_x + vI_y - I(x, y)]^2 \quad \text{II.12}$$

$$E(u, v) \approx [u \quad v] \sum_{x,y} w(x, y) \begin{bmatrix} I_x^2 & I_x I_y \\ I_x I_y & I_y^2 \end{bmatrix} \begin{bmatrix} u \\ v \end{bmatrix} \quad \text{II.13}$$

Let M be the summed matrix, so that (eq. II.14):

$$M = \sum_{x,y} w(x, y) \begin{bmatrix} I_x^2 & I_x I_y \\ I_x I_y & I_y^2 \end{bmatrix} \quad E(u, v) \approx [u \quad v] M \begin{bmatrix} u \\ v \end{bmatrix} \quad \text{II.14}$$

A score R associated to each window leads to determine the corner (eq. II.15).

$$R = \det M - k(\text{trace } M)^2 \quad \text{II.15}$$

Even if the Harris corner detector is usually employed in machine vision, this method presents a number of limitations related to the location of patterns, the number of pixels and the defects of the lenses [HaCM15, SáMS18b].

(b) Calibration

According to Zhang [FCWC08, LWYC19, RiSa07], the calibration stage can be carried out in steps (3) and (4): (3) Homography estimation using Direct Linear Transformation (DLT) [Sigh22] and (4) identification of the camera parameters.

- Step 3: Homography estimation using DLT

Homography meaning is “similar drawing” (assuming a pinhole camera model), used to study the projection and perspective in Euclidean geometry [RaOl14, RaST14]. Homography is a bijective projective transformation allowing to map pairs of points that belong to two different planes, and to rectify an image to front-on view [Open00].

The estimation of the homography is independent from the previous steps described in the Figure II.6. The knowledge on camera poses or internal parameters is not required for the estimation of the homography matrix. However, at least 3 camera poses in the 3D world scene and their corresponding pixels on the image plane are compulsory while computing the homography between the 3D world and the image coordinate systems, [BeCG05]. Let K be the intrinsic matrix and $[R \ T]$ the extrinsic matrix. The Zh-method exploits flat surfaces where the points of interest are assumed to lie on XY-plane (Figure II.9) since all the points have very small Z coordinates (up to 100 nm thickness for ceramic chrome coating [Cust00]) (eq. II.16).

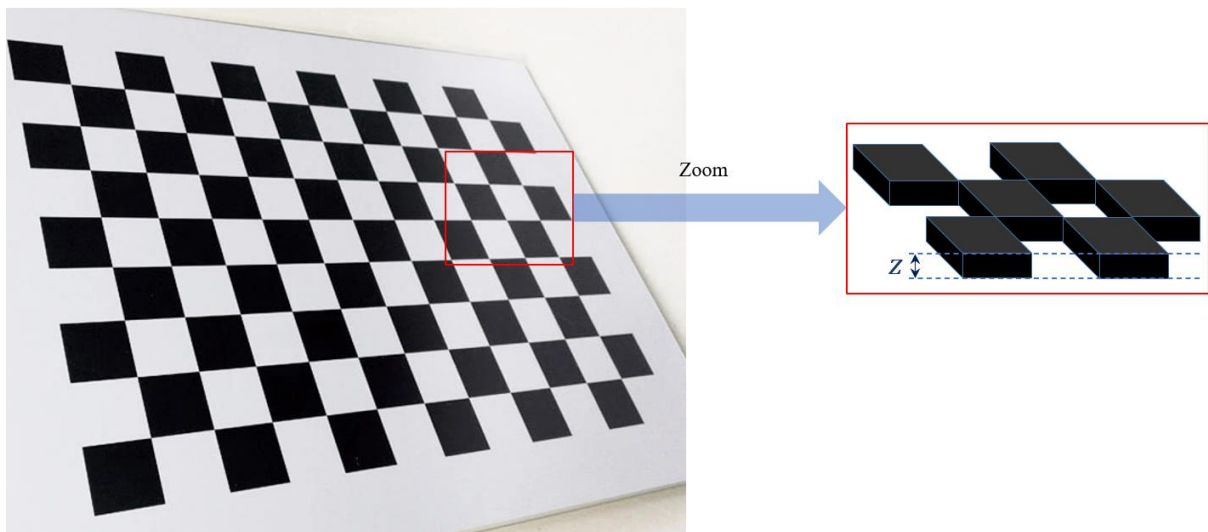


Figure II.9 Ceramic chrome coating with a checkerboard pattern

$$\begin{pmatrix} u_i \\ v_i \\ 1 \end{pmatrix} = K \begin{bmatrix} \vdots & \vdots & \vdots & \vdots \\ r_{i,0} & r_{i,1} & r_{i,2} & t_i \\ \vdots & \vdots & \vdots & \vdots \end{bmatrix} \begin{pmatrix} X_i \\ Y_i \\ 0 \\ 1 \end{pmatrix} = K \begin{bmatrix} \vdots & \vdots & \vdots \\ r_{i,0} & r_{i,1} & t_i \\ \vdots & \vdots & \vdots \end{bmatrix} \begin{pmatrix} X_i \\ Y_i \\ 1 \end{pmatrix} \quad \text{II.16}$$

$r_{i,0}$, $r_{i,1}$ and $r_{i,2}$ define the column vector of the rotation matrix R_i , and t_i is the translation vector for each image i . The 2D homography matrix H that relates pixels in the imaging sensor to the points of interest in the calibration grid is modelled as in eq. II.17.

$$\begin{pmatrix} u_j \\ v_j \\ 1 \end{pmatrix} = H \begin{pmatrix} X_i \\ Y_i \\ 1 \end{pmatrix} \quad \text{with: } H = K \begin{bmatrix} \vdots & \vdots & \vdots \\ r_{i,0} & r_{i,1} & t_i \\ \vdots & \vdots & \vdots \end{bmatrix} \quad \text{II.17}$$

$$= \begin{bmatrix} h_{0,0} & h_{0,1} & h_{0,2} \\ h_{1,0} & h_{1,1} & h_{1,2} \\ h_{2,0} & h_{2,1} & h_{2,2} \end{bmatrix}$$

The homography matrix H estimated through Direct Linear Transformation (DLT) can be rearranged as follows (eq. II.18):

$$\begin{cases} u_j(h_{2,0}X_j + h_{2,1}Y_j + h_{2,2}) - h_{0,0}X_j - h_{0,1}Y_j - h_{0,2} = 0 \\ v_j(h_{2,0}X_j + h_{2,1}Y_j + h_{2,2}) - h_{1,0}X_j - h_{1,1}Y_j - h_{1,2} = 0 \end{cases} \quad \text{II.18}$$

By collecting the 9 elements of the homography into a vector $\mathbf{h} = (h_{0,0}, h_{0,1}, h_{0,2}, h_{1,0}, h_{1,1}, h_{1,2}, h_{2,0}, h_{2,1}, h_{2,2})^T$, eq. II.18 can be rewritten as (eq. II.19):

$$\begin{pmatrix} -X_j & -Y_j & -1 & 0 & 0 & 0 & u_jX_j & u_jY_j & u_j \\ 0 & 0 & 0 & -X_j & -Y_j & -Y_j & v_jX_j & v_jY_j & v_j \end{pmatrix} \cdot \mathbf{h} = \begin{pmatrix} 0 \\ 0 \end{pmatrix} \quad \text{II.19}$$

For an image with N points assumed to be related with the same homography vector, the system of linear equations becomes (eq. II.20):

$$\begin{pmatrix} -X_0 & -Y_0 & -1 & 0 & 0 & 0 & u_0X_0 & u_0Y_0 & u_0 \\ 0 & 0 & 0 & -X_0 & -Y_0 & -1 & v_0X_0 & v_0Y_0 & v_0 \\ -X_1 & -Y_1 & -1 & 0 & 0 & 0 & u_1X_1 & u_1Y_1 & u_1 \\ 0 & 0 & 0 & -X_1 & -Y_1 & -Y_1 & v_1X_1 & v_1Y_1 & v_1 \\ & & & & \vdots & & & & \\ -X_{N-1} & -Y_{N-1} & -1 & 0 & 0 & 0 & u_{N-1}X_{N-1} & u_{N-1}Y_{N-1} & u_{N-1} \\ 0 & 0 & 0 & -X_{N-1} & -Y_{N-1} & -Y_{N-1} & v_{N-1}X_{N-1} & v_{N-1}Y_{N-1} & v_{N-1} \end{pmatrix} \cdot \begin{pmatrix} h_{0,0} \\ h_{0,1} \\ h_{0,2} \\ h_{1,0} \\ h_{1,1} \\ h_{1,2} \\ h_{2,0} \\ h_{2,1} \\ h_{2,2} \end{pmatrix} = \begin{pmatrix} 0 \\ 0 \end{pmatrix} \quad \text{II.20}$$

Afterwards, the singular-value decomposition (SVD) [YaTT11] is applied to solve a homogenous system of linear equations $M \cdot \mathbf{h} = 0$, $M = U \cdot S \cdot V^T$ where U is the unitary $2N \times$

$2N$ matrix, S is a rectangular diagonal $2N \times 9$ matrix and V is an unitary 9×9 matrix. The matrix S contains the singular values, each value is associated with a *left singular vector* from matrix U and a *right singular vector* from matrix V . The solution of the matrix system is the *right singular vector* $\mathbf{h} = v_k$ associated with the smallest *singular value* $s_k = \min(s_0, \dots, s_8)$.

- Step 4: Identification of the camera parameters

❖ *Identification of intrinsic parameters*

The homography, estimated for each view, contains both intrinsic and extrinsic parameters of the camera. To extract the intrinsic parameters from the homography, the orthonormality constraint between rotation vectors r_0 and r_1 can be written as (eq. II.21):

$$r_0^T \cdot r_1 = r_1^T \cdot r_0 = 0 \quad \text{and} \quad r_0^T \cdot r_0 = r_1^T \cdot r_1 = 1 \quad \text{II.21}$$

Let \bar{h}_l be the vectors of the homography matrix (eq. II.22) with $l = \{0, 1, 2\}$

$$H = (\bar{h}_0 \quad \bar{h}_1 \quad \bar{h}_2) = K(r_0 \quad r_1 \quad t) \quad \text{II.22}$$

$$\begin{cases} \bar{h}_0 = Kr_0 \\ \bar{h}_1 = Kr_1 \\ \bar{h}_2 = Kt \end{cases} \Rightarrow \begin{cases} \bar{h}_0^T (K^{-1})^T = r_0^T \\ \bar{h}_1^T (K^{-1})^T = r_1^T \\ \bar{h}_2^T (K^{-1})^T = t^T \end{cases}$$

By replacing r_0 and r_1 in eq. II.21, the following equations can be deduced (eq. II.23):

$$\bar{h}_0^T (K^{-1})^T K^{-1} \bar{h}_0 = 0 \quad \Rightarrow \quad \bar{h}_0^T (K^{-1})^T K^{-1} \bar{h}_0 = \bar{h}_1^T (K^{-1})^T K^{-1} \bar{h}_1 \quad \text{II.23}$$

Let's consider B a 3×3 symmetric matrix with six elements $b_i, i=\{0,\dots,5\}$ such as

$B = (K^{-1})^T \cdot K^{-1}$, b_i could be expressed as follows:

$$b_0 = \frac{1}{f_u^2} \quad b_1 = -\frac{s_x}{f_u^2 f_v} \quad b_2 = \frac{s^2}{f_u^2 f_v^2} + \frac{1}{f_v^2}$$

$$b_3 = \frac{c_v s - c_u f_v}{f_u^2 f_v} \quad b_4 = -\frac{s(c_v s - c_v f_v)}{f_u^2 f_v^2} - \frac{v_c}{f_v^2} \quad b_5 = \frac{(c_v s - c_v f_v)^2}{f_u^2 f_v^2} + \frac{c_v^2}{f_v^2} + 1$$

Vector $\hat{b} = (B_0, B_1, B_2, B_3, B_4, B_5)^T$ could be applied such as $\bar{h}_p^T B h_q = v_{p,q}(H) \hat{b}$ where $v_{p,q}$ is a 6-dimensional row vector obtained from a single homography H (eq. II.24).

$$v_{p,q}(H) = \begin{pmatrix} \bar{h}_{0,p} \bar{h}_{0,q} \\ \bar{h}_{0,p} \bar{h}_{1,q} + \bar{h}_{1,p} \bar{h}_{0,q} \\ \bar{h}_{1,p} \bar{h}_{1,q} \\ \bar{h}_{2,p} \bar{h}_{0,q} + \bar{h}_{0,p} \bar{h}_{2,q} \\ \bar{h}_{2,p} \bar{h}_{1,q} + \bar{h}_{1,p} \bar{h}_{2,q} \\ \bar{h}_{2,p} \bar{h}_{2,q} \end{pmatrix} \quad \text{II.24}$$

For a single view with a homography H , the constraints expressed in eq. II.21 can be reformulated into a pair of linear equation (eq. II.25):

$$\text{where} \quad \begin{pmatrix} v_{0,1}(H) \\ v_{0,0}(H) - v_{1,1}(H) \end{pmatrix} \cdot \hat{b} = \begin{pmatrix} 0 \\ 0 \end{pmatrix} \quad \text{II.25}$$

The Zh-method requires more than a single view. Thence, for M homographies estimated with M views, the linear equations system of pairs can be written as (eq. II.26):

$$\text{where} \quad \begin{pmatrix} v_{0,1}(H_0) \\ v_{0,0}(H_0) - v_{1,1}(H_0) \\ v_{0,1}(H_1) \\ v_{0,0}(H_1) - v_{1,1}(H_1) \\ \vdots \\ v_{0,1}(H_i) \\ v_{0,0}(H_i) - v_{1,1}(H_i) \\ \vdots \\ v_{0,1}(H_{M-1}) \\ v_{0,0}(H_{M-1}) - v_{1,1}(H_{M-1}) \end{pmatrix} \cdot \hat{b} = \begin{pmatrix} 0 \\ 0 \\ 0 \\ 0 \\ \vdots \\ 0 \\ 0 \\ \vdots \\ 0 \\ 0 \end{pmatrix} \quad \text{II.26}$$

The homogenous linear equations system in eq. II.26 is solved through SVD calculation. The calculated parameters $b_i, i=\{0,..,5\}$ leads to identify matrix K when applying $B = (K^{-1})^T \cdot K^{-1}$. Zhang [Zhan00b] proposed a closed form calculation of matrix K so that (eq. II.27):

$$\begin{aligned} f_u &= \sqrt{\frac{w}{db_0}} & f_v &= \sqrt{\frac{w}{d^2} \cdot b_0} & s_x &= \sqrt{\frac{w}{d^2 B_0}} \cdot b_1 \\ c_u &= \frac{b_1 b_4 - b_2 b_3}{d} & c_v &= \frac{b_1 b_3 - b_0 b_4}{d} \end{aligned} \quad \text{II.27}$$

where $w = b_0 b_2 b_5 - b_1^2 b_5 - b_0 b_4^2 + 2b_1 b_3 b_4 - b_2 b_3^2$ and $d = b_0 b_2 - b_1^2$

❖ Identification of extrinsic parameters

The extrinsic matrix is the rotation and translation vectors which define the camera pose in 3D world. Since homography depends on both intrinsic and extrinsic matrices, the extrinsic vectors can be calculated from the system of equation as follows (eq. II.28):

$$\begin{cases} r_0 = K^{-1}h_0 \\ r_1 = K^{-1}h_1 \\ r_2 = r_0r_1 \\ t = K^{-1}h_2 \end{cases} \quad \text{II.28}$$

The extrinsic parameters represent the position and the orientation of the camera with respect to the calibration grid. Unlike the intrinsic parameters which are fixed regardless of the pose, those extrinsic parameters are unique for each image.

❖ *Estimation of distortion coefficients*

Until this step, the parameters have been estimated without taking into consideration any distortion. Thus, a non-linear lens distortion model is added to the projection pipeline and its parameters are estimated from the taken images. To calculate the deviation between the projected points $(u_{i,j}, v_{i,j})$ and the observed ones $(\hat{u}_{i,j}, \hat{v}_{i,j})$ (where i is the image index and j is the feature point index), the distance $d_{i,j} = \sqrt{(\hat{u}_{i,j} - u_{i,j})^2 + (\hat{v}_{i,j} - v_{i,j})^2}$ known as the *observed distortion vector* is calculated. The two main distortion components are: tangential errors caused by lenses displacement from the optical axis, and radial distortion caused by light refractions variation inside the camera scope (Figure II.10).

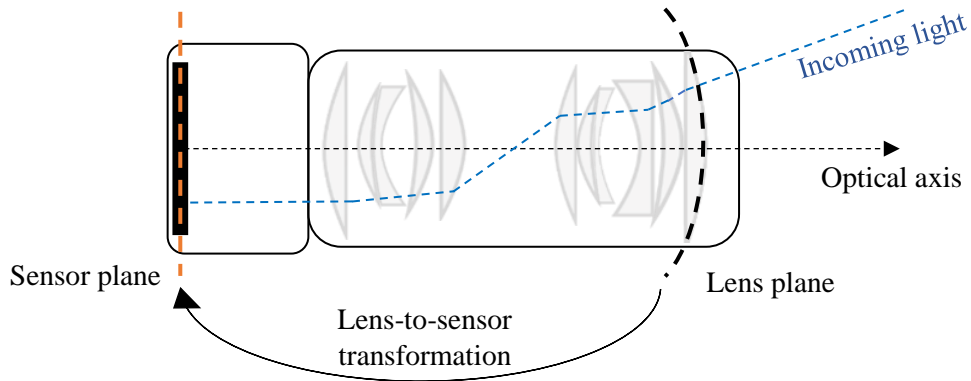


Figure II.10 *Projection of the incoming light (reflected on the 3D scene) on the image sensor*

The radial distortion is expressed in eq. II.29 where $\check{r}_{i,j}$ is the radial distance of the pixel point and the centre of the image, and k_0, k_1 the distortion coefficients:

$$D(r_{i,j}, k) = k_0 \check{r}_{i,j}^2 + k_1 \check{r}_{i,j}^4 \quad \text{II.29}$$

$$= (k_0, k_1) \cdot \begin{pmatrix} \ddot{r}_{i,j}^2 \\ \ddot{r}_{i,j}^4 \end{pmatrix}$$

Based on the estimated projected centre u_c and the non-linear function $D(\ddot{r}_{i,j}, k)$, the parameters k_0 and k_1 are estimated using the resulting distortion vector $d_{i,j}$ expressed in the following equation (eq. II.30) where $u_{i,j}$ is the projected sensor point.

$$d_{i,j} = (u_{i,j} - u_c) \cdot D(\ddot{r}_{i,j}, k) \quad \text{II.30}$$

The pin-cushion distortions are caused by a positive value of the function $D(\ddot{r}_{i,j}, k)$, while the barrel distortions result from a negative value of this function. A minimization based on least square solution $\min \sum_{i,j} \|d_{i,j} - \dot{d}_{i,j}\|$ of the variation between the distortion model $d_{i,j}$ and the associated observed distortion $\dot{d}_{i,j}$ leads to estimate the coefficients k_0 and k_1 . The distortion function $D(\ddot{r}_{i,j}, k)$ becomes (eq. II.31):

$$\begin{cases} (\dot{u}_{i,j} - u_c) \ddot{r}_{i,j}^2 k_0 + (\dot{u}_{i,j} - u_c) \ddot{r}_{i,j}^4 k_1 = (\dot{u}_{i,j} - u_{i,j}) \\ (\dot{v}_{i,j} - v_c) \ddot{r}_{i,j}^2 k_0 + (\dot{v}_{i,j} - v_c) \ddot{r}_{i,j}^4 k_1 = (\dot{v}_{i,j} - v_{i,j}) \end{cases} \quad \text{II.31}$$

eq. II.31 can also be written in a matrix form (eq. II.32) and solved using standard methods of linear algebra for each point N in a view:

$$\begin{pmatrix} (\dot{u}_{i,j} - u_c) \ddot{r}_{i,j}^2 & (\dot{u}_{i,j} - u_c) \ddot{r}_{i,j}^4 \\ (\dot{v}_{i,j} - v_c) \ddot{r}_{i,j}^2 & (\dot{v}_{i,j} - v_c) \ddot{r}_{i,j}^4 \end{pmatrix} \begin{pmatrix} k_0 \\ k_1 \end{pmatrix} = \begin{pmatrix} \dot{u}_{i,j} - u_{i,j} \\ \dot{v}_{i,j} - v_{i,j} \end{pmatrix} \quad \text{II.32}$$

The system of equations when considering M views is formulated with $2 \times M \times N$ linear equations as expressed in eq. II.33.

$$\begin{pmatrix} (\dot{u}_{0,0} - u_c) \ddot{r}_{0,0}^2 & (\dot{u}_{0,0} - u_c) \ddot{r}_{0,0}^4 \\ (\dot{v}_{0,0} - v_c) \ddot{r}_{0,0}^2 & (\dot{v}_{0,0} - v_c) \ddot{r}_{0,0}^4 \\ (\dot{u}_{0,1} - u_c) \ddot{r}_{0,1}^2 & (\dot{u}_{0,1} - u_c) \ddot{r}_{0,1}^4 \\ (\dot{v}_{0,1} - v_c) \ddot{r}_{0,1}^2 & (\dot{v}_{0,1} - v_c) \ddot{r}_{0,1}^4 \\ \vdots & \vdots \\ (\dot{u}_{i,j} - u_c) \ddot{r}_{i,j}^2 & (\dot{u}_{i,j} - u_c) \ddot{r}_{i,j}^4 \\ (\dot{v}_{i,j} - v_c) \ddot{r}_{i,j}^2 & (\dot{v}_{i,j} - v_c) \ddot{r}_{i,j}^4 \\ \vdots & \vdots \\ (\dot{u}_{M-1,N-1} - u_c) \ddot{r}_{M-1,N-1}^2 & (\dot{u}_{M-1,N-1} - u_c) \ddot{r}_{M-1,N-1}^4 \\ (\dot{v}_{M-1,N-1} - v_c) \ddot{r}_{M-1,N-1}^2 & (\dot{v}_{M-1,N-1} - v_c) \ddot{r}_{M-1,N-1}^4 \end{pmatrix} \begin{pmatrix} k_0 \\ k_1 \end{pmatrix} = \begin{pmatrix} \dot{u}_{0,0} - u_{0,0} \\ \dot{v}_{0,0} - v_{0,0} \\ \dot{u}_{0,1} - u_{0,1} \\ \dot{v}_{0,1} - v_{0,1} \\ \vdots \\ \dot{u}_{i,j} - u_{i,j} \\ \dot{v}_{i,j} - v_{i,j} \\ \vdots \\ \dot{u}_{M-1,N-1} - u_{M-1,N-1} \\ \dot{v}_{M-1,N-1} - v_{M-1,N-1} \end{pmatrix} \quad \text{II.33}$$

This latter can be solved using SVD [Till13] or QR-decomposition [NuBa12].

(c) Verification

The last verification stage (figure II.6) includes two steps (5) and (6): (5) refinement based non-linear optimisation using Levenberg-Marquardt (LM) and (6) threshold verification.

- Step 5: LM-based refinement method

The refinement step mainly targets the optimisation of the intrinsic and extrinsic calibration parameters as well as the lens distortion for N observed points in M views. A first vector \hat{I} including both the intrinsic parameters and the distortion coefficients is defined as $\hat{I} = (f_u, f_v, s, c_u, c_v, k_0, k_1)^T$, and a second vector E_i for the extrinsic parameters $E_i = (\alpha_i, \beta_i, \gamma_i, t_{i,x}, t_{i,y}, t_{i,z})^T$ is defined for each image i .

The non-linear least square minimization Levenberg–Marquardt (LM) method ([appendix B](#)) of the reprojection error R_E (eq. II.34) is applied as to estimate the camera parameters at each iteration. Here, the values of the projected sensor points $(u_{i,j}, v_{i,j})$ are calculated with the implemented Harris corner detector and the values of the observed point $(p_u(\hat{I}, E_i), p_v(\hat{I}, E_i))$ estimated in the previous step.

$$\min_{\hat{I}, \{E_i\}} R_E = \min_{\hat{I}, \{E_i\}} \left(\sum_{i=0}^{M-1} \sum_{j=0}^{N-1} |u_{i,j} - p_u(\hat{I}, E_i)|^2 + |v_{i,j} - p_v(\hat{I}, E_i)|^2 \right) \quad \text{II.34}$$

The rotation matrix has 3 degrees of freedom and consists of nine coefficients, which makes it subject to strong constraints due to the dependence between the matrix elements. Therefore the Euler-to-Rodrigues method [Mebi07] is applied while obtaining the 3D rotation vectors ρ_x, ρ_y, ρ_z ([appendix C](#)).

- Step 6: Reprojection error threshold

Depending on the aimed accuracy, the obtained reprojection error could be optimised by adding more images or by changing the stopping criteria of the LM optimisation until reaching a predefined threshold value. Usually, the number of images required to achieve a stable calibration needs to be in the range of [10, 20] according to Jin [JLGF22].

II.3. Modelling and calibration of stereo vision systems

A computer stereo vision is a measurement process that consists of using images taken from different points of view, to estimate the 3D information such as the dimension, shape errors, areal surface texture parameters, positions of objects, etc.) [LiAg05]. By analysing the images

taken at two different angles, the real-world dimensions can be recovered. Two types of stereo vision scanners exist [BeBa14, BGBM13, ChZh95], both based on the same model: (1) passive stereo vision that consists of **two cameras** and (2) active stereo systems involving **cameras and projectors**. Stereo cameras and camera-projector systems modelling are similar, while considering the **projector as an inverse camera** since the light is sent rather than received [MaKL11].

II.3.1. Stereo vision model

One of the limits of a single camera is the depth recovering. In fact, multiple 3D points [$P (X_p, Y_p, Z_p)$, $G (X_G, Y_G, Z_G)$, $N (X_N, Y_N, Z_N) \dots$] (Figure II.11-a) could correspond to the same pixel point $p (u, v)$ on the image. A stereo vision is conventionally defined by the use of two cameras mounted on a rig. It can provide the same images as a single camera, and the depth parameter could be estimated using the triangulation principle [HaSt97].

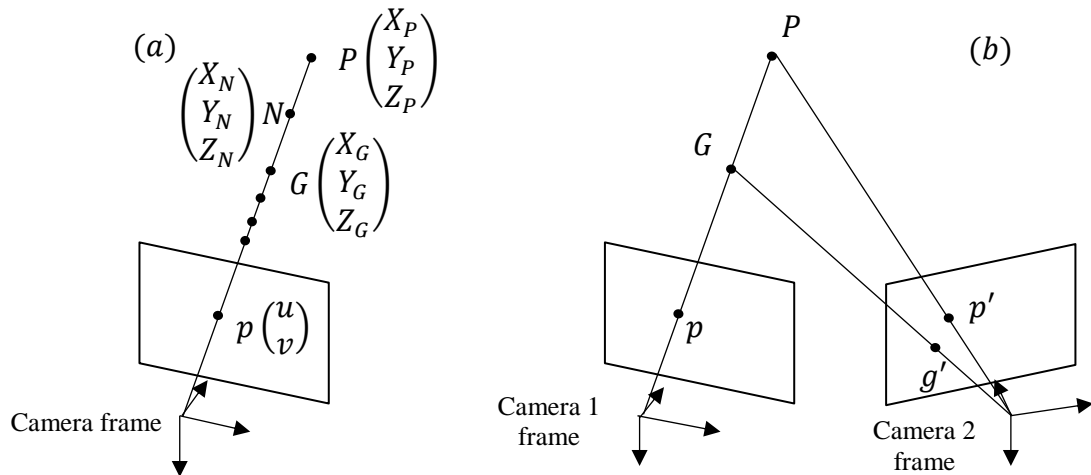


Figure II.11 (a) single camera capture, (b) advantage of using stereo vision inspired from [FSLY20]

Let's consider K_1 and K_2 respectively the intrinsic matrices of each of the camera 1 and the camera 2. Let's also note E the essential matrix that defines the rigid transformation between the two cameras. The relationship between the points p and p' in the image plane of each camera is called the epipolar constraint, expressed as (eq. II.35):

$$p' = E \times p \quad \Leftrightarrow \quad p'^T \times E \times p = 0 \quad \text{II.35}$$

The essential matrix E can be written as follows (eq. II.36):

$$E = \begin{pmatrix} 0 & -t_{12,Z} & t_{12,Y} \\ t_{12,Z} & 0 & -t_{12,X} \\ -t_{12,Y} & t_{12,X} & 0 \end{pmatrix} \times R_{12} \quad \text{II.36}$$

The fundamental matrix F could be calculated using eqs. II.37 and II.38.

$$F = K_2^{-T} \times E_{12} \times K_1^{-1} \quad \text{II.37}$$

$$m_2^T \times F \times m_1 = I \quad \text{II.38}$$

Both E and F matrices describe the geometric relationship between the corresponding points in two cameras. The difference is that E deals with calibrated cameras since intrinsic parameters are supposed to be known, whereas F is for uncalibrated ones [Stan16].

The 3D coordinates (X_p, Y_p, Z_p) of point P in the scene can be recovered from its projection on the image planes of both cameras, if the relative position and orientation of the two cameras are known. The estimation of 3D coordinates depends on the selected configuration of the stereo system. Two configurations of the system could exist with parallel or non-parallel optical axes of the cameras.

For the parallel configuration, illustrated in Figure II.12-a, the distance between the two cameras coordinates frames centres C_1 and C_2 noted b is called baseline. Moreover, x_1 and x_2 , are the distances in pixel with respect to the principal point. The coordinates of P (X_p, Y_p, Z_p) can be recovered using eq. II.39.

$$X_p = \frac{Z_p x_1}{f} \quad Y_p = \frac{Z_p y_1}{f} \quad Z_p = \frac{bf}{x_1 - x_2} \quad \text{II.39}$$

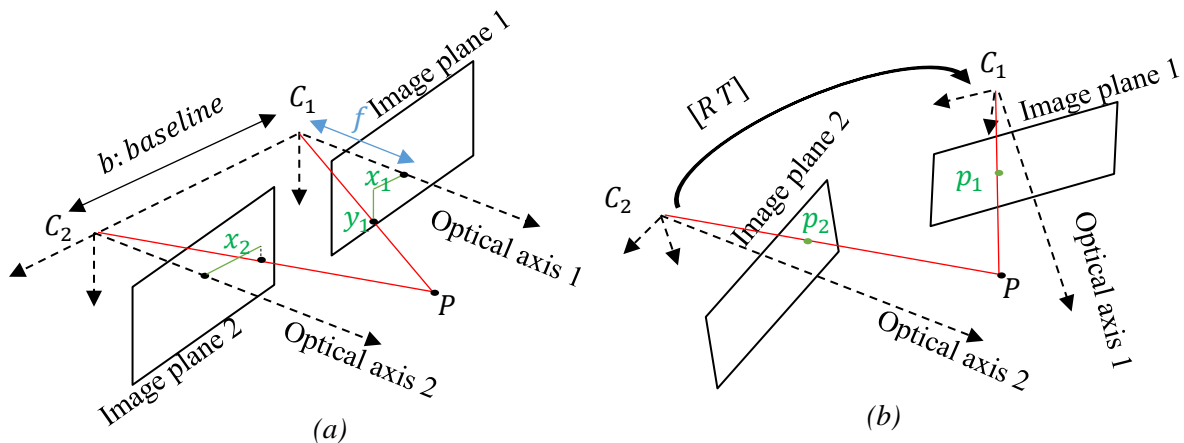


Figure II.12 Triangulation configuration : (a) Cameras separated by a distance b called baseline and located such as the optical axes 1 and 2 are parallel (b) $[R T]$ transformation between C_1 and C_2 [Yama00].

In general, the optical axes of the two cameras are not parallel, either because of the errors due to the manufacturing process and assembly of the elements, or because of the adopted non-parallel configuration (Figure II.12-*b*). Consequently, the transformation between cameras can be formulated as in eq. II.40.

$$p_1 = RT(p - T) \quad \text{II.40}$$

II.3.2. Calibration of stereo systems

The calibration of a stereo vision system is quite similar to a single camera calibration. The only difference consists in estimating the essential matrix E that represents the rigid transformation between the two cameras. The implemented Zh-method for stereo system calibration respects the following steps:

- 1- Acquisition: the calibration grid is positioned at different positions and orientations in both cameras FoVs. A constraint on pattern visibility should be respected, which consists in keeping the calibration grid pattern visible from both camera perspectives.
- 2- Feature points extraction: on each pair of images, feature point detection algorithms are applied to extract the corners of the checkerboard.
- 3- Homography estimation: it leads to identify the transformation from the calibration grid coordinates frame to each camera coordinate frame.
- 4- Intrinsic, extrinsic and distortion parameters estimation: the SVD is applied on the estimated homography matrix to extract the pinhole parameters in addition to the radial and tangential distortions of each optical element.
- 5- Refinement: the estimated pinhole parameters are refined by minimizing the reprojection error function R_E using LM optimisation for each camera.
- 6- Essential matrix E estimation: Finally, the rigid transformation between the cameras or camera-projector is deduced from the extrinsic matrices estimated at the 4th step.

As the projector is considered as an inverse camera, structured light systems are calibrated in similar way as stereo cameras, with an additional step called correspondence identification.

II.3.3. Inverse camera/projector calibration

Considering the inverse modelling for a projector, the correspondences between the 3D world points and the image plane are identified through the estimation of the pinhole parameters when using the same checkerboard. The main challenge is the identification of the projector view since projectors cannot observe the scene.

To identify the projector view, the correspondences between the projector pixel and the checkerboard are established through a calibration strategy that involves the projection of a known pattern [MaKL11]. Using this approach, the points of interest can be identified from the camera perspective. Based on the projected pattern, their locations in the projector pixel plane are also recovered. This process is known as the codification strategy. Many codification strategies have been proposed to calibrate projectors. Some are manual and require the adaptation of the projector view, while the others are automated.

A projector can only be calibrated within a camera-projector pair. Sadlo *et al.* [SWPG05] propose a calibration procedure in 7 steps:

- (1) the camera is first calibrated using the Zh-method and its parameters are estimated,
- (2) the projector illumination is set such that a uniform colour is distributed along the calibration grid,
- (3) the projector calibration is performed by projecting an image of the calibration grid with known geometry at multiple poses,
- (4) the calibration grid pose is manually set such as to align the projected and the physical calibration grid. The estimated camera parameters are used to extract the transformation between the projected plane and the camera,
- (5) this procedure is repeated for the other poses of the projected calibration grid images,
- (6) the estimated coordinates of the projected calibration grid images are extracted using the Harris corner detector and the Zh-method is applied to estimate the projector intrinsic parameters,
- (7) a single pose is used to estimate the rigid transformation between camera and projector.

Audet *et al.* [AuOk09] proposed an enhanced calibration technique for manual positioning of the physical calibration grid on the projected one. The enhanced technique uses ArUco markers instead of standard checkerboards. An ArUco marker is a binary square marker formed of a wide dark boundary and a specific white shape used as an identifier. To calibrate the camera-projector system, a physical grid with ArUco markers is printed on a white board and an image with inverted colours of ArUco grid is generated and projected with the projector. Then, the calibration grids are aligned to merge both into a single grid.

The methods presented above lack in terms of accuracy because the distortion coefficients of the projector are not deemed. In addition, the manual positioning is subjective and leads to inaccurate estimation of pinhole parameters. Some progresses have been made recently on the

calibration of camera-projector systems based on structured light pattern projections. Those methods are more automated and does not necessarily necessitate a pre-calibrated camera. They also provide a better estimation of the intrinsic and extrinsic parameters of both camera and projector. Such methods [JoGr10, LiZh14, LSWW08, LuSo12] rely on the same projection used to perform 3D reconstruction of the scene. Instead of manually positioning the physical calibration grids on projected ones, a set of projections is programmed while observing several poses of the calibration grid and recovering the correspondence between the projector pixels and the physical calibration grid.

One popular calibration methods is the Gray-code based calibration. The Gray-code consists of projecting several horizontal and vertical patterns that can be distinguished by the black-to-white transition. A binary code is associated to each pixel of the projector plane (Figure II.13).

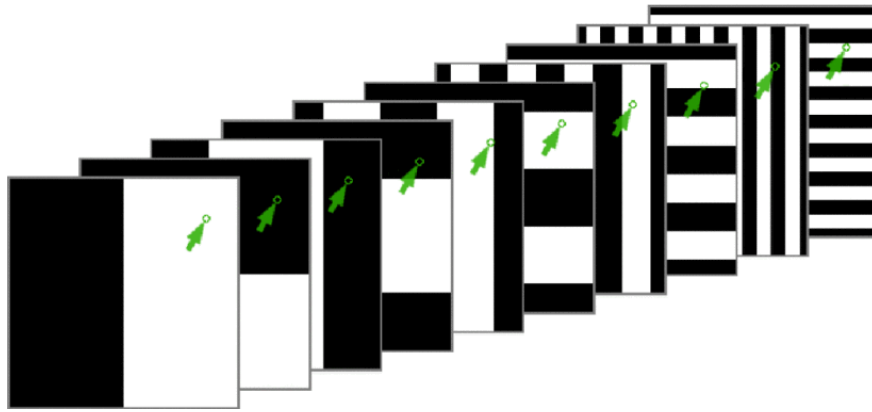


Figure II.13 Example of pixel coding using Gray-code pattern. Where black is identified by 0 and white by 1. The green point can be identified by the string [1000111101] [JoGr10]

First, a uniform projection is applied to acquire the image used to calibrate the camera. Afterwards, the patterns are successively projected in multiple levels, where each level is associated to a unique Gray-code frequency. The total number of Gray-code patterns p_d required to encode N pixels in a given dimension d is formulated as following (eq. II.41):

$$p_d = \log_2(N) \tag{II.41}$$

Let's take the example of a projector with a native resolution of 1024×768 , The p_u and p_v are the number of Gray-code patterns to encode the pixels in u and v dimensions so that (eq. II.42)

$$p_u = \log_2(1024) = 10 \quad \text{and} \quad p_v = \log_2(768) \sim 10 \tag{II.42}$$

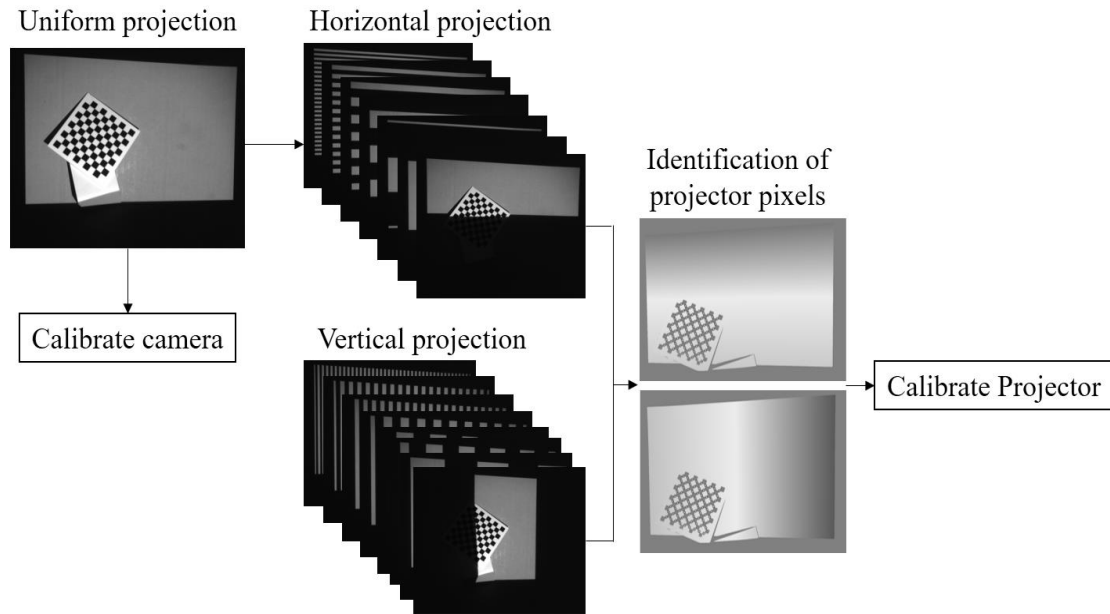


Figure II.14 *Illustration of Gray-code steps for the calibration of camera-projector systems*

Therefore, 20 total patterns are required to fully encode the projector pixels: 10 horizontal and 10 vertical. Once the number of patterns is defined, it is projected onto a calibration grid already observed by a fixed camera. Using this strategy, the positions of the calibration grid feature points can be identified on the camera pixels plane and, with the help of the Gray-code pattern (Figure II.14), their locations in the projector pixels can also be identified. Finally, using the identified correspondence between the projector and the calibration grid, the Zh-method can be applied to estimate the pinhole parameters and the projector distortion coefficients.

II.4. Conclusion

In this chapter, a literature review on camera/projector modelling has been conducted and detailed. The model allows to perform a triangulation to collect a 3D point-cloud of a scanned surface. However, some parameters relevant to the triangulation are prerequisite in a post-processing step called calibration. The process of calibration consists of estimating the parameters of the optical elements (camera and projector) defined as the intrinsic and extrinsic parameters.

The state of the art of the proposed techniques have been presented. In the case of close-range photogrammetry, the most suitable technique is the one proposed by Zhang (Zh-method). The Zh-method is based on the exploitation of a flat surface printed with a known pattern called calibration grid. The calibration grid is placed at different positions and orientations in the camera FoV to estimate the parameters of the camera. This method is also extended to stereo

systems including SL scanners. For stereo systems, additional parameters need to be estimated, like the rigid transformation between the optical elements (camera-camera or camera-projector). For SL systems, a codification strategy is used to identify the projector view in order to perform the Zh-method. The Gray-code have been selected as a codification strategy due to its performance compared to other methods.

The Zh-method involves six steps: acquisition, feature detection, homography estimation, intrinsic and extrinsic parameter estimation, global refinement, and finally a verification step. Many optimisation methods have been proposed to improve the Zh-method steps. The optimisation concerns the feature detection (by proposing an improved algorithm of feature detection) and the global refinement (such as using advanced optimisation methods to minimize reprojection error). However, the most influencing component is the calibration grid positioning at the acquisition step, because singular poses lead to inaccurate estimation of intrinsic parameters, regardless of the next steps.

Subsequently, the following chapter focuses on the acquisition step where a novel optimisation method for the calibration of close-range photogrammetry systems is proposed. The method is based on the optimal positioning of the camera with respect to the calibration grid and could be used for single camera systems and easily adapted to stereo systems.

CHAPTER . III Optimised calibration of camera-based systems

A panel of optimisation methods have been proposed in literature for the improvement of the calibration accuracy of machine vision systems. In this chapter, a novel optimisation method of camera-based system is proposed such as to increase the accuracy of the calibration process. Therefore, the chapter III is presented as following: section III.1 is an overview of the recently proposed approaches in literature. Section III.2 describes the mathematical model of a novel approach based on Zhang's calibration. Section III.3 discusses the adaptation of this method to stereo systems. Section III.4 presents a synthetic evaluation of the proposed approach on single camera. Finally, section III.5 and III.6 details the experimental validation.

CHAPTER . III	Optimised calibration of camera-based systems	54
III.1.	Introduction	55
III.2.	Novel optimisation method for a camera-based system	56
III.2.1.	Polynomial approximation	56
III.2.2.	Particle swarm optimisation	58
III.2.3.	Full implemented calibration flowchart	60
III.3.	Optimisation for stereo systems	61
III.3.1.	Polynomial regression of the extrinsic parameters	62
III.3.2.	Weighted sum of the estimated polynomials	62
III.3.3.	Multiobjective function minimization	63
III.4.	Synthetic evaluation of the proposed optimisation	65
III.4.1.	Simulation of the calibration process	65
III.4.2.	Simulation results and analysis	66
III.5.	Experimental validation of a single camera	70
III.5.1.	Experimental setup	70
III.5.2.	Traceability establishment through CMM measurements	71
III.5.3.	Calibration of an industrial camera	74
III.5.4.	Time complexity analysis	77
III.5.5.	Comparison of results and discussion	78
III.6.	Experimental validation of the SL scanner	80
III.6.1.	Pose optimisation	80
III.6.2.	Coordinate measuring system based on multilateration	82
III.6.3.	Comparison of the transformations between robot poses	86
III.7.	Conclusion	88

III.1. Introduction

The adopted calibration strategy usually influences the performance of used optical scanners. Consequently, the need for an optimal calibration approach results in accurate 3D scans. A number of studies have been proposed to improve and automatise the calibration process [DKKP08], in particular the Zh-method, including the optimisation of feature point detection [GhVN20, HEBA17, LWWP17] and the optimisation of the checkerboard views per image [GAPK19]. Rojtberg [RoKu18] investigated the influence of the number of poses of the calibration grid in the camera FoV and established a correlation between the selected poses and the calibration uncertainty. Furthermore, Rojtberg [RoKu18] proposed one interactive calibration method (R-method) based on the selection of efficient poses with respect to a next-pose generation protocol, while performing a stable calibration. The next-pose generation protocol considers some predefined constraints to avoid pinhole model singularities. Pinhole singularities are defined as the poses for which a number of intrinsic parameters are estimated inaccurately. The key constraints of the R-method are:

- (1) selection of multiple calibration grid poses along the optical axis while estimating an accurate focal length,
- (2) covering the entire camera FoV when taking images of the calibration grid, while improving the distortion coefficients estimation.

Even if those constraints lead to improve the calibration process, they are not sufficient to optimise all the pinhole parameters.

Peng [PeSt19] proposed an iterative optimisation technique of the Zh-method called the calibration Wizard (CW). The CW procedure starts by initializing the Zh-method with three random views, then updated at each iteration with one new identified optimal pose based on the Jacobian estimation of the reprojection error. The CW technique returns a better estimation of the intrinsic parameters of the camera (focal length, principal point and distortion coefficients) and performs well in uncontrolled environments. Nevertheless, the main noticeable drawback is the processing time. In addition, the given CW results depend on the initialization step based on a random selection of three poses/images, which downgrades the estimated uncertainty of the intrinsic parameters.

III.2. Novel optimisation method for a camera-based system

The calibration of a machine vision system allows once to estimate the pinhole parameters that are essential for the 3D scanning of the scene. The proposed approach based on ML aims to optimise the camera poses with respect to the calibration grid in order to minimize the reprojection error and consequently enhance the accuracy of the estimated pinhole parameters. The Figure III.1 illustrates the evolution of reprojection error as function of two extrinsic parameters when the shape could be approximated as a polynomial.

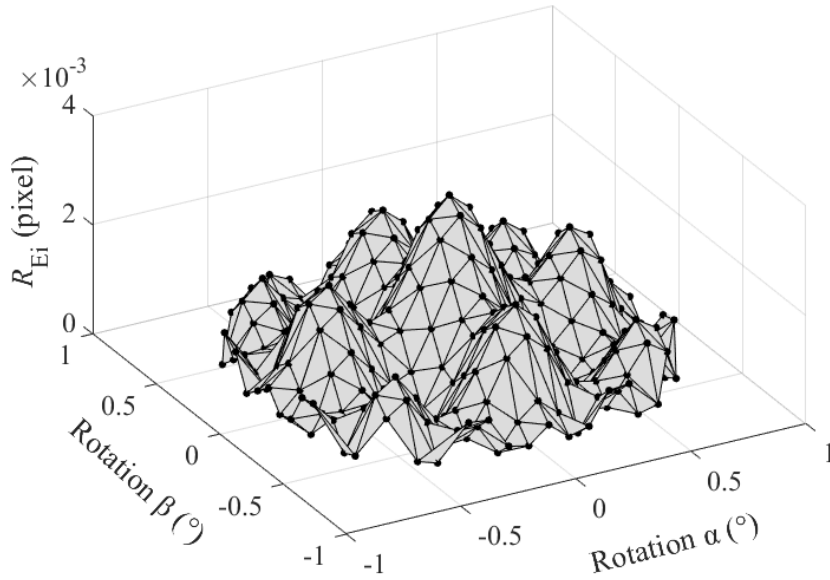


Figure III.1 Evolution of the reprojection error R_{E_i} vs. the orientations α and β for the case of a single camera system

III.2.1. Polynomial approximation

A regression-based ML function of the extrinsic vector W_i (eq. III.1) or poses was selected for modelling the evolution of the reprojection error (eq. III.2).

$$W_i = [\alpha_i, \beta_i, \gamma_i, t_{Xi}, t_{Yi}, t_{Zi}] \quad \text{III.1}$$

$$R_{E_i} = f(W_i) \quad \text{III.2}$$

where $(\alpha_i, \beta_i, \gamma_i)$ are the orientations and (t_{Xi}, t_{Yi}, t_{Zi}) are the translations of the calibration grid along the x-, y- and z-axis, respectively, and f is the polynomial regression.

For a multivariate polynomial regression of degree D with six variables W_i , defined for a pose i the polynomial model is formulated as in eqs. III.3 and III.4.

$$f(W_i) = \hat{f}(W_i) + \varepsilon(W_i) \quad \text{III.3}$$

$$\begin{aligned} \hat{f}(W_i) = & p_0 + p_1\alpha_i + p_2\beta_i + \dots + p_7\alpha_i\beta_i + p_8\alpha_i\gamma_i + \\ & \dots + p_{22}\alpha_i^2 + p_{23}\beta_i^2 + \dots + p_{27}t_{zi}^2 + \dots \end{aligned} \quad \text{III.4}$$

where \hat{f} is the predicted polynomial function and ε the polynomial regression residuals.

Therefore, a large set of calibration grid images needs to be collected with respect to the multiple poses. Afterwards, the Zh-method is applied while identifying both the extrinsic parameters and the associated reprojection errors R_{E_i} to build the learning base of the ML-algorithm. Based on [Lu10], the learning base is splitted into two data sets: 70% of the images are used as a training set whereas the remaining 30% of the images are the testing set. Since the learning base contains a limited number of inputs and outputs, the application of a single stratified splitting strategy is not appropriate to reach an accurate estimation of the algorithm's performance. In this context, Xu [XuGo18] underlines the benefit of multiplying the train/test sets rather than using a single split. Consequently, the reliability of the stratified train/test partitioning was reinforced by adopting the cross-validation method described in [Berr18]. It often involves a randomly stratified resampling of the dataset to assess the ability of the predictive model and to prevent over fitting. In k -fold cross-validation, the learning base is partitioned into k disjoint subsets of approximately equal size and without overlap as illustrated in Figure III.2. The polynomial regression model is trained using $k - 1$ subsets, then applied to the remaining subset (or validation/testing set), and the performance is measured. This procedure is repeated until each of the k disjoint subsets has been served as a validation set.

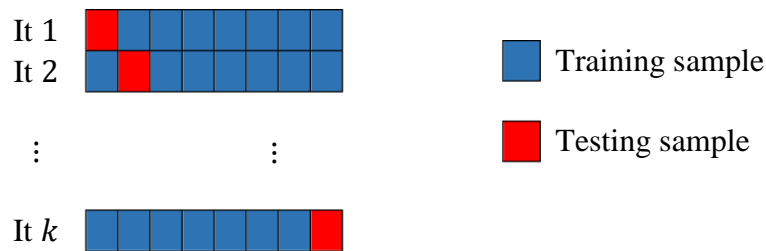


Figure III.2 Illustration of the k -fold cross-validation principle

The implemented cross-validation method is applied so as to optimise the degree D of the polynomial regression ($1 \leq D \leq 13$). The selected criterion is the mean absolute error (MAE)

expressed in eq. III.5 where T is the test set. The evolutions of both training and testing MAE lead to select the appropriate degree of the polynomial model.

$$MAE = \frac{1}{|T|} \sum_{i \in T} |R_{E_i} - \hat{f}(W_i)| \quad \text{III.5}$$

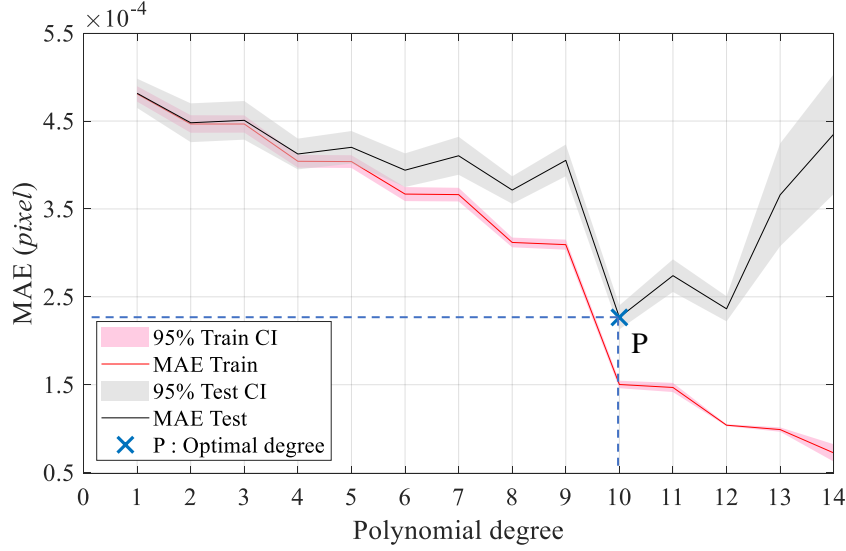


Figure III.3 Evolution of the MAE vs. the polynomial degree when applying the k -fold cross-validation method (CI is the confidence interval)

According to Figure III.3, the train curve decreases when the polynomial order increases. The test curve also decreases until the polynomial degree reaches $D = 10$ to increase again. This is due to the overfitting [Ragh21] defined as the polynomial model describing the noise in the data rather than the underlying model.

III.2.2. Particle swarm optimisation

The extraction of the optimal poses associated to the polynomial minimums and the identification of the appropriated extrinsic parameters can be accomplished by solving a constrained minimization problem, with respect to the following linear and nonlinear conditions identified from Rojberg study:

- visibility of the calibration grid: this criterion is defined by the inequality expressed in (eq. III.6), where (U_{max}, V_{max}) is the pixel resolution of the imaging sensor:

$$\begin{cases} u_{i,j} - P_u(\emptyset, \mathbf{\Pi}_i, X_j) < U_{max} \\ v_{i,j} - P_v(\emptyset, \mathbf{\Pi}_i, X_j) < V_{max} \end{cases} \quad \text{III.6}$$

- FoV coverage: criteria on the translations t_x and t_y are defined in order to split the space into several searching areas to fully cover the camera FoV
- angular positioning: the maximum angle between the calibration grid normal $\overrightarrow{N_G}$ and the camera optical axis $\overrightarrow{N_C}$ should be below 60° (eq. III.7).

$$\left\| \overrightarrow{N_G} \right\| \times \left\| \overrightarrow{N_C} \right\| \times \cos \left(\widehat{N_G, N_C} \right) < \cos(60^\circ) \quad \text{III.7}$$

where $\left\| \dots \right\|$ is the vector norm.

To find the minima of the polynomial, many techniques are proposed in literature, all adapted for concave, convex and unimodal functions. Some of those techniques are: gradient descent, LM, BFGS, etc. [Osbo76, Rude17, XiWW08]. Nonetheless, they are not efficient for optimisation problems under linear and nonlinear constraints. Based on [CoHa03, YiAM20], the particle swarm optimisation (PSO) seems to be an appropriate method for such an optimisation problem. It aims to minimize a fitness function by undertaking a population search in a D-dimensional search space [Tamb19]. The swarm is composed of multiple particles, each is characterized by its position in the model and its velocity ([appendix D](#)).

Let k be an iteration index in the optimisation context, the position of a particle in the swarm, at iteration k in a six-dimensional space (3 translations and 3 rotations) is defined by a homogeneous vector X_i^k .

The velocity parameter (eq. III.8) depends on three components: (1) the inertia is a parameter affecting the convergence, (2) the cognitive component is the individual behaviour that defines the best value obtained by each particle l at each iteration k , (3) the global component is the optimum found by the whole swarm, updated at each new global optimum.

$$\overrightarrow{V_i^{k+1}} = w\overrightarrow{V_i^k} + c_1r_1 \left(\overrightarrow{P_i^k} - \overrightarrow{X_i^k} \right) + c_2r_2 \left(\overrightarrow{G^k} - \overrightarrow{X_i^k} \right) \quad \text{III.8}$$

- Where:
- $\overrightarrow{V_i^k}$: velocity vector of the particle at iteration k
 - w : inertia weight
 - c_1, c_2 : cognitive and social acceleration (positive constants)
 - r_1, r_2 : random values in the interval $[0,1]$, sampled from a uniform distribution
 - $\overrightarrow{P_i^k}$: best individual position associated with particle l
 - $\overrightarrow{G^k}$: best position associated with the set of particles in the swarm

The PSO apply a limited number of parameters. The number of particles in any swarm is often selected with respect to the complexity of the problem, usually in the range [20, 50] [PiNP20]. Bansal *et al* [BSSV11] and Maurya [MBPB19] reveal that the best inertia weight (w) range [0.4, 0.9] could guarantee a convergence to the minimum. The cognitive and social acceleration coefficients c_1 , c_2 are usually set to 0.7 [ALMC19].

III.2.3. Full implemented calibration flowchart

The implemented calibration flowchart is illustrated in Figure III.4, where three main steps could be distinguished: (1) acquisition step where a set of images of the calibration grid are taken so as to build the learning base, (2) the ML-approach is applied to extract the input/output data needed to perform the polynomial regression. It includes the reprojection errors R_{E_i} and the associated extrinsic parameters, (3) the application of the polynomial regression to estimate the polynomial degree D , combined with the PSO to extract the associated optimal poses.

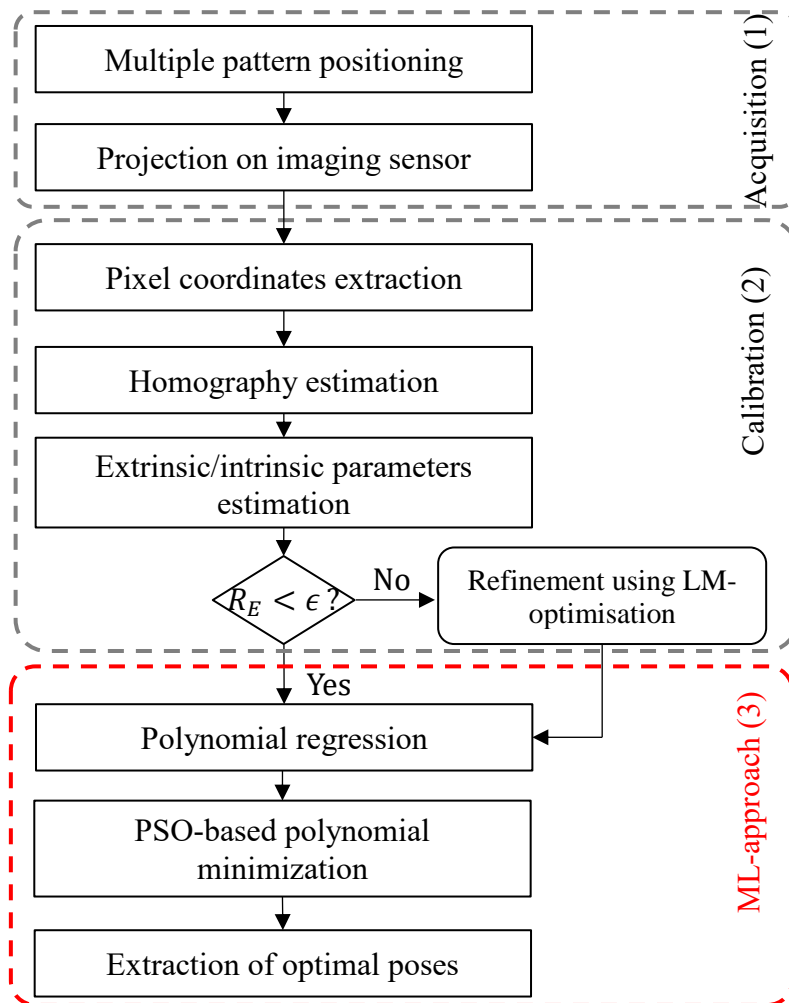


Figure III.4 Full flowchart of the proposed methodology for machine vision calibration. R_E is the average reprojection error and ϵ is the threshold

III.3. Optimisation for stereo systems

One of the major drawbacks of the pose-based optimisation methods proposed in the literature is their adaptation to stereo systems and more specifically to SL scanners. The ML-approach is effective for single camera but can also be adapted to SL scanner through some modifications.

Let's consider a pair of camera-projector system. In addition to the intrinsic parameters, the stereo calibration includes the rigid transformation between the two optical components. Let's also remind that SL systems are based on the projector of a pattern to establish the correspondence between the projector pixels and the calibration grid feature points.

Figure III.5 illustrates the calibration process of an active stereo system using a single pose of the calibration grid, where $[R_1 \ T_1]$ is the transformation from the projector to the calibration grid called projector extrinsic matrix and $[R_2 \ T_2]$ is the camera extrinsic matrix. For each calibration grid pose, a reprojection error can be associated to each element.

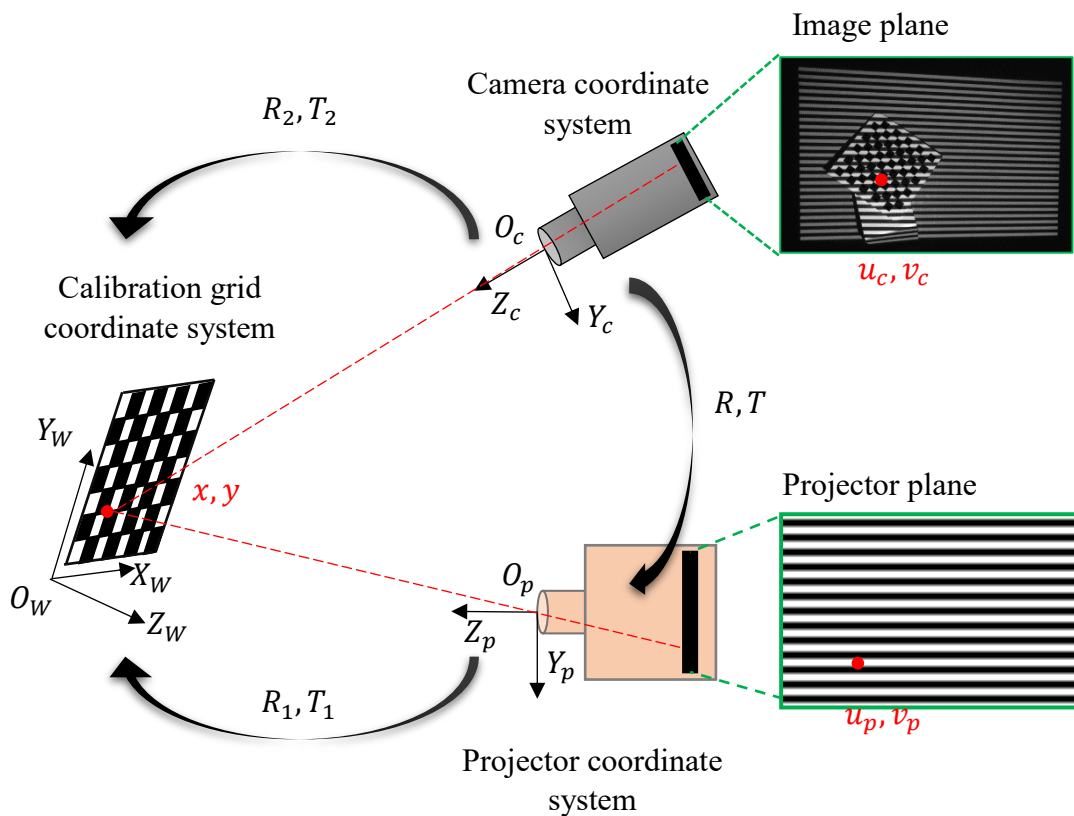


Figure III.5 Illustration of plane-based calibration of an active stereo system

III.3.1. Polynomial regression of the extrinsic parameters

As described for single camera, the learning base of the ML algorithm needs to be built. Hence, N poses of the calibration grids are adopted and images are taken using the 3D scanner. For each pose, the SL pattern is projected, and images are taken using the camera. At least 1000 poses need to be generated to obtain a good estimation of the polynomial model. Using the Zh-method, the extrinsic parameters and the reprojection error of each image of the calibration grid are extracted. Table III.2 illustrates the process used to build the learning base of the ML algorithm.

Table III.2 : *Building process of the learning base*

Image index	W_i	Projector	Camera
1	$\alpha_1, \beta_1, \gamma_1, t_{x_1}, t_{y_1}, t_{z_1}$	$R_{E_1}^P$	$R_{E_1}^C$
\vdots	\vdots	\vdots	\vdots
M	$\alpha_M, \beta_M, \gamma_M, t_{x_M}, t_{y_M}, t_{z_M}$	$R_{E_M}^P$	$R_{E_M}^C$

Once the data set is created, the polynomial regression is applied to estimate the polynomial function that models the relationship between the extrinsic parameters W_i and the reprojection errors R_{E_i} . Here, two functions are estimated as expressed in eq. III.9, where $\widehat{R}_E^C(W_i)$ and $\widehat{R}_E^P(W_i)$ are respectively the camera and projector polynomials.

$$\begin{cases} R_{E_i}^C = \widehat{R}_E^C(W_i) + \varepsilon_C(W_i) \\ R_{E_i}^P = \widehat{R}_E^P(W_i) + \varepsilon_P(W_i) \end{cases} \quad \text{III.9}$$

- Where:
- $R_{E_i}^C$ and $R_{E_i}^P$: camera and projector reprojection errors in the data set
 - ε_C and ε_P : camera and projector polynomial residuals

The polynomial degree (for both camera and projector) has been set to 10 according to the cross validation applied in the case of a single camera calibration as to avoid the overfitting.

III.3.2. Weighted sum of the estimated polynomials

The optimisation of SL scanner poses usually leads to obtain some outstanding poses that might be optimal for the camera, but are not optimal for the projector or vice versa. In order to optimise the positioning for both elements, the SL scanner can be modelled as a linear combination of two polynomials, $\widehat{R}_E^C(W_i)$ and $\widehat{R}_E^P(W_i)$.

Afterwards, a weighted sum is proposed to combine the two polynomials and create a fully integrated analysis. The function that models the camera-projector pair can be defined using multiobjective optimisation methods. The weighted sum method transforms multiple objective functions into a scalar single-objective function by associating a weight to each polynomial [Coel18].

Weights w_i are positive integers such as: $\sum_{i=0}^k w_i = 1, w_i \in [0,1]$. Therefore, the subsequent minimization results depend on the values of the chosen weights. For SL scanner, the projector reprojection error is usually higher than the one of the camera [WiOL14]. It is due to the use of the camera for the identification of the projector parameters, which introduces errors in the projector calibration process, and leads to selected weights such as $w_{proj} > w_{cam}$. The resulting multivariate polynomial that models the SL scanner is expressed in eq. III.10.

$$\widehat{R}_E(W_i) = w_{cam}\widehat{R}_E^C(W_i) + w_{proj}\widehat{R}_E^P(W_i) \quad \text{III.10}$$

III.3.3. Multiobjective function minimization

Extracting the minima of the multivariate polynomial $\widehat{R}(W_i)$ can be done by solving a constrained minimization problem, involving linear and non-linear constraints defined by Rojtberg for single camera [RoKu18]. An adaptation of those constraints for SL scanners is required since both optical components are simultaneously calibrated. Therefore, those constraints could be defined as follows:

- (1) the calibration pattern must be visible from both the camera and the projector perspectives,
- (2) both the camera and the projector FoVs must be fully covered while taking images of the calibration pattern,
- (3) the angle between the normal of the calibration grid $\overrightarrow{N_G}$ and the camera optical axis $\overrightarrow{N_C}$ should be below 60° ,
- (4) the angle between the normal of the calibration grid $\overrightarrow{N_G}$ and the projector optical axis $\overrightarrow{N_P}$ should also be below 60° .

The PSO could be applied to minimise $\widehat{R}(W_i)$ while considering the previous constraints. The suggested full flowchart is illustrated in Figure III.6, where two steps are involved: (1) the parallel calibration of the camera and the projector, (2) the proposed optimisation that consists of a multivariate polynomial regression followed by a weighed sum and the PSO minimization.

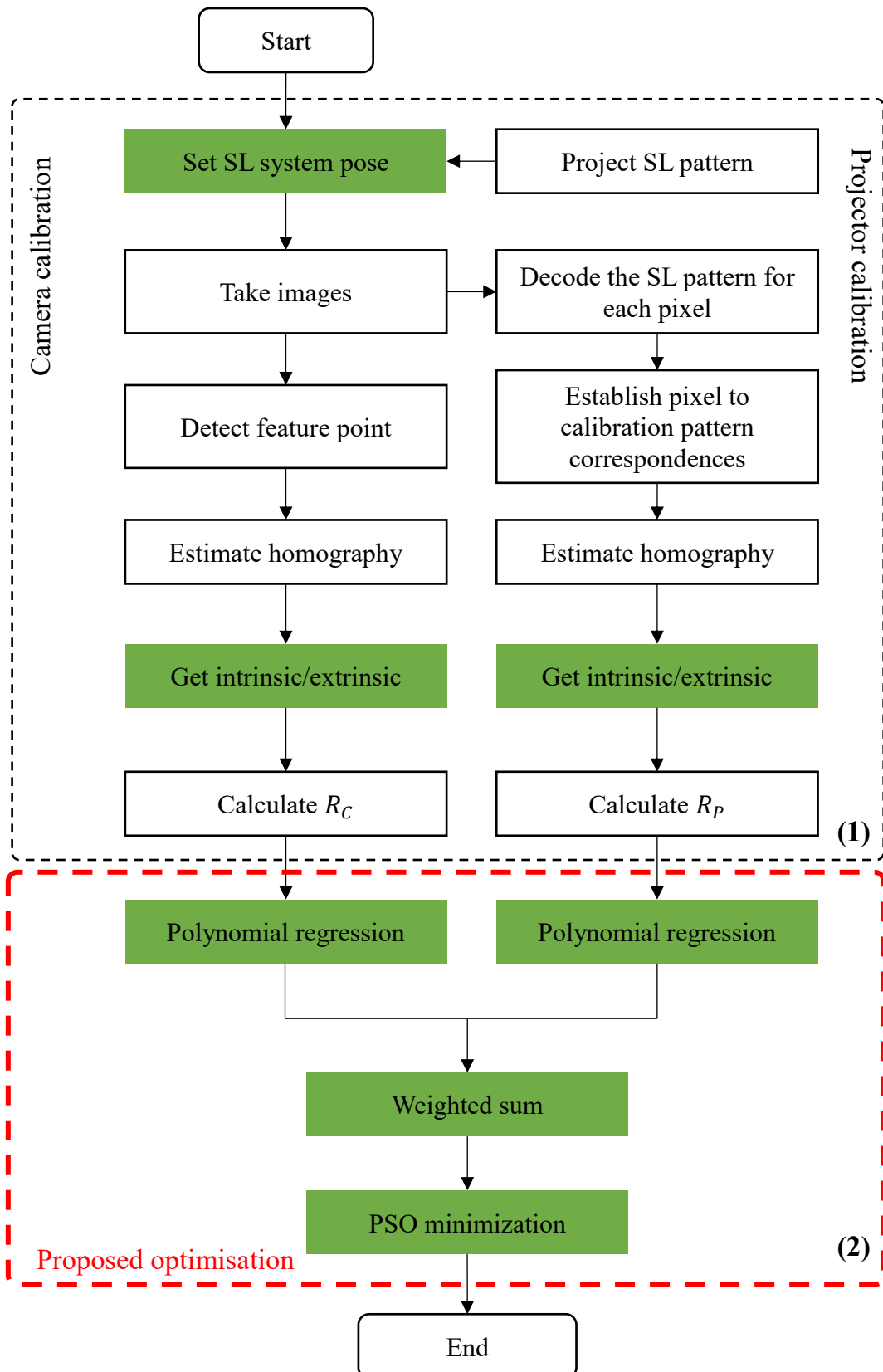


Figure III.6 Flowchart of the proposed positioning optimisation method [EGVL22]

III.4. Synthetic evaluation of the proposed optimisation

III.4.1. Simulation of the calibration process

To evaluate the effectiveness of the ML-approach, a simulation of the calibration process is performed, while considering predefined intrinsic parameters. Afterwards, the residuals between the estimated and the predefined parameters are evaluated. The predefined intrinsic parameters are presented in Table III.3.

Table III.3 *Predefined intrinsic parameters of the virtual camera*

Parameter	Value
Focal length f_u	8 mm
Focal length f_v	8 mm
Principal point (c_u, c_v)	(640, 512) pixels
Sensor size	1280 × 1024 (pixels)
Radial dist. Coeff.	$k_1 = -0.05$ and $k_2 = 0.05$

The simulation consists of creating one virtual camera and one virtual checkerboard through a very simplified graphics engine. Pixels effect were taken into consideration as shown in Figure III.7.a, for which the anti-aliasing (Figure III.7.b) and the depth of field effect (Figure III.7.c) were considered. The anti-aliasing is defined by Jiang *et al.* [JSL14] as the property in digital imaging used to smooth out irregular edges (or "Jaggies") to avoid displaying rectangular pixels. Hence, the Harris feature points detection [SáMS18a] was applied while estimating the coordinates of the points of interest in the imaging sensor.

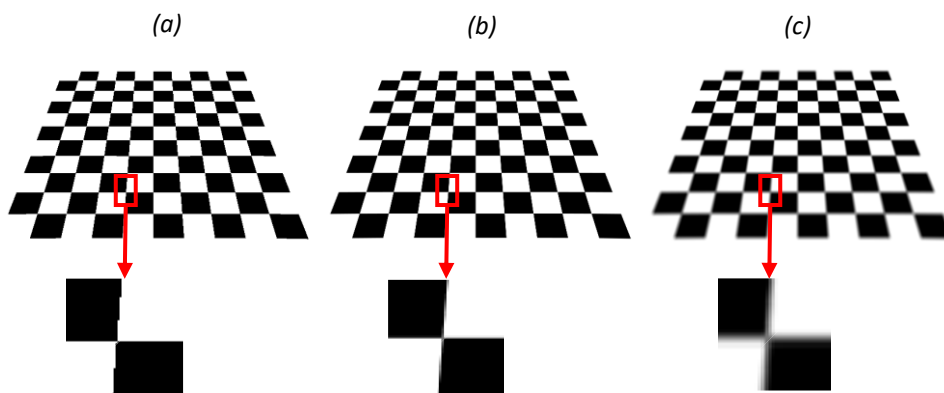


Figure III.7 *Illustration of the proposed virtual checkerboard simulation: (a) without effect, (b) using anti-aliasing, (c) adding the depth of field effect.*

The virtual checkerboard contains 10×9 points of interest, considered as reference points, with a distance of 6 mm between the intersections. The origin of the coordinates frame for the checkerboard is defined at its centre and its normal vector selected along the z -axis. The simulated camera is initially located 400 mm away from the virtual checkerboard along the z -axis, and oriented so that its optical axis passes through the checkerboard centre. 1000 poses of the virtual camera were generated along the x -axis in the range $[0, 60]^\circ$ and the z -axis in the range $[0, 360]^\circ$ (see Figure III.8). Translations of the camera were also applied along the x - and y -axis to cover the entire FoV.

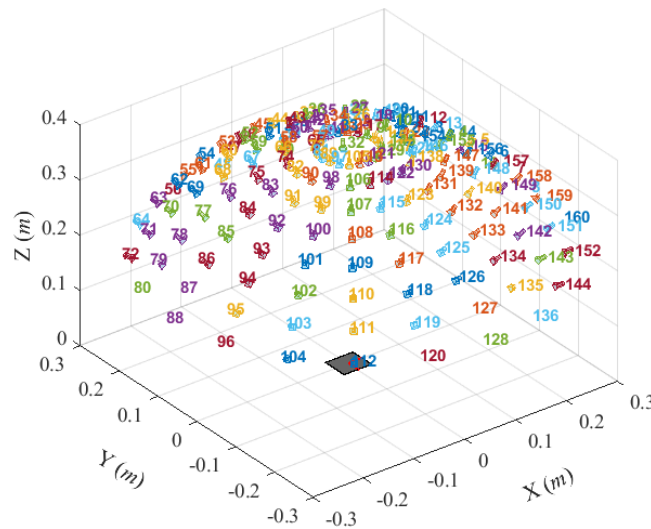


Figure III.8 Simulated views for image acquisition in the checkerboard coordinate frame (only rotations are applied and presented in this figure)

The implemented ML-approach was applied to estimate both the extrinsic parameters and the reprojection error at each generated pose. Afterwards, the polynomial regressions were calculated, and the optimal polynomial degree D was identified through the implemented PSO. Here, a partitioning of the camera FoV in 30 zones was carried out and the PSO was applied to extract the optimal poses associated with the lowest reprojection errors. The results returned by the ML-approach [EVLB22] were compared to those given by the recently published CW-method [PeSt19] and the R-method [RoKu18], when considering reprojection errors, intrinsic parameters (f_u, f_v, c_u, c_v) , radial distortion coefficients (k_1, k_2) and extrinsic parameters (R, t) .

III.4.2. Simulation results and analysis

A uniform distribution of about 1000 poses of the synthetic camera is defined with respect to the calibration grid. Then, the ML-approach is applied while identifying the most appropriate

poses. Finally, the estimated intrinsic and extrinsic parameters are compared to the ground truth. Figure III.9 shows the feature points in the checkerboard visualized by the camera.

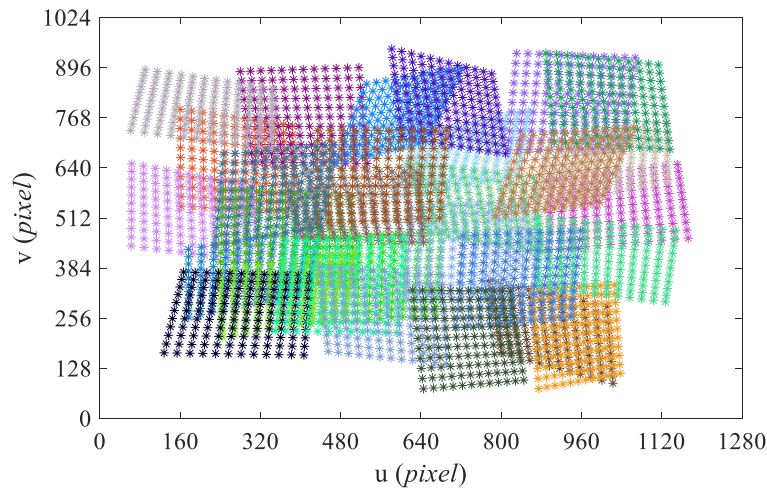


Figure III.9 Visualization of selected feature points in the checkerboard seen by to the camera with regard of the set of optimal poses returned by the ML-approach

The evolution of the camera reprojection errors estimated at each resulting optimal pose returned by the implemented ML-approach, CW-method and R-method is illustrated in Figure III.10. The identified optimal poses given by the ML-approach present lower reprojection errors compared to CW and R-method. Furthermore, the returned optimal poses by the CW-method depends on the initial random poses of the calibration grid. This constraint is appropriated for the case of dynamic environments, such as variable brightness, nonetheless the returned reprojection errors are not certainly optimal. In contrast, the proposed ML-approach is deterministic and the same poses are used for consecutive calibrations. Unlike the CW-method, the ML-approach performs better in controlled environments.

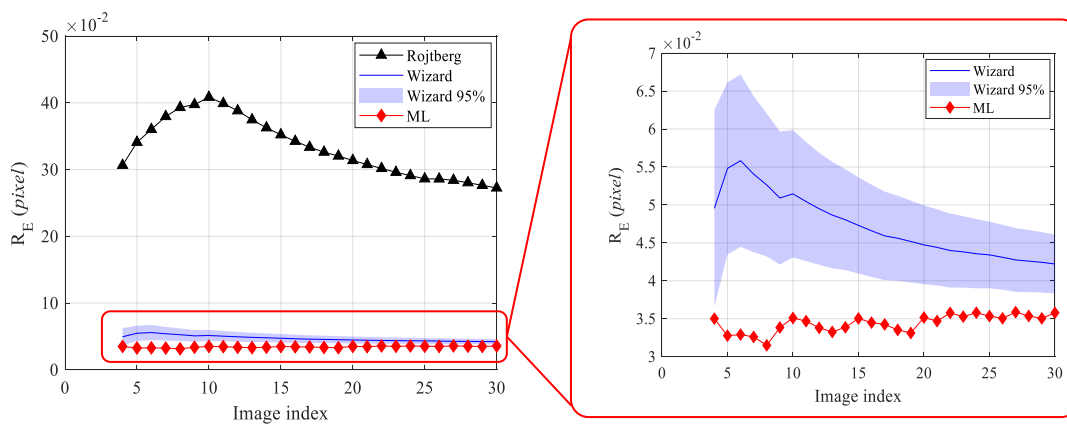
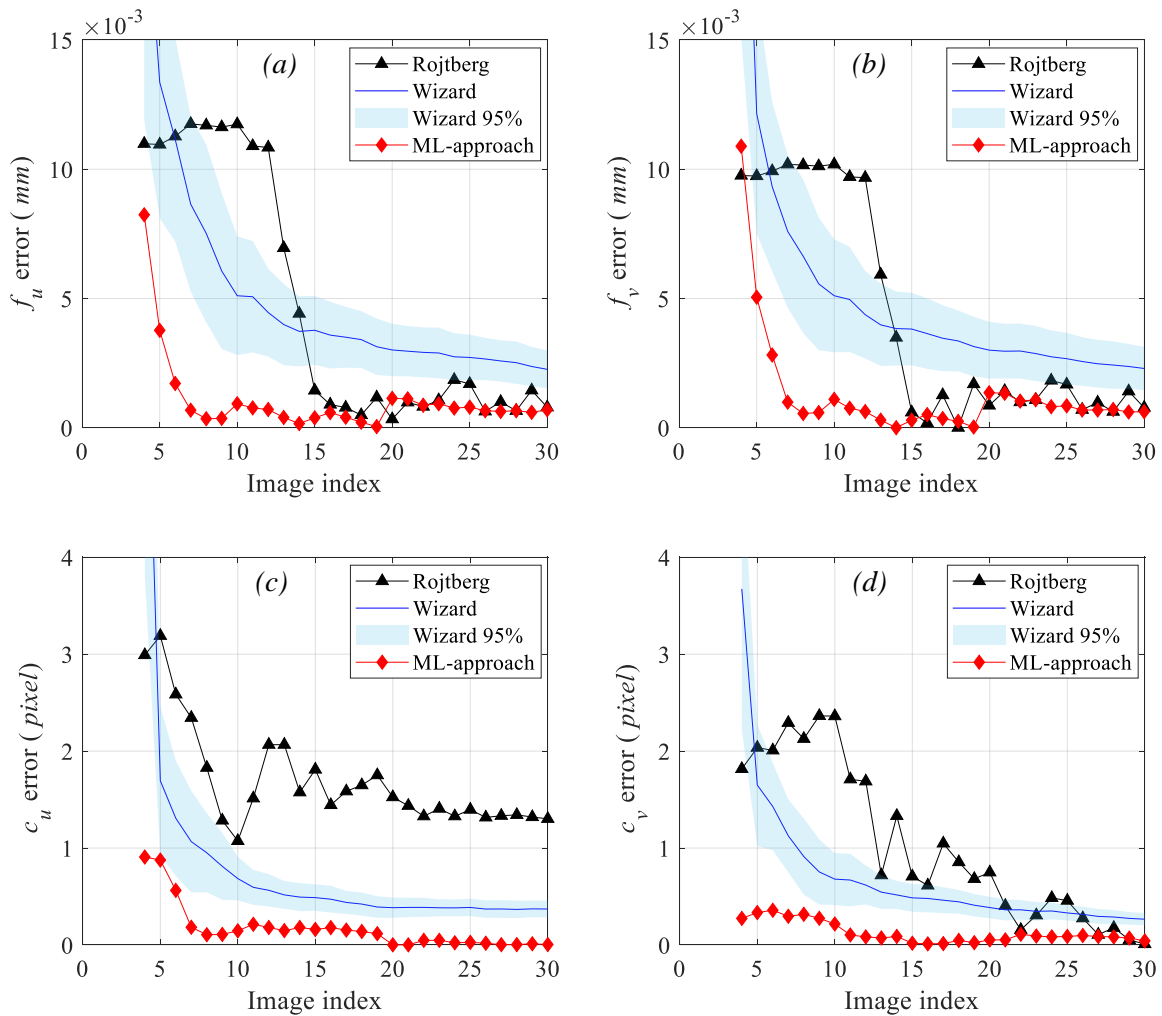


Figure III.10 Comparison of reprojection errors estimated using ML-approach CW and R-method

The evolution of the errors between the predefined and estimated intrinsic parameters (f_u, f_v, c_u, c_v), radial distortion coefficients (k_1, k_2) and extrinsic parameters (R,t) when applying the proposed ML-approach and both the recent published CW- and R-method are illustrated in Figure III.11. Therefore, it is noticeable that the estimated parameters reach a horizontal asymptote within a limited number of images (about 15 images), even if the distortion coefficients present instability. This instability could be explained by the space partitioning constraint adopted at the minimum identification step. Nonetheless, the proposed ML-approach estimates more accurate intrinsic, distortion and extrinsic parameters in comparison to CW and R-method.



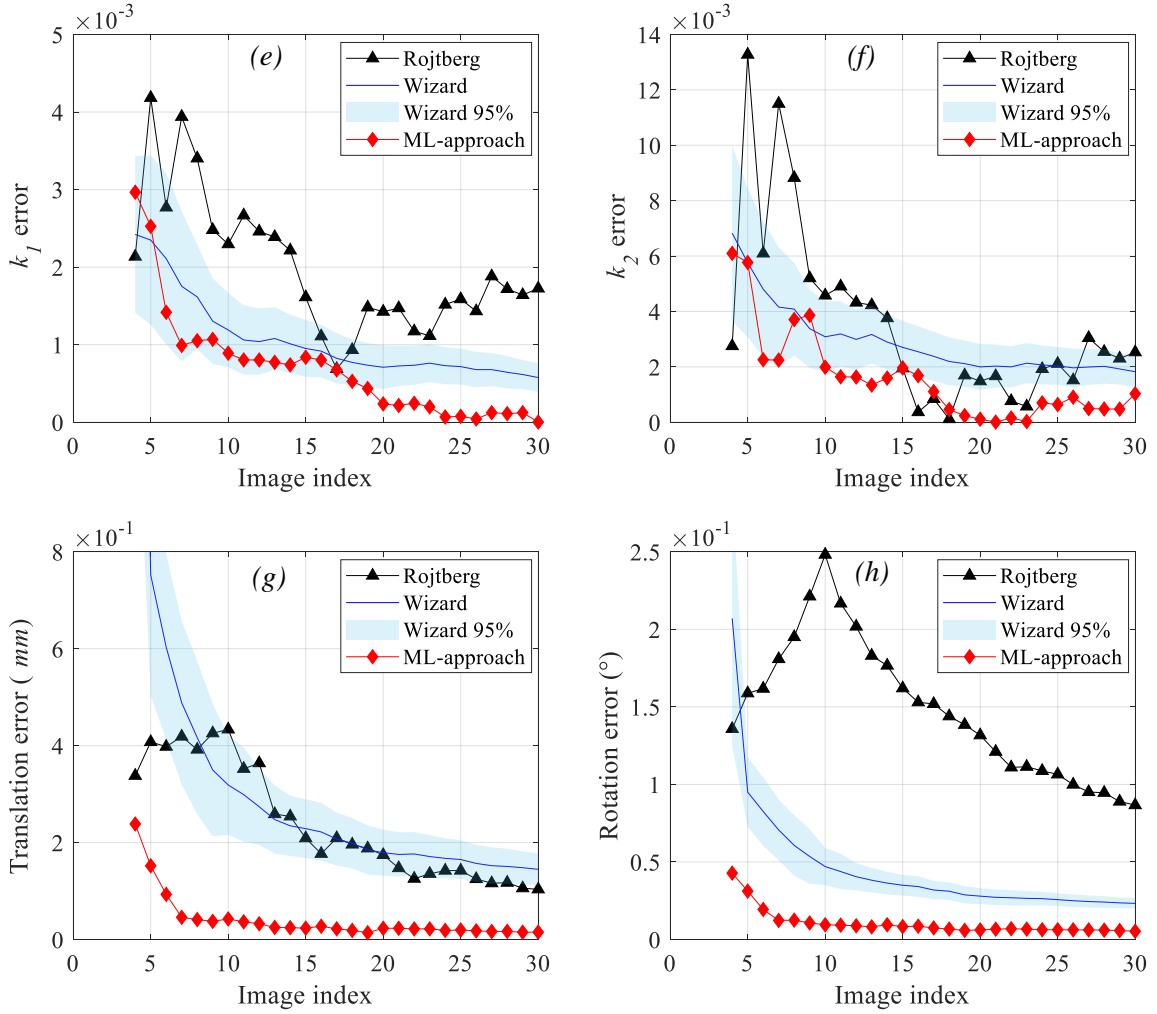


Figure III.11 Evolution of the pinhole camera parameters returned by ML-approach, CW- (Calibration Wizard) and R-method (R: Rojtberg): (a) & (b) is the focal length, (c) & (d) are the principal point coordinates, (e) & (f) are the coefficients of radial distortion and (g) & (h) are the extrinsic parameter. Note : the initial points for k_1 and k_2 are not illustrated since they present high values of errors

The performances of the investigated ML-approach, CW- and R-method, are detailed in Table III.4, when considering images index between 20 and 30 (Figure III.11). All pinhole parameters (f_u , f_v , c_u , c_v , k_1 , k_2 , R and t) and additional percentage parameters $E_{ML/Ro}$ and $E_{ML/CW}$ (errors between the predefined and estimated parameters returned by the ML-approach divided by Rojtberg ($E_{ML/Ro}$) and CW ($E_{ML/CW}$) errors, respectively) are illustrated in Table III.4.

For focal length parameters (f_u , f_v), the percentages of the ML-approach errors are about 80% of the Rojtberg errors and 30% of the CW errors. The ML-approach returns a highly accurate estimation of all other pinhole parameters, including the extrinsic parameters, as shown in

Table 1, and therefore validates the superiority of the proposed ML-approach over the CW- and R-method. Furthermore, the CW-method returns more accurate results than R-method, except for c_u , k_1 and T .

Table III.4 : Pinhole (intrinsic and extrinsic) parameters errors estimated on image index between 20 and 30 when applying the investigated R-method, CW-method and ML-approach

	R-method	CW-method	ML-approach	$E_{ML/Ro}$ (%)	$E_{ML/CW}$ (%)
f_u (mm)	0.0010	0.0027	0.0008	80	29.63
f_v (mm)	0.0011	0.0027	0.0009	81.82	33.33
c_u (pixels)	1.3667	0.3787	0.0173	1.26	4.57
c_v (pixels)	0.2892	0.3253	0.0782	27.04	24.04
k_1	0.0015	0.0007	0.0001	6.67	14.28
k_2	0.0019	0.0020	0.0005	26.31	25
R (°)	0.1304	0.1625	0.0191	14.65	11.75
t (mm)	0.1050	0.0256	0.0062	5.90	24.22

III.5. Experimental validation of a single camera

In this section, an experimental evaluation is proposed as to demonstrate the effectiveness of the ML-approach. Thus, the performed experiment leads to compare the feature points intersections measured by a camera (calibrated using the ML-approach) to those measured by a traceable optical CMM.

III.5.1. Experimental setup

The experimental calibration is performed with the developed 3D scanner, illustrated in Figure III.12. The scanner is rigidly attached to the robot end-effector through a fixing part. Only one camera is considered for this study. To acquire the data, 1000 end-effector poses have been defined using the robot software. At each pose, a picture of the calibration grid is acquired using the camera to be calibrated. The used camera is a monochrome Ximea *MQ013rg-e2* equipped with digital lens *LM8JCM-V* of 8.5 mm focal length. The camera rotational structure is

configured so that the z-axis end-effector and the optical axis camera are as parallel as possible in order to have a uniform distribution of poses around the calibration grid.

The 3D scanner is mounted on the end-effector of the KAWASAKI industrial robot (*d*), with a maximum reach of 620 mm and a positioning repeatability of 20 μm .

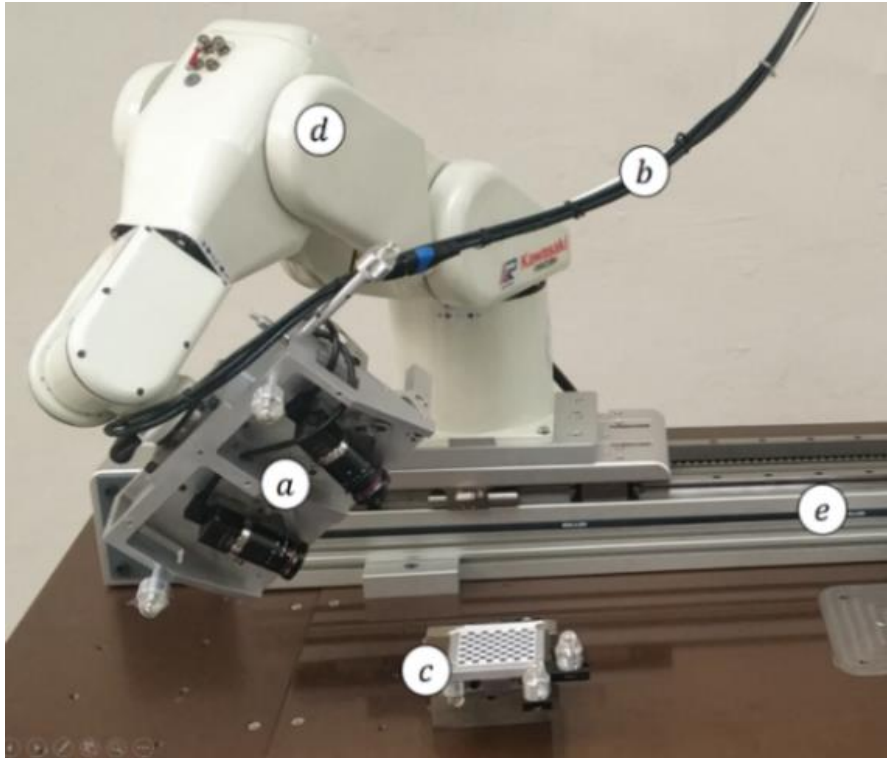


Figure III.12 Calibration process of a single camera using the ML-approach: (a) 3D scanning system; (b) Connection cables to the terminal computer; (c) Checkerboard calibration grid; (d) Industrial 6-axis KAWASAKI robot; (e) 7th motion axis.

III.5.2. Traceability establishment through CMM measurements

To perform the experimental calibration using the implemented ML-approach, one thermo-invariant (low coefficient of thermal expansion) ceramic calibration grid printed with chrome is used. The nominal distance between each neighbour points of interest is about 6 mm.

A traceable optical Micro-Vu Excel CMM (Figure III.13-a), accurate at the sub-micrometre level ($< 1 \mu\text{m}$), was selected for the identification of the 2D coordinate of each point of interest. The Micro-Vu Excel CMM is a gantry stage system equipped with a high-resolution camera-based measuring system to get fast and accurate measurements on a wide variety of mechanical parts. Figure III.13-b illustrates a zoom of the ceramic calibration grid printed with a checkerboard pattern.

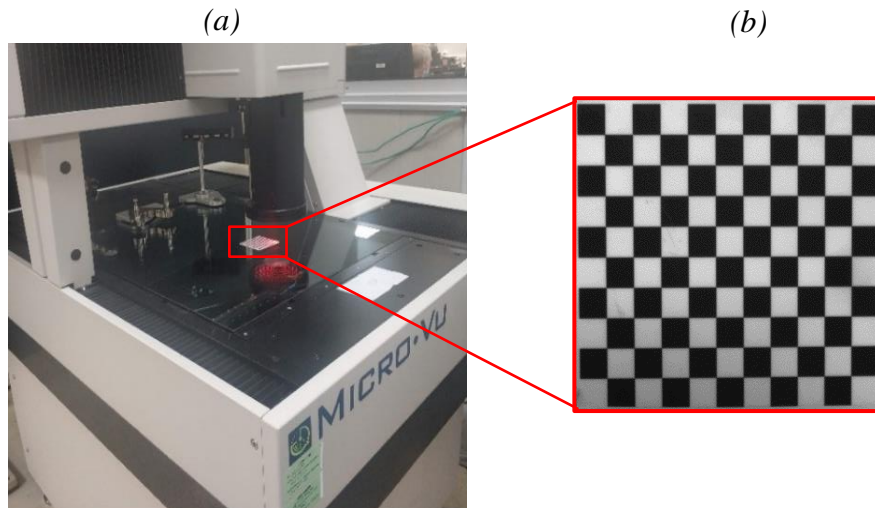


Figure III.13 (a) Traceable optical Micro-Vu Excel CMM, (b) Ceramic calibration grid printed with checkerboard pattern

Since the Micro-Vu Excel CMM is traceable to the definition of the International System (SI) metre [ScYK20, SDMM19], the traceability of the ceramic calibration grid becomes guaranteed with respect to the full traceability pyramid shown in Figure III.14. Therefore, the measurement uncertainty tends towards zero at the top of the traceability pyramid and deteriorates at the bottom, to reach a value of some 10^{-5} m.

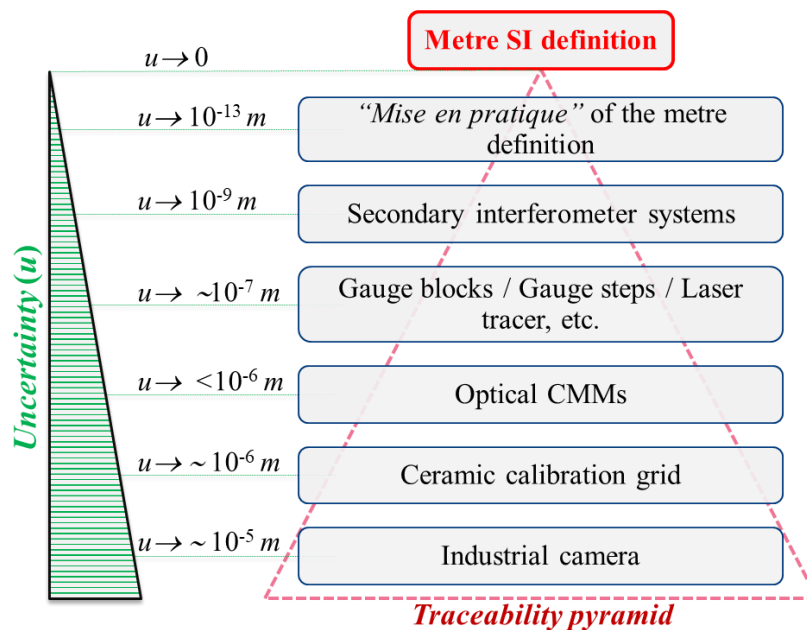


Figure III.14 Detailed full traceability pyramid adopted for the calibration of cameras

The calibration of the ceramic calibration grid has been carried inside the LNE cleanroom where both the temperature and hygrometry are controlled to $20^{\pm 0.3} \text{ }^\circ\text{C}$ and $50\%^{\pm 5}$ respectively. The used Micro-Vu Excel is an optical CMM with a measurement capacity up to

$400 \times 500 \times 250 \text{ mm}^3$. The scale resolution of the CMM is about $0.4 \text{ }\mu\text{m}$ and a measurement accuracy in the XY plane is measured by $2.8 + \frac{L}{200} (\mu\text{m})$, where L is the length of the object. Here, a calibration grid with 11×10 square of 6 mm length has been used. The dimensions of the calibration grid are about $660 \times 600 \text{ mm}^2$.

The calibration grid was positioned in the middle of the optical Micro-Vu Excel CMM table. The origin of the checkerboard frame is set at the point of intersection between the first horizontal and vertical lines H_1 and V_1 (Figure III.15-*a* and *b*). The x - and y - axes of the calibration grid and the CMM were roughly aligned. Then, a scan of the full surface of the calibration grid was performed with uniform sampling of $100 \text{ }\mu\text{m}$, aiming to extract the checkerboard vertical (with blue colour) and horizontal (with green colour) lines (Figure III.15-*a* and *b*). Afterwards, all black-to-white transitions corresponding to a fixed threshold grey value of 125 were identified as mentioned in Figure III.16.

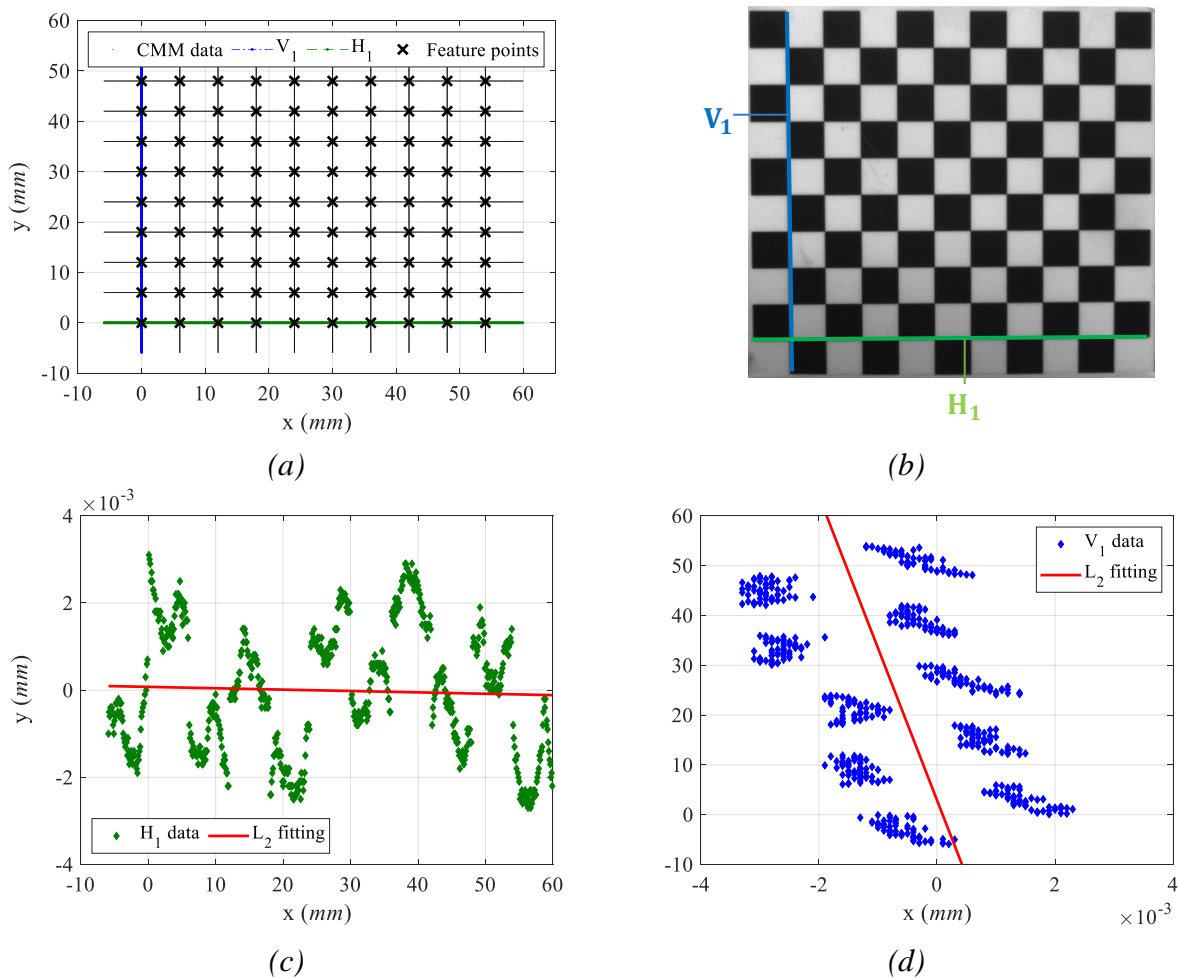


Figure III.15 (a) CMM 2D reconstruction of the checkerboard where H_1 is the first horizontal line and V_1 the first vertical line; (b) the checkerboard to be calibrated; (c) Least-square fitting of the line H_1 ; (d) Least-square fitting of the line V_1



Figure III.16 Example of the process of extracting points for vertical line using black-to-white threshold of 125

The identified points were structured as in Figure III.15-*c* and *d*, as well as each group of points was fitted with a least squares (L_2) model. The intersection of all vertical and horizontal least square models V_i and H_i leads to extract the full number of points of interest which in this case equals 90. Furthermore, this procedure including the scanning of the calibration grid and the identification of the points of interests was repeated five times as to upgrade the measurement accuracy.

III.5.3. Calibration of an industrial camera

The monochrome industrial camera, Ximea *MQ013rg-e2* equipped with a digital lens *LM8JCM-V* of 8.5 mm focal length, is calibrated. Here, the camera resolution is set to 1280×1024 pixels. The initial distance between the monochrome industrial camera and the ceramic calibration grid is fixed to about 310 mm. The following criteria, detailed by Rojtberg [RoKu18] for the minimum identification of a stable calibration were also respected:

- variation of the distance between the camera and the calibration grid to have an appropriate estimation of the focal [300, 320] mm,
- full covering of the camera FoV to estimate accurately the distortion coefficients,
- variation of the maximum angular up to 60° between the camera optical axis and the calibration grid normal axis to maximize the angular spread.

About 1000 poses of the monochrome industrial camera were set in order to build the learning base of the ML-approach. The evolution of the reprojection errors versus poses was modelled by a quadratic polynomial regression and the number of requested poses was optimised thanks to the implemented PSO. The adopted objective function is formulated in eq. III.11, where the

error ϵ' is fixed to 10^{-5} . A second stop criterion of maximum 500 iterations is considered. The evolution of the objective function is reported in Figure III.17 versus the PSO iterations.

$$\begin{cases} \epsilon' = R_{Ei}(k+1) - R_{Ei}(k) \\ k \leq 500 \end{cases} \quad \text{stop if } \begin{cases} \epsilon' \leq 10^{-5} \text{ pixels} \\ R_{Ei}(k+1) - R_{Ei}(k) \neq 0 \end{cases} \quad \& \quad k: \text{iteration} \quad \text{III.11}$$

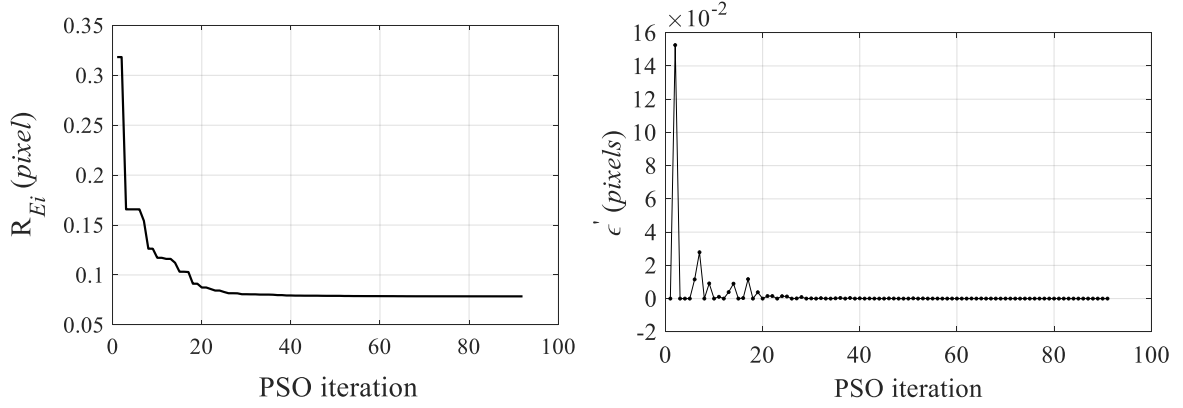


Figure III.17 Minimal objective function's particle value vs. the PSO iterations

Therefore, a set of 18 best calibration poses of the traceable ceramic calibration grid is identified while reaching an optimal calibration of the industrial camera. The estimated optimal poses from the camera perspective are presented in Figure III.18.

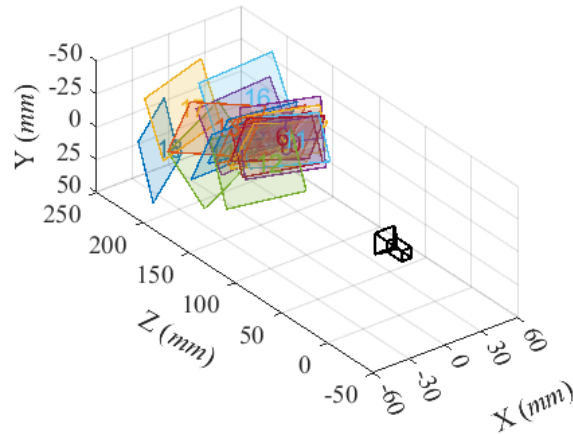


Figure III.18 Estimated optimal extrinsic parameters from camera perspective

The implemented Zh-method is applied to estimate the reprojection error of each optimal pose, as illustrated in Figure III.19, and the global distribution is illustrated in Figure III.20 with red colour. The calculated average reprojection error R_E is about $R_E \approx 0.05$ pixel with a standard deviation of 0.015 pixel. Furthermore, the Zh-method is applied on 10 calibration tests to extract the reprojection errors, where each calibration test contains 18 random poses of the traceable ceramic calibration grid. The average reprojection errors are calculated as detailed in Table III.5, and compared to the returned results when applying the ML-approach. Even if the number

of poses is similar for all calibration tests, the proposed ML-approach returns considerably smaller average reprojection error (about $R_E = 0.05$ pixel) with comparison to random selected poses. This result could validate the robustness of the implemented ML-approach.

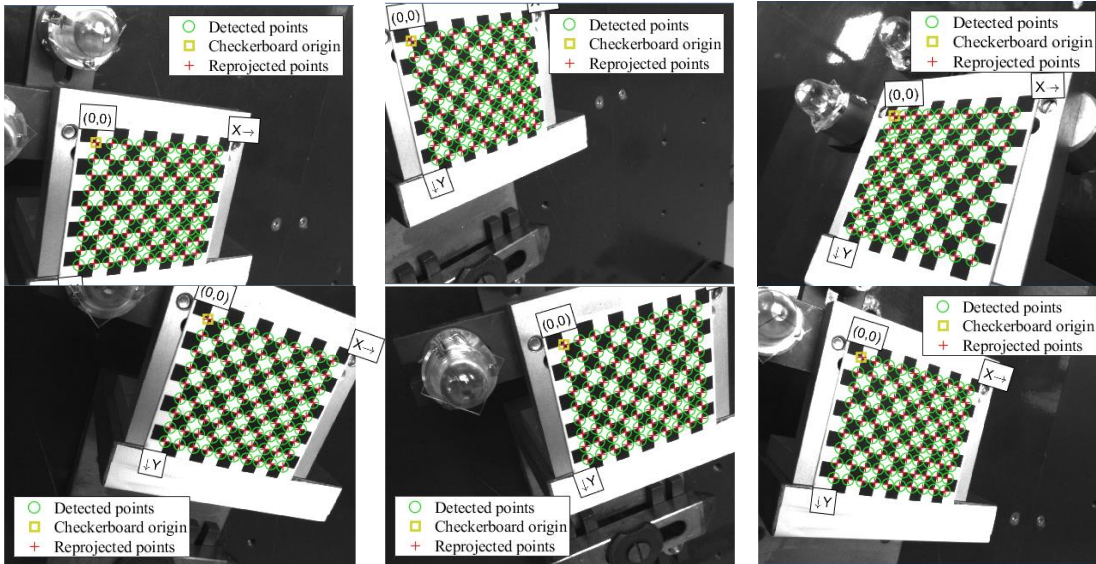


Figure III.19 Samples of resulting optimal poses returned by the ML-approach.

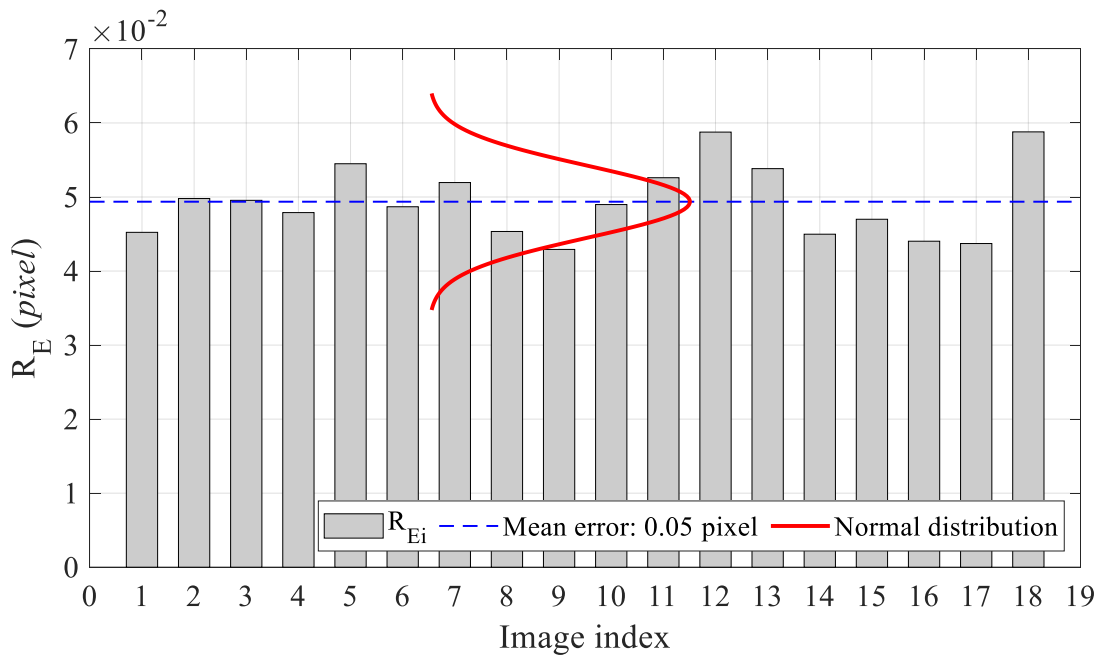


Figure III.20 Bar chart of reprojection errors estimated for each identified best pose using the ML-approach. Each bar represents the average reprojection error calculated for the image of the ceramic calibration grid.

Table III.5 Average reprojection errors (in pixel) estimated for each calibration test (each test contains the 18 optimal poses identified)

Calibration tests	1	2	3	4	5	6	7	8	9	10	ML
$\min_i R_{E_i}$	0.20	0.15	0.08	0.18	0.22	0.10	0.15	0.22	0.17	0.11	0.043
R_E	0.37	0.27	0.23	0.40	0.29	0.21	0.24	0.38	0.25	0.18	0.049
$\max_i R_{E_i}$	0.77	0.47	0.51	0.62	0.43	0.56	0.60	0.54	0.41	0.36	0.059

III.5.4. Time complexity analysis

The time complexity of the proposed optimisation method could be evaluated for each individual operation. Two phases of the algorithm are considered: (1) multivariate polynomial regression and (2) PSO minimization.

For cross-validation (phase (1)), the multivariate polynomial regression is repeated 14 times to estimate the optimal polynomial degree $D = \{1,14\}$. This operation can be parallelized, therefore time complexity of only one single polynomial regression is considered. The computation time of cross-validation has been estimated to about 14.5 min using 8 CPU workers of a 2 GHz Intel core i7.

The theoretical time complexity of the polynomial regression is formulated as $O(p^2 N_p + p^3)$ where N_p is the training sample and p is the number of coefficients of the polynomial. In practice, the time complexity depends on the used solver. Here the Scikit-learn (python) is selected to perform a multivariate polynomial regression using the gradient descent solver. $N_p = 1000$ images is considered for the ML-approach training, leading to a computation time of about 1.98 s for a multivariate polynomial regression with a degree of 10.

The time complexity of the PSO minimization (phase 2) depends on the stopping criteria. Let the total number of iterations be It and M the swarm size, the fitness is estimated for a particle with a time complexity of $O(1)$ at each iteration. Therefore, the PSO complexity is expressed by $O(It.M)$, and evaluated to about 11.03 s per minimum identification.

The global time complexity of the proposed ML-approach is formulated in eq. III.12.

$$T = O(It.M + p^2 N_p + p^3) \quad \text{III.12}$$

III.5.5. Comparison of results and discussion

The ML-approach assessment is fulfilled by calculating the error defined as the distance between the coordinates of the points of interest given by the traceable optical Micro-Vu Excel CMM and the reconstructed calibration grid using the inverse pinhole model expressed in eq. III.13.

$$\mathbf{\Pi}^{-1} \cdot \mathcal{O}^{-1} \begin{pmatrix} u \\ v \\ 1 \end{pmatrix} = \begin{pmatrix} X \\ Y \\ 1 \end{pmatrix} \quad \text{III.13}$$

The 90 errors Δ_i , formulated in eq. III.14, corresponding to the distance between the points of interest coordinates returned by both the optical Micro-Vu Excel CMM \mathbf{X} and the monochrome industrial camera \mathbf{Y} are evaluated (where $P = 90$ is the number of points of interest). The evaluation was carried out on one validation image of the checkerboard collected in the middle of the camera FoV and parallel to the imaging sensor. The new estimated extrinsic parameters lead to extract the coordinates of the points of interest.

$$\Delta_i = \frac{1}{P} \sum_{k=1}^P \|\mathbf{X}_k - \mathbf{Y}_k\| \quad \text{III.14}$$

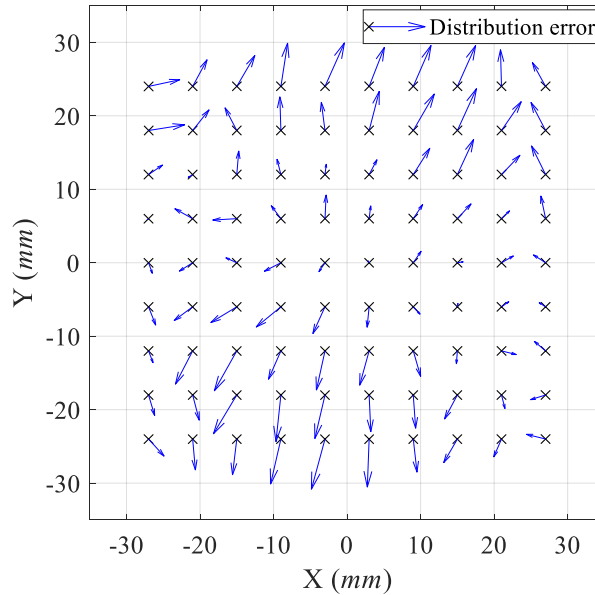


Figure III.21 *Error distribution of the estimated 2D coordinates of the traceable ceramic calibration grid.*

The distribution of errors, scaled by 300, along the checkerboard's x- and y-axis is reported in Figure III.21 where each arrow indicates the direction and magnitude of the error and 'x' indicates the coordinates of the points of interest measured by the traceable optical Micro-Vu

Excel CMM. The obtained average error Δ (mean of errors Δ_i) is about 11.68 μm . In addition, the calibration process is repeated 20 times to evaluate the repeatability of the average error Δ . Each test contains 18 optimal poses extracted when applying the ML-approach. Figure III.22 illustrates the repeatability of the vector distribution across the 20 tests (each repeated measure is represented by a colour in the figure). It is noticeable that the resulting vectors follow almost the same path and the magnitude of the vector is quite the same for each point.

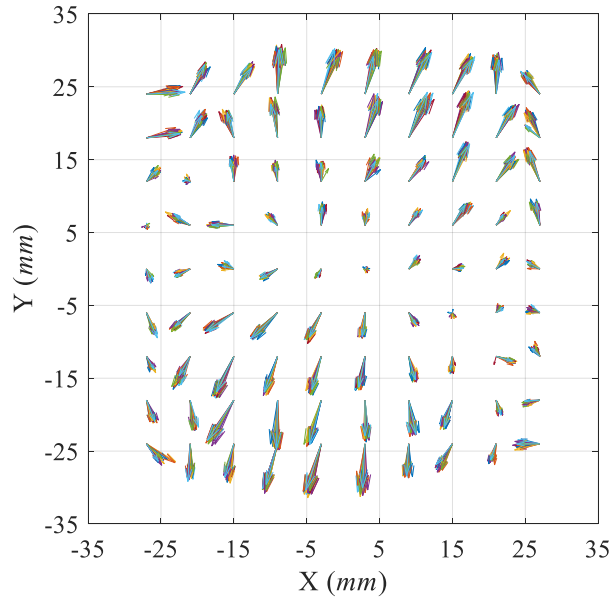


Figure III.22 Repeatability test of the norm vector across 20 tests

The mean error value Δ and the standard deviation are equal to $\sim 11.9 \mu\text{m}$ and $\sim 0.04 \mu\text{m}$, respectively (Table III.6). The estimated mean error value is small in comparison to the accepted target tolerances in manufactured large volume parts in the aeronautic domain, according to the ISO 2768-1 standard [Iso89].

Table III.6 Evolution of the average errors (Δ) using 20 validation images

Test index	Δ (μm)	Min	Max	Mean	Standard deviation
1	11.68				
⋮	⋮	11.66	12.0	11.87	≈ 0.04
20	11.91				

The returned results of the intrinsic parameters are presented in Table III.7. The estimated focal length of the calibrated camera is 7.87 mm with a standard deviation of 8 μm . The values of both f_u and f_v are approximately the same, this is due to the use of a CMOS sensor whose pixel

form is square. It is observable that the estimation of the intrinsic parameters is repeatable, as the relative standard deviations are estimated to $\sim 0.1\%$ for the focal length f_u and f_v , $\sim 0.09\%$ for c_u and 0.11% for c_v .

Table III.7 Evaluation of the repeatability test for the estimation of camera internal parameters

Calibration index	f_u (μm)	f_v (μm)	c_u (pixel)	c_v (pixel)	k_1	k_2
1	7863.0	7863.1	627.0	526.4	-0.063	0.059
\vdots	\vdots	\vdots	\vdots	\vdots	\vdots	\vdots
20	7863.0	7863.2	627.0	526.3	-0.059	0.062
Mean	7868.7	7868.6	627.2	526.5	-0.063	0.052
Standard deviation	8.6	8.6	0.6	0.6	0.005	0.009

Let (640, 512) be the nominal value of the image centre. According to Table III.7, the estimated coordinates of the principal point (c_u, c_v) are about (627.2, 526.5) pixels. The observed shift between both the nominal and the estimated values seem to be caused by the imperfections of the industrial monochrome camera including geometry errors of the optical aspherical lenses, assembly errors of the mechanical components, misalignment of optical lenses, etc.

III.6. Experimental validation of the SL scanner

Since SL scanner is composed of two optical components, only the extrinsic calibration will be evaluated. The extrinsic parameters estimated using the proposed optimisation will be compared to the robot and the laser rangefinders.

III.6.1. Pose optimisation

A set of 1000 poses are adopted using the robot so as to cover the area around the calibration pattern. For each pose of the SL system, a sequence of 10 Gray-code is projected on the calibration pattern in the horizontal and vertical directions while taking images (Figure III.23).

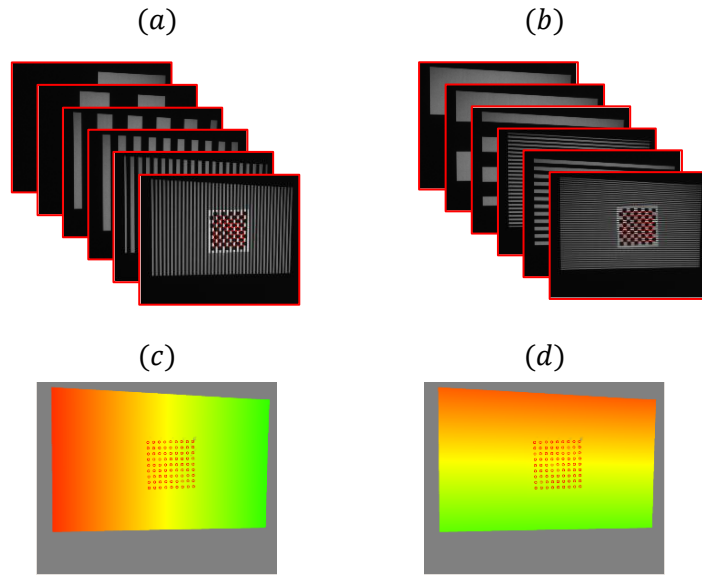


Figure III.23 Visualisation of the calibration process using a single pose

Afterwards, the camera-projector system is calibrated using the Zh-method to estimate the six extrinsic parameters W_i and the associated reprojection errors R_{C_i} and R_{P_i} for the camera and the projector respectively. Finally, PSO is applied under the linear and non-linear constraints to extract the 20 minimum reprojection errors associated to the optimal poses (Figure III.24). 20 optimal poses have been extracted due to the space partitioning which differs from the configuration of the single camera system. Table III.6 details the estimated intrinsic parameters of the camera and the projector components.

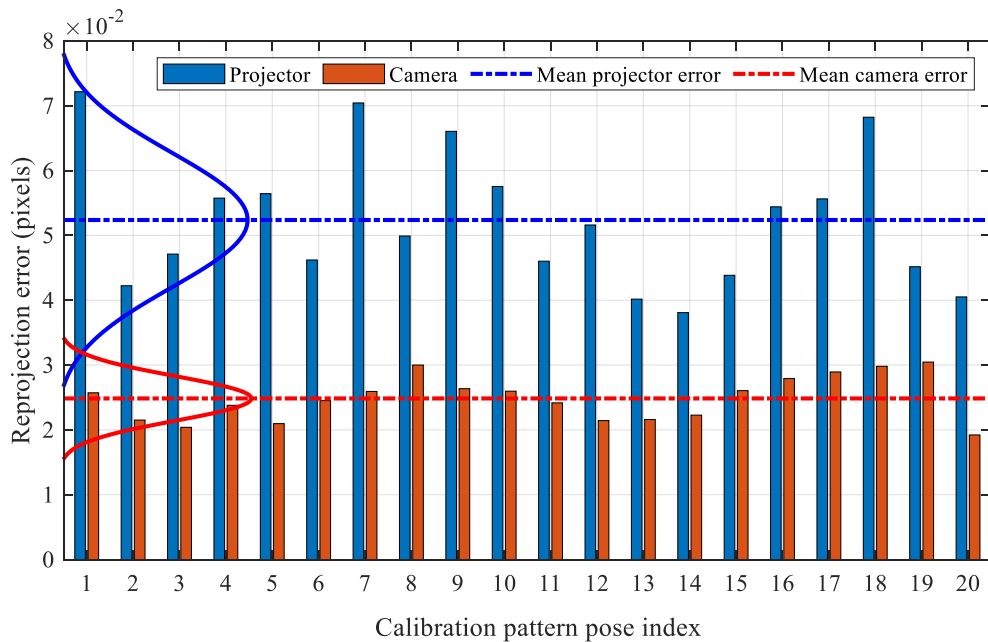


Figure III.24 Estimated camera and projector reprojection errors when applying the ML-approach [EGVL22]

Table III.8 *Estimated intrinsic parameters of the camera and projector based on the proposed method*

	f_u (pixel)	f_v (pixel)	c_u (pixel)	c_v (pixel)	k_1	k_2
Camera	1463.29	1463.24	628.18	519.92	-0.0277	0.0047
projector	393.43	787.16	392.74	853.85	0.0385	-0.1171

To evaluate the optimisation method, the relative transformations between the optimal poses are calculated and compared to those estimated by the external coordinate measuring system.

III.6.2. Coordinate measuring system based on multilateration

The coordinate measuring system, developed at the LCM [GuTW20b], is composed of a common absolute distance meter and of four measurement heads named A, B, C and D, as shown in Figure III.25. The positions in space of optical retroreflectors, i.e. the targets, are determined from the knowledge of the multiple distances measured between these targets and the four heads. This technique is called multilateration with self-calibration as the coordinates of the measurement heads and the targets are determined simultaneously.

In practice, the four measurement heads form a tetrahedron close to an isosceles, which is one of the optimal arrangements to minimize the uncertainty on the measured positions. The targets are retroreflecting spheres of glass index $n = 2$ [GTWA22]. Such targets are lightweight and visible from all angle; however, they induce high optical losses due to bad reflectivity and beam deflection at their output, which leads to a limited range of operation.

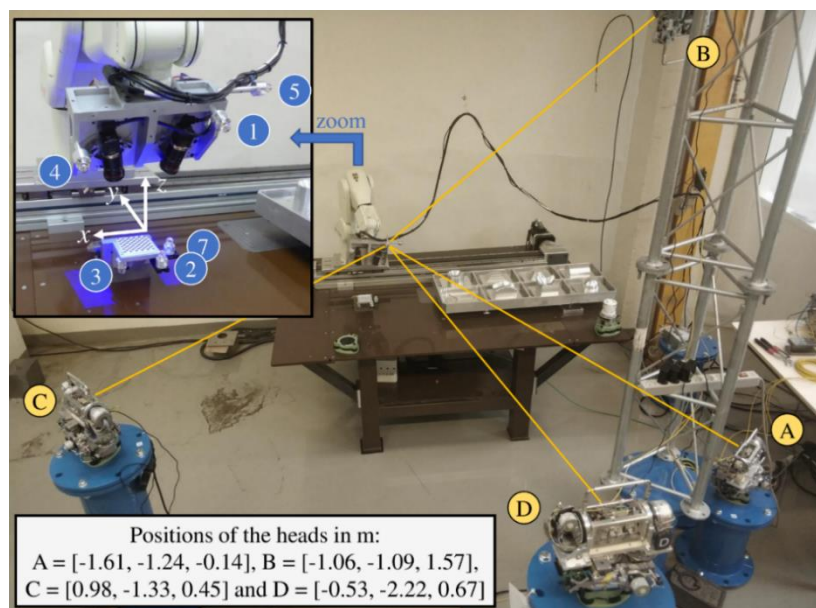


Figure III.25 *Photograph of the experimental setup*

First, on the table where the robot and the checkerboard were installed, a sphere of 14.2 mm in diameter has been moved into three different points to define the plane xOy of the table, and so the orientation of our Cartesian coordinate system. Then, three spheres of 14.0 mm in diameter have been mounted around the checkerboard as shown at the top left in Figure III.25. Their number are 3, 2 and 7. The latter have been measured 3 times during the day to verify the stability of the checkerboard pattern with respect to the 4 measurement heads, at 8:30 am, at 12:40 pm and at 4:30 pm. Lastly, three other spheres of 14.0 mm in diameter have been mounted on the SL system to determine its poses, i.e. both its positions in space and its orientations. Their number are 4, 1 and 5. The developed multilateration system has measured only 11 poses over the 20 performed by the robot due to time constraints. Our objective was to perform all the measurements in a single day to limit the risk of drifts from the different systems, for instance mechanical changes due to the thermal expansion.

At the end of the 45 measurements of sphere position (3 on the table + 3×3 on the checkerboard + 11×3 on the SL system), 38 of the sphere positions, the ones visible by the 4 measurement heads simultaneously, have been used in the multilateration algorithm with self-calibration to determine the coordinates of the four measurement heads. The remaining 7 sphere positions, visible by only three measuring heads due to beam occlusions, have been estimated by a classic trilateration technique. This represents a total of 173 distance measurements ($38 \times 4 + 7 \times 3$) performed in 8 hours. These distances range from 0.98 m to 2.54 m. At such distances the received radiofrequency (RF) power was sufficient to obtain a high signal, and thus an uncertainty on the distance measurements better than $4.3 \mu\text{m}$ (coverage factor k equals to 1) as demonstrated in [LiZh03]. However, in this experiment, the instrument offsets have not been determined by self-calibration, but rather measured before the multilateration. Taking the instrument offsets into account, the uncertainty on the distance measurement is equal to $4.9 \mu\text{m}$ ($k = 1$).

The multilateration algorithm with self-calibration has determined the coordinates of both the targets and the measurement heads. The differences between the distances calculated from these coordinates and the ones measured by each head, named error in Figure III.26, are lower than $22 \mu\text{m}$ with a global standard deviation of only $5.4 \mu\text{m}$. The multilateration algorithm has therefore perfectly converged.

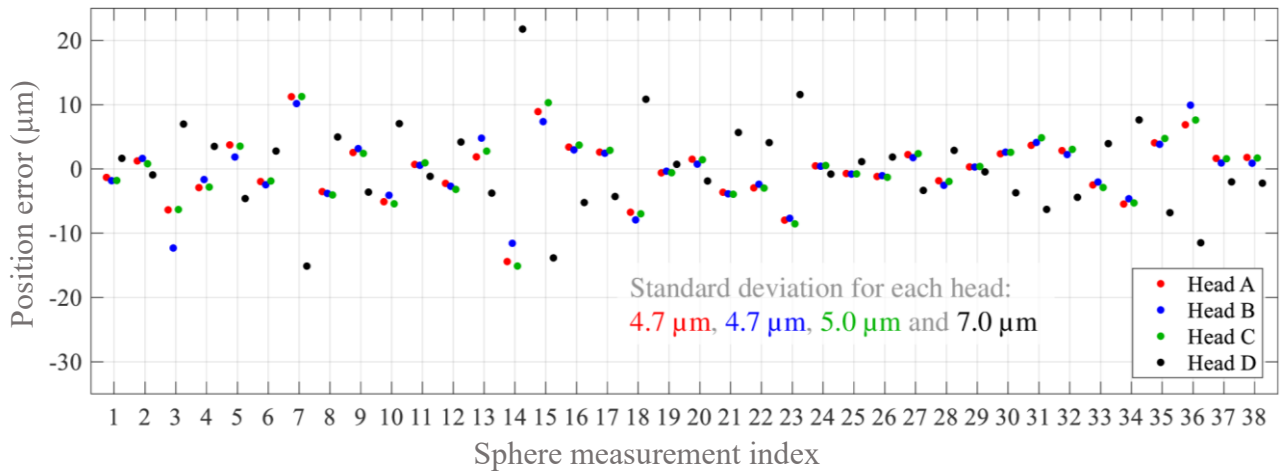


Figure III.26 Experimental results of the multilateration with self-calibration

Moreover, the covariance matrix of each target position has been calculated [GuTW22]. Thus, the uncertainty values, expressed as the trace of the covariance matrices, are provided in Figure III.27. The uncertainty on the target positions measured by multilateration is around 16 μm (confidence interval of 68%).

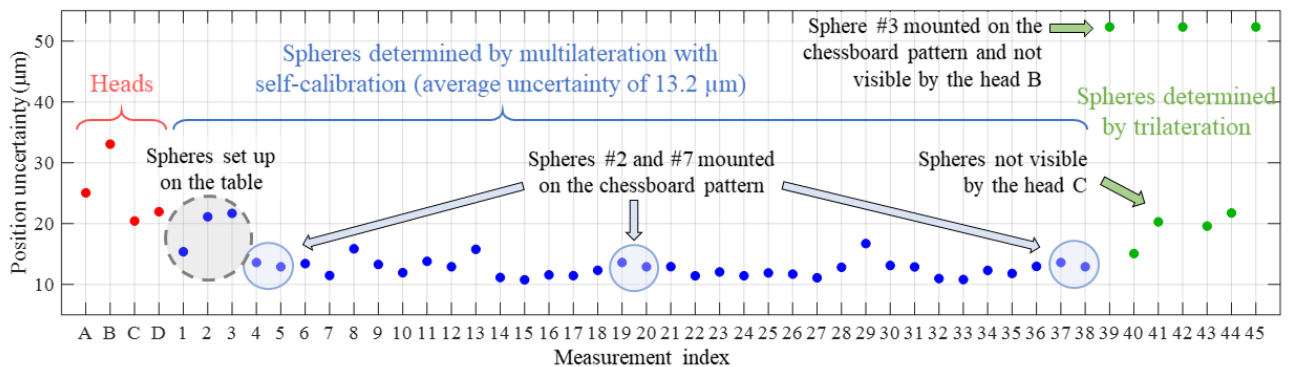


Figure III.27 Uncertainties on position of both the heads and the targets

When a target is not visible from a head, the uncertainty on its position is higher. This is true for the sphere 3 mounted on the checkerboard, with an uncertainty of 52 μm . This limits our knowledge of the checkerboard’s position and orientation. Lastly, the heads present higher uncertainties than the spheres because for a given sphere, the heads are well spread around it (especially along the x- and z- axes), while for a given head, the spheres are almost all located in the same area.

The spheres set up around the checkerboard have been measured three times during the day. From the beginning to the end of the day, the relative displacement of the checkerboard (reduced to a single point, the centroid of the triangle formed by these spheres) was below

30 μm . Therefore, the experimental setup has been considered stable during the day since the measured displacement can be included within the uncertainties of the checkerboard position.

Besides, the relative distances between the 3 spheres mounted on the SL scanner, named interpoint distances, should be the same for different robot poses. In practice, the measured interpoint distances display a reproducibility with a standard deviation of around 20 μm , which is consistent with the combined uncertainty of the two sphere positions (Figure III.28). The SL system is therefore also considered stable during the day.

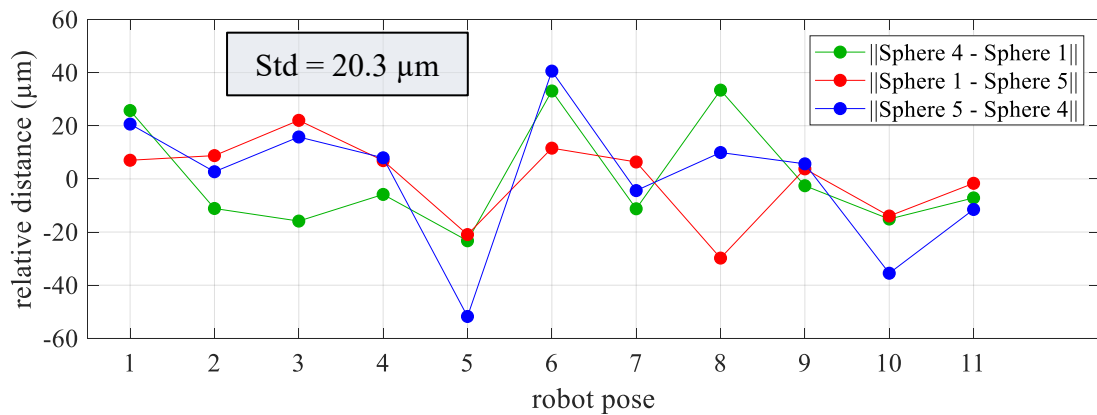


Figure III.28 *Reproducibility of the interpoint distances of the targets mounted on the SL system*

Lastly, it can be noted that the comparison of the positions measured by the multilateration system with the ones that have been returned by the Kawasaki RS003N robot shows errors on the positions with a standard deviation of 1.9 mm. There is a need for an external coordinate measuring system. Such a value was anticipated since the robot is uncalibrated, and the SL system exceeds the maximum allowed payload (4.3 kg for 3.0 kg max).

The motion of the robot can be described by a rotation around a fixed point in space as shown in Figure III.29. This point, named P_{rotation} , is at fixed distances from the three spheres mounted on the SL system. Its value was determined by a least-squares method by minimizing its displacement (i.e. the interpoint distance) between two robot poses among the 11 poses measured by the multilateration system (55 possible combinations). At the end, this point is located at 292.841 mm from sphere 4, at 326.424 mm from sphere 1 and at 370.134 mm from sphere 5. The standard deviation of its coordinates over all robot poses is around 3 mm.

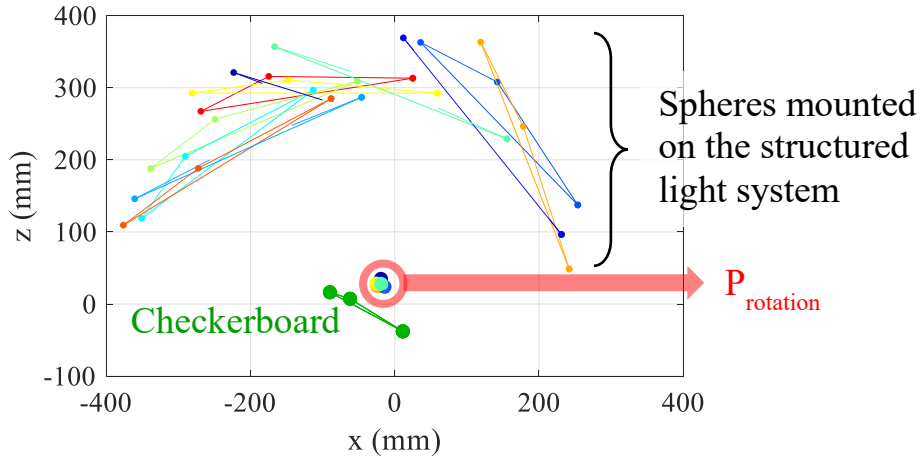


Figure III.29 Illustration of the motion of targets on the SL scanner

III.6.3. Comparison of the transformations between robot poses

The transformation matrix between two poses of the robot can be deduced in two different ways, using the extrinsic parameters estimated by the calibration of the SL scanner or using the measurements of the external coordinate measuring system. Thus, the multilateration system, with an uncertainty of about $16 \mu\text{m}$ determined with a consistent metrological approach and traceable to the SI definition of the metre (International System of units), has been used as a reference for validation of the extrinsic parameters estimated by the calibration of the SL scanner.

To summarise, the transformation from pose P_1 to pose P_6 is composed of a rotation matrix $R_{1 \rightarrow 6}$ and of a translation vector $t_{1 \rightarrow 6}$ (Eq. III.16).

$$P_6 = R_{1 \rightarrow 6} \times P_1 + t_{1 \rightarrow 6} \quad \text{III.15}$$

In practice, the transformations calculated from the multilateration measurements were determined using a Horn's quaternion-based method [Abso00]: the latter finds the rotation and the translation that best match the sphere coordinates of one pose to those of another pose. However, to obtain the same results as the SL scanner, the coordinate system has been adapted. The origin and the orientation of the multilateration coordinate frame were modified so as to minimize the difference between the transformations of the multilateration system and the ones of the SL scanner, in a least-squares sense.

The results are depicted in Figure III.30, where the rotation matrices are converted into rotation vectors following the Z-Y-Z Euler angle convention. The difference between the translations is lower than $200 \mu\text{m}$ with a standard deviation of $88 \mu\text{m}$, while the difference between the rotations is lower than 0.3° with a standard deviation of 0.15° .

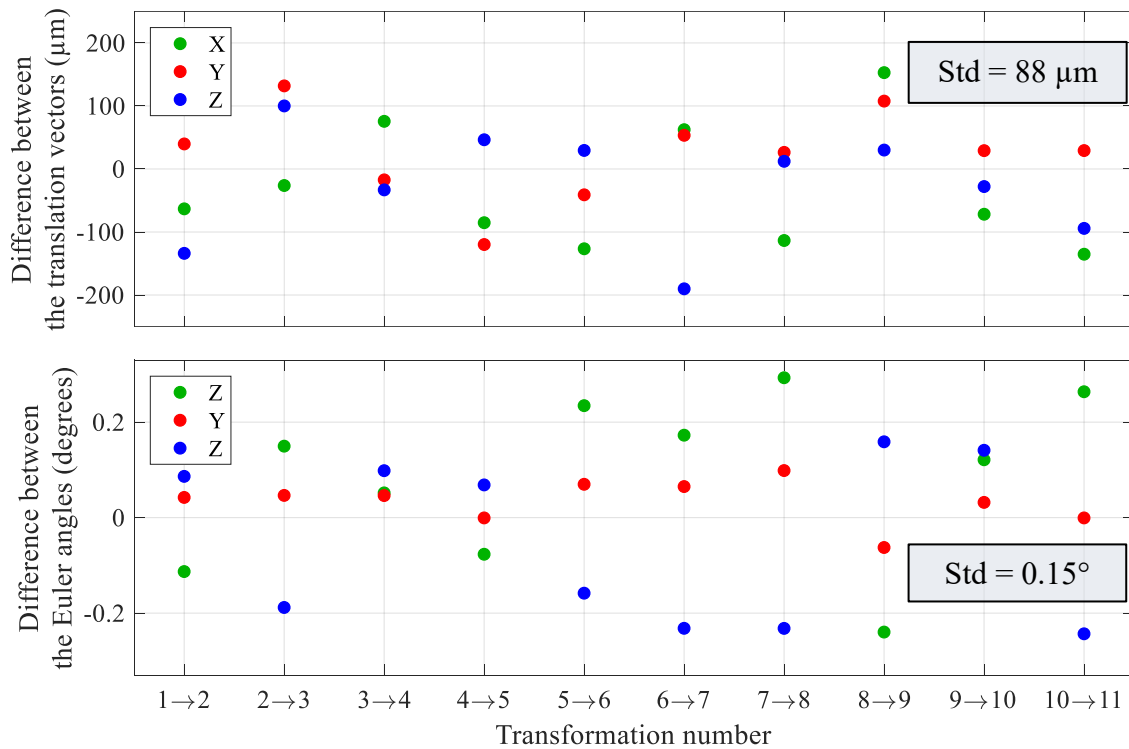


Figure III.30 *Difference between the transformations obtained by the calibration of the SL scanner and the ones obtained by the external coordinate measuring system.*

The estimated rotation and translation errors between the laser rangefinder and both the SL scanner and the robot systems are summarized in Table III.8. The SL scanner provides accurate estimations of the translations and rotations compared to the robot. The obtained mean values for the translation errors have been estimated to about $\sim 71 \mu\text{m}$ for the SL scanner and $\sim 2.28 \text{ mm}$ for the robot, and the rotation errors is in average $\sim 0.12^\circ$ for SL scanner compared to $\sim 2.10^\circ$ for the robot.

Table III.9 Comparison between the multilateration system, the robot, and the SL scanner calibrated using the proposed optimisation (with t the translation vector, α , β and γ the angles following the Z-Y-Z Euler convention)

Transform	Multilateration system vs. robot			Multilateration system vs. SL scanner		
	$ \Delta t_x $ (mm)	$ \Delta t_y $ (mm)	$ \Delta t_z $ (mm)	$ \Delta t_x $ (mm)	$ \Delta t_y $ (mm)	$ \Delta t_z $ (mm)
1 → 2	0.488	0.978	0.618	0.063	0.040	0.134
2 → 3	0.603	3.286	2.905	0.026	0.132	0.100
3 → 4	0.574	4.009	1.176	0.076	0.017	0.033
4 → 5	2.022	3.047	0.664	0.085	0.120	0.046
5 → 6	3.351	1.579	4.464	0.127	0.041	0.029
6 → 7	1.276	3.230	1.261	0.062	0.053	0.190
7 → 8	0.904	4.828	0.526	0.114	0.026	0.012
8 → 9	1.866	3.583	6.884	0.153	0.108	0.030
9 → 10	0.172	4.175	0.011	-0.072	0.029	0.028
10 → 11	4.131	3.146	2.707	-0.135	0.029	0.094
Mean	1.539	3.186	2.122	0.091	0.059	0.069
Min	0.172	0.978	0.011	0.026	0.017	0.012
Max	4.131	4.828	6.884	0.153	0.132	0.19

	$ \Delta\alpha $ (°)	$ \Delta\beta $ (°)	$ \Delta\gamma $ (°)	$ \Delta\alpha $ (°)	$ \Delta\beta $ (°)	$ \Delta\gamma $ (°)
1 → 2	1.829	0.577	1.449	0.113	0.042	0.086
2 → 3	0.134	0.231	3.545	0.150	0.047	0.188
3 → 4	4.196	2.341	3.413	0.052	0.046	0.098
4 → 5	1.191	2.067	1.638	0.077	0.001	0.069
5 → 6	2.466	2.028	0.589	0.235	0.070	0.158
6 → 7	1.168	1.634	2.839	0.173	0.065	0.232
7 → 8	1.021	0.884	0.335	0.293	0.099	0.232
8 → 9	4.366	1.232	3.238	0.240	0.063	0.159
9 → 10	2.333	1.669	4.306	0.121	0.032	0.141
10 → 11	4.771	0.439	5.030	0.264	0.001	0.243
Mean	2.347	1.310	2.638	0.172	0.047	0.161
Min	0.134	0.231	0.335	0.052	0.001	0.069
Max	4.771	2.341	5.030	0.293	0.099	0.243

III.7. Conclusion

In this chapter, the camera calibration process is detailed and a literature review of the existing techniques have been briefly presented. The calibration of a single camera requires the

observation of a 2D pattern printed on a flat surface called calibration grid. By using multiple images of the calibration grid positioned differently (at least 3 poses), the pinhole parameters can be recovered as well as the distortion coefficients.

Since the 3D scanner is based on the SL technique, the calibration needs additional steps. The coding strategy is deployed as to establish a correspondence between the pixels from the projector and the calibration grid. Once the calibration grid points of interest are identified, the calibration of the projector can be performed when following a similar strategy for a camera calibration.

Optimisation methods of the Zh-method are proposed in literature and discussed. The Zh-method can be thus optimised including the feature point detection, the homography and the global refinement. However, the most influencing component is the calibration grid positioning with respect to the camera. This observation was studied by Rojtberg (R-method) and by Peng (CW-method). The common drawback between those methods is the difficulty of adaptation to stereo systems and more specifically to SL scanners.

Subsequently, the novel ML-approach is developed which is an optimisation of the Zh-method based on the choice of ideal poses of the calibration grid with respect to the camera. The ML-approach can be performed on single cameras and also stereo systems such as SL scanners. For single cameras, the ML-approach involves two steps: polynomial approximation and polynomial minimization. An additional step is needed for SL scanners, which consists of merging both polynomials in a single objective function using weighted sum.

The ML-approach aims to provide an accurate estimation of the internal and external parameters of the camera in order to improve the accuracy of the 3D scanning. The input of the ML-approach is a data set built from extrinsic parameters and reprojection errors acquired from multiple images of the calibration grid. The output is a set of ideal poses that can be adopted to calibrate the camera.

A simulation was proposed and the returned result shows a better performance than the existing methods (R-method and CW-method). Indeed, the convergence to the real values predefined for the virtual camera for both intrinsic and extrinsic parameters is faster. An experimental evaluation has also been carried out and demonstrated a trueness value of 11.9 μm .

A repeatability test has shown that the obtained standard deviation of the trueness across 20 tests is at the nanometre level. Intrinsic parameters have also been analysed for the 20 tests: the

standard deviation of focal length and the principal point coordinates are respectively $8.6 \mu\text{m}$ and 0.6 pixels. Hence, the ML-approach is efficient for the calibration of single cameras. The proposed method could also be extended to the calibration of fisheye cameras by taking into account complex distortion models.

The proposed ML-method can also be adapted to SL system where a camera and projector are involved. It is done by the mean of a weighted sum of the polynomials after the regression. The objective is to model the SL scanner as a whole instead of optimising individual components. The methods have been implemented and evaluated experimentally by comparing the result of the extrinsic calibration to a reference system. Since the scanner is equipped on the end-effector of a robot, four laser rangefinders are used to track the pose of the SL scanner. The relative transformations between the optimal poses could be estimated with each of the three systems (SL scanner, robot and laser rangefinders). The result of the comparison shows an accurate estimation of the extrinsic parameters with a mean error of $71 \mu\text{m}$ translation and 0.12° rotation for the SL scanner compared to 2.28 mm and 2.10° for the robot when compared to the reference laser rangefinders.

Once the system is calibrated, the next step is to perform a triangulation in order to collect a dense point cloud. The next chapter focuses on the 3D scanning of a large volume mechanical part using the intrinsic and extrinsic parameters estimated using the ML-approach.

CHAPTER . IV Quality control of large and complex parts

Both the experiment and the assessment strategy are described. First, the scanning principle using the developed SL scanner is briefly reminded in section IV.1. Then, the evaluation method is detailed in section IV.2. The measurement protocol of the designed LVP is given in section IV.3. The evaluation of the single view scanning is described in section IV.4 and the multiple views scanning in IV.5. Finally, a point-cloud registration pipeline is proposed and evaluated synthetically and experimentally in section IV.6.

CHAPTER . IV Quality control of large and complex part	91
IV.1. Approach for data acquisition using the calibrated scanner	92
IV.1.1. Single view: triangulation.....	92
IV.1.2. Multiple views: point-cloud registration	93
IV.2. Evaluation method of the 3D scanner.....	93
IV.2.1. Single view: repeatability and trueness	93
IV.2.2. Multiple views: point-cloud registration	93
IV.3. Measurement protocol on proposed material standard.....	94
IV.3.1. Suggested material standard.....	94
IV.3.2. SL scanning protocol.....	97
IV.4. Evaluation: single view scanning	99
IV.4.1. Flatness.....	99
IV.4.2. Semi-sphere	102
IV.4.3. Semi-cylinder	103
IV.5. Evaluation: multiple view scanning	105
IV.5.1. Pairwise registration	107
IV.5.2. Groupwise registration	112
IV.6. Proposed pipeline for point-cloud registration	113
IV.6.1. Tracking-based registration using industrial robot.....	113
IV.6.2. Global registration pipeline	114
IV.6.3. Synthetic evaluation of the proposed pipeline.....	115
IV.6.4. Experimental evaluation of the proposed pipeline (3D scanning of the LVS) and analysis of the returned results	118
IV.7. Conclusion.....	122

IV.1. Approach for data acquisition using the calibrated scanner

IV.1.1. Single view: triangulation

The calibration parameters are taken into account when performing 3D scanning on LVP with the SL scanner. Those parameters are estimated using the proposed optimisation approach discussed in chapter III (section III.3).

Therefore, the SL scanner is used first for the scanning of elementary surfaces. The elementary surfaces scanning is the process of the point-cloud generation for a limited area of the mechanical part using only a fixed position of the scanner in the measurement space, which will be referred to as the *single view scanning*.

To generate the point-cloud of the surface, a Gray-code in horizontal and vertical directions is projected onto the mechanical part then decoded from the camera perspective. Thus, allowing to detect all the projector pixels that are visible to the camera. Once the projector pixels are detected, a triangulation between the camera pixels and the projector pixels can be performed using the estimated intrinsic and extrinsic parameters resulting from the calibration. Finally, the recorded point-cloud data is post-processed and the visualized (Figure IV.1).

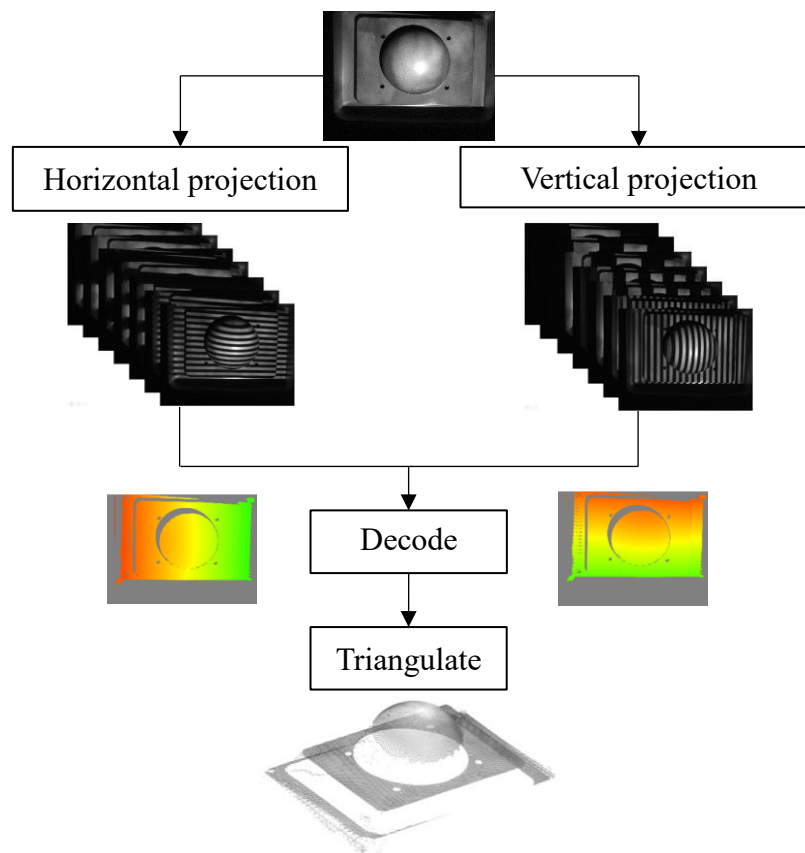


Figure IV.1 Steps of 3D reconstruction of an elementary surface

IV.1.2. Multiple views: point-cloud registration

The assessment of the SL scanner performance is achieved with regard to the elementary surfaces and the large volume part evaluations. LVP are characterised by their dimensions that exceeds the 3D scanner FoV. Thus, multiple scans are required at multiple views to fully reconstruct the object. The multiple views scanning is evaluated by calculating the residual errors between the scanned data, when using the SL scanner and the traceable CMM, and the nominal shape (CAD model). Therefore, the residual errors are obtained by aligning the point-cloud to the CAD model.

IV.2. Evaluation method of the 3D scanner

IV.2.1. Single view: repeatability and trueness

The SL scanner is fixed with respect to the elementary mechanical part and the visible zone is scanned. Afterwards, the form parameters are calculated and the repeatability is evaluated. Some example of parameters that could be evaluated in dimensional metrology are flatness, cylindricity and sphericity, as they are widely used in large volume industries according to [Feng00, PrPo10].

According to the VIM [Inte12], the trueness is defined as the “*closeness of agreement between the average of an infinite number of replicate measured quantity values and a reference quantity value*”, and the repeatability is defined as “*measurement precision under a set of repeatability conditions of measurement*”. Therefore, the repeatability is obtained by repeating the process of single view scanning and by calculating the standard deviation of the obtained form error. Then, the mean value is compared to the form error given by a reference measurement machine to obtain the trueness.

IV.2.2. Multiple views: point-cloud registration

The SL scanner motion in the measurement space is defined so that the LVP is fully scanned by generating multiple scans at different poses. The alignment of the recorded point-clouds is studied with two registration methods: the **pairwise registration** where a maximum of two point-clouds are aligned and the **groupwise registration** that involves more than three point-clouds. The registered dataset is fitted to the CAD and also compared to the traceable CMM results Figure IV.2.

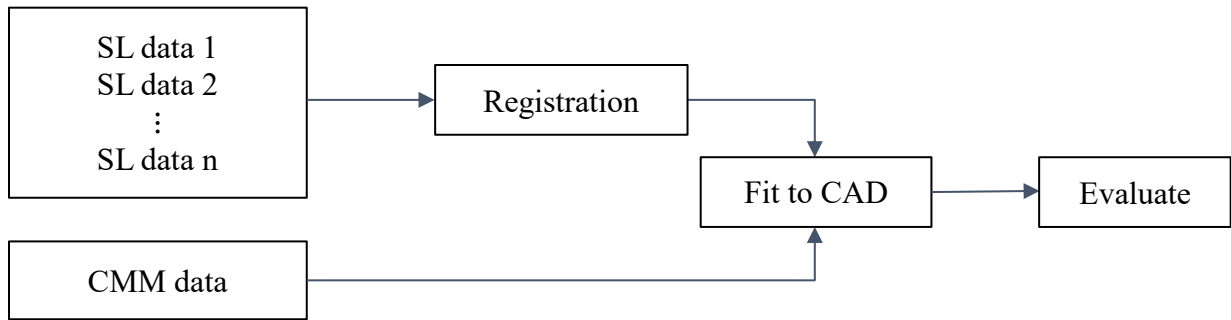


Figure IV.2 Evaluation method of a fully reconstructed mechanical part

The metric used when analysing the scanned dataset is the residuals between the scanned points and the CAD model, leading to calculate the following parameters: RMSE (Root mean square error) [URKG19], MAE (Mean absolute error) [BABB18] and PV (Peak to valley) [GoSe17].

IV.3. Measurement protocol on proposed material standard

IV.3.1. Suggested material standard

IV.3.1.1. Large volume standard (LVS)

The LVS is a designed mechanical part with large dimensions and complex shape to be scanned using the developed 3D scanner. Figure IV.3 shows the CAD of the LVS. The LVS is made of aluminium material with dimensions $L = 1000$ mm, $l = 400$ mm, $H = 60$ mm. The LVS contains ribs and shape variations, such as depth variations and holes.

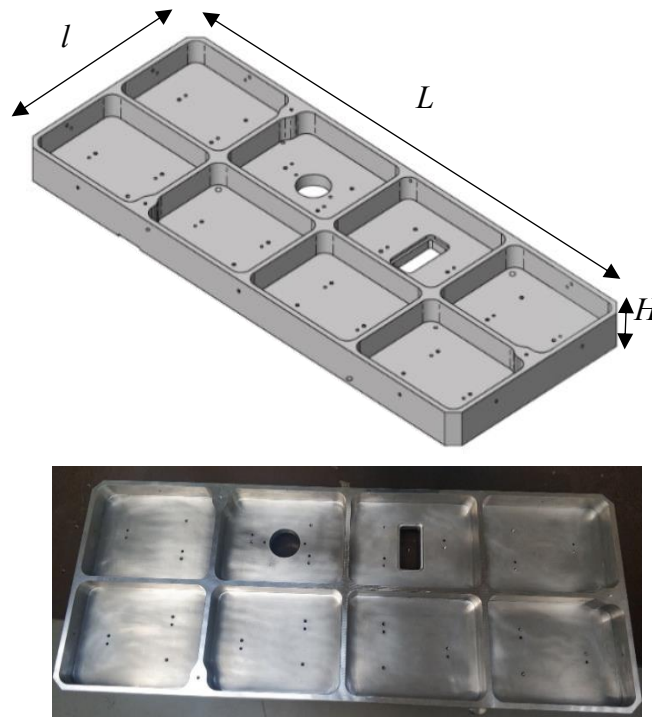
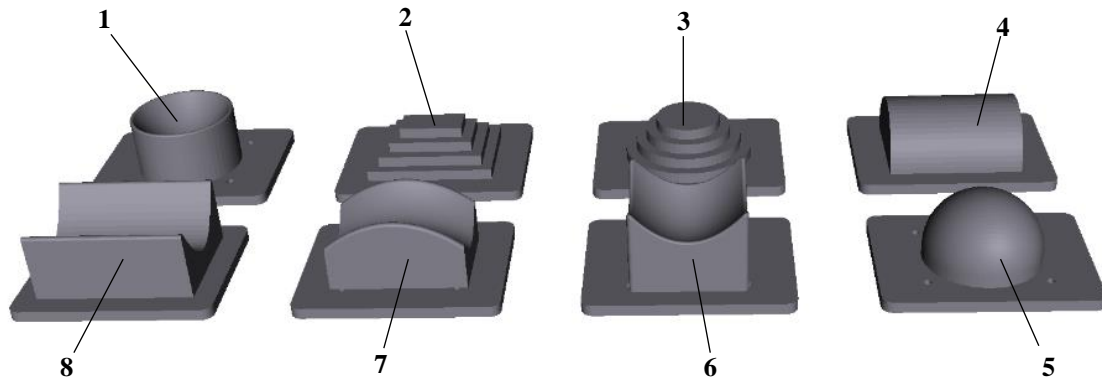


Figure IV.3 Design and conception of a large volume standard

The designed LVS is quite similar to aeronautical parts such as propellers, aircraft wing edges and ailerons.

IV.3.1.2. Secondary artefacts

Eight secondary artefacts have been designed Figure IV.4. The objective is to simulate other shapes including complex that might be used in the aeronautical and automotive fields. Those shapes are described by an analytical model such as cylinder, aspherical shape, etc.



Secondary artefacts

- 1 parabolic cylinder
- 2 stepped rectangular pyramid
- 3 stepped circular pyramid
- 4 half cylinder
- 5 half sphere
- 6 elliptical paraboloid
- 7 cylindrical paraboloid
- 8 hyperbolic paraboloid

Figure IV.4 CAD of the designed secondary artefacts

IV.3.1.3. Large volume standard with the secondary artefacts

The secondary artefacts could be deposited in the LVS on three spheres as to guarantee an isostatic link and avoid any clumping deformation (Figure IV.5-1). One additional isostatic lying system (Figure IV.5-2) is designed to prevent the deformation of the designed LVS. The LVS is equipped with optical spherical targets (Figure IV.5-2) useful for the identification of its absolute position in the rangefinder frame. Furthermore, it allows to track the position of the SL scanner. Here, only rigid transformation is considered, and non-rigid transformations of the LVS are neglected.

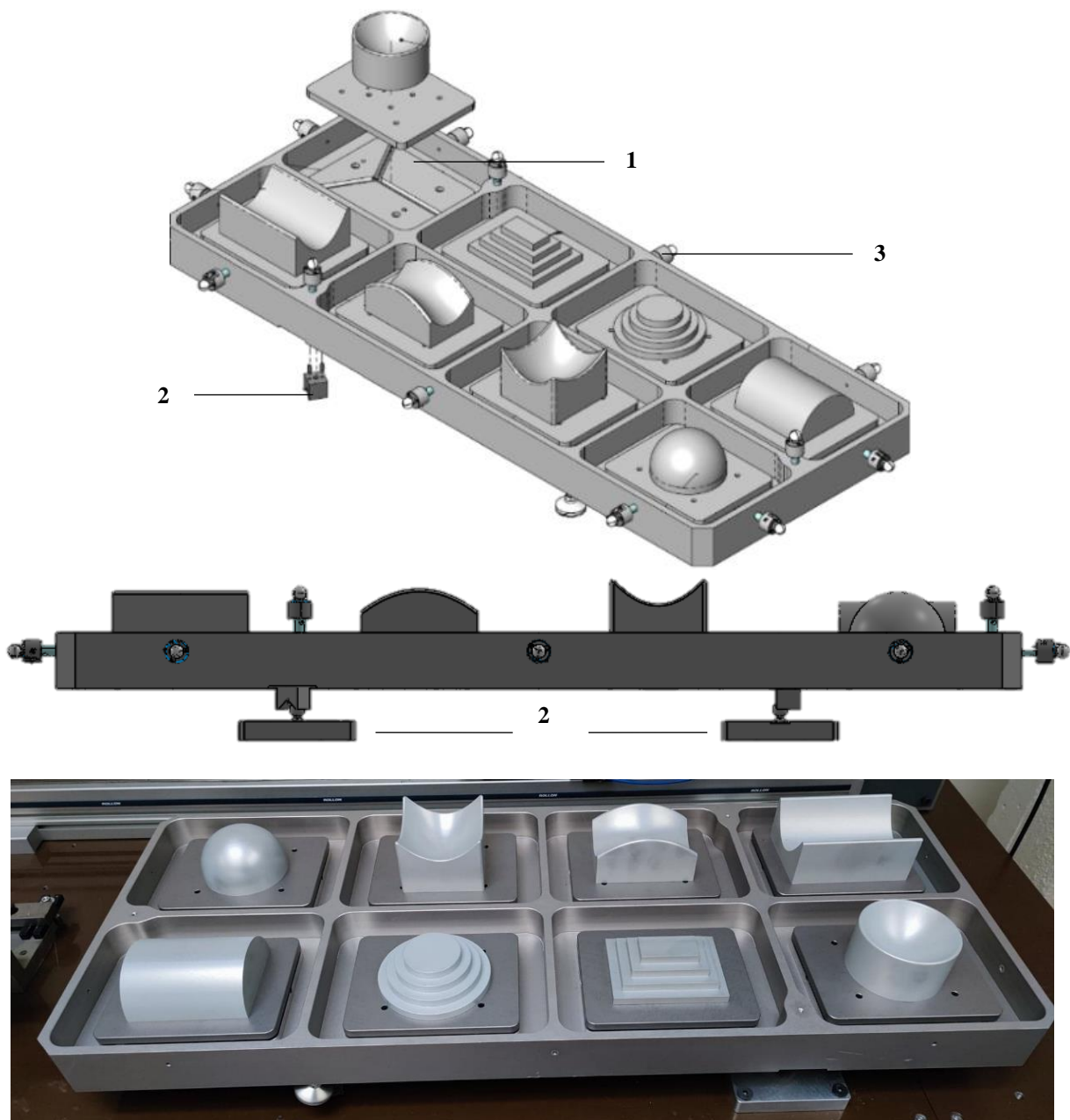


Figure IV.5 3D model of the LVS equipped with secondary artefacts

IV.3.1.4. Reflectivity effect on 3D scanning

The selected aluminium material for the LVS presents generate high reflectivity. This reflectivity downgraded the decoding of the projected SL pattern from the camera perspective. Therefore, two possibilities are considered as to solve the observed issue: (1) to use a mattifying spray usually adopted by industrials to reduce the reflectivity of the surface, or (2) to limit the shiny aspect by a colourless anodization. Aluminium anodizing is an electrochemical process that converts the metal surface into a durable, corrosion-resistant and less reflective surface finish. The second anodization solution is selected and the LVS has been anodized. However, the secondary artefacts still presents a high reflectivity due to the selected complex shapes. Then, the mattifying spray has been used as a backup solution.

IV.3.2. SL scanning protocol

IV.3.2.1. SL scanner

The measurement protocol of the SL scanner consists of generating point-clouds with single views and multiple views. The single view allows to assess the performance of the SL scanner in static where both the position and orientation of the SL scanner are fixed with respect to the part. The analysis of the recorded scan is carried out by applying validated least squares fitting algorithms. The output is the form error. In practice, large dimensions objects require more than one scanning. Therefore, multiple scans are acquired and merged together.

IV.3.2.2. Probe-contact CMM

A traceable tactile CMM (Zeiss UPMC carat) is used for the scanning of the manufactured LVS and secondary artefacts. The tactile Zeiss CMM measurements represent the reference datasets.

The measurement of each individual mechanical part has been carried out inside the LNE cleanroom. The temperature is controlled to about $20^{\pm 0.1}$ °C and the hygrometry to $50\%^{\pm 5}$.

The thermal expansion coefficient of the aluminium is $23.1 \mu\text{m}/^\circ\text{m}$. Since this value is high, the mechanical part is placed at the LNE cleanroom 2 days before the scanning for stabilisation.

The measurement range of the CMM is $1200 \times 850 \times 600$ mm, and the measurement uncertainty is estimated to $0.7 + \frac{L}{1200} \mu\text{m}$, where L is the length of the object. The scale resolution of the CMM is about 100 nm.

The LVS and each of the secondary artefacts is individually placed on the rotary table of the Zeiss CMM, then three plans are scanned to establish the mechanical part coordinate system (Figure IV.6-b). Afterwards, the paths are defined with the ZEISS CALYPSO software for each surface, with regular step of $100\ \mu\text{m}$ along X-, Y- and Z- axis (Figure IV.6-c). The measured datasets are illustrated in Figure IV.7, where the colours correspond to the Z- value of the points in the 3D scan (blue at $Z = 0\ \text{mm}$ and yellow at $Z = 60\ \text{mm}$).

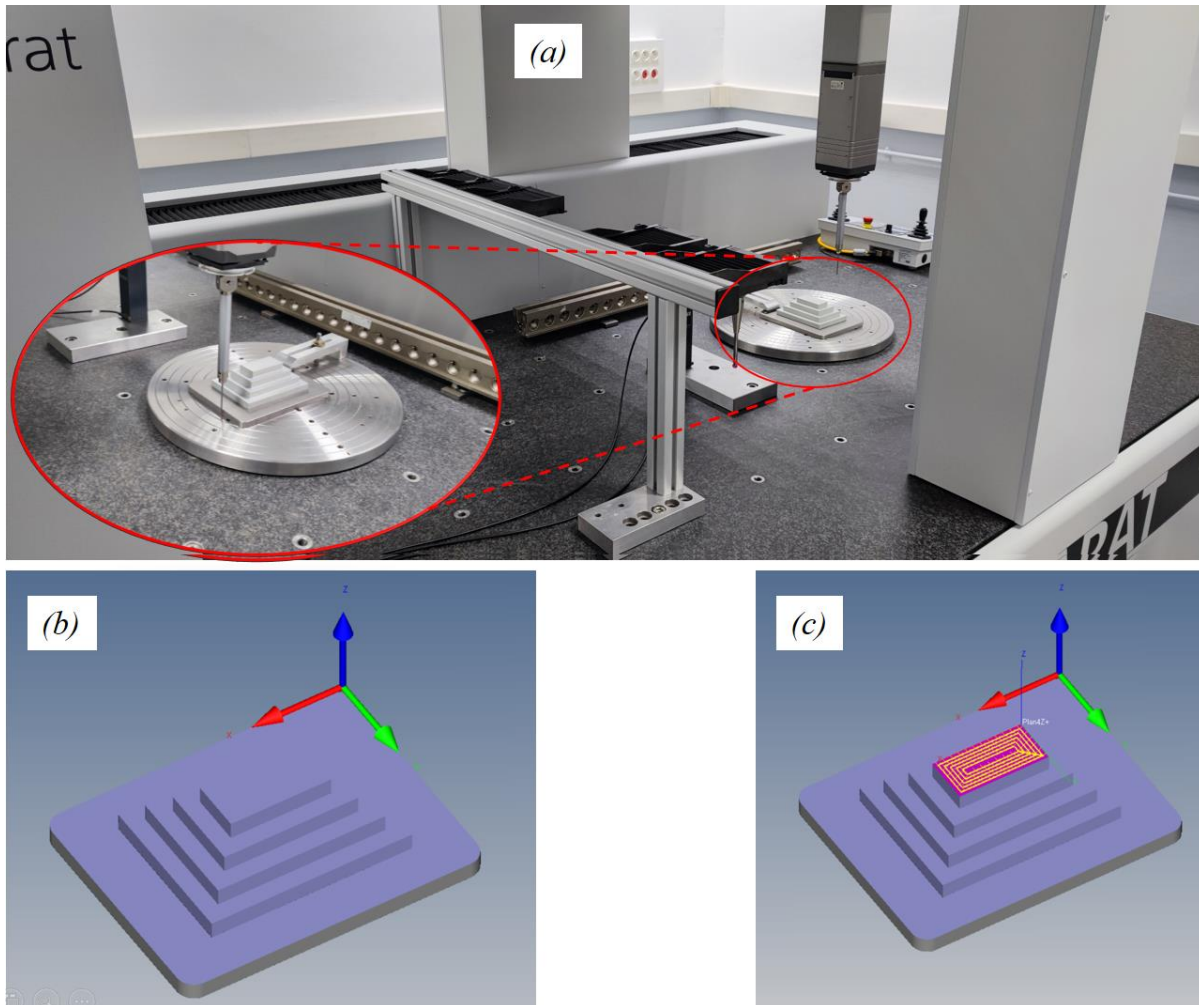


Figure IV.6 Point-cloud generation process using Zeiss probe-contact CMM (a) process of probe scanning (b) definition of the coordinates frame of the mechanical part, (c) definition of the scanning points and the path

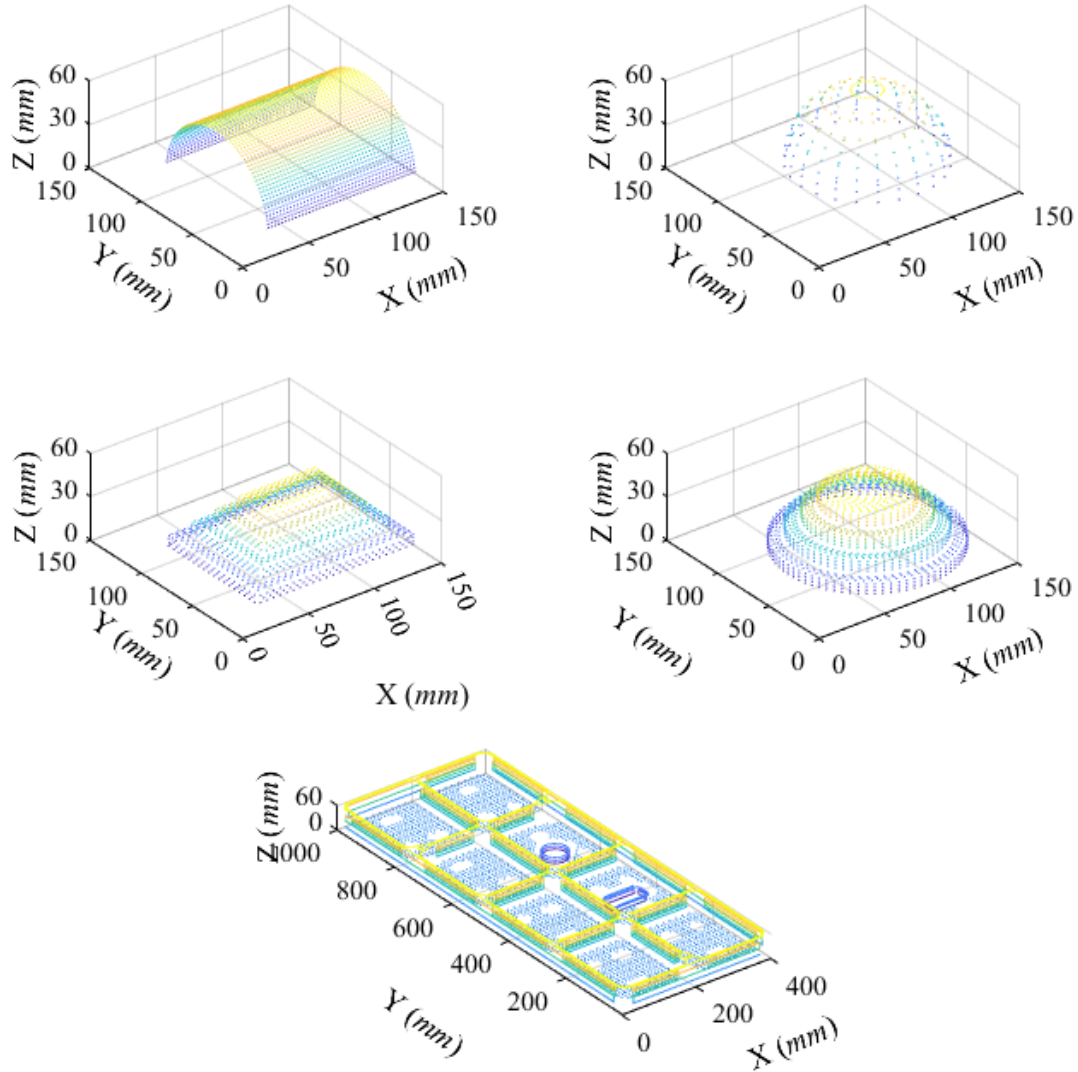


Figure IV.7 Measured datasets with the traceable tactile Zeiss CMM: the LVS and the semi sphere, semi-cylinder and stepped pyramidal shapes.

IV.4. Evaluation: single view scanning

IV.4.1. Flatness

Given a set of points with the coordinates (x_i, y_i, z_i) generated for the scanned flat surface. A plane could be described by its normal vector $N = [A, B, C]^T$ and a distance D , such that a point $P(x_p, y_p, z_p)$ from the surface can be expressed as (eq.IV.1):

$$N \cdot P + D = 0 \quad \text{IV.1}$$

From eq. IV.1, the equation of a plane can be written as (eq. IV.2):

$$Ax_i + By_i + Cz_i + D = 0 \quad \text{IV.2}$$

It is an overdetermined system since the plane is in three dimensions and four values must be estimated. To solve the overdetermined system, a value of $C = 1$ is assigned to express z_i as function of x_i and y_i (knowing that for a flat surface, all the points are assumed to have the same z_i value). Thus, the new problem can be written as in (eq. IV.3) or in matrix form (eq. IV.4):

$$Ax_i + By_i + D = -z_i \quad \text{IV.3}$$

$$\begin{pmatrix} x_0 & y_0 & 1 \\ x_1 & y_1 & 1 \\ \dots & \dots & \dots \\ x_n & y_n & 1 \end{pmatrix} \begin{pmatrix} A \\ B \\ D \end{pmatrix} = \begin{pmatrix} -z_0 \\ -z_1 \\ \dots \\ -z_n \end{pmatrix} \quad \text{IV.4}$$

By multiplying by the transpose of the first matrix, eq. IV.5 can be obtained (where n is the number of points in the data set).

$$\begin{pmatrix} x_0 & x_1 & \dots & x_n \\ y_0 & y_1 & \dots & y_n \\ 1 & 1 & \dots & 1 \end{pmatrix} \begin{pmatrix} x_0 & y_0 & 1 \\ x_1 & y_1 & 1 \\ \dots & \dots & \dots \\ x_n & y_n & 1 \end{pmatrix} \begin{pmatrix} A \\ B \\ D \end{pmatrix} = \begin{pmatrix} x_0 & x_1 & \dots & x_n \\ y_0 & y_1 & \dots & y_n \\ 1 & 1 & \dots & 1 \end{pmatrix} \begin{pmatrix} -z_0 \\ -z_1 \\ \dots \\ -z_n \end{pmatrix} \quad \text{IV.5}$$

$$\begin{pmatrix} \Sigma x_i x_i & \Sigma x_i y_i & \Sigma x_i \\ \Sigma y_i x_i & \Sigma y_i y_i & \Sigma y_i \\ \Sigma x_i & \Sigma y_i & n \end{pmatrix} \begin{pmatrix} A \\ B \\ D \end{pmatrix} = - \begin{pmatrix} \Sigma x_i z_i \\ \Sigma x_i z_i \\ \Sigma z_i \end{pmatrix}$$

For points that are in the centroid of the point-cloud $\Sigma x_i = \Sigma y_i = \Sigma z_i = 0$, the system can be expressed in eq. IV.6. Therefore, the dimension D could be set to 0 since $n D = 0$.

$$\begin{pmatrix} \Sigma x_i x_i & \Sigma x_i y_i & 0 \\ \Sigma y_i x_i & \Sigma y_i y_i & 0 \\ 0 & 0 & n \end{pmatrix} \begin{pmatrix} A \\ B \\ D \end{pmatrix} = - \begin{pmatrix} \Sigma x_i z_i \\ \Sigma x_i z_i \\ 0 \end{pmatrix} \quad \text{IV.6}$$

$$\begin{pmatrix} \Sigma x_i x_i & \Sigma x_i y_i \\ \Sigma y_i x_i & \Sigma y_i y_i \end{pmatrix} \begin{pmatrix} A \\ B \end{pmatrix} = - \begin{pmatrix} \Sigma x_i z_i \\ \Sigma x_i z_i \end{pmatrix}$$

Finally, the system can be solved using Cramer's rule [Leiv15] for linear systems to obtain the parameters of the plane equation so that (eq. IV.7):

$$\begin{cases} \tau = \Sigma x_i x_i \cdot \Sigma y_i y_i - \Sigma x_i y_i \cdot \Sigma x_i y_i \\ A = \frac{\Sigma y_i x_i \cdot \Sigma x_i y_i - \Sigma x_i z_i \cdot \Sigma y_i y_i}{\tau} \\ B = \frac{\Sigma x_i y_i \cdot \Sigma x_i z_i - \Sigma x_i x_i \cdot \Sigma x_i z_i}{\tau} \end{cases} \quad \text{IV.7}$$

One flat surface of the LVS is scanned with the SL scanner 70 times and the recorded datasets are fitted to a nominal plane. Figure IV.8 illustrates the obtained least square fitting. The *outliers*

are the points that have not been used to estimate the flatness. The scanned surface has a flatness of about 88 μm .

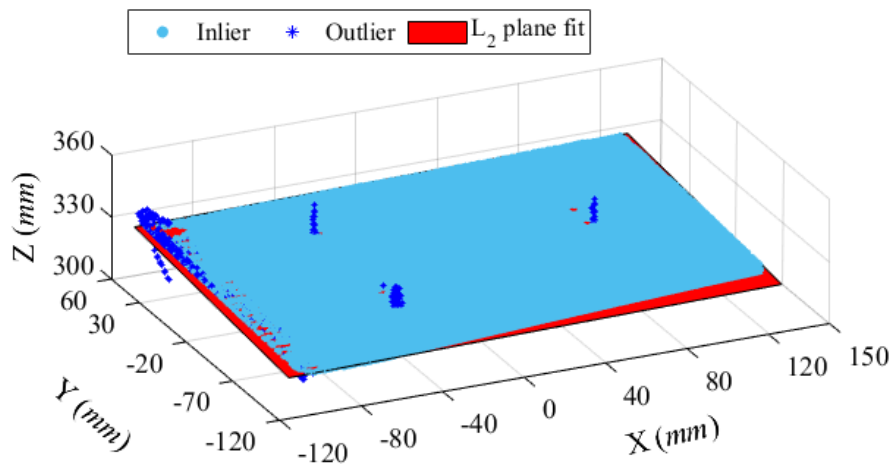


Figure IV.8 Visualization of the least square fitting of a point-cloud to a plane

IV.4.1.1. Repeatability evaluation

To evaluate the performance of the developed SL scanner, a repeatability test is performed 70 times on the same elementary flat surface. The recorded scans are fitted with a least square plane and the flatness is calculated (Figure IV.9).

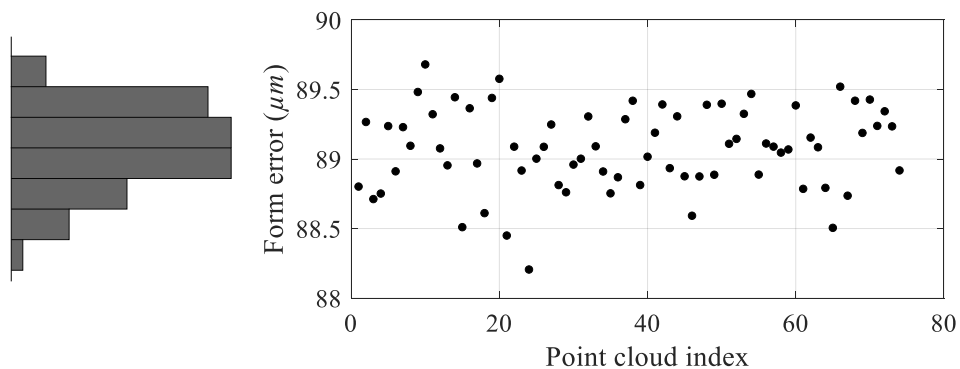


Figure IV.9 Repeatability test of flatness across 70 tests

The returned results (form errors) have a standard deviation less than 2 μm with a confidence level k 95% and the average flatness is equals to 89 μm .

IV.4.1.2. Trueness evaluation

The fitting has also been applied on the reference measurements carried out with the traceable tactile CMM. The calculated flatness has been is equals to 77 μm , and the difference between both the CMM flatness and the SL scanner flatness is equals to 12 μm .

IV.4.2. Semi-sphere

For sphericity evaluation, the point-cloud needs to be fitted to a nominal sphere. Considering a sphere for which the centre coordinates are (a, b, c) and a radius \bar{r} . The mathematical expression of the sphere can be expressed in eq. IV.8, which also can be rearranged as expressed in eq. IV.9:

$$(x - a)^2 + (y - b)^2 + (z - c)^2 = \bar{r}^2 \quad \text{IV.8}$$

$$x^2 + y^2 + z^2 = 2ax + 2by + 2cz + \bar{r}^2 - a^2 - b^2 - c^2 \quad \text{IV.9}$$

Sphere fitting aims to find the centre coordinates (a, b, c) and the radius r . For a point-cloud with n points (x_i, y_i, z_i) , eq.IV.9 becomes a system of linear equations as expressed in eq. IV.10 and IV.11.

$$\vec{f} = A\vec{C}^T \quad \text{IV.10}$$

$$\vec{f} = \begin{pmatrix} x_0^2 + y_0^2 + z_0^2 \\ \vdots \\ x_i^2 + y_i^2 + z_i^2 \\ \vdots \\ x_n^2 + y_n^2 + z_n^2 \end{pmatrix} \quad A = \begin{pmatrix} 2x_0 & 2y_0 & 2z_0 & 1 \\ \vdots & \vdots & \vdots & \vdots \\ 2x_i & 2y_i & 2z_i & 1 \\ \vdots & \vdots & \vdots & \vdots \\ 2x_n & 2y_n & 2z_n & 1 \end{pmatrix} \quad \vec{C}^T = \begin{pmatrix} a \\ b \\ c \\ \bar{r}^2 - a^2 - b^2 - c^2 \end{pmatrix} \quad \text{IV.11}$$

Thus, an overdetermined system suitable for least square optimisation could be obtained. The objective is to determine the vector \vec{C}^T that best minimizes the function $E(\vec{C}^T) = \vec{f} - A\vec{C}^T$. Figure IV.10 illustrates the result of least square fitting on a semi-sphere mounted on its base. The obtained sphere fitting error is estimated to 116 μm where the fitting error is defined as the projection of the points from the point-cloud on the nominal sphere.

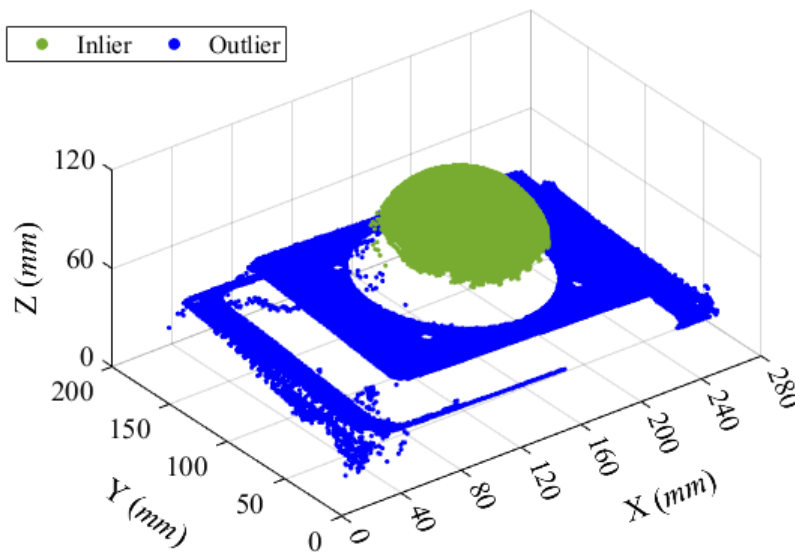


Figure IV.10 Visualization of the least square fitting of a point-cloud to a sphere

IV.4.2.1. Repeatability evaluation

To evaluate the repeatability of the sphericity parameter, the scanning tests were repeated 70 times. The obtained distribution is shown in Figure IV.11. The calculated mean value is about 113 μm with a standard deviation of 4 μm .

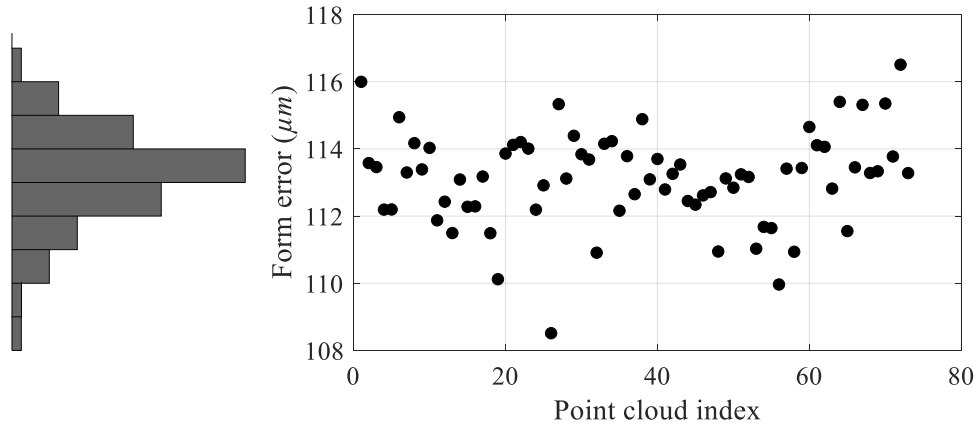


Figure IV.11 *Repeatability test of the sphericity parameter across 70 tests*

IV.4.2.2. Trueness evaluation

The comparison of the sphericity calculated on the measurement data with the traceable Zeiss CMM (17.19 μm) and the sphericity calculated on the scan recorded with the SL scanner (116 μm) leads to have the trueness estimated to about 115.97 μm . The form errors are mainly observed on the top of the sphere for the SL scan. This is due to the high reflectivity of the surface which gives a biased estimation of the point coordinates.

IV.4.3. Semi-cylinder

Cylinders are one of the most commonly used shapes in the industry [Togu22, S.]. Unlike plane fitting, cylindrical fitting is given in the form of a computational algorithm using iteration approximations [Niev13, NuSL17, Sher00]. A cylinder could be defined by its radius $r > 0$ and its axis. Assuming that the point C belongs to the cylinder, and that $\{U, V, W\}$ are the unit-length vector of orthonormal basis, a point X can be written as (eq. IV.12), where ω_i is the weight associated to each unit-length vector.

$$X = C + \omega_1 U + \omega_2 V + \omega_3 W \quad \text{IV.12}$$

Let's consider the matrix $R = (U \ V \ W)$ and the column vector $\boldsymbol{\omega} = (\omega_1 \ \omega_2 \ \omega_3)^T$. Then, eq. IV.12 is reformulated in eq. IV.13:

$$X = C + R\boldsymbol{\omega} \quad \text{IV.13}$$

If point X belongs to the cylinder surface, then eq. IV.14 can be deduced, so that the identity matrix $I = UU^T + VV^T + WW^T$

$$\begin{aligned}
 r &= \omega_1^2 + \omega_2^2 && \text{IV.14} \\
 &= (U \cdot (X - C))^2 + (V \cdot (X - C))^2 \\
 &= (X - C)^T (UU^T + VV^T) (X - C) \\
 &= (X - C)^T (I - WW^T) (X - C)
 \end{aligned}$$

Therefore, the parameter ω_3 , defining the height of the cylinder can be obtained using eq. IV.15.

$$|\omega_3| = |W \cdot (X - C)| \quad \text{IV.15}$$

Let's suppose a set of points $X_i, i \in [1, N_p]$. The least square error function that needs to be minimized to fit the point-cloud to a cylinder, based on eq. IV.15 is expressed as (eq. IV.16).

$$E(r^2, C, W) = \sum_{i=1}^{N_p} [(X_i - C)^T (I - WW^T) (X_i - C) - r^2]^2 \quad \text{IV.16}$$

Figure IV.12 illustrates the fitting result of the scanned cylindrical artefact to a nominal cylinder using the least squares algorithm.

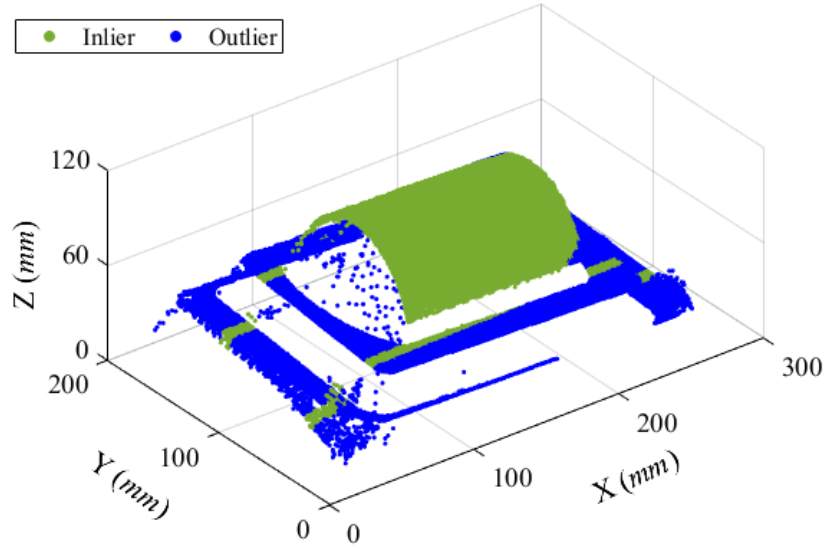


Figure IV.12 Visualization of the least squares fitting of a point-cloud to a cylinder

In order to obtain the repeatability and the trueness, the scanning is repeated also 70 times. The trueness is deduced by comparing the average form error to the one calculated on the tactile CMM measurements.

IV.4.3.1. Repeatability evaluation

The repeatability test of cylindricity scanning across 70 tests shows a standard deviation of $6\ \mu\text{m}$ (Figure IV.13).

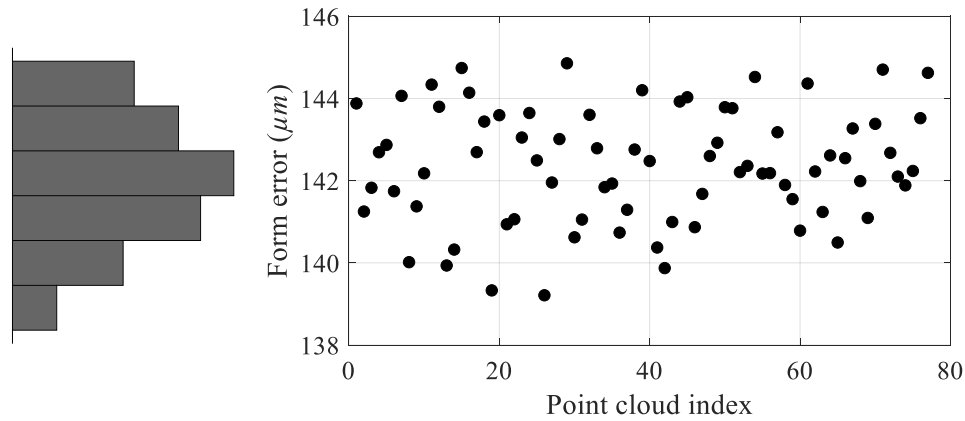


Figure IV.13 Repeatability test of the cylindricity across 70 tests

IV.4.3.2. Trueness evaluation

The fitting of the CMM measurement data to the analytical model gives an error of $19.25\ \mu\text{m}$. Whereas, for the 3D scanner, the average error is estimated to $142.41\ \mu\text{m}$ leading to a trueness of about $123.16\ \mu\text{m}$. The form errors for the 3D scanner are observed on the top of the cylinder, this is due to the same reason described for the sphere related to reflectivity.

IV.5. Evaluation: multiple view scanning

One of the limitations of the SL scanner is the occlusions and the scanner FoV, since several areas of the object might be hidden due to its shape or due to the dimensions of the object. Thus, point-clouds needs to be generated along the scanned surface by partially scanning multiple areas and fusing them into a single coordinate system (Figure IV.14). Each scan generates a point-cloud in the camera coordinate system. Knowing the camera poses, it becomes possible to merge all the point-clouds into a single coordinate system by identifying the relative transformations between the views through the process of *point-cloud registration* [Brow92].

Point-cloud registration is needed in many applications of machine vision such as 3D mapping and 3D reconstruction of objects. Two types of registration can be distinguished: *coarse* and *fine registration* [RNAS15, Zhu19]. Coarse registration consists of finding the initial transformation between point-clouds without necessarily imposing high tolerances for the rotations and translations (usually few degrees for rotations and few millimetres for

translations). Whereas fine registration is applied as to have an accurate 3D alignment of datasets.

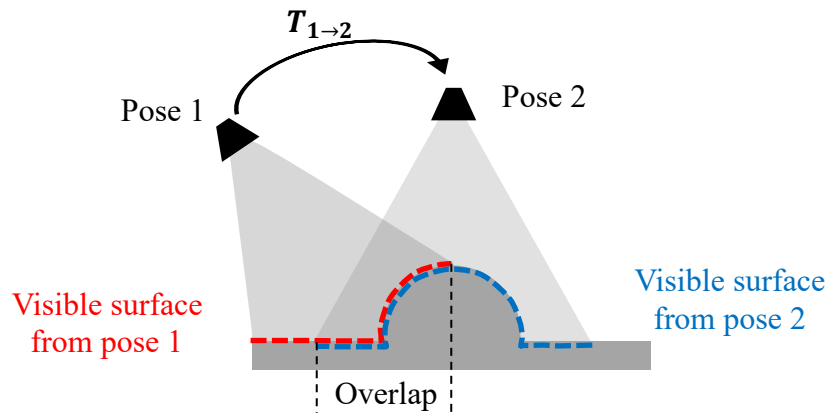


Figure IV.14 Example of a point-cloud registration for a complex part

In literature, a number of methods have been proposed. All can be classified in tracking-based registration and feature-based registration [Bosc12]. For, *tracking-based registration*, an external tracking device is used to estimate the poses of the 3D scanner in the measurement space. The scanner can be for example fixed to a robot end-effector or equipped with displacement sensors such as wire-draw displacement sensors or laser rangefinder targets. It allows to estimate the relative transformations between the scanner poses. Nevertheless, the *feature-based registration* aims to use the intrinsic characteristic of the surface to perform the alignment. There are three categories of feature registration:

- The manual registration is performed on feature manually detected. This method is usually avoided because it's time consuming and the registration accuracy depends on the operator.
- The target-based registration aims to align point-clouds when exploiting physical markers placed on the surface, which can be easily detected. The registration is performed so that at least 3 targets can be detected in two successive point-clouds. The detected targets in point-clouds are called pair of correspondence [Pan19]. The distances between the detected 3 pair of correspondence can then be minimized to obtain a full reconstruction of the object. This method is more accurate. However, it is also time consuming because it requires a preparation using step that consists of placing the targets on the mechanical part.
- The feature-detection based registration is an automated method that relies on the local or global information from the point-cloud. It works similarly to the target-based

registration without the need of adding physical targets to the mechanical part. Information such as local neighbourhoods, form parameters and texture can be used to register point-clouds [GMDD13, RNAM15, RNAM16]. Feature-based methods are usually used due to their accuracy and simplicity, since they are fully automated.

All those techniques can be used to register two point-clouds. However, for larger objects, the reconstruction usually requires more than two point-clouds. This distinction has been studied in the literature and presented as *pairwise registration* and *groupwise registration* [ZGZL19].

IV.5.1. Pairwise registration

Let's consider two sets of points where the pairs of correspondences are defined as the points $\{X_i, i \in [1, N_p]\}$ from point-cloud 1 and $\{Y_i, i \in [1, N_p]\}$ from point-cloud 2 (N_p is the number of points in the set). An example of pairwise registration is given in Figure IV.15. Pairwise registration involves two steps. The first one is to find the correspondence between pair in the point-clouds. The second step is to minimize that distance using optimisation techniques such as gradient descent.

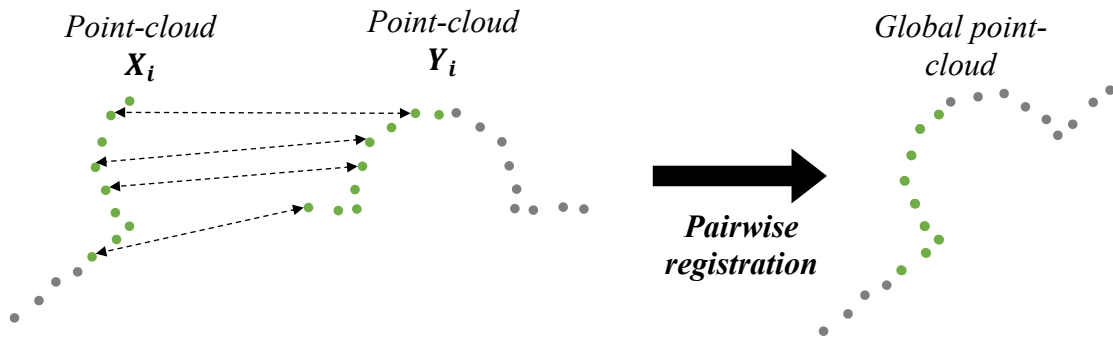


Figure IV.15 illustration of pairwise registration process

The *Iterative Closest Point* (ICP) is one of the most used algorithms for fine registration. ICP performs a L_2 minimization through several iterations to find the rotation and translation parameters that minimize the error function expressed in eq. IV.17.

$$E(R, T) = \frac{1}{N_p} \sum_{i=1}^{N_p} \|X_i - R Y_i - t\|^2 \quad \text{IV.17}$$

The main drawback of the ICP is that the minimization is very likely to become stuck in a nearby local minimum, thus leading to misalignment of point-clouds. Subsequently, advanced ICP variants have been proposed to solve this problem [DXWH17, LHZA22, YLCJ16,

ZhYD21]. Additional methods based on the estimation of the probability density are also widely used due to their fast convergence or accuracy, such as *Normal Distribution Transform* (NDT).

NDT, introduced by Biber [BiSt03], is based on the modelling of the point-cloud by a linear combination of normal distribution. The main key of NDT is the representation of the 3D data, as the point-cloud is discretized into regular cells called voxels. If the number of points in the voxel is more than 3, the voxel can be modelled as a Gaussian probability distribution (GPD) of mean $q = \frac{1}{N_p} \sum_i \mathbf{X}_i$ and a covariance matrix $\Sigma = \frac{1}{N_p-1} \sum_i (\mathbf{X}_i - q)(\mathbf{X}_i - q)^T$. Normal distributions give a smooth representation of the scanned surface with continuous first and second order derivatives. Then, numerical optimisation methods are used for the registration. The probability distribution function is expressed in eq. IV.18 where μ is the mean value of the distribution and δ is the covariance of the distribution.

$$Distr = \frac{1}{\sqrt{(2\pi)^k |\Sigma|}} e^{-\frac{1}{2}(X-q)\Sigma^{-1}(X-q)^T} \quad \text{IV.18}$$

In practice, the generated point-clouds present noises, thus all the points cannot have their correspondence in the other point-cloud. Therefore, instead of matching the points, the normal distribution is analysed for several voxels and used as a feature as illustrated in the example shown in Figure IV.16 (where the voxels volume is about $20 \times 20 \times 20 \text{ mm}^3$ and the distribution of points is calculated at each voxel). The distribution at each voxel is projected on XY- XZ- and ZY- plane to improve the readability.

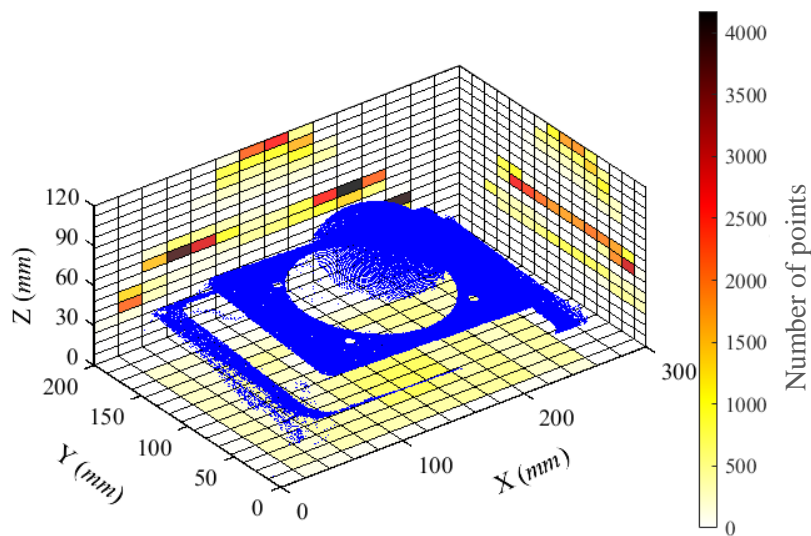


Figure IV.16 Estimation of normal distributions at each voxel of SL point-cloud

A recently proposed algorithm also based on probability namely *Coherent Point Drift* (CPD) [MySo10] have been widely used for point-cloud registration. CPD fits the Gaussian mixture model (GMM) [Reyn09] centroids to the target point-clouds and considers the registration as a histogram distance minimization problem. GMM, expressed in eq. IV.19, is a category of probabilistic models that assumes that all data derive from a mixture of finite Gaussian distributions.

$$p(\mathbf{X}) = \sum_{i=1}^{N_p} P(i)p(\mathbf{X}|i) \quad \text{IV.19}$$

Where:

$$p(\mathbf{X}|i) = \frac{1}{(2\pi\sigma^2)^{\frac{D}{2}}} e^{-\frac{\|\mathbf{X}-\mathbf{Y}_i\|^2}{2\sigma^2}} \quad P(i) = \frac{1}{N_p}$$

Thus, CPD aims to move a point set coherently as a group to preserve the structure of the whole point-cloud.

IV.5.1.1. Comparative study between ICP, NDT and CPD

To evaluate the effectiveness of each algorithm to align the SL point-clouds, the RMSE value and the computation time are estimated and compared. First, two point clouds are generated with an overlapping of 100%, taken at two different poses, then ICP, NDT and CPD are applied to estimate the transformation that aligns both point-clouds. For each algorithm, two parameters are evaluated: RMSE which is a distance defined as the root mean square error of the registration and time complexity describing the required time to perform the registration.

Denoising is applied to each set of point-cloud using a segmentation algorithm. Points are usually generated with noises, called outliers that comes from inaccurate estimation of point coordinates due to the reflectance of the object or from the triangulation. The outliers must be eliminated before performing the registration. One of the most popular outlier's removal methods is the morphological filtering, which is a statistical method that relies on the density of the point set. A volume is defined so that a required minimum number of points is considered as inliers (point set without noise).

For the NDT algorithm, the volume is subdivided into voxels with a step size of 20 mm. Thus, each voxel volume is $20 \times 20 \times 20 \text{ mm}^3$ for which the points density is calculated. It is noticeable from Table IV.10 that the overall performances of ICP exceeds NDT and CPD, apart from the elliptical paraboloid where the estimated RMSE_{CPD} is slightly less than RMSE_{ICP} .

Three stopping criteria are set for NDT, ICP and CPD:

- Max iterations : $i = 500$
- Tolerance on rotation : $\text{rot}(i+1) - \text{rot}(i) < 10^{-5}$ (°)
- Tolerance on translation : $\text{Trans}(i+1) - \text{Trans}(i) < 10^{-5}$ μm

Table IV.10 Convergence comparison between ICP, NDT and CPD

		NDT	ICP	CPD
Semi-sphere	<i>RMSE</i> (mm)	0.5411	0.1887	0.7217
	<i>Time</i> (s)	51.34	0.58	193.68
Semi-cylinder	<i>RMSE</i> (mm)	1.1205	0.1486	0.3673
	<i>Time</i> (s)	40.45	0.63	460.85
Circular pyramid	<i>RMSE</i> (mm)	0.5212	0.0868	0.4125
	<i>Time</i> (s)	20.09	0.39	708.38
Rectangular pyramid	<i>RMSE</i> (mm)	2.8969	0.1577	0.2483
	<i>Time</i> (s)	30.91	2.51	403.59
Elliptical paraboloid	<i>RMSE</i> (mm)	4.59	0.1813	0.1311
	<i>Time</i> (s)	6.18	0.37	181.06
Parabolic cylinder	<i>RMSE</i> (mm)	0.8254	0.2431	0.5593
	<i>Time</i> (s)	37.08	0.49	322.90
Cylindrical paraboloid	<i>RMSE</i> (mm)	1.8520	0.9659	1.7868
	<i>Time</i> (s)	16.64	0.74	371.53
Hyperbolic paraboloid	<i>RMSE</i> (mm)	1.0518	0.5272	0.6972
	<i>Time</i> (s)	26.80	0.44	151.71

IV.5.1.2. Selection of pairwise registration method

The CPD and NDT computation times are very high in comparison to the studied ICP algorithm for registration. Therefore, the ICP is considered as a reference algorithm, and it allows having more accurate results within very low computation time. Figure IV.17 presents a visualization of the resulting point-clouds after registration when NDT, ICP and CPD are applied for the semi-spherical and semi-cylindrical shapes. The pairwise registration considers a maximum of two point sets. In practice, many scans are needed to reconstruct large volume objects, which justify the application of the groupwise registration method.

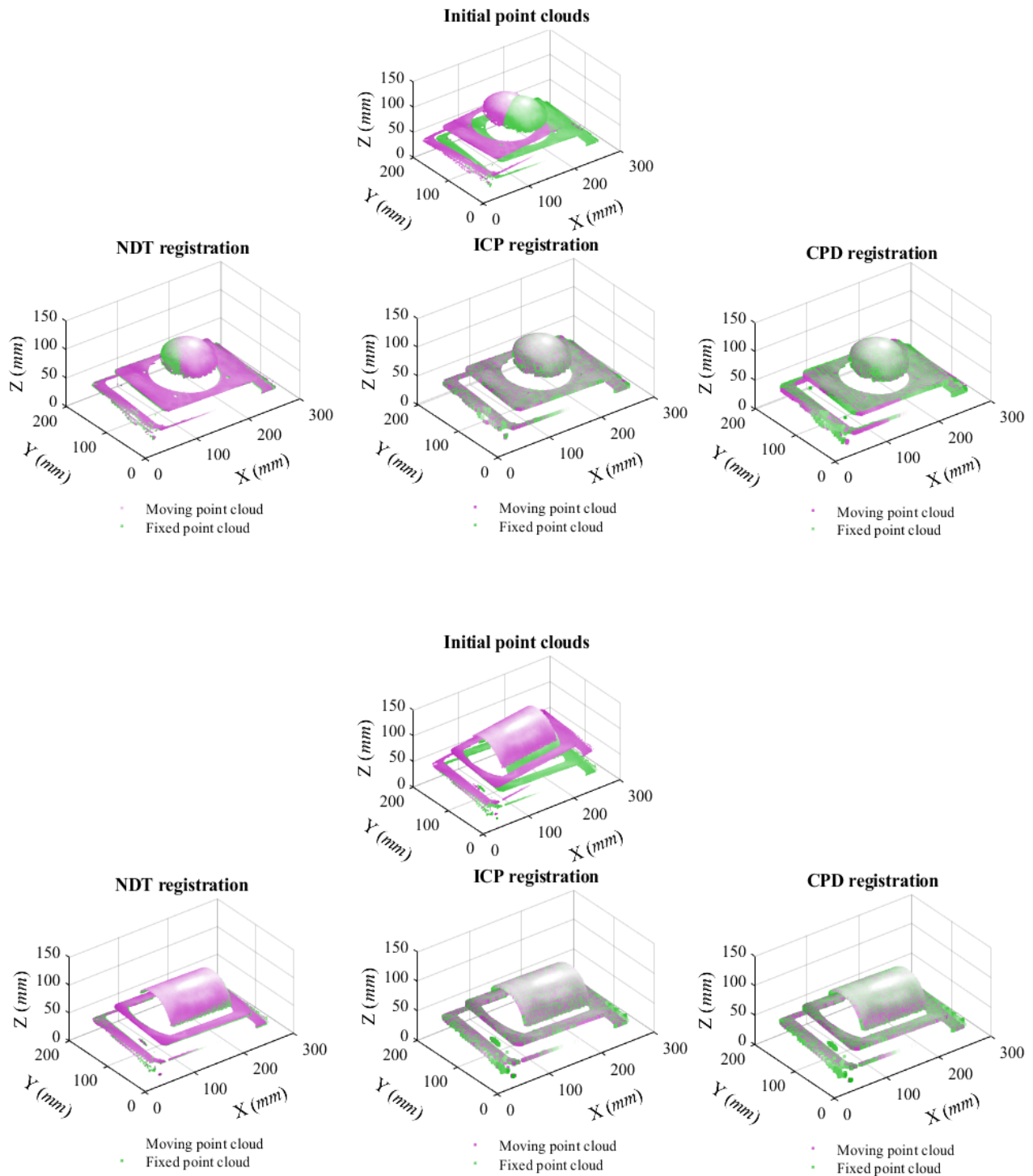


Figure IV.17 Visualization of point-clouds registration using NDT, ICP and CPD for semi-sphere and semi-cylinder

IV.5.2. Groupwise registration

Traditionally, one strategy involves registering of successive scans using pairwise registration algorithms. Those algorithms could be classified into sequential strategy [BILe95, EKHP14, IKHM11, MaYo94] and one-to-all strategy [BSGL96, CaFM02, HuHe03]. They consist of aligning the point-clouds with an overlap constraint. However, systematic errors such as distortion can propagate through the process of regression from the first point-cloud to the last one [EKHP14, EvHo18]. An additional constraint is set for one-to-all strategies, which involves choosing a reference point-cloud that needs to be related to the surrounding ones. Thus, to simultaneously perform the registration when several point-clouds are available, methods of groupwise registration are used.

Let $M_j = \{M_1, M_2, \dots, M_N\}$ be a set of point-clouds and $M = \{M_j, j \in [1, N]\}$ the union of all the data sets where N is the number of point-clouds. The groupwise optimisation was introduced by Lu & Milios [LuMi97] and is yet still widely used in robotics [CuNe08, GKSB10, KaRD08]. The common drawback of this method is the propagation error, because of the use of successive pairwise registrations as demonstrated in [BILe95, ChMe91, GSBL94, Neug97, SHIR98]. Recently, Choi [ChZK15] proposed a robust graph pose method that does not rely only on pairwise registration, but additionally uses line process optimisation [BIRa96]. The line process has been introduced for automatic detection of edges and discontinuities in image processing.

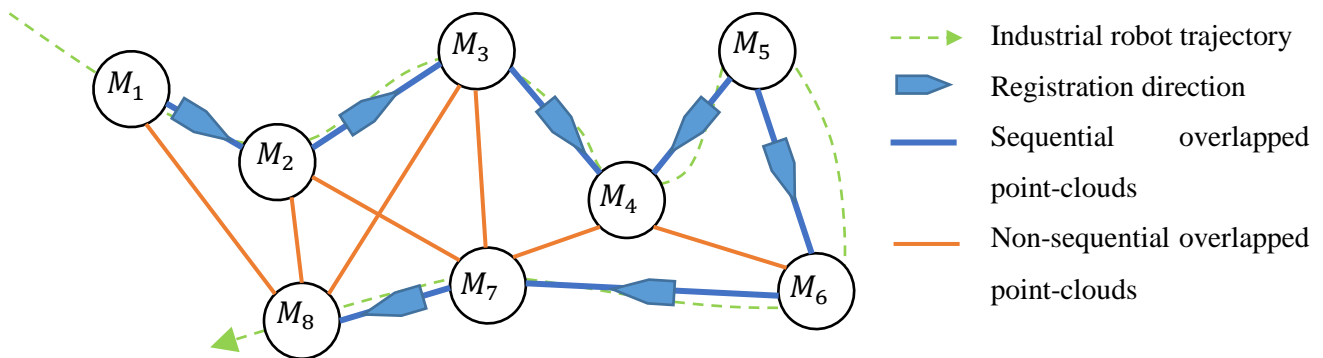


Figure IV.18 Visualization of pose graph optimisation of multiple point-clouds

One advantage of the line process is the formulation since it is presented in a least-squares form, which can be solved using least squares optimisation solvers. The graph pose effectiveness has been demonstrated and the results are significantly better in comparison to other methods for

dense reconstruction of indoor scenes. Figure IV.18 illustrates an example of pose graph optimisation using 8-point-clouds $M_i, i = \{1, \dots, 8\}$.

For the aimed application, a pipeline of point-cloud registration that makes use of the robot, pairwise and groupwise techniques needs to be defined.

IV.6. Proposed pipeline for point-cloud registration

IV.6.1. Tracking-based registration using industrial robot

First, the acquisition consists of manually defining the scanning poses of the KAWASAKI robot so that the surface is globally scanned. KAWASAKI software provides an estimation of the end-effector transformation to the robot base. Thus, the objective is to find the rigid transformation T_{CE} (Figure IV.19) between the camera coordinate system and the end-effector, as to perform a coarse registration of the recorded point-clouds in the robot base. Hence, T_{CE} could be estimated using the eq. IV.20.

$$T_{C_1E_1} \times T_{E_1B} \times T_{E_2B}^{-1} \times T_{C_2E_2}^{-1} \times T_{C_2C_1} = I \quad \text{IV.20}$$

Since the camera is rigidly fixed to the end-effector, then $T_{C_1E_1} = T_{C_2E_2} = T_{CE}$. In addition, the transformations T_{E_1B} and T_{E_2B} are returned by the KAWASAKI soft, therefore, $T_{C_1C_2}$ could be estimated with the ICP fine registration. The transformation T_{CE} is unknown. Thus, eq.IV.20 can be rearranged in eq. IV.21 for a pair of poses.

$$T_{CE} \times T_{E_1B} = T_{C_1C_2}^{-1} \times T_{CE} \times T_{E_2B} \quad \text{IV.21}$$

For k pair of poses, the following system (eq. IV.22) can be solved using a least squares optimisation (eq. IV.23).

$$\begin{cases} T_{CE} \times T_{E_1B} - T_{C_1C_2}^{-1} \times T_{CE} \times T_{E_2B} = 0 \\ \vdots \\ T_{CE} \times T_{E_kB} - T_{C_kC_{k+1}}^{-1} \times T_{CE} \times T_{E_{k+1}B} = 0 \end{cases} \quad \text{IV.22}$$

$$\widehat{T}_{CE} = \arg \min_{T_{CE}} \left(\sum_{i=1}^k T_{CE} \times T_{E_iB} - T_{C_iC_{i+1}}^{-1} \times T_{CE} \times T_{E_{i+1}B} \right) \quad \text{IV.23}$$

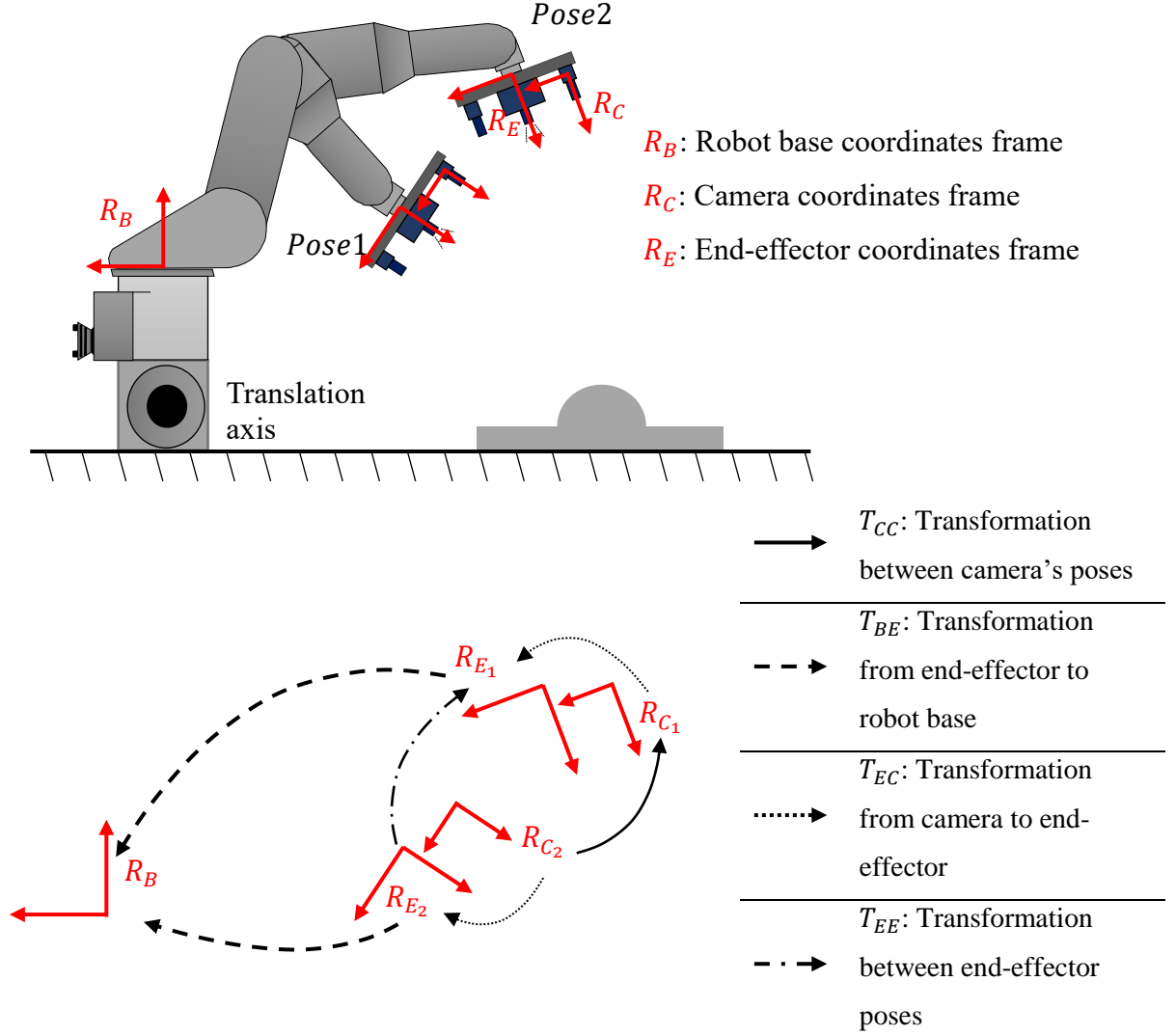


Figure IV.19 Illustration of the transformations between the different coordinate frames

Once the transformation T_{EC} is estimated, the acquired point-clouds M_j^C can then be transformed to M_j^B in the robot base using eq. IV.24. Afterwards, the point-clouds can be cropped along the Z- dimension to eliminate the outliers, usually caused by the surface reflectivity, by applying a morphological filtering. The morphological filtering eliminates points that does not satisfy the constraints of N points in a sphere of radius r . Those parameters have been set to $r = 0.8$ mm and $N = 3$ pts for point-clouds generated from the SL scanner.

$$M_j^C \times T_{CEj} \times T_{EjB} = M_j^B \quad \text{IV.24}$$

IV.6.2. Global registration pipeline

Using the estimated transformation between the scanner and the robot end-effector, the collected point-clouds could be transformed to a single coordinate system, resulting in a

registration with an error of about 2 mm (which corresponds to the robot uncertainty). Afterwards, the pairwise and groupwise registration algorithms could be applied to affine the registration of the point-clouds leading to a lower registration uncertainty.

The selected algorithms for fine registration are ICP for pairwise registration between successive overlapped 3D scans, followed by graph pose optimisation. Hence, the obtained point-cloud can be fitted to the nominal model to analyse the surface of the LVS. The flowchart of the point-clouds registration pipeline is shown in Figure IV.20.

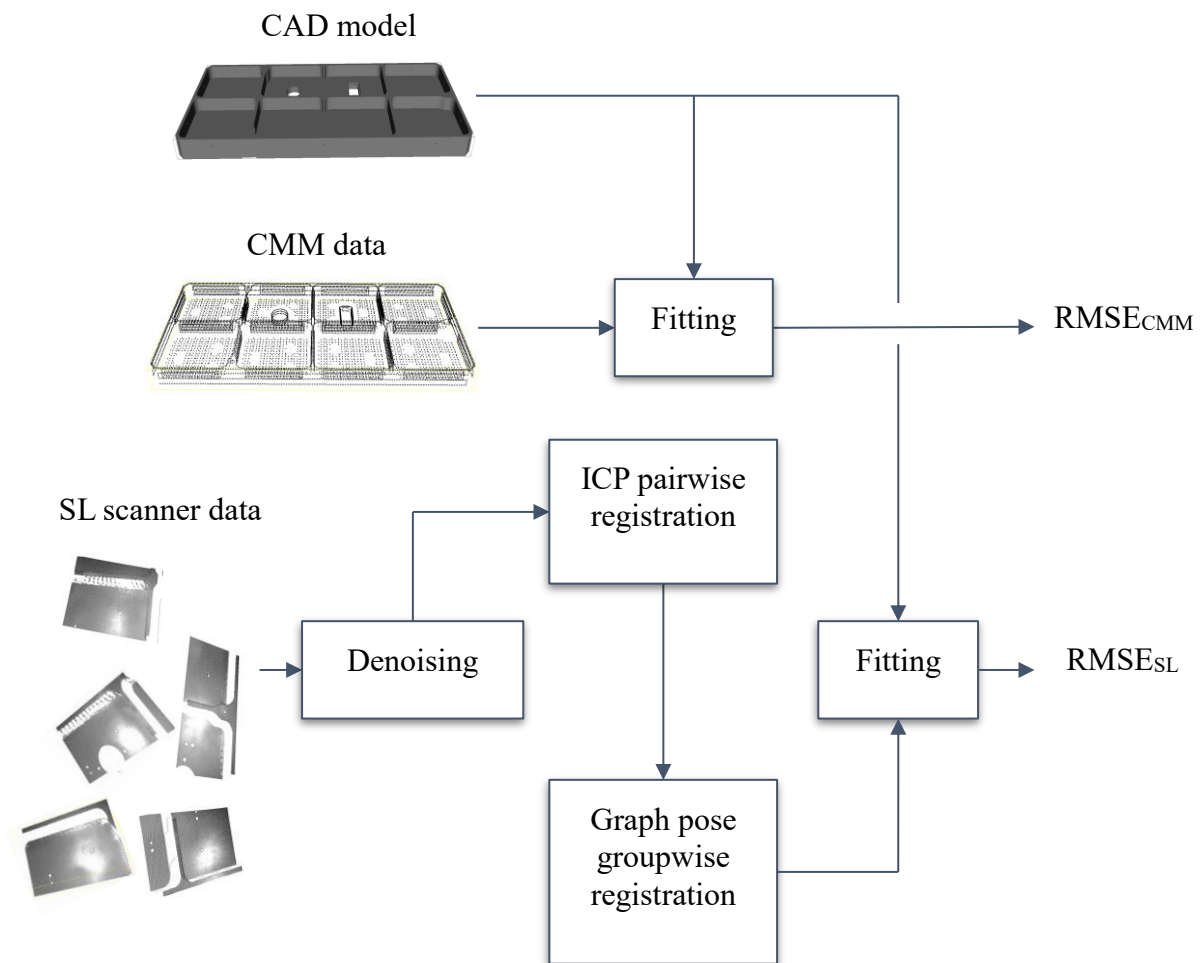


Figure IV.20 Flowchart of the proposed point-cloud registration pipeline

IV.6.3. Synthetic evaluation of the proposed pipeline

The scanning process of the LVS is simulated while evaluating the accuracy of the proposed registration pipeline. A mesh of the CAD model is generated. In computer graphics and 3D modelling, the mesh could be used to define the shape of an object as a composition of vertices, edges and faces. To simplify the rendering, the most suitable faces are triangles, quadrilaterals,

or other simple convex polygons, but may also be more generally composed of concave polygons [BLPP12, Scra00, VaCP08]. In the following case, the triangular meshing has been selected and points are generated across each surface from the mesh.

In practice, the camera can only cover, within a single position, some zones of the surface depending on the FoV, which prevents the optical triangulation in some areas of the surface. Thus, only the visible parts from the camera's perspective will be reconstructed in 3D. To simulate the FoV and the point density, points are sampled along the CAD model in a limited region as illustrated in Figure IV.21.

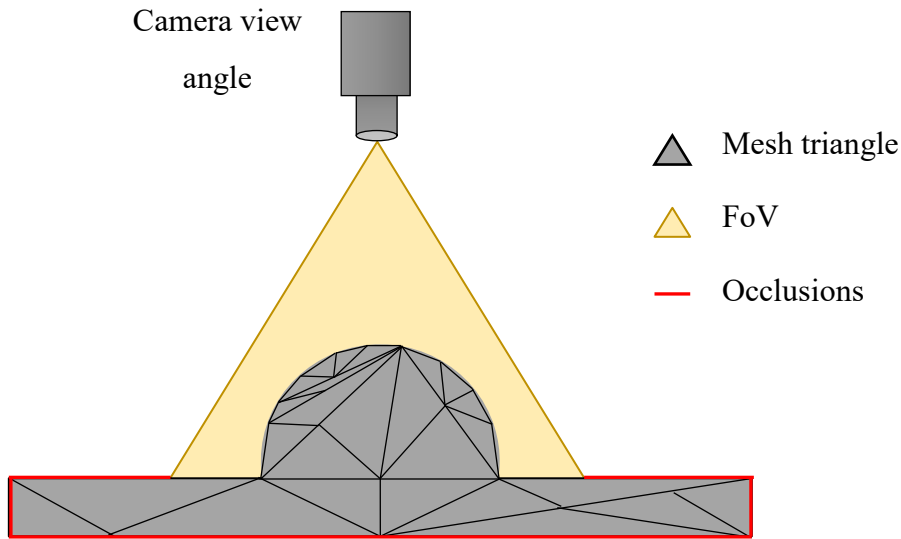


Figure IV.21 *Illustration of view sampling on a complex part*

Once the points are generated on the visible surface, a Gaussian noise is added with an amplitude of $10\ \mu\text{m}$ per point in the x-, y- and z- directions. To simulate the robot displacement error, each point-cloud is transformed using a ground truth transformation namely T_{GT} so it can be used later to evaluate the accuracy of the registration. Then, the proposed registration pipeline is applied to estimate the mutual transformations T_{est} between all point-clouds.

The used metrics to evaluate the registration pipeline are RMSE, MAE and PV, respectively formulated in eq. IV.25, IV.26 and IV.27.

$$\text{RMSE} = \sqrt{\frac{1}{N_p} \sum_{j=1}^{N_p} \|X_j - Y_j\|^2} \quad \text{IV.25}$$

$$\text{MAE} = \frac{1}{N_p} \sum_{j=1}^{N_p} \|X_j - Y_j\| \quad \text{IV.26}$$

$$\text{PV} = \max_j (\|X_j - Y_j\|_s) - \min_j (\|X_j - Y_j\|_s) \quad \text{IV.27}$$

- Where:
- N_p is the number of points
 - $\|... \|$ is the Euclidian distance
 - $\|... \|_s$ is the signed Euclidian distance

For each metric, three outputs are considered as shown in Figure IV.22: RMSE, MAE and PV.

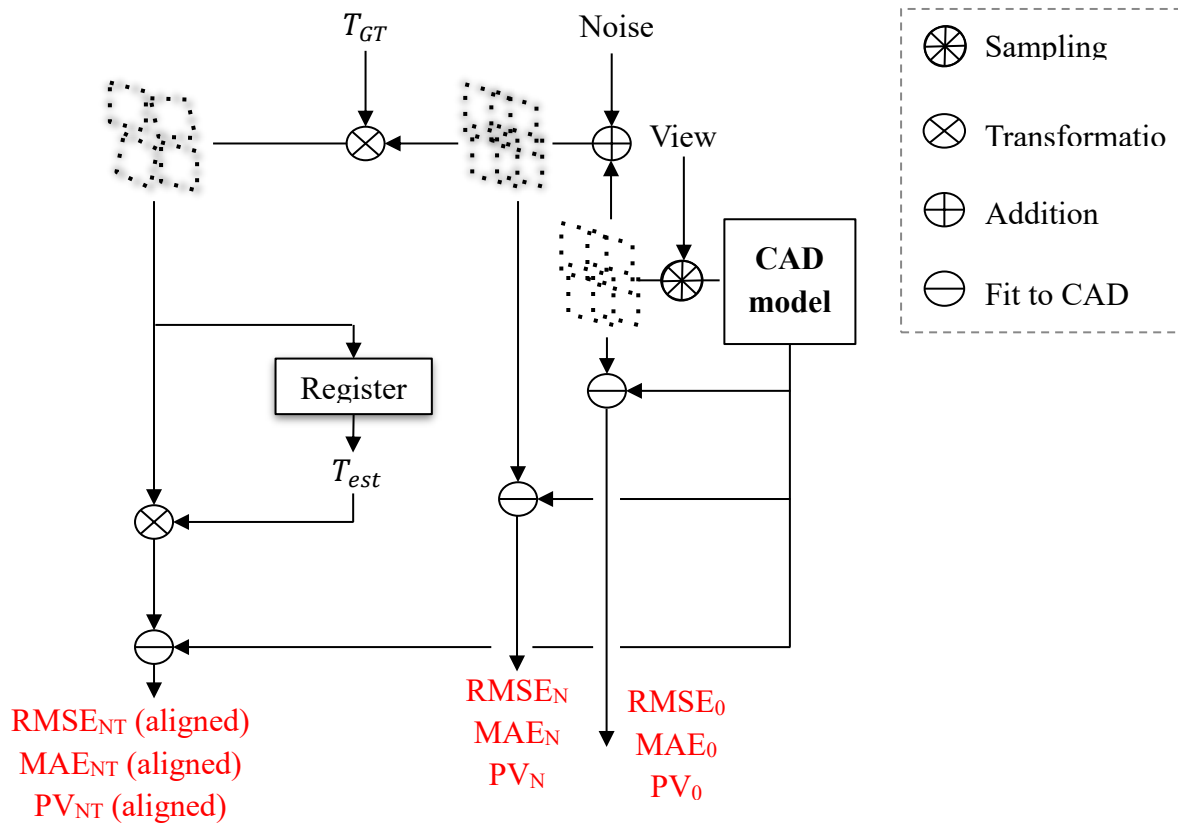


Figure IV.22 Flowchart of the synthetic evaluation of the registration pipeline. Where T_{GT} ground truth transformation, T_{est} is the estimated one and view is the simulated position of the scanner with respect to the CAD

- RMSE₀ describes the fitting errors between the CAD sampling without noise and the CAD. This error allows to estimate the computational error which should be very low compared to other metrics.

- $RMSE_N$ describes the fitting of noisy point-clouds to the CAD model before applying transformations. This metric allows to verify the accuracy of the least squares fitting since it should be equal to the amplitude of the added noise.
- $RMSE_{NT}$ is finally the fitting error of the registration for noisy and transformed point-clouds and the CAD model. This metric allows to evaluate the effectiveness of the registration by comparing the obtained registrations to the ground truth ($RMSE_N$).

Figure IV.23 shows the obtained values for the metrics RMSE, MAE and PV as well as their associated uncertainties. To obtain the uncertainties with a 95% confidence interval, the process has been repeated 10 times. The result of the registration simulation shows a negligible value of $RMSE_0$ (about 3×10^{-12} mm) compared to the other metrics $RMSE_{NT}$ and $RMSE_N$, respectively estimated to 166 μm and 97 μm .

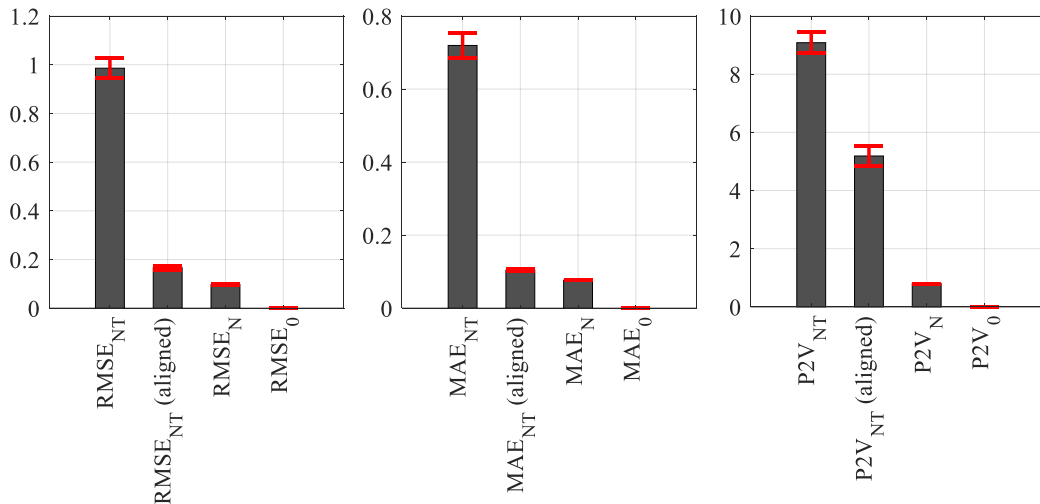


Figure IV.23 Obtained RMSE, MAE and PV values (in mm) and their associated uncertainties

IV.6.4. Experimental evaluation of the proposed pipeline (3D scanning of the LVS) and analysis of the returned results

First, elementary surfaces of the LVS are scanned using the SL scanner. Multiple poses of the robot end-effector are set to cover the whole surface of the LVS, while ensuring approximately 60% of overlap between successive 3D scans. In total, 45 poses of the robot end-effector have been set, and at each pose, the point-cloud of the observed surface is reconstructed in the camera frame. Figure IV.24 shows an example of the SL scanner positioning in the measurement space using the industrial robot.

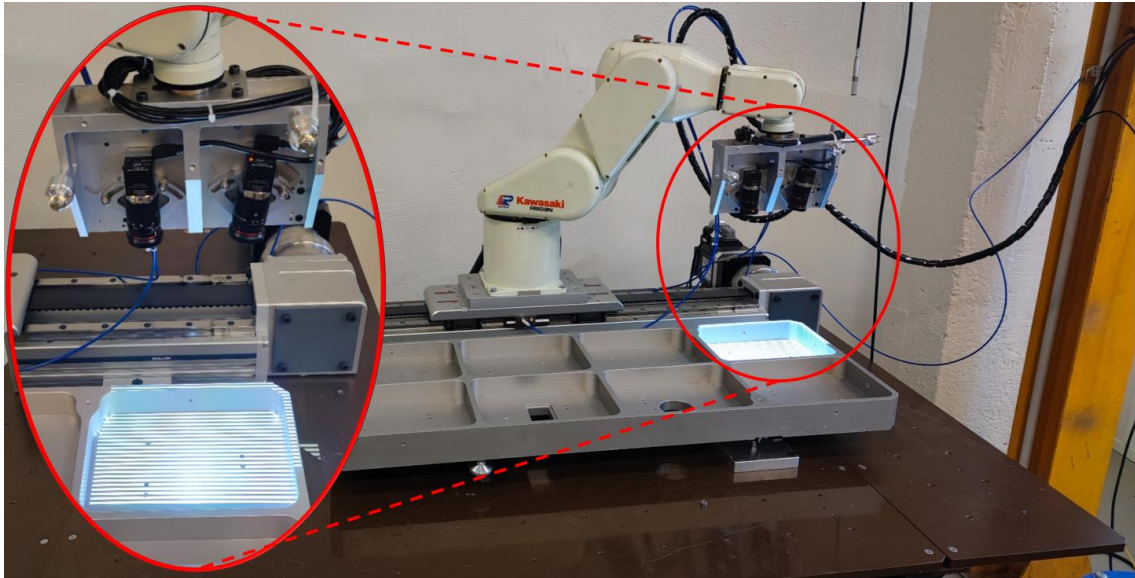


Figure IV.24 *End-effector positioning of the industrial robot to scan an edge of the large volume part*

To perform the coarse registration, the coordinates of the end-effector are recovered and used to transform the point-cloud from the camera frame to the robot-base coordinate frame. Then, the proposed registration pipeline is applied to align the set of point-clouds. Finally, a resampling is used to obtain a uniform number of points, since the overlap areas between successive acquisitions contain higher number of points. Figure IV.25 shows the result of point-clouds registration using the proposed pipeline, where each colour defines a single 3D reconstruction at a specific pose.

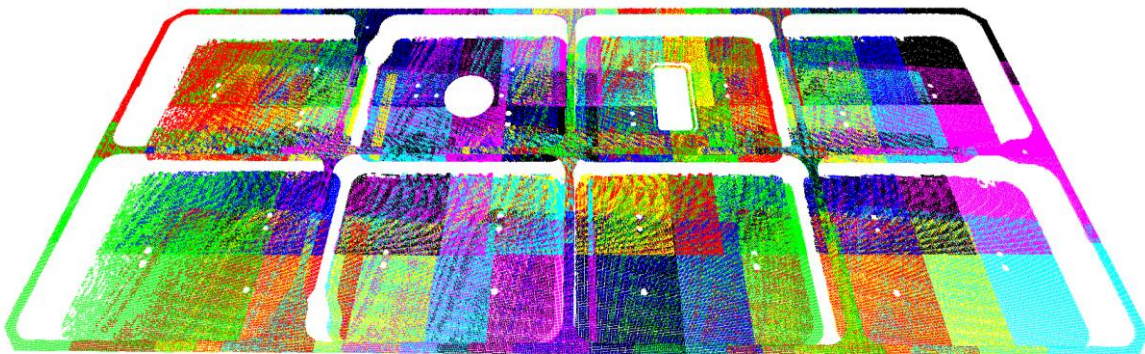


Figure IV.25 *Obtained 3D reconstruction of the large volume part using the proposed registration pipeline. Each colour defines a point-cloud generated from a specific pose of the SL scanner*

The ICP registration is performed in two steps: step (1) involves aligning the pairwise with a corresponding distance of 2 mm to eliminate outliers and keep only the inliers to find the point-

to-point correspondences, step (2) where the corresponding distance is minimized as to refine the pairwise registration.

The RMSE reaches the convergence stage (of about 0.05 mm) after less than 10 iterations for the first step. For the second step, the convergence requires more iterations, but the RMSE of inlier correspondence decreases to about 10 μm for the large volume point-clouds registration (Figure IV.26). The term inliers refer to the subset of the point-cloud used to find the correspondence between two scans.

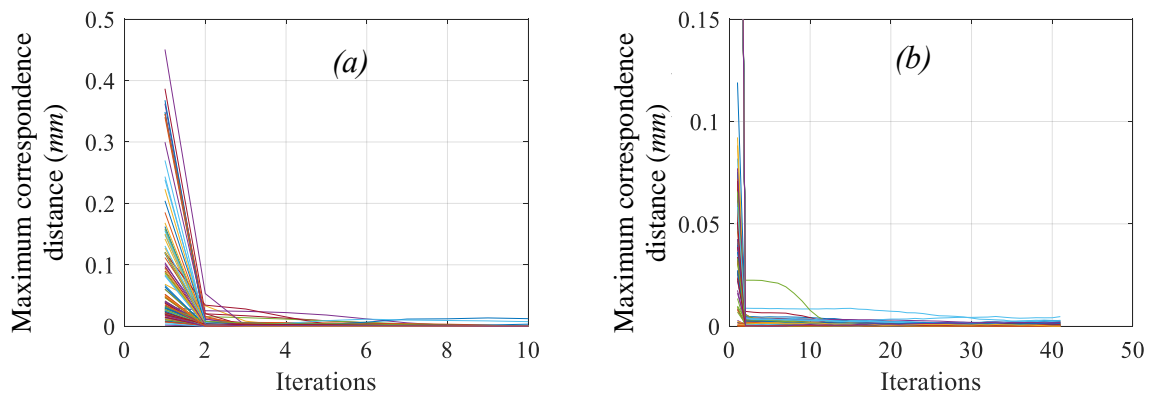


Figure IV.26 RMSE evolution of the ICP registration (a) ICP with correspondence distance of 2 mm, (b) ICP with correspondence distance set to 1 mm

If the corresponding distance is minimized even more, local minimums prevent ICP from converging. This could be explained as an over estimation of the point-to-point distances, because the ICP would adapt the noise rather than the underlying model.

A registration of the tactile Zeiss CMM measurements to the CAD model is also carried out, which leads to the evaluation of the manufacturing process of the LVS.

The difference in point density between the tactile Zeiss CMM measurements of the LVS and the SL scans is noticeable in the Figure IV.27. The tactile Zeiss CMM provide $5 \cdot 10^3$ points where the SL density is about $3 \cdot 10^6$ points. Additionally, a deformation tendency is observed on the CMM measured data, where the fitting errors are grouped in the edges and in the middle of the LVS (Figure IV.27-b). This tendency can be explained either by the manufacturing errors or by the mechanical deformation of the LVS due to its weight (20 kg).

Furthermore, the fitting error of the SL scan is higher than the fitting error of the CMM measurement. The RMSE value calculated on CMM measured data equals to 65.92 μm while RMSE is equals to 165.94 μm for the SL scanner (Table IV.11). The errors can be categorized for each measurement instrument. For SL scanner, the errors are mainly grouped in the edges

of the top plane (Figure IV.27). The reflectivity on the edges is significant in close relation to the curved shape, thus it prevents the triangulation to accurately estimate the coordinates of the points on the edges. However, the distribution across the point-clouds is globally uniform as it is noticeable on the bottom plan (Figure IV.27-a).

Table IV.11 Comparison between the CMM and SL reconstruction

	RMSE (μm)	MAE (μm)	PV (mm)
CMM	65.92	56.08	0.29
SL	165.94	120.03	3.47

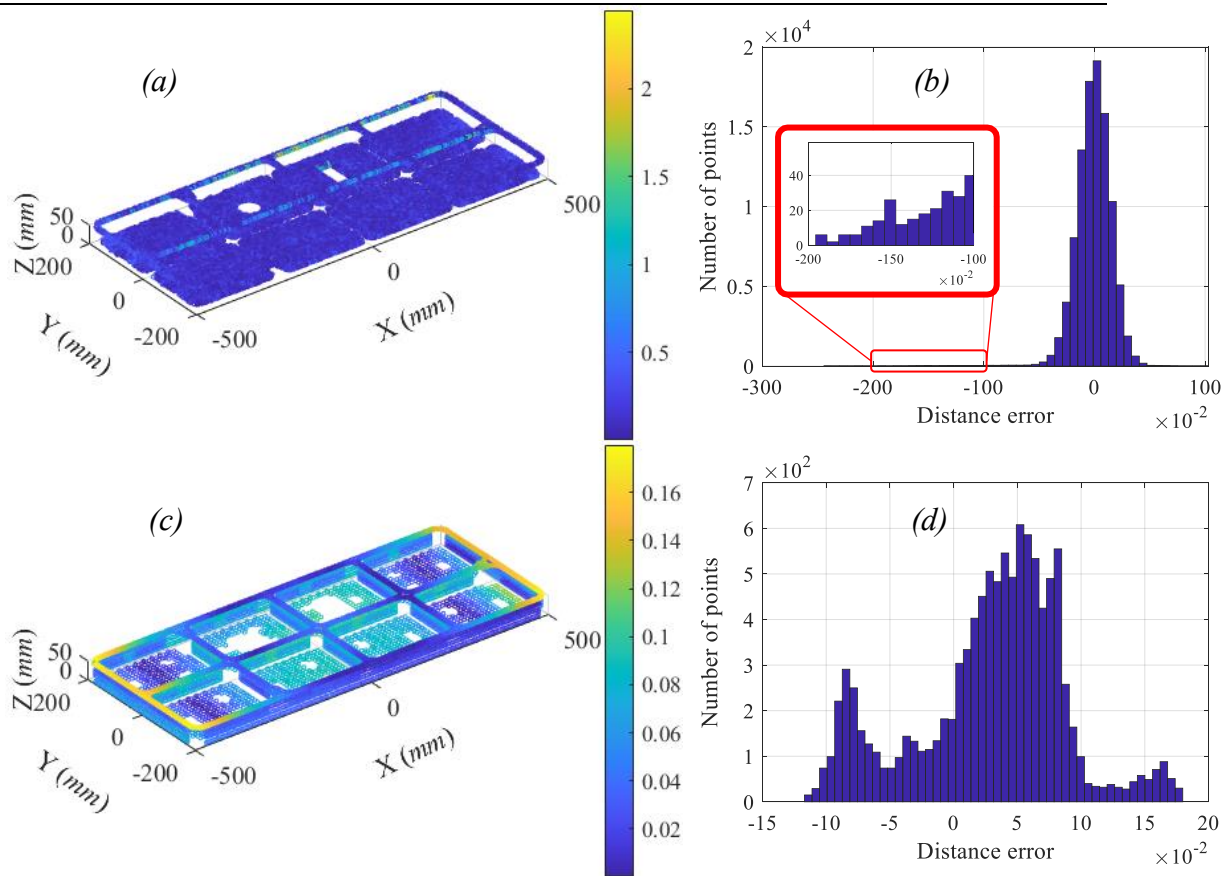


Figure IV.27 Comparison of CMM and SL fitting of the large volume part. (a) SL point-cloud, (b) Distance error distribution of SL point-cloud to the CAD model, (c) CMM point-cloud, (d) Distance error distribution of CMM point-cloud to the CAD model.

The difference in accuracy between the CMM measures and the developed SL scanner is obvious. This was expected as CMMs have better accuracy despite their low density and high measurement time. However, for large volume quality control SL scanners are the best choice

due to their measurement speed and the high density of the data. Although the accuracy is lower than that of the CMM, it is still within the ISO standards for geometric tolerances [Iso100].

IV.7. Conclusion

The performance of the developed SL scanner has been studied in static and dynamic. First, a complex and large volume standard (LVS) as well as eight secondary artefacts have been designed and manufactured. For the static evaluation, the pose of the scanner in the measurement space has been fixed, and point-clouds are generated successively. Then form errors such as sphericity, cylindricity and flatness have been evaluated. The results of the tests show a repeatability about 4 μm .

For the 3D scanning of LVS, a motion of the SL scanner in the measurement space is required, as the dimensions of the object are significant in comparison to the SL scanner FoV. Thus, point-cloud registration methods are also requested. Registration is the process of aligning multiple point-cloud in a single frame. Two categories of registration are distinguished in the literature: coarse registration, and fine registration. Coarse registration allows to align point-clouds without necessarily searching for high tolerances. For fine registration, the distance between the correspondence points is minimized. Here, the end-effectors are used for coarse registration. Multiple poses are set using the robot software so that approximately 60% overlap between successive scans is satisfied. This constraint allows to perform fine registration using ICP. ICP is a pairwise registration usually used to align two point-clouds. However, it is not sufficient for multiple views registration because successive point-clouds could propagate the error in the registration process. Thus, the graph pose optimisation is adopted to optimise the registration process.

The proposed pipeline has been evaluated both synthetically and experimentally. In the synthetic evaluation, the process of point-cloud generation has been simulated on the LVS. First, the view sampling is used to recover the visible surfaces from a simulated pose of the SL scanner. Then, it is applied over the LVS while adding noise to simulate the SL errors. The point-clouds are aligned using the proposed registration pipeline and compared to the ground truth. The resulting RMSE was estimated to 166 μm for simulated data.

An experimental evaluation has also been presented, where the LVS and the secondary artefacts have been scanned using the SL scanner and compared to the results of the tactile Zeiss CMM measurement data. The obtained RMSE value is quite similar to the one obtained with the simulated data as the RMSE has been estimated to about 150 μm .

Conclusion and perspectives

This thesis highlights the investigation of 3D scanning methods for the quality control of mechanical parts. As part of the European project LaVA, a focus is specifically made on large volume parts from the aeronautical field, where traditional measurement techniques, such as CMMs, are not efficient. The degradation in performance is due to the dimensions of the mechanical part and also to its complex shape. Therefore, more robust methods must be adopted. Robustness could be defined as the possibility to generate a dense 3D scan of an object in real time with acceptable accuracy. One efficient solution consists of using optical methods, and more specifically camera-based techniques known as photogrammetry techniques.

In literature, there are two photogrammetry categories: passive photogrammetry and active photogrammetry. Passive photogrammetry uses ambient light to reconstruct the scene. Usually, the 3D scanning is based on the identification of feature points in two different images, then the triangulation is applied to generate the point-cloud. This technique is not suitable for mechanical investigation because scanned parts present uniformity in their colour distribution. Therefore, the feature points are difficult to identify on two images. On the other hand, active photogrammetry uses a controlled light source to perform the triangulation. Active photogrammetry is similar to the stereovision system, but instead of using two cameras, one is replaced by a lighting source. Those techniques are more accurate and often used to scan objects for which feature points cannot be easily identified.

The solution offered in the present work uses the SL projection to solve the triangulation problem of large volume surfaces. SL is an active photogrammetry technique similar to laser triangulation. Rather than projecting a single laser dot or line, multiple horizontal and vertical lines called fringes are projected, leading to a more dense reconstruction of larger areas within only few seconds.

The thesis starts by a general literature review of the 3D scanning techniques. A focus is pointed on SL techniques and their classifications. Different methods of 3D scanning, based on the coding of SL, are presented including those mainly used for quality control of mechanical part. The classification of these techniques with respect to their accuracy, density and real-time

aspect brings valuable guidelines for the choice of the 3D scanning technique in the case of mechanical quality control. Another contribution in this chapter is related to the design and development of the SL scanner, that is able to provide 3D information on large volume mechanical part. The 3D scanner consists of two industrial cameras placed above the projector. The three components are rigidly fixed to an aluminium structure that is placed on the end-effector of an industrial KAWASAKI 6-axis robot. The robot is used to move the SL scanner in the 3D space in order to scan different areas of the mechanical part. In some cases, the object dimensions might exceed the robot range, thus a 7th motion axis is added to the robot to improve the scanning range, leading to a complete measurement system of large and complex parts.

To perform triangulation, it is important to identify the internal parameters of the used cameras and projector as well as the rigid transformation between these components. The identification of these parameters is called camera calibration. This step is critical when performing 3D scanning. Camera calibration is the process of estimating extrinsic and intrinsic parameters of the camera and the projector. Different techniques have been studied and proposed; however, a focus is made on the Zhang method (Zh-method), due to its accuracy compared to other methods. Zhang uses a 2D flat surface printed with an easily detectible pattern (called calibration grid) to calibrate cameras. By taking pictures of the calibration grid placed at different poses, intrinsic and extrinsic parameters can be identified. The Zh-method includes 5 steps: image acquisition, feature point detection, homography estimation, intrinsic and extrinsic identification, global refinement. An additional verification step could be added to satisfy a predefined error threshold. This method is more robust compared to the others, but still not accurate enough. Therefore, some optimisation methods have been advanced to overcome some inaccuracies in the original Zh-method, such as the use of more robust feature point detection algorithm or the optimisation of global refinement. However, the most influencing component is the camera positioning with respect to the calibration grid, according to the literature. In this context, we proposed a novel optimisation method based on ML, which provides a set of optimal poses. The method has been evaluated synthetically and experimentally, and the assessment shows a better performance. The ML-approach is ideal for camera calibration in controlled environments. Nevertheless, if the brightness changes the accuracy is degraded. This aspect can be further optimised by adding to the ML model a parameter that defines the brightness.

Once the SL scanner is calibrated, triangulation between camera and projector pixels can be performed, leading to the generation of a point-cloud. To evaluate the performance of the 3D

scanner, designed mechanical parts have been scanned and their form errors evaluated. The form parameters that have been evaluated are flatness, sphericity and cylindricity. The test shows an overall repeatability of about $6\ \mu\text{m}$ and form errors of about $90\ \mu\text{m}$. This test was performed by fixing the position and orientation of the scanner in the measurement space. In practice, large volume objects require more than a single scan. Subsequently, we proposed a complete pipeline adapted to the SL scanner in order to align the point-clouds and to have a global scan of large volume parts. This step is called registration. The pipeline is divided into two phases: (1) the end-effector coordinates are used for coarse alignment, so that all the point-clouds are transformed to the robot-base, (2) the fine registration is performed with the ICP, followed by a graph pose optimisation. The accuracy of the proposed registration pipeline has been evaluated both synthetically and experimentally. The synthetic evaluation is based on the CAD model of the large volume part, on which point-clouds have been generated with noise. Three metrics were used to evaluate registration error: RMSE, MAE and PV. The application of the pipeline on the simulated data shows a registration error of the respective metrics of $166\ \mu\text{m}$, $107\ \mu\text{m}$ and $5\ \text{mm}$. As for the experimental validation, the large volume part and the secondary standards were reconstructed in 3D and the pipeline was applied. The registration errors obtained are similar to those previously obtained in the simulation, except that some additional errors caused by the surface reflectivity could be observed within the registration. The respective metrics have been evaluated to $165.94\ \mu\text{m}$, $120.03\ \mu\text{m}$ and $3.47\ \text{mm}$.

The future research could be the optimisation of the triangulation and the registration process as to perform operations in real time. For example, surface reflectivity is a highly limiting parameter for SL scanners, because it prevents accurate estimation of coordinates. Two solutions can be studied: to use devices operating in the non-visible spectrum such as IR cameras and projectors, or a post-processing solution that eliminates outliers more effectively. Some denoising algorithms in ML and DL have already been proposed. Their adaptation to the SL scanner could optimise the 3D measurement.

References

- [Abso00] *Absolute Orientation - Horn's method.* URL <https://fr.mathworks.com/matlabcentral/fileexchange/26186-absolute-orientation-horn-s-method>. - abgerufen am 2022-04-18
- [Alis11] AL ISMAEIL, KASSEM: *Structure from Motion & Camera Self-Calibration*, 2011
- [ALMC19] ALSHAREEF, MUHANNAD ; LIN, ZHENGYU ; MA, MINGYAO ; CAO, WENPING: Accelerated Particle Swarm Optimization for Photovoltaic Maximum Power Point Tracking under Partial Shading Conditions. In: *Energies* Bd. 12, Multidisciplinary Digital Publishing Institute (2019), Nr. 4, S. 623
- [AmHS09] AMAD-UD-DIN ; HALIN, IZHAL ABDUL ; SHAFIE, SUHAIDI B.: A review on Solid State time of flight TOF range image sensors. In: *2009 IEEE Student Conference on Research and Development (SCORED)*, 2009, S. 246–249
- [AMRA19] ABER, JAMES ; MARZOLFF, IRENE ; RIES, JOHANNES ; ABER, SUSAN: Principles of Photogrammetry. In: , 2019 — ISBN 978-0-12-812942-5, S. 19–38
- [Atos00] *ATOS / GOM.* URL <https://www.gom.com/fr/systemes-de-mesure/atos.html>. - abgerufen am 2022-06-22
- [AuOk09] AUDET, SAMUEL ; OKUTOMI, MASATOSHI: A user-friendly method to geometrically calibrate projector-camera systems. In: *2009 IEEE Computer Society Conference on Computer Vision and Pattern Recognition Workshops*, 2009, S. 47–54
- [BABB18] BIASUTTI, PIERRE ; AUJOL, JEAN-FRANÇOIS ; BREDIF, MATHIEU ; BUGEAU, AURELIE: Range-Image: Incorporating Sensor Topology for Lidar Point Cloud Processing. In: *Photogrammetric Engineering & Remote Sensing* Bd. 84 (2018)
- [BaLu12] BAGROWSKI, GRZEGORZ ; LUCKNER, MARCIN: Comparison of Corner Detectors for Revolving Objects Matching Task. In: RUTKOWSKI, L. ; KORYTKOWSKI, M. ; SCHERER, R. ; TADEUSIEWICZ, R. ; ZADEH, L. A. ; ZURADA, J. M. (Hrsg.): *Artificial Intelligence and Soft Computing, Lecture Notes in Computer Science*. Berlin, Heidelberg : Springer, 2012 — ISBN 978-3-642-29347-4, S. 459–467
- [BBPP21] BARTOL, KRISTIJAN ; BOJANIĆ, DAVID ; PETKOVIĆ, TOMISLAV ; PRIBANIĆ, TOMISLAV: A Review of Body Measurement Using 3D Scanning. In: *IEEE Access* Bd. 9 (2021), S. 67281–67301
- [BeBa14] BELTRAN, DIANA ; BASAÑEZ, LUIS: A Comparison between Active and Passive 3D Vision Sensors: BumblebeeXB3 and Microsoft Kinect. In: ARMADA, M. A. ; SANFELIU, A. ; FERRE, M. (Hrsg.):

- ROBOT2013: First Iberian Robotics Conference, Advances in Intelligent Systems and Computing*. Bd. 252. Cham : Springer International Publishing, 2014 — ISBN 978-3-319-03412-6, S. 725–734
- [BeCG05] BENTKOWSKA-KAFEL, ANNA ; CASHEN, TRISH ; GARDINER, HAZEL: *Digital Art History: A Subject in Transition* : Intellect Books, 2005. — Google-Books-ID: VdX6MYM0bHEC — ISBN 978-1-84150-116-1
- [BeGR18] BELLAVIA, STEFANIA ; GRATTON, SERGE ; RICCIETTI, ELISA: A Levenberg-Marquardt method for large nonlinear least-squares problems with dynamic accuracy in functions and gradients. In: *Numerische Mathematik* Bd. 140, Springer Verlag (2018), Nr. 3, S. 791–825
- [BeLZ16] BELL, TYLER ; LI, BEIWEN ; ZHANG, SONG: Structured Light Techniques and Applications. In: *Wiley Encyclopedia of Electrical and Electronics Engineering* : American Cancer Society, 2016 — ISBN 978-0-471-34608-1, S. 1–24
- [Berr18] BERRAR, DANIEL: Cross-Validation. In: , 2018 — ISBN 978-0-12-809633-8
- [BGBM13] BIANCO, GIANFRANCO ; GALLO, ALESSANDRO ; BRUNO, FABIO ; MUZZUPAPPA, MAURIZIO: A comparative analysis between active and passive techniques for underwater 3D reconstruction of close-range objects. In: *Sensors (Basel, Switzerland)* Bd. 13 (2013), Nr. 8, S. 11007–11031
- [BGTV14] BALLETTI, CATERINA ; GUERRA, FRANCESCO ; TSIUKAS, VASSILIOS ; VERNIER, PAOLO: Calibration of Action Cameras for Photogrammetric Purposes. In: *Sensors* Bd. 14, Multidisciplinary Digital Publishing Institute (2014), Nr. 9, S. 17471–17490
- [BiJa04] BIERI, LOUIS-SEVERIN ; JACOT, JACQUES: Three-dimensional vision using structured light applied to quality control in production line. In: *Optical Metrology in Production Engineering*. Bd. 5457 : SPIE, 2004, S. 463–471
- [BiSt03] BIBER, P. ; STRASSER, W.: The normal distributions transform: a new approach to laser scan matching. In: *Proceedings 2003 IEEE/RSJ International Conference on Intelligent Robots and Systems (IROS 2003) (Cat. No.03CH37453)*. Bd. 3, 2003, S. 2743–2748 Bd.3
- [BlAh89] BLOSTEIN, D. ; AHUJA, N.: Shape from texture: integrating texture-element extraction and surface estimation. In: *IEEE Transactions on Pattern Analysis and Machine Intelligence* Bd. 11 (1989), Nr. 12, S. 1233–1251

- [BILe95] BLAIS, G. ; LEVINE, M.D.: Registering multiview range data to create 3D computer objects. In: *IEEE Transactions on Pattern Analysis and Machine Intelligence* Bd. 17 (1995), Nr. 8, S. 820–824
- [BLPP12] BOMMES, DAVID ; LEVY, BRUNO ; PIETRONI, NICO ; PUPPO, ENRICO ; SILVA, CLÁUDIO ; ZORIN, DENIS: State of the Art in Quad Meshing (2012)
- [BIRa96] BLACK, MICHAEL J. ; RANGARAJAN, ANAND: On the unification of line processes, outlier rejection, and robust statistics with applications in early vision. In: *International Journal of Computer Vision* Bd. 19 (1996), Nr. 1, S. 57–91
- [Bosc12] BOSCHÉ, FRÉDÉRIC: Plane-based registration of construction laser scans with 3D/4D building models. In: *Advanced Engineering Informatics, Network and Supply Chain System Integration for Mass Customization and Sustainable Behavior*. Bd. 26 (2012), Nr. 1, S. 90–102
- [Brow00] BROWN, DUANE C: Decentering Distortion of Lenses. In: *PHOTOGRAMMETRIC ENGINEERING*, S. 19
- [Brow92] BROWN, LISA GOTTESFELD: A survey of image registration techniques. In: *ACM Computing Surveys* Bd. 24 (1992), Nr. 4, S. 325–376
- [BSGL96] BERGEVIN, R. ; SOUCY, M. ; GAGNON, H. ; LAURENDEAU, D.: Towards a general multi-view registration technique. In: *IEEE Transactions on Pattern Analysis and Machine Intelligence* Bd. 18 (1996), Nr. 5, S. 540–547
- [BSSV11] BANSAL, J. C. ; SINGH, P. K. ; SARASWAT, MUKESH ; VERMA, ABHISHEK ; JADON, SHIMPI SINGH ; ABRAHAM, AJITH: Inertia Weight strategies in Particle Swarm Optimization. In: *2011 Third World Congress on Nature and Biologically Inspired Computing*, 2011, S. 633–640
- [Burg16] BURGER, WILHELM: Zhang’s Camera Calibration Algorithm: In-Depth Tutorial and Implementation (2016), Nr. HGB16-05
- [CaAn90] CAENEN, J.L. ; ANGUE, J.C.: Identification of geometric and nongeometric parameters of robots. In: , *IEEE International Conference on Robotics and Automation Proceedings*, 1990, S. 1032–1037 Bd.2
- [CaFM02] CASTELLANI, UMBERTO ; FUSIELLO, ANDREA ; MURINO, VITTORIO: Registration of Multiple Acoustic Range Views for Underwater Scene Reconstruction. In: *Computer Vision and Image Understanding* Bd. 87 (2002), S. 78–89

- [CaKS98] CASPI, D. ; KIRYATI, N. ; SHAMIR, J.: Range imaging with adaptive color structured light. In: *IEEE Transactions on Pattern Analysis and Machine Intelligence* Bd. 20 (1998), Nr. 5, S. 470–480
- [Cara20] CARARE: Passive systems: photogrammetry and other image based methods. In: *Introduction to the 3D workflow*. Gitbook., 2020
- [ChBK04] CHEUNG, GERMAN K. M. ; BAKER, SIMON ; KANADE, TAKEO: Shape-From-Silhouette Across Time Part I: Theory and Algorithms. (2004)
- [Chec00] *Checking robot-camera calibration — Pickit 2.4 documentation*. URL <https://docs.pickit3d.com/en/2.4/documentation/calibration/checking-robot-camera-calibration.html>. - abgerufen am 2022-07-12
- [ChMe91] CHEN, Y. ; MEDIONI, G.: Object modeling by registration of multiple range images. In: *1991 IEEE International Conference on Robotics and Automation Proceedings*, 1991, S. 2724–2729 Bd.3
- [ChZh95] CHEN, CHICHYANG ; ZHENG, Y.F.: Passive and active stereo vision for smooth surface detection of deformed plates. In: *IEEE Transactions on Industrial Electronics* Bd. 42 (1995), Nr. 3, S. 300–306
- [ChZK15] CHOI, SUNGJOON ; ZHOU, QIAN-YI ; KOLTUN, VLADLEN: Robust reconstruction of indoor scenes. In: *2015 IEEE Conference on Computer Vision and Pattern Recognition (CVPR)*, 2015, S. 5556–5565
- [Cisz18] CISZAK, OLAF: Industry 4.0 – industrial robots. In: *Proceedings of the 3rd EAI International Conference on Management of Manufacturing Systems*. Dubrovnik, Croatia : EAI, 2018 — ISBN 978-1-63190-167-6
- [CIWF98] CLARKE, T. A. ; WANG, X. ; FRYER, J. G.: The Principal Point and CCD Cameras. In: *The Photogrammetric Record* Bd. 16 (1998), Nr. 92, S. 293–312
- [Coel18] COELLO, CARLOS A. COELLO: Multi-objective Optimization. In: *Handbook of Heuristics*, Springer, Cham (2018), S. 1–28
- [CoHa03] COATH, G. ; HALGAMUGE, S.K.: A comparison of constraint-handling methods for the application of particle swarm optimization to constrained nonlinear optimization problems. In: *The 2003 Congress on Evolutionary Computation, 2003. CEC '03.* Bd. 4, 2003, S. 2419-2425 Vol.4
- [Conr19] CONRADY, A. E.: Decentred Lens-Systems. In: *Monthly Notices of the Royal Astronomical Society* Bd. 79, Oxford Academic (1919), Nr. 5, S. 384–390
- [Crea00] CREAFORM: *HandySCAN 3D Scanner for 3D Metrology*. URL <https://www.creaform3d.com/en/portable-3d-scanner-handyscan-3d/technical-specifications>. - abgerufen am 2022-06-15

- [CSCT10] CUI, YAN ; SCHUON, SEBASTIAN ; CHAN, DEREK ; THRUN, S. ; THEOBALT, C.: 3D shape scanning with a time-of-flight camera. In: *2010 IEEE Computer Society Conference on Computer Vision and Pattern Recognition* (2010)
- [CuNe08] CUMMINS, MARK ; NEWMAN, PAUL: FAB-MAP: Probabilistic Localization and Mapping in the Space of Appearance. In: *The International Journal of Robotics Research* Bd. 27, SAGE Publications Ltd STM (2008), Nr. 6, S. 647–665
- [Cust00] *Custom Chrome on ceramic test&calibration target, chrome mask--Dot Vision focus on test&calibration targets*. URL <https://www.dot-vision.com/CustomizationMaterial/20190512172556.html>. - abgerufen am 2022-07-13
- [CZLF07] CHEN, H. J. ; ZHANG, J. ; LV, D. J. ; FANG, J.: 3-D shape measurement by composite pattern projection and hybrid processing. In: *Optics Express* Bd. 15, Optical Society of America (2007), Nr. 19, S. 12318–12330
- [DaGD04] DAMAK, MOHAMED ; GROSBOIS, JÉRÔME ; DESMET, PIERRE: *VISION ROBOT BASED ABSOLUTE ACCURACY MEASUREMENT - CALIBRATION AND UNCERTAINTY EVALUATION*, 2004
- [Davi00] *DAVID SLS 1 Structured Light 3D Scanner*. URL <http://survey-equipments.com/home/178-david-sls-1-structured-light-3d-scanner.html>. - abgerufen am 2022-06-15. — Survey Equipments Store
- [DGLL20] DENG, XIN ; GE, LIANZHENG ; LI, RUIFENG ; LIU, ZHIHENG: Research on the kinematic parameter calibration method of industrial robot based on LM and PF algorithm. In: *2020 Chinese Control And Decision Conference (CCDC)*, 2020, S. 2198–2203
- [DHAN18] DANESHMAND, MORTEZA ; HELMI, AHMED ; AVOTS, EGILS ; NOROOZI, FATEMEH ; ALISINANOGLU, FATIH ; ARSLAN, HASAN SAIT ; GORBOVA, JELENA ; HAAMER, RAIN ERIC ; U. A.: *3D Scanning: A Comprehensive Survey* (Nr. arXiv:1801.08863) : arXiv, 2018. — arXiv:1801.08863 [cs]type: article
- [DKKP08] DOUSKOS, V. ; KALISPERAKIS, I. ; KARRAS, G. ; PETSAS, E.: FULLY AUTOMATIC CAMERA CALIBRATION USING REGULAR PLANAR PATTERNS. In: *ISPRS - International Archives of the Photogrammetry, Remote Sensing and Spatial Information Sciences* (2008)
- [Dlp100] *DLPLCR4500EVM Evaluation board | TI.com*. URL <https://www.ti.com/tool/DLPLCR4500EVM>. - abgerufen am 2022-07-13

- [DNBD12] DEY, NILANJAN ; NANDI, PRADIPTI ; BARMAN, NILANJANA ; DAS, DEBOLINA ; CHAKRABORTY, SUBHABRATA: A Comparative Study between Moravec and Harris Corner Detection of Noisy Images Using Adaptive Wavelet Thresholding Technique. In: *International Journal of Engineering Research and Applications* Bd. 2 (2012), Nr. 1, S. 8
- [DrLe16] DRAP, PIERRE ; LEFEVRE, JULIEN: An Exact Formula for Calculating Inverse Radial Lens Distortions. In: *Sensors* Bd. 16 (2016), Nr. 6, S. 807
- [Dron00] DRONE, CENTER: *Photogrammétrie par drone: expert en modélisation 3D - Drones Center.*
- [Dubr09] DUBROFSKY, ELAN: Homography Estimation.
- [DXWH17] DU, SHAOYI ; XU, YITING ; WAN, TENG ; HU, HUAIZHONG ; ZHANG, SIRUI ; XU, GUANGLIN ; ZHANG, XUETAO: Robust iterative closest point algorithm based on global reference point for rotation invariant registration. In: *PLOS ONE* Bd. 12, Public Library of Science (2017), Nr. 11, S. e0188039
- [EGVL22] EL GHAZOUALI, SAFOUANE ; GUILLORY, JOFFRAY ; VISSIERE, ALAIN ; LAFON, LOUIS-FERDINAND ; BOUAZIZI, MOHAMED-LAMJED ; NOUIRA, HICHEM: Validation of Extrinsic Parameters of a Structured Light Scanner by a Multilateration with Self-Calibration Technique. In: *SSRN Electronic Journal* (2022)
- [Eins00] *EinScan-Pro+ - Shining3D Multifunctional Handheld Scanner.* URL <https://www.einscan.com/einscan-pro/>. - abgerufen am 2022-06-15. — EinScan
- [EKHP14] EVANGELIDIS, G. ; KOUNADES-BASTIAN, DIONYSSOS ; HORAUD, R. ; PSARAKIS, E.: A Generative Model for the Joint Registration of Multiple Point Sets. In: *ECCV, 2014*
- [EIBB95] EL-HAKIM, S. F. ; BERARDIN, J.-A. ; BLAIS, F.: A Comparative Evaluation of the Performance of Passive and Active 3-D Vision Systems.
- [Elha14] EL-HAYEK, NADIM: *Contribution à la reconstruction de surfaces complexes à partir d'un grand flot de données non organisées pour la métrologie 3D.*, Ecole nationale supérieure d'arts et métiers - ENSAM, phdthesis, 2014
- [EvHo18] EVANGELIDIS, GEORGIOS DIMITRIOS ; HORAUD, RADU: Joint Alignment of Multiple Point Sets with Batch and Incremental Expectation-Maximization. In: *IEEE Transactions on Pattern Analysis and Machine Intelligence* Bd. 40 (2018), Nr. 6, S. 1397–1410

- [EVLB22] EL GHAZOUALI, SAFOUANE ; VISSIERE, ALAIN ; LAFON, LOUIS-FERDINAND ; BOUAZIZI, MOHAMED-LAMJED ; NOUIRA, HICHEM: Optimised calibration of machine vision system for close range photogrammetry based on machine learning. In: *Journal of King Saud University - Computer and Information Sciences* (2022)
- [FCWC08] FENG, XIUXIA ; CAO, MAOYONG ; WANG, HAIXIA ; COLLIER, MICHAEL: The Comparison of Camera Calibration Methods Based on Structured-Light Measurement. In: *2008 Congress on Image and Signal Processing*. Sanya, China : IEEE, 2008 — ISBN 978-0-7695-3119-9, S. 155–160
- [Feng00] FENG, SHAW C: A review of current geometric tolerancing theories and inspection data analysis algorithms, S. 30
- [FiSh05] FIALA, MARK ; SHU, CHANG: Fully Automatic Camera Calibration Using Self-Identifying Calibration Targets (2005)
- [Fras97] FRASER, CLIVE S.: Digital camera self-calibration. In: *ISPRS Journal of Photogrammetry and Remote Sensing* Bd. 52 (1997), Nr. 4, S. 149–159
- [FSLY20] FENG, WEIWU ; SHUIQIANG, ZHANG ; LIU, HAIBO ; YU, QIFENG ; WU, SHEN ; ZHANG, DONGSHENG: Unmanned aerial vehicle-aided stereo camera calibration for outdoor applications. In: *Optical Engineering* Bd. 59 (2020), S. 1
- [GAPK19] GRAMMATIKOPOULOS, L. ; ADAM, K. ; PETA, E. ; KARRAS, G.: CAMERA CALIBRATION USING MULTIPLE UNORDERED COPLANAR CHESSBOARDS. In: *The International Archives of the Photogrammetry, Remote Sensing and Spatial Information Sciences*. Bd. XLII-2-W18 : Copernicus GmbH, 2019, S. 59–66
- [Geng11] GENG, JASON: Structured-light 3D surface imaging: a tutorial. In: *Advances in Optics and Photonics* Bd. 3, Optical Society of America (2011), Nr. 2, S. 128–160
- [GhVN20] GHAZOUALI, SAFOUANE EL ; VISSIERE, A. ; NOUIRA, H.: *A metrologic approach for camera calibration using traceable artefact*. URL <https://www.semanticscholar.org/paper/A-metrologic-approach-for-camera-calibration-using-Ghazouali-Vissiere/ca32a93d7891c4ed1ceb032511e4eacf52e04>. - abgerufen am 2022-07-13
- [GKSB10] GRISETTI, GIORGIO ; KÜMMERLE, RAINER ; STACHNISS, CYRILL ; BURGARD, WOLFRAM: A Tutorial on Graph-Based SLAM. In: *IEEE Intelligent Transportation Systems Magazine* Bd. 2 (2010), Nr. 4, S. 31–43
- [GMDD13] GRESSIN, ADRIEN ; MALLET, CLÉMENT ; DEMANTKÉ, JÉRÔME ; DAVID, NICOLAS: Towards 3D lidar point cloud registration

- improvement using optimal neighborhood knowledge. In: *ISPRS Journal of Photogrammetry and Remote Sensing* Bd. 79, Elsevier (2013), S. 240–251
- [GMRD20] GHOSH, CHINMOY ; MAJUMDER, SUMAN ; RAY, SANGRAM ; DATTA, SHRAYASI ; MANDAL, SATYENDRA NATH: Different EDGE Detection Techniques: A Review. In: MALLICK, P. K. ; MEHER, P. ; MAJUMDER, A. ; DAS, S. K. (Hrsg.): *Electronic Systems and Intelligent Computing, Lecture Notes in Electrical Engineering*. Singapore : Springer, 2020 — ISBN 9789811570315, S. 885–898
- [GoSe17] GONG, YUANZHENG ; SEIBEL, ERIC J.: Three-dimensional measurement of small inner surface profiles using feature-based 3-D panoramic registration. In: *Optical Engineering* Bd. 56, SPIE (2017), Nr. 1, S. 014108
- [Goul99] GOULETTE, FRANÇOIS: *Modélisation 3D automatique : outils de géométrie différentielle* : Presse des Mines, 1999 — ISBN 978-2-911762-18-5
- [GSBL94] GAGNON, HERVÉ ; SOUCY, M. ; BERGEVIN, R. ; LAURENDEAU, D.: Registration of multiple range views for automatic 3-D model building. In: *1994 Proceedings of IEEE Conference on Computer Vision and Pattern Recognition* (1994)
- [GTWA22] GUILLORY, J. ; TRUONG, D. ; WALLERAND, J. -P. ; ALEXANDRE, C.: Absolute multilateration-based coordinate measurement system using retroreflecting glass spheres. In: *Precision Engineering* Bd. 73 (2022), S. 214–227
- [GuTW20a] GUILLORY, JOFFRAY ; TRUONG, DANIEL ; WALLERAND, J.-P: Assessment of the mechanical errors of a prototype of an optical multilateration system. In: *Review of Scientific Instruments* Bd. 91 (2020), S. 025004
- [GuTW20b] GUILLORY, JOFFRAY ; TRUONG, DANIEL ; WALLERAND, JEAN-PIERRE: Uncertainty assessment of a prototype of multilateration coordinate measurement system. In: *Precision Engineering* Bd. 66 (2020), S. 496–506
- [GuTW22] GUILLORY, JOFFRAY ; TRUONG, DANIEL ; WALLERAND, JEAN-PIERRE: Multilateration with Self-Calibration: Uncertainty Assessment, Experimental Measurements and Monte-Carlo Simulations. In: *Metrology* Bd. 2, Multidisciplinary Digital Publishing Institute (2022), Nr. 2, S. 241–262
- [HaCM15] HAN, YUANFENG ; CHEN, PEIJIANG ; MENG, TIAN: Harris Corner Detection Algorithm at Sub-pixel Level and Its Application. In: : Atlantis Press, 2015 — ISBN 978-94-6252-089-9, S. 133–137

- [HaDu14] HAFFNER, OTO ; DUCHOŇ, FRANTIŠEK: *Making a map for mobile robot using laser rangefinder*, 2014
- [HaSa00] HATA, KENJI ; SAVARESE, SILVIO: CS231A Course Notes 1: Camera Models, S. 16
- [HaSt88] HARRIS, C. ; STEPHENS, M.: A Combined Corner and Edge Detector. In: *Proceedings of the Alvey Vision Conference 1988*. Manchester : Alvey Vision Club, 1988, S. 23.1-23.6
- [HaSt97] HARTLEY, RICHARD I. ; STURM, PETER: Triangulation. In: *Computer Vision and Image Understanding* Bd. 68 (1997), Nr. 2, S. 146–157
- [Hawi11] HAWI, F.: SYSTÈMES DE STÉRÉOVISION PASSIVE DÉDIÉS À UN STIMULATEUR INTRA-CORTICAL VISUEL. In: *undefined* (2011)
- [HaZi04] HARTLEY, RICHARD ; ZISSERMAN, ANDREW: *Multiple View Geometry in Computer Vision*. URL <https://www.cambridge.org/core/books/multiple-view-geometry-in-computer-vision/0B6F289C78B2B23F596CAA76D3D43F7A>. - abgerufen am 2022-01-12. — Cambridge Core
- [HEBA17] HOFFMANN, MATHIS ; ERNST, ANDREAS ; BERGEN, TOBIAS ; AL, ET: A robust chessboard detector for geometric camera calibration. In: *12th International Conference on Computer Vision Theory and Applications, VISIGRAPP 2017. Proceedings. Vol.4: VISAPP, 2017* — ISBN 978-989-758-225-7, S. 34–43
- [Heik00] HEIKKILA, J.: Geometric camera calibration using circular control points. In: *IEEE Transactions on Pattern Analysis and Machine Intelligence* Bd. 22 (2000), Nr. 10, S. 1066–1077
- [HeLe21] HELLE, ROBIN H. ; LEMU, HIRPA G.: A case study on use of 3D scanning for reverse engineering and quality control. In: *Materials Today: Proceedings, Second International Conference on Aspects of Materials Science and Engineering (ICAMSE 2021)*. Bd. 45 (2021), S. 5255–5262
- [HKJK13] HA, JAEWOOK ; KWON, SOON ; JEONG, JAEKYO ; KIM, HYUNWOO: 3D Reconstruction Method Based on Binary coded Pattern. In: *International Journal of Signal Processing, Image Processing and Pattern Recognition* Bd. 6 (2013), Nr. 6, S. 59–68
- [Horn00] HORN, BERTHOLD K P: Tsai's Camera Calibration Method Revisited, S. 13
- [Howc01] *How Cameras Work*. URL <https://electronics.howstuffworks.com/camera.htm>. - abgerufen am 2022-07-11. — HowStuffWorks

- [HuFF20] HUDSON, R. ; FARAJ, F. ; FOTOPOULOS, G.: Review of close-range three-dimensional laser scanning of geological hand samples. In: *Earth-Science Reviews* Bd. 210 (2020), S. 103321
- [HuHe03] HUBER, DANIEL F. ; HEBERT, MARTIAL: Fully automatic registration of multiple 3D data sets. In: *Image and Vision Computing* Bd. 21 (2003), Nr. 7, S. 637–650
- [HuMa89] HUGLI, HEINZ ; MAITRE, GILBERT: Generation And Use Of Color Pseudo Random Sequences For Coding Structured Light In Active Ranging. In: *Industrial Inspection*. Bd. 1010 : SPIE, 1989, S. 75–82
- [IfAw12] IFTEKHARUDDIN, KHAN ; AWWAL, ABDUL: Spatial Redundancy. In: *Field Guide to Image Processing* Bd. FG25, SPIE (2012), S. 71–72
- [IhRM16] IHRKE, IVO ; RESTREPO, JOHN ; MIGNARD-DEBISE, LOIS: Principles of Light Field Imaging: Briefly revisiting 25 years of research. In: *IEEE Signal Processing Magazine* Bd. 33 (2016), Nr. 5, S. 59–69
- [IKHM11] IZADI, SHAHRAM ; KIM, DAVID ; HILLIGES, OTMAR ; MOLYNEAUX, DAVID ; NEWCOMBE, RICHARD ; KOHLI, PUSHMEET ; SHOTTON, JAMIE ; HODGES, STEVE ; U. A.: KinectFusion: Real-time 3D Reconstruction and Interaction Using a Moving Depth Camera. In: , 2011, S. 559–568
- [Inte12] International Vocabulary of Metrology – Basic and General Concepts and Associated Terms JCGM 200:2012. In: *VIM*. BIPM, 2012
- [Iso89] ISO 2768-1: ISO 2768-1:1989(en), General tolerances — Part 1: Tolerances for linear and angular dimensions without individual tolerance indications. ISO (1989)
- [Iso100] *ISO 14638:2015(en), Geometrical product specifications (GPS) — Matrix model.* URL <https://www.iso.org/obp/ui/#iso:std:iso:14638:ed-1:v1:en>. - abgerufen am 2022-03-31
- [IYDT07] ISHII, I. ; YAMAMOTO, I. ; DOI, K. ; TSUJI, TOKUO: High-speed 3D image acquisition using coded structured light projection. In: *2007 IEEE/RSJ International Conference on Intelligent Robots and Systems* (2007)
- [JHPS21] JAVAID, MOHD ; HALEEM, ABID ; PRATAP SINGH, RAVI ; SUMAN, RAJIV: Industrial perspectives of 3D scanning: Features, roles and it's analytical applications. In: *Sensors International* Bd. 2 (2021), S. 100114
- [Jian12] JIANG, LIANYUAN: Efficient randomized Hough transform for circle detection using novel probability sampling and feature points. In: *Optik* Bd. 123 (2012), Nr. 20, S. 1834–1840

- [JLGF22] JIN, ZIYI ; LI, ZHIXUE ; GAN, TIANYUAN ; FU, ZUOMING ; ZHANG, CHONGAN ; HE, ZHONGYU ; ZHANG, HONG ; WANG, PENG ; U. A.: A Novel Central Camera Calibration Method Recording Point-to-Point Distortion for Vision-Based Human Activity Recognition. In: *Sensors* Bd. 22, Multidisciplinary Digital Publishing Institute (2022), Nr. 9, S. 3524
- [JoGr10] JORDAN, SAMUEL ; GREENSPAN, MICHAEL: Projector optical distortion calibration using Gray-code patterns. In: *2010 IEEE Computer Society Conference on Computer Vision and Pattern Recognition - Workshops*, 2010, S. 72–79
- [Jori00] JORISSEN, SVEN: 3D Real-time Scanning Using a Projector-based Structured Light System, S. 83
- [JSLL14] JIANG, XU-DONG ; SHENG, BIN ; LIN, WEI-YAO ; LU, WEI ; MA, LI-ZHUANG: Image anti-aliasing techniques for Internet visual media processing: a review. In: *Journal of Zhejiang University SCIENCE C* Bd. 15 (2014), Nr. 9, S. 717–728
- [JŠŠŠ15] JERBIĆ, BOJAN ; ŠULIGOJ, FILIP ; ŠVACO, MARKO ; ŠEKORANJA, BOJAN: Robot Assisted 3D Point Cloud Object Registration. In: *Procedia Engineering, 25th DAAAM International Symposium on Intelligent Manufacturing and Automation, 2014*. Bd. 100 (2015), S. 847–852
- [JuKn90] JUDD, R.P. ; KNASINSKI, A.B.: A technique to calibrate industrial robots with experimental verification. In: *IEEE Transactions on Robotics and Automation* Bd. 6 (1990), Nr. 1, S. 20–30
- [KaBr06] KANNALA, JUHO ; BRANDT, SAMI: A Generic Camera Model and Calibration Method for Conventional, Wide-Angle, and Fish-Eye Lenses. In: *IEEE transactions on pattern analysis and machine intelligence* Bd. 28 (2006), S. 1335–40
- [KaRD08] KAESS, MICHAEL ; RANGANATHAN, ANANTH ; DELLAERT, FRANK: iSAM: Incremental Smoothing and Mapping. In: *IEEE Transactions on Robotics* Bd. 24 (2008), Nr. 6, S. 1365–1378
- [Kauf16] KAUFMANN, PETRA: Two Dimensional Phase Unwrapping Theory Algorithms And Software. In: *undefined* (2016)
- [KiRL08] KIM, DAESIK ; RYU, MOONWOOK ; LEE, SUKHAN: Antipodal Gray-codes for structured light. In: *2008 IEEE International Conference on Robotics and Automation* (2008)
- [KILa80] KLEMA, V. ; LAUB, A.: The singular value decomposition: Its computation and some applications. In: *IEEE Transactions on Automatic Control* Bd. 25 (1980), Nr. 2, S. 164–176

- [KZBŠ17] KLANČAR, GREGOR ; ZDEŠAR, ANDREJ ; BLAŽIČ, SAŠO ; ŠKRJANC, IGOR: Chapter 8 - Project Examples for Laboratory Practice. In: KLANČAR, G. ; ZDEŠAR, A. ; BLAŽIČ, S. ; ŠKRJANC, I. (Hrsg.): *Wheeled Mobile Robotics* : Butterworth-Heinemann, 2017 — ISBN 978-0-12-804204-5, S. 419–481
- [Leiv15] LEIVA, HUGO: A Generalization of Cramer’s Rule. In: *Advances in Linear Algebra & Matrix Theory* Bd. 05 (2015), S. 156–166
- [LeWS85] LE MOIGNE, JACQUELINE ; WAXMAN, ALLEN M ; SOCIETY OF MANUFACTURING ENGINEERS: *Multi-resolution grid patterns for building range maps*. Dearborn, Mich. : Society of Manufacturing Engineers, 1985
- [LHZA22] LI, JIAYUAN ; HU, QINGWU ; ZHANG, YONGJUN ; AI, MINGYAO: Robust symmetric iterative closest point. In: *ISPRS Journal of Photogrammetry and Remote Sensing* Bd. 185 (2022), S. 219–231
- [LiAg05] LIU, YANG ; AGGARWAL, J. K.: 3.12 - Local and Global Stereo Methods. In: BOVIK, A. (Hrsg.): *Handbook of Image and Video Processing (Second Edition), Communications, Networking and Multimedia*. Burlington : Academic Press, 2005 — ISBN 978-0-12-119792-6, S. 297–308
- [LiLi14] LIU, JIANYANG ; LI, YOUFU: Performance analysis of 3-D shape measurement algorithm with a short baseline projector-camera system. In: *Robotics and Biomimetics* Bd. 1 (2014), Nr. 1, S. 1
- [Liu06] LIU, YONGHUAI: Automatic registration of overlapping 3D point clouds using closest points. In: *Image Vision Comput* (2006), S. 762–781
- [LiXW21] LIU, CUIYIN ; XU, JISHANG ; WANG, FENG: A Review of Keypoints’ Detection and Feature Description in Image Registration. In: *Scientific Programming* Bd. 2021, Hindawi (2021), S. e8509164
- [LiZh03] LIN, YONGBING ; ZHANG, GUOXIONG: The optimal arrangement of four laser tracking interferometers in 3D coordinate measuring system based on multi-lateration. In: *IEEE International Symposium on Virtual Environments, Human-Computer Interfaces and Measurement Systems, 2003. VECIMS '03. 2003*, 2003, S. 138–143
- [LiZh14] LI, BEIWEN ; ZHANG, SONG: Structured light system calibration method with optimal fringe angle. In: *Applied Optics* Bd. 53, Optica Publishing Group (2014), Nr. 33, S. 7942–7950
- [LLSK06] LEE, HEEJEONG ; LEE, SANG-CHUL ; SEO, YOUNG-WHA ; KIM, TAE-WAN: Registering 3D Scanned Point Cloud Using Markers International Joint Conference 2006 (SICE-ICCAS 2006). In: *2006 SICE-ICASE International Joint Conference*, 2006, S. 4634–4638

- [Lmig00] *LMI Gocator 3000*. URL <https://www.stemmer-imaging.com/fr-fr/produits/serie/lmi-gocator-3100/>. - abgerufen am 2022-06-22. — STEMMER IMAGING
- [LSWW08] LI, ZHONGWEI ; SHI, YUSHENG ; WANG, CONGJUN ; WANG, YUANYUAN: Accurate calibration method for a structured light system. In: *Optical Engineering - OPT ENG* Bd. 47 (2008)
- [Lu10] LU, Z. Q. JOHN: The Elements of Statistical Learning: Data Mining, Inference, and Prediction. In: *Journal of the Royal Statistical Society: Series A (Statistics in Society)* Bd. 173 (2010), Nr. 3, S. 693–694
- [Luhm10] LUHMANN, THOMAS: Close range photogrammetry for industrial applications. In: *ISPRS Journal of Photogrammetry and Remote Sensing, ISPRS Centenary Celebration Issue*. Bd. 65 (2010), Nr. 6, S. 558–569
- [LuMi02] LUCCHESI, L. ; MITRA, S.K.: Using saddle points for subpixel feature detection in camera calibration targets. In: *Asia-Pacific Conference on Circuits and Systems*. Bd. 2, 2002, S. 191–195 Bd.2
- [LuMi97] LU, F. ; MILIOS, E.: Globally Consistent Range Scan Alignment for Environment Mapping. In: *Autonomous Robots* Bd. 4 (1997), Nr. 4, S. 333–349
- [LuSo12] LU, J. ; SONG, C.-Y: Structured light system calibration based on Gray-code combined with line-shift. In: *Guangdianzi Jiguang/Journal of Optoelectronics Laser* Bd. 23 (2012), S. 1146–1151
- [LWWP17] LIU, ZHEN ; WU, QUN ; WU, SUNING ; PAN, XIAO: Flexible and accurate camera calibration using grid spherical images. In: *Optics Express* Bd. 25 (2017), Nr. 13, S. 15269–15285
- [LWYC19] LI, HUABING ; WANG, KAIWEI ; YANG, KAILUN ; CHENG, RUIQI ; WANG, CHEN ; FEI, LEI: Unconstrained self-calibration of stereo camera on visually impaired assistance devices. In: *Applied Optics* Bd. 58 (2019), S. 6377
- [LZHT13] LI, YUNTING ; ZHANG, JUN ; HU, WENWEN ; TIAN, JINWEN: Laboratory calibration of star sensor with installation error using a nonlinear distortion model. In: *Applied Physics B: Lasers and Optics* Bd. 115 (2013), S. 561–570, 2014
- [MaCM03] MA, LILI ; CHEN, YANGQUAN ; MOORE, KEVIN L.: Rational Radial Distortion Models with Analytical Undistortion Formulae. In: *arXiv:cs/0307047* (2003). — arXiv: cs/0307047
- [MaKL11] MARTYNOV, IVAN ; KAMARAINEN, JONI-KRISTIAN ; LENSU, LASSE: Projector Calibration by “Inverse Camera Calibration”. In: HEYDEN, A. ; KAHL, F. (Hrsg.): *Image Analysis, Lecture Notes in Computer*

-
- Science*. Berlin, Heidelberg : Springer, 2011 — ISBN 978-3-642-21227-7, S. 536–544
- [Matt18] MATTHIAS, STEFFEN: *A flexible endoscopic structured light 3-D sensor: Design, models and image processing*, 2018
- [MaWh00] MALLON, JOHN ; WHELAN, PAUL F.: Which Pattern? Biasing Aspects of Planar Calibration Patterns and Detection Methods Abstract.
- [MaYo94] MASUDA, T. ; YOKOYA, N.: A robust method for registration and segmentation of multiple range images. In: *Proceedings of 1994 IEEE 2nd CAD-Based Vision Workshop*, 1994, S. 106–113
- [MBPB19] MAURYA, HARSHIT ; BOHRA, VIVEK KUMAR ; PAL, NIDHI SINGH ; BHADORIA, VIKAS SINGH: Effect of Inertia Weight of PSO on Optimal Placement of DG. In: *IOP Conference Series: Materials Science and Engineering* (2019)
- [MCHD07] MA, LILI ; CAO, CHENGYU ; HOVAKIMYAN, NAIRA ; DIXON, WARREN ; WOOLSEY, CRAIG: *Range Identification in the Presence of Unknown Motion Parameters for Perspective Vision Systems*, 2007. — journalAbbreviation: *Proceedings of the American Control Conference*
- [Mebi07] MEBIUS, JOHAN E.: Derivation of the Euler-Rodrigues formula for three-dimensional rotations from the general formula for four-dimensional rotations (2007)
- [MeNR90] MEHROTRA, RAJIV ; NICHANI, SANJAY ; RANGANATHAN, N.: Corner detection. In: *Pattern Recognition* Bd. 23 (1990), Nr. 11, S. 1223–1233
- [Mitt00] MITTRAPIYANURUK, PRADIT: A Memo on How to Use the Levenberg-Marquardt Algorithm for Refining Camera Calibration Parameters
- [Mora00] MORAVEC, HANS P.: *Techniques Towards Automatic Visual Obstacle Avoidance*
- [Mour16] MOURA PAREDES, GUILHERME: *Study of Mooring Systems for Offshore Wave Energy Converters*, 2016
- [MRGO14] MADRIGAL, CARLOS ; RAMIREZ, LUISA ; GUTIERREZ, ANDRÉS ; OCAMPO, LUIS ; BRANCH, JOHN ; RESTREPO-MARTINEZ, ALEJANDRO: *Extraction of correspondences in color coded pattern for the 3D reconstruction using structured light*, 2014. — journalAbbreviation: *2014 19th Symposium on Image, Signal Processing and Artificial Vision, STSIVA 2014*
- [MSTM15] MUNARO, MATTEO ; SO, EDMOND ; TONELLO, STEFANO ; MENEGATTI, EMANUELE: Efficient Completeness Inspection Using Real-Time 3D Color Reconstruction with a Dual-Laser Triangulation System. In:

- Advances in Computer Vision and Pattern Recognition* Bd. 48 (2015), S. 201–225
- [MTLP12] MARKELJ, P. ; TOMAŽEVIČ, D. ; LIKAR, B. ; PERNUŠ, F.: A review of 3D/2D registration methods for image-guided interventions. In: *Medical Image Analysis* Bd. 16 (2012), Nr. 3, S. 642–661
- [MySo10] MYRONENKO, ANDRIY ; SONG, XUBO: Point-Set Registration: Coherent Point Drift. In: *IEEE Transactions on Pattern Analysis and Machine Intelligence* Bd. 32 (2010), Nr. 12, S. 2262–2275. — arXiv: 0905.2635
- [NaNa94] NAYAR, S.K. ; NAKAGAWA, Y.: Shape from focus. In: *IEEE Transactions on Pattern Analysis and Machine Intelligence* Bd. 16 (1994), Nr. 8, S. 824–831
- [Naou06] NAOULOU, ABDELELAH: *Architectures pour la stéréovision passive dense temps réel : application à la stéréo-endoscopie*, Université Paul Sabatier - Toulouse III, phdthesis, 2006
- [NBSR20] NEBEL, STEVE ; BEEGE, MAIK ; SCHNEIDER, SASCHA ; REY, GÜNTER DANIEL: A Review of Photogrammetry and Photorealistic 3D Models in Education From a Psychological Perspective. In: *Frontiers in Education* Bd. 5 (2020)
- [Neug97] NEUGEBAUER, P.J.: Geometrical cloning of 3D objects via simultaneous registration of multiple range images. In: *Proceedings of 1997 International Conference on Shape Modeling and Applications*, 1997, S. 130–139
- [NiAg12] NIXON, MARK S. ; AGUADO, ALBERTO S.: Chapter 10 - Appendix 1: Camera geometry fundamentals. In: NIXON, M. S. ; AGUADO, A. S. (Hrsg.): *Feature Extraction & Image Processing for Computer Vision (Third Edition)*. Oxford : Academic Press, 2012 — ISBN 978-0-12-396549-3, S. 489–518
- [Niev13] NIEVERGELT, YVES: Fitting cylinders to data. In: *Journal of Computational and Applied Mathematics* Bd. 239 (2013), S. 250–269
- [NuBa12] NUGRAHA, A.S. ; BASARUDDIN, T.: *Analysis and comparison of QR decomposition algorithm in some types of matrix*, 2012. — journalAbbreviation: 2012 Federated Conference on Computer Science and Information Systems, FedCSIS 2012 — ISBN 978-1-4673-0708-6
- [NuSL17] NURUNNABI, A. ; SADAHIRO, Y. ; LINDENBERGH, R.: ROBUST CYLINDER FITTING IN THREE-DIMENSIONAL POINT CLOUD DATA. In: *The International Archives of the Photogrammetry, Remote Sensing and Spatial Information Sciences*. Bd. XLII-1-W1 : Copernicus GmbH, 2017, S. 63–70

- [ONTD18] O' RIORDAN, ANDREW ; NEWE, THOMAS ; TOAL, DANIEL ; DOOLY, GERARD: *Stereo Vision Sensing: Review of existing systems*, 2018
- [Open00] *OpenCV: Basic concepts of the homography explained with code*. URL https://docs.opencv.org/3.4/d9/dab/tutorial_homography.html. - abgerufen am 2020-05-27
- [Osbo76] OSBORNE, M. R.: Nonlinear least squares — the Levenberg algorithm revisited*. In: *The ANZIAM Journal* Bd. 19, Cambridge University Press (1976), Nr. 3, S. 343–357
- [OVBS17] OZYESIL, ONUR ; VORONINSKI, VLADISLAV ; BASRI, RONEN ; SINGER, AMIT: A Survey of Structure from Motion. In: *arXiv:1701.08493 [cs]* (2017). — arXiv: 1701.08493
- [PaDe09] PAYEUR, PIERRE ; DESJARDINS, DANICK: *Structured Light Stereoscopic Imaging with Dynamic Pseudo-random Patterns*, 2009 — ISBN 978-3-642-02610-2
- [Pan19] PAN, YUE: Target-less registration of point clouds: A review. In: *arXiv:1912.12756 [cs]* (2019). — arXiv: 1912.12756
- [Part00] *Particle Swarm Optimization (PSO) — pagmo 2.17.0 documentation*. URL <https://esa.github.io/pagmo2/docs/cpp/algorithms/pso.html>. - abgerufen am 2021-03-20
- [Pedr08] PEDROTTI, LENO S.: Basic Geometrical Optics. In: *Fundamentals of Photonics* Bd. TT79, SPIE (2008), S. 73–117
- [PeKo02] PERS, JANEZ ; KOVAČIČ, STANISLAV: Nonparametric, Model-Based Radial Lens Distortion Correction Using Tilted Camera Assumption (2002)
- [PeSt19] PENG, SONGYOU ; STURM, PETER: Calibration Wizard: A Guidance System for Camera Calibration Based on Modelling Geometric and Corner Uncertainty. In: *ICCV 2019 - International Conference on Computer Vision*. Seoul, South Korea : IEEE, 2019, S. 1497–1505
- [PiNP20] PIOTROWSKI, ADAM P. ; NAPIORKOWSKI, JAROSLAW J. ; PIOTROWSKA, AGNIESZKA E.: Population size in Particle Swarm Optimization. In: *Swarm and Evolutionary Computation* Bd. 58 (2020), S. 100718
- [PLMG20] PENTTILÄ, SAKARI ; LUND, HANNU ; MARTIKAINEN, ANTTI ; GYASI, EMMANUEL ; SKRIKO, TUOMAS: Weld Quality Verification by Using Laser Triangulation Measurement. In: *Procedia Manufacturing, 30th International Conference on Flexible Automation and Intelligent Manufacturing (FAIM2021)*. Bd. 51 (2020), S. 408–415
- [PiPi18a] PŁACZEK, M. ; PISZCZEK, Ł.: Testing of an industrial robot's accuracy and repeatability in off and online environment. In: *Eksploracja i niezawodność* Bd. Vol. 20 (2018), Nr. 3

- [PiPi18b] PŁACZEK, MAREK ; PISZCZEK, ŁUKASZ: Testing of an industrial robot's accuracy and repeatability in off and online environment. In: *Eksploatacja i Niezawodność - Maintenance and Reliability* Bd. 20 (2018), Nr. 3, S. 455–464
- [Prin00] Principles of Remote Sensing. In: . Centre for Remote Imaging, Sensing & Processing
- [Prof19] PROF. KHARAT RAJESH, SAINATH: Review Paper of Jacobian. In: *International Journal of Emerging Technologies and Innovative Research JETIR* Bd. Issue 1 (2019), S. 260–262
- [PrPo10] PRISCO, U. ; POLINI, W.: Flatness, Cylindricity and Sphericity Assessment Based on the Seven Classes of Symmetry of the Surfaces. In: *Advances in Mechanical Engineering* Bd. 2, SAGE Publications (2010), S. 154287
- [QCVG06] QUIROGA, ANTONIO ; CRESPO, DANIEL ; VARGAS, JAVIER ; GOMEZ-PEDRERO, JOSE ANTONIO: Adaptive spatiotemporal structured light method for fast three-dimensional measurement. In: *Optical Engineering* Bd. 45, SPIE (2006), Nr. 10, S. 107203
- [Ragh21] RAGHAV, AGRAWAL: *Polynomial Regression / What is Polynomial Regression*. . - abgerufen am 2021-12-27. — Analytics Vidhya
- [RaOl14] RANGANATHAN, PRADEEP ; OLSON, EDWIN: Locally-weighted homographies for calibration of imaging systems. In: *IEEE International Conference on Intelligent Robots and Systems* (2014), S. 404–409
- [RaPR20] RAKSIRI, CHANA ; PA-IM, KRITTIYA ; RODKWAN, SUPASIT: An Analysis of Joint Assembly Geometric Errors Affecting End-Effector for Six-Axis Robots. In: *Robotics* Bd. 9, Multidisciplinary Digital Publishing Institute (2020), Nr. 2, S. 27
- [RaST14] RAI, KARTIK ; SHARMA, AYUSH ; TANWAR, MOHIT: Projective geometry Bd. 1 (2014), Nr. 5, S. 4
- [RDHV07] RABBANI, TAHIR ; DIJKMAN, SANDER ; VAN DEN HEUVEL, FRANK ; VOSSelman, GEORGE: An integrated approach for modelling and global registration of point clouds. In: *ISPRS Journal of Photogrammetry and Remote Sensing* Bd. 61 (2007), Nr. 6, S. 355–370
- [ReBF10] REBSAMEN, MARYLINE ; BOUCHEIX, JEAN-MICHEL ; FAYOL, MICHEL: Quality control in the optical industry: From a work analysis of lens inspection to a training programme, an experimental case study. In: *Applied Ergonomics* Bd. 41 (2010), Nr. 1, S. 150–160

- [Reyn09] REYNOLDS, DOUGLAS: Gaussian Mixture Models. In: LI, S. Z. ; JAIN, A. (Hrsg.): *Encyclopedia of Biometrics*. Boston, MA : Springer US, 2009 — ISBN 978-0-387-73003-5, S. 659–663
- [RiSa07] RICOLFE-VIALA, CARLOS ; SANCHEZ-SALMERON, ANTONIO-JOSE: Improved Camera Calibration Method Based on a Two-Dimensional Template. In: *Proceedings of the 3rd Iberian conference on Pattern Recognition and Image Analysis, Part II, IbPRIA '07*. Berlin, Heidelberg : Springer-Verlag, 2007 — ISBN 978-3-540-72848-1, S. 420–427
- [RNAS15] RANTOSON, RINDRA ; NOUIRA, HICHEM ; ANWER, NABIL ; MEHDI-SOUZANI, CHARYAR: Novel automated methods for coarse and fine registrations of point clouds in high precision metrology. In: *International Journal of Advanced Manufacturing Technology*, Springer Verlag (2015), S. 16
- [RNAS16] RANTOSON, RINDRA ; NOUIRA, HICHEM ; ANWER, NABIL ; MEHDI-SOUZANI, CHARYAR: Improved curvature-based registration methods for high-precision dimensional metrology. In: *Precision Engineering* Bd. 46 (2016), S. 232–242
- [Rodi06] RODIN, V.: *Stéréovision axiale : modélisation et calibrage du système de prises de vues , reconstruction 3 D d ' objets naturels Axial Stereovision : Modeling and Calibration of the Optical System , 3 D Reconstruction of Natural Objects*. . - abgerufen am 2021-05-29
- [RoKu18] ROJTBURG, PAVEL ; KUIJPER, ARJAN: Efficient Pose Selection for Interactive Camera Calibration. In: *2018 IEEE International Symposium on Mixed and Augmented Reality (ISMAR)* (2018), S. 31–36. — arXiv: 1907.04096
- [Roud04] ROUDENKO, SVETLANA: Noise and Texture Detection in Image Processing (2004), S. 11
- [Rude17] RUDER, SEBASTIAN: An overview of gradient descent optimization algorithms. In: *Computer Science* (2017). — arXiv: 1609.04747
- [SáMS18a] SÁNCHEZ, JAVIER ; MONZÓN, NELSON ; SALGADO, AGUSTÍN: An Analysis and Implementation of the Harris Corner Detector. In: *Image Processing On Line* Bd. 8 (2018), S. 305–328
- [SáMS18b] SÁNCHEZ, JAVIER ; MONZÓN, NELSON ; SALGADO, AGUSTÍN: An Analysis and Implementation of the Harris Corner Detector. In: *Image Processing On Line* Bd. 8 (2018), S. 305–328
- [SaPB04] SALVI, JOAQUIM ; PAGÈS, JORDI ; BATLLE, JOAN: Pattern codification strategies in structured light systems. In: *Pattern Recognition, Agent Based Computer Vision*. Bd. 37 (2004), Nr. 4, S. 827–849
- [Scra00] SCRATCHPIXEL: Introduction to Polygon Meshes. *Scratchapixel*.

- [ScSa00] SCHOCH, ALEXANDER ; SAVIO, ENRICO: High-speed measurement of complex shaped parts by laser triangulation for in-process inspection, S. 22
- [ScYK20] SCHLAMMINGER, S. ; YANG, I. ; KUMAR, H.: Redefinition of SI Units and Its Implications. In: *MAPAN* Bd. 35 (2020), Nr. 4, S. 471–474
- [SDMM19] STOCK, MICHAEL ; DAVIS, RICHARD ; MIRANDÉS, ESTEFANÍA DE ; MILTON, MARTIN J. T.: The revision of the SI—the result of three decades of progress in metrology. In: *Metrologia* Bd. 56, IOP Publishing (2019), Nr. 2, S. 022001
- [SeDP17] SECHER, JESPER JARED ; DARVANN, TRON ANDRE ; PINHOLT, ELSE MARIE: Accuracy and reproducibility of the DAVID SLS-2 scanner in three-dimensional facial imaging. In: *Journal of Cranio-Maxillofacial Surgery* Bd. 45 (2017), Nr. 10, S. 1662–1670
- [Sher00] SHERROD PH: Cylindrical Regression - Fit a Cylinder to Data Points. *NLREG*.
- [SHIR98] SHUM, H.-Y ; HEBERT, MARTIAL ; IKEUCHI, KATSUSHI ; REDDY, RAJ: An integral approach to free-form object modeling. In: *Pattern Analysis and Machine Intelligence, IEEE Transactions on* Bd. 19 (1998), S. 1366–1370
- [Shug20] SHUGAROV, ANDREY: *An Overview of Modern CMOS and CCD Detectors for Wide Field Telescopes*, 2020
- [Sigh22] SIGHT, INSIGHT IN PLAIN: *Estimating the Homography Matrix with the Direct Linear Transform (DLT)*. URL <https://medium.com/@insight-in-plain-sight/estimating-the-homography-matrix-with-the-direct-linear-transform-dlt-ec6bbb82ee2b>. - abgerufen am 2022-07-12. — Medium
- [Sinh00] SINHA, UTKARSH: *Two major physical defects in cameras - AI Shack*. URL <https://aishack.in/tutorials/major-physical-defects-cameras/>. - abgerufen am 2022-07-11
- [Smit78] SMITH, ALVY: *Color Gamut Transform Pairs*. Bd. 12, 1978. — journalAbbreviation: ACM Siggraph Computer Graphics
- [SMMR19] SIEKAŃSKI, PIOTR ; MAGDA, KRZYSZTOF ; MALOWANY, KRZYSZTOF ; RUTKIEWICZ, JAN ; STYK, ADAM ; KRZESLOWSKI, JAKUB ; KOWALUK, TOMASZ ; ZAGÓRSKI, ANDRZEJ: On-Line Laser Triangulation Scanner for Wood Logs Surface Geometry Measurement. In: *Sensors* Bd. 19 (2019), S. 1074
- [SSBM11] SAMPER, DAVID ; SANTOLARIA, JORGE ; BROSED, FRANCISCO ; MAJARENA, ANA ; AGUILAR, J.: Analysis of Tsai calibration method using two- and three-dimensional calibration objects. In: *Machine Vision and Applications* Bd. 24 (2011)

- [Stan16] STANLEY, BIRCHFIELD: Essential and fundamental matrices. In: *Projective Geometry Applied to Computer Vision*. Stanford Robotic. Clemson University, 2016
- [Stew21] STEWARD, JEREMY: Camera Modeling: Exploring Distortion and Distortion Models. In: *Tangram Vision Bd. Part II* (2021)
- [StLD18] STANKIEWICZ, OLGIERD ; LAFRUIT, GAUTHIER ; DOMAŃSKI, MAREK: Chapter 1 - Multiview video: Acquisition, processing, compression, and virtual view rendering. In: CHELLAPPA, R. ; THEODORIDIS, S. (Hrsg.): *Academic Press Library in Signal Processing, Volume 6* : Academic Press, 2018 — ISBN 978-0-12-811889-4, S. 3–74
- [Stur14] STURM, PETER: Optical Axis. In: IKEUCHI, K. (Hrsg.): *Computer Vision: A Reference Guide*. Boston, MA : Springer US, 2014 — ISBN 978-0-387-31439-6, S. 564–565
- [Svil18] SVILAINIS, LINAS: 21 - LEDs for large displays. In: HUANG, J. ; KUO, H.-C. ; SHEN, S.-C. (Hrsg.): *Nitride Semiconductor Light-Emitting Diodes (LEDs) (Second Edition)*, *Woodhead Publishing Series in Electronic and Optical Materials* : Woodhead Publishing, 2018 — ISBN 978-0-08-101942-9, S. 659–736
- [SwNa00] SWAMINATHAN, RAHUL ; NAYAR, SHREE K: Non-Metric Calibration of Wide-Angle Lenses and Polycameras, S. 7
- [SWPG05] SADLO, F. ; WEYRICH, T. ; PEIKERT, R. ; GROSS, M.: A practical structured light acquisition system for point-based geometry and texture. In: *Proceedings Eurographics/IEEE VGTC Symposium Point-Based Graphics, 2005.*, 2005, S. 89–145
- [SZPY12] SANDBACH, GEORGIA ; ZAFEIRIOU, STEFANOS ; PANTIC, MAJA ; YIN, LIJUN: Static and dynamic 3D facial expression recognition: A comprehensive survey. In: *Image and Vision Computing Bd. 30* (2012), Nr. 10, S. 683–697
- [TaAh15] TABB, AMY ; AHMAD YOUSEF, KHALIL: *Parameterizations for Reducing Camera Reprojection Error for Robot-World Hand-Eye Calibration*, 2015
- [TaAh17] TABB, AMY ; AHMAD YOUSEF, KHALIL: Solving the robot-world hand-eye(s) calibration problem with iterative methods. In: *Machine Vision and Applications* (2017), S. 1–22
- [Tamb19] TAMBOURATZIS, GEORGE: PSO Optimal Parameters and Fitness Functions in an NLP Task. In: *2019 IEEE Congress on Evolutionary Computation (CEC)*, 2019, S. 611–618
- [TaML14] TAUBIN, GABRIEL ; MORENO, DANIEL ; LANMAN, DOUGLAS: 3D scanning for personal 3D printing: Build your own desktop 3D scanner. In: *ACM SIGGRAPH 2014 Studio, SIGGRAPH 2014* (2014)

- [Tay120] Taylor series. *Wikipedia*.
- [TGMM17] TANG, ZHONGWEI ; GROMPONE VON GIOI, RAFAEL ; MONASSE, PASCAL ; MOREL, JEAN-MICHEL: A Precision Analysis of Camera Distortion Models. In: *IEEE Transactions on Image Processing* Bd. 26 (2017), Nr. 6, S. 2694–2704
- [Thom00] THOMSON, CHARLES: *Is robust 3D point cloud registration without targets possible?* URL <https://info.vercator.com/blog/is-robust-3d-point-cloud-registration-without-targets-possible>. - abgerufen am 2022-04-12
- [TiAS19] TISCAREÑO, JULIETA ; ALBAJEZ, JOSÉ A. ; SANTOLARIA, JORGE: Analysis of different camera calibration methods on a camera-projector measuring system. In: *Procedia Manufacturing* Bd. 41 (2019), S. 539–546
- [Till13] TILLOTSON, REED: A Review of a Singularly Valuable Decomposition: The SVD of a Matrix. In: *Washington Edu* (2013), S. 12
- [Togu22] TOGUEM TAGNE, SAINT-CLAIR: *Development of a cylindricity measurement with nanometre uncertainty*, université Paris-Saclay, These de doctorat, 2022
- [Tsai87a] TSAI, R.: A versatile camera calibration technique for high-accuracy 3D machine vision metrology using off-the-shelf TV cameras and lenses. In: *IEEE Journal on Robotics and Automation* Bd. 3 (1987), Nr. 4, S. 323–344
- [Tsai87b] TSAI, R.: A versatile camera calibration technique for high-accuracy 3D machine vision metrology using off-the-shelf TV cameras and lenses. In: *IEEE Journal on Robotics and Automation* Bd. 3 (1987), Nr. 4, S. 323–344
- [TTAM18] TORNERO MARTÍNEZ, NADIA ; TRUJILLO-SCHIAFFINO, GERARDO ; ANGUIANO-MORALES, MARCELINO ; MENDOZA-VILLEGAS, P. ; SALAS-PEIMBERT, D. ; CORRAL-MARTINEZ, LUIS: Color profilometry techniques: A review. In: *Optica Pura y Aplicada* Bd. 51 (2018), S. 1–26
- [Unde20] *Understanding Lens Distortion | LearnOpenCV #*. URL <https://learnopencv.com/understanding-lens-distortion/>. - abgerufen am 2022-07-11
- [URKG19] URBANČIČ, TILEN ; ROŠKAR, ŽIGA ; KOSMATIN FRAS, MOJCA ; GRIGILLO, DEJAN: New Target for Accurate Terrestrial Laser Scanning and Unmanned Aerial Vehicle Point Cloud Registration. In: *Sensors (Basel, Switzerland)* Bd. 19 (2019), Nr. 14, S. 3179

- [USAN05] UCHIDA, N. ; SHIBAHARA, T. ; AOKI, T. ; NAKAJIMA, H. ; KOBAYASHI, K.: 3D face recognition using passive stereo vision. In: *IEEE International Conference on Image Processing 2005*. Genova, Italy : IEEE, 2005 — ISBN 978-0-7803-9134-5, S. II–950
- [VaCP08] VALETTE, SÉBASTIEN ; CHASSERY, JEAN-MARC ; PROST, RÉMY: Generic remeshing of 3D triangular meshes with metric-dependent discrete Voronoi Diagrams. In: *IEEE Transactions on Visualization and Computer Graphics* Bd. 14, Institute of Electrical and Electronics Engineers (2008), Nr. 2, S. 369–381
- [VBRF21] VILA, ORIOL ; BOADA, IMMA ; RABA, DAVID ; FARRES, ESTEVE: A Method to Compensate for the Errors Caused by Temperature in Structured-Light 3D Cameras. In: *Sensors* Bd. 21, Multidisciplinary Digital Publishing Institute (2021), Nr. 6, S. 2073
- [Vill00] VILLESAS, MARTIN ROA: 3D Face Reconstruction using Structured Light on a Hand-held Device, S. 88
- [WCWM19] WANG, ZHIRONG ; CHEN, ZHANGWEI ; WANG, YUXIANG ; MAO, CHENTAO ; HANG, QIANG: A Robot Calibration Method Based on Joint Angle Division and an Artificial Neural Network. In: *Mathematical Problems in Engineering* Bd. 2019, Hindawi (2019), S. e9293484
- [WeCH92] WENG, J. ; COHEN, P. ; HERNIOU, M.: Camera calibration with distortion models and accuracy evaluation. In: *IEEE Transactions on Pattern Analysis and Machine Intelligence* Bd. 14 (1992), Nr. 10, S. 965–980
- [Weij05] WEIJER, JOOST VAN DE: Color features and local structure in images. In: *undefined* (2005)
- [What00] *What Is Camera Calibration? - MATLAB & Simulink - MathWorks France*. URL <https://fr.mathworks.com/help/vision/ug/camera-calibration.html>. - abgerufen am 2020-05-27
- [Whee19] WHEELER, ANDREW: The Benefits of Structured-Light Scanning for Manufacturing, Reverse Engineering and Quality Control Workflows. In: *Engineering.com* (2019)
- [WiBP12] WIJENAYAKE, UDAYA ; BAEK, SEUNG-HAE ; PARK, SOON-YONG: *An Error Correcting 3D Scanning Technique Using Dual Pseudorandom Arrays*, 2012
- [Will94] WILLSON, REG G.: Modeling and calibration of automated zoom lenses. In: EL-HAKIM, S. F. (Hrsg.): . Boston, MA, 1994, S. 170–186
- [WiOL14] WILM, JAKOB ; OLESEN, OLIVE VINTER ; LARSEN, RASMUS: Accurate and Simple Calibration of DLP Projector Systems. In: *Proceedings of SPIE, the International Society for Optical Engineering*. Bd. 8979 : S

- P I E - International Society for Optical Engineering, 2014.
—journalAbbreviation: PROGRESS IN BIOMEDICAL OPTICS
AND IMAGIN, S. 897909
- [WPXW17] WAN, W. ; PENG, M. ; XING, Y. ; WANG, Y. ; LIU, Z. ; DI, K. ; TENG, B. ; MAO, X. ; U. A.: a Performance Comparison of Feature Detectors for Planetary Rover Mapping and Localization. In: *ISPRS - International Archives of the Photogrammetry, Remote Sensing and Spatial Information Sciences* Bd. 62W1 (2017), S. 149–154
- [WSRK11] WEINMANN, MICHAEL ; SCHWARTZ, CHRISTOPHER ; RUITERS, ROLAND ; KLEIN, REINHARD: *A Multi-camera, Multi-projector Super-Resolution Framework for Structured Light*, 2011
- [WSZL08] WANG, JIANHUA ; SHI, FANHUI ; ZHANG, JING ; LIU, YUNCAI: A new calibration model of camera lens distortion. In: *Pattern Recognition* Bd. 41 (2008), Nr. 2, S. 607–615
- [WuHC06] WU, DANIEL JIH-HUAH ; HORNG, KUO-YANG ; CHANG, RONG-SENG: Triangulation-based laser range finder using a complementary metal-oxide semiconductor image sensor for application to automotive systems. In: *Optical Engineering* Bd. 45, SPIE (2006), Nr. 4, S. 044302
- [WYDL21] WU, RUIBING ; YU, ZIPING ; DING, DONGHONG ; LU, QINGHUA ; PAN, ZENGXI ; LI, HUIJUN: OICP: An Online Fast Registration Algorithm Based on Rigid Translation Applied to Wire Arc Additive Manufacturing of Mold Repair. In: *Materials (Basel, Switzerland)* Bd. 14 (2021), Nr. 6, S. 1563
- [Xime00] XIMEA - MQ013RG-E2. URL <https://www.ximea.com/en/products/cameras-filtered-by-sensor-types/mq013rg-e2>. - abgerufen am 2022-07-12
- [XiWW08] XIAO, YUNHAI ; WEI, ZENGXIN ; WANG, ZHIGUO: A limited memory BFGS-type method for large-scale unconstrained optimization. In: *Computers & Mathematics with Applications* Bd. 56 (2008), Nr. 4, S. 1001–1009
- [XuAl09] XU, YI ; ALIAGA, DANIEL G.: An Adaptive Correspondence Algorithm for Modeling Scenes with Strong Interreflections. In: *IEEE Transactions on Visualization and Computer Graphics* Bd. 15 (2009), Nr. 3, S. 465–480
- [XuGo18] XU, YUN ; GOODACRE, ROYSTON: On Splitting Training and Validation Set: A Comparative Study of Cross-Validation, Bootstrap and Systematic Sampling for Estimating the Generalization Performance of Supervised Learning. In: *Journal of Analysis and Testing* Bd. 2 (2018), Nr. 3, S. 249–262

- [Yama00] YAMANOUE, H.: The Differences Between Toed-in Camera Configurations and Parallel Camera Configurations in Shooting Stereoscopic Images.
- [YaTT11] YANAI, HARUO ; TAKEUCHI, KEI ; TAKANE, YOSHIO: Singular Value Decomposition (SVD). In: YANAI, H. ; TAKEUCHI, K. ; TAKANE, Y. (Hrsg.): *Projection Matrices, Generalized Inverse Matrices, and Singular Value Decomposition, Statistics for Social and Behavioral Sciences*. New York, NY : Springer, 2011 — ISBN 978-1-4419-9887-3, S. 125–149
- [YiAM20] YILDIZ, ALI RIZA ; ABDERAZEK, HAMMOUDI ; MIRJALILI, SEYEDALI: A Comparative Study of Recent Non-traditional Methods for Mechanical Design Optimization. In: *Archives of Computational Methods in Engineering* Bd. 27 (2020), Nr. 4, S. 1031–1048
- [YLCJ16] YANG, JIAOLONG ; LI, HONGDONG ; CAMPBELL, DYLAN ; JIA, YUNDE: Go-ICP: A Globally Optimal Solution to 3D ICP Point-Set Registration. In: *IEEE Transactions on Pattern Analysis and Machine Intelligence* Bd. 38 (2016), Nr. 11, S. 2241–2254. — arXiv: 1605.03344
- [YMMY21] YIN, YONGKAI ; MAO, JIAQI ; MENG, XIANGFENG ; YANG, XIULUN ; WU, KE ; XI, JIANGTAO ; SUN, BAOQING: A two-step phase-shifting algorithm dedicated to fringe projection profilometry. In: *Optics and Lasers in Engineering* Bd. 137 (2021), S. 106372
- [YMYW14] YING, XIANGHUA ; MEI, XIANG ; YANG, SEN ; WANG, GANWEN ; ZHA, HONGBIN: Radial distortion correction from a single image of a planar calibration pattern using convex optimization. In: *2014 IEEE International Conference on Image Processing (ICIP)*. Paris, France : IEEE, 2014 — ISBN 978-1-4799-5751-4, S. 3440–3443
- [ZaPr97] ZANG, WEIJUN ; PRASAD, AJAY K.: Performance evaluation of a Scheimpflug stereocamera for particle image velocimetry. In: *Applied Optics* Bd. 36, Optica Publishing Group (1997), Nr. 33, S. 8738–8744
- [ZDKS17] ZHENG, DONGLIANG ; DA, FEIPENG ; KEMAO, QIAN ; SEAH, HOCK SOON: Phase-shifting profilometry combined with Gray-code patterns projection: unwrapping error removal by an adaptive median filter. In: *Optics Express* Bd. 25, Optica Publishing Group (2017), Nr. 5, S. 4700–4713
- [ZGZL19] ZHU, HAO ; GUO, BIN ; ZOU, KE ; LI, YONGFU ; YUEN, KA-VEENG ; MIHAYLOVA, LYUDMILA ; LEUNG, HENRY: A Review of Point Set Registration: From Pairwise Registration to Groupwise Registration. In: *Sensors (Basel, Switzerland)* Bd. 19 (2019), Nr. 5, S. 1191
- [Zhan00a] ZHANG, Z.: A flexible new technique for camera calibration. In: *IEEE Transactions on Pattern Analysis and Machine Intelligence* Bd. 22 (2000), Nr. 11, S. 1330–1334

-
- [Zhan00b] ZHANG, Z.: A flexible new technique for camera calibration. In: *IEEE Transactions on Pattern Analysis and Machine Intelligence* Bd. 22 (2000), Nr. 11, S. 1330–1334
- [ZhCS02] ZHANG, LI ; CURLESS, BRIAN ; SEITZ, STEVEN M.: Rapid Shape Acquisition Using Color Structured Light and Multi-pass Dynamic Programming. In: : IEEE Computer Society, 2002 — ISBN 978-0-7695-1521-2, S. 24–24
- [Zhu19] ZHU, ZUOWEI: *Modèles géométriques avec défauts pour la fabrication additive*, 2019
- [ZhYD21] ZHANG, JUYONG ; YAO, YUXIN ; DENG, BAILIN: Fast and Robust Iterative Closest Point. In: *IEEE Transactions on Pattern Analysis and Machine Intelligence* (2021), S. 1–1. — arXiv: 2007.07627

Résumé substantiel en français

1. Introduction générale

Dans un souci permanent de contrôle qualité, le besoin en numérisation 3D de pièces mécaniques est en croissance depuis une vingtaine d'années. Bien que de nombreux scanners 3D commercialisés soient fonctionnels, leurs traçabilités ainsi que l'estimation des incertitudes de mesure sont souvent négligées, et représentent un verrou important à lever [Inte12]. Actuellement, la traçabilité des systèmes de vision n'est pas garantie par les laboratoires nationaux de métrologie.

Dans ce contexte, le LCM (LNE-CNAM) a participé au projet européen LaVA-17IND03 dont l'objectif consiste à développer des systèmes de mesures pour le contrôle de pièces complexes de grandes dimensions avec une incertitude de mesure inférieure à 100 μm . Le LNE-CNAM, partenaire du projet, s'est focalisé sur le développement d'un système de mesure tridimensionnel pour la caractérisation de pièces complexes de grands volumes, destinées principalement à des applications dans l'aéronautique. Ce type de pièces est généralement difficile à contrôler en raison de leurs dimensions et de la complexité des formes qui les constituent. Le contrôle des sous-ensembles, comme les cellules ou les sections d'avion, nécessite l'utilisation de systèmes de mesures flexibles, exacts et traçables, qui peuvent être installés à proximité de la chaîne de production, pour améliorer le cycle de fabrication.

Le contrôle classique des pièces mécaniques se fait généralement avec des machines de mesure tridimensionnelle (MMT) tactiles. Ces MMTs tactiles offrent la possibilité de réaliser des mesures dimensionnelles avec des incertitudes micrométriques. Cependant deux inconvénients se présentent : (1) le cycle de mesure est très long en particulier quand il s'agit d'une pièce de grand volume et (2) le volume de mesure est limité. Pour pallier cette problématique, plusieurs études sur les techniques de mesure 3D ont été initiées pour développer des solutions alternatives. Ces études ont abouti aux développements de nouvelles techniques de numérisation 3D sans contact (photogrammétrie, triangulation laser, vision stéréoscopique) [AMRA19, HuFF20, ONTD18]. Ce type de technologies, utilisées pour du contrôle non-destructif, permet d'acquérir un grand nombre de points en un temps très court avec une résolution élevée comparé aux scanners tactiles.

Compte tenu des limitations observées dans les domaines académique et industriel, j'ai effectué mes travaux de thèse sur le développement d'un nouveau scanner 3D traçable à la définition du mètre et à l'implémentation des algorithmes associés de traitement de données. Le scanner 3D est constitué de deux caméras industrielles et d'un projecteur de lumière structurée, l'ensemble est intégré sur un robot industriel. Des télémètres sont utilisés pour identifier les positions et les orientations du scanner dans l'espace de travail. Les étapes de ce travail de recherche sont les suivantes : (1) étude des systèmes de numérisation 3D (choix de la technologie et de la méthode d'étalonnage) et des méthodes d'étalonnage de scanners optiques, identification des paramètres requis pour numériser une pièce en 3D, et enfin estimation des incertitudes d'étalonnage ; (2) développement du scanner 3D traçable combinant les caméras industrielles, le projecteur de lumière structurée, le robot industriel et les capteurs de tracking (télémètres) ; (3)

développement, conception et fabrication d'un étalon matériel avec une géométrie similaire aux pièces utilisées dans l'aéronautique. L'étalon est raccordé à la définition SI du mètre par l'intermédiaire de mesures sur une MMT traçable ; (4) sélection et adaptation d'un algorithme pour le traitement et la fusion des données en exploitant des paramètres intrinsèques à la surface, telle que la variation de forme et/ou des données issues des capteurs de tracking.

2. Etat de l'art : Numérisation 3D & étalonnage des capteurs d'imagerie

2.1. Utilité des systèmes de mesure sans contact

Les systèmes de numérisation 3D sans contact sont largement adoptés dans l'industrie. Plus spécifiquement, il s'agit de la numérisation 3D des objets par le biais de l'imagerie qui est appelé "photogrammétrie". Les techniques de photogrammétrie font l'objet de plusieurs études de recherche en raison des avantages qu'elles offrent. Aujourd'hui, la photogrammétrie est employée dans divers domaines comme l'industrie militaire, l'aéronautique, l'automobile, l'horlogerie, le médical, etc. Les recherches dans ce domaine s'orientent principalement vers l'automatisation et l'optimisation des algorithmes de scanning 3D avec des méthodes de détection et de suivi (tracking) d'objets en utilisant une ou plusieurs caméras et projecteurs.

Il existe principalement deux catégories de techniques de photogrammétrie [BGBM13, EIBB95] : passive et active. Plusieurs systèmes dans chacune des catégories répondent aux exigences de la numérisation 3D [BBPP21, DHAN18, ReBF10, SZPY12]. Pour le contrôle qualité des pièces mécaniques les techniques actives sont majoritairement adoptées [BiJa04, PLMG20] car elles offrent le meilleur compromis entre l'exactitude, la vitesse de numérisation et la densité du nuage de points.

2.2. Avantages/inconvénients des méthodes existantes

Les techniques de numérisation 3D ont été proposées pour répondre à des enjeux et besoins spécifiques. Certaines techniques par exemple ont pour objectif le repérage dans l'espace, en temps réel, avec des applications directes dans le domaine de la robotique principalement [GhTZ00, InTI92].

Dans le cadre de mon projet de recherche, l'objectif est d'effectuer une reconstruction 3D en collectant un nuage de points dense et exact résultant de la numérisation d'une pièce de grand volume. Dans ce cas, les méthodes actives sont les plus appropriées car elles permettent la numérisation 3D quelle que soit la texture de l'objet. A titre d'exemple, la technique de triangulation laser est basée sur la projection d'un faisceau laser sur la surface, puis collecté par une caméra. Néanmoins, le principal inconvénient de cette technique réside dans le temps de scanning.

Comme le temps de scanning représente un critère fondamental, la technique de lumière structurée (SL – structured light) constitue une solution appropriée en termes de vitesse de scanning, mais aussi en termes de robustesse, de densité du nuage de points et d'exactitude. La SL est une technique active dont le principe est basé sur la projection d'un motif bien connu sur la surface à mesurer. Les motifs projetés sont déformés selon la forme de l'objet, puis exploités pour récupérer des données 3D. L'exemple le plus simple est la projection d'une ligne (frange) sur une sphère, qui déformera la projection en raison de sa forme arrondie.

2.3. Lumière structurée

Le principe de la SL est similaire à celui de la triangulation laser. La seule différence réside dans l'utilisation d'un projecteur plutôt que d'une source laser. La numérisation 3D est basée sur le principe de triangulation, effectué entre chaque pixel du projecteur (u_p, v_p) et sa projection (u_c, v_c) sur le plan image.

Le processus d'identification des pixels projetés sur le capteur d'image est appelé stratégie de codification [SaPB04]. Une classification des systèmes de scanning 3D en fonction du nombre et de la séquence de prises (multi-shots pour des prises multiples d'images / single-shot pour une prise unique d'image) a été proposée par Geng [Geng11] :

- (1) **Technique multi-shot** : elle est basée sur la projection de motifs différents lors de la prise d'images. Cette technique est utilisée pour numériser des objets statiques et permet d'obtenir des résultats plus exacts que ceux obtenus avec la technique single-shot [Geng11].
- (2) **Technique single-shot** : elle est basée sur la projection d'un seul type de motif. Cette technique est principalement utilisée pour le scan d'objets en dynamique et en temps réel avec une exactitude moindre [TTAM18].

En métrologie dimensionnelle, l'étalon est souvent fixe par rapport au scanner. Par conséquent, les techniques multi-shots sont sélectionnées afin d'atteindre une meilleure exactitude. D'après [ZDKS17], les techniques multi-shots peuvent être catégorisées en *spatiale* et *temporelle*. La projection par décalage de phase est une technique temporelle proposée pour numériser des objets 3D en temps-réel sans compromettre l'exactitude. Cependant, la performance de celle-ci est dégradée lorsque la surface scannée présente des formes complexes et/ou des angles droits. D'autre part, le code Gray est une méthode spatiale qui repose sur l'analyse du voisinage des pixels pour fournir une estimation 3D des coordonnées des points. Celle-ci n'est pas optimisée pour la numérisation en temps réel, mais principalement choisie pour numériser des formes complexes [QCVG06].

Pour le codage de motifs binaires, le choix du code Gray est lié à sa robustesse au bruit et aux interférences entre pixels voisins [Matt18]. Le code Gray [IYDT07] [KiRL08] utilise deux valeurs d'intensité : le noir (intensité 0) et le blanc (intensité 1) pour former une séquence de motifs de projection, de sorte que chaque point de la surface de l'objet possède un code unique. En général, n motifs peuvent coder 2^n franges. Le choix du code Gray est motivé par sa capacité à scanner des objets avec des formes complexes [XuAl09].

2.4. Etalonnage des capteurs d'imagerie

Dans le domaine de vision par ordinateur, l'utilisation d'un système d'imagerie est étroitement liée à l'étalonnage géométrique. Il s'agit d'un processus d'estimation des paramètres de la caméra qui sont utiles pour générer une image correcte de la scène [HaZi04]. Ces paramètres sont classés en deux catégories : (1) les paramètres intrinsèques qui décrivent la géométrie interne de la caméra, tels que la distance focale f_u, f_v , les coordonnées du pixel du point principal (c_u, c_v) et les coefficients de distorsion de l'objectif k_0, k_1 , (2) les paramètres extrinsèques qui définissent la position et l'orientation de la caméra par rapport au système de coordonnées de la pièce [Burg16].

Deux méthodologies d'étalonnage co-existent : (I) l'auto-étalonnage est pratiqué quand les applications nécessitent un grand champ de vue. Cela ne nécessite pas l'utilisation d'une cible physique. L'exactitude de l'auto-étalonnage est relativement médiocre comparée aux méthodes utilisant des cibles [Tsai87a, Zhan00a] ; (II) une deuxième méthodologie proposée par Zhang, reposant sur le modèle du sténopé, est la méthode la plus couramment utilisée pour étalonner les caméras en raison de sa flexibilité et de sa justesse [FCWC08, LWYC19, RiSa07]. La méthode originale de Zhang, basée sur l'observation d'une grille d'étalonnage 2D, comprend six étapes : (1) acquisition de plusieurs images sur la grille 2D sous plusieurs poses, (2) détection des points caractéristiques [Jian12, SáMS18a], (3) estimation de l'homographie à l'aide de la Transformée Linéaire Directe [Dubr09], (4) identification des paramètres du sténopé à l'aide de la décomposition en valeurs singulières [KILa80], (5) raffinement global [Mitt00], et enfin (6) calcul de l'erreur de reprojection. Ces six étapes sont classées en trois principales phases : (A) prétraitement, (B) étalonnage et (C) vérification.

Initialement, Zhang a proposé cette méthode pour étalonner les systèmes à camera unique pour les applications de balayage 3D à courte portée. La méthode a par la suite été adaptée aux systèmes stéréos passifs [HaSt97] puis aux systèmes à base de lumière structurée [HOTL18], ce qui représente la base de ce travail de recherche. Le défi consiste à identifier ce que voit le projecteur, puisque ce dernier ne peut pas réellement observer la scène. Pour identifier ce que voit le projecteur, les correspondances entre les pixels du projecteur et la grille d'étalonnage sont établies par une stratégie d'étalonnage qui implique la projection d'un motif connu [MaKL11]. Cette procédure est connue sous le nom de stratégie de codification.

De nombreuses stratégies ont été proposées dans la littérature. Certaines sont manuelles et nécessitent une adaptation de la grille d'étalonnage à la zone de projection, tandis que les autres sont automatisées. Un inconvénient majeur des méthodes manuelles réside dans leurs fortes incertitudes pour l'estimation des paramètres intrinsèques du projecteur, plus spécifiquement les coefficients de distorsions. En outre, le positionnement manuel est subjectif et conduit souvent à une estimation inexacte. Les méthodes automatisées permettent une meilleure estimation des paramètres du projecteur et ne nécessitent pas obligatoirement une caméra pré-étalonnée [JoGr10, LiZh14, LSWW08, LuSo12]. Ces méthodes s'appuient sur la même projection utilisée pour effectuer une numérisation 3D. Au lieu de positionner manuellement les grilles d'étalonnage, un ensemble de motifs est projeté en l'observant à plusieurs poses et en récupérant la correspondance entre les pixels du projecteur et la grille d'étalonnage. Une méthode d'étalonnage populaire est celle basée sur le code Gray permettant d'identifier un code binaire à chaque pixel du projecteur (Figure II.131).

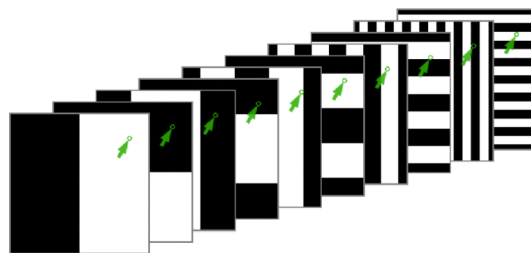


Figure 1 Exemple de code Gray. Le point vert est représenté par $[1000111101]$ [JoGr10]

Tout d'abord, une projection uniforme est appliquée pour acquérir l'image utilisée pour étalonner la caméra. Ensuite, les motifs sont successivement projetés en plusieurs niveaux, où chaque niveau est associé à une fréquence unique de code Gray. Le nombre total de motifs du code Gray p_d nécessaire pour coder N pixels dans une dimension d donnée est formulé par $p_d = \log_2(N)$.

Grâce à cette stratégie, les positions des points de la grille d'étalonnage peuvent être identifiées et, à l'aide du motif de code Gray, leurs emplacements dans les pixels du projecteur peuvent également être récupérés. Enfin, en utilisant la correspondance identifiée entre le projecteur et la grille d'étalonnage, la méthode de Zhang peut être appliquée pour estimer les paramètres de projection et ses coefficients de distorsion.

2.5. Conception du scanner 3D

Un scanner 3D constitué de deux caméras industrielles et d'un projecteur de lumière structurée a été conçu (Figure 2). Les caméras sélectionnées sont des Ximea MQ013rg-e2 (Figure 2-a), de résolution 1280×1024 pixels, équipées d'un objectif numérique de type *LM8JCM V* avec une focale de 8 mm. Le projecteur est un DLP Lightcrafter 4500 (b) de résolution native 912×1140 pixels. Les distances entre les différents éléments (caméras et projecteur) sont choisies de façon à obtenir un système compact regroupé en une pièce (c) pouvant être équipée sur l'effecteur d'un robot industriel.

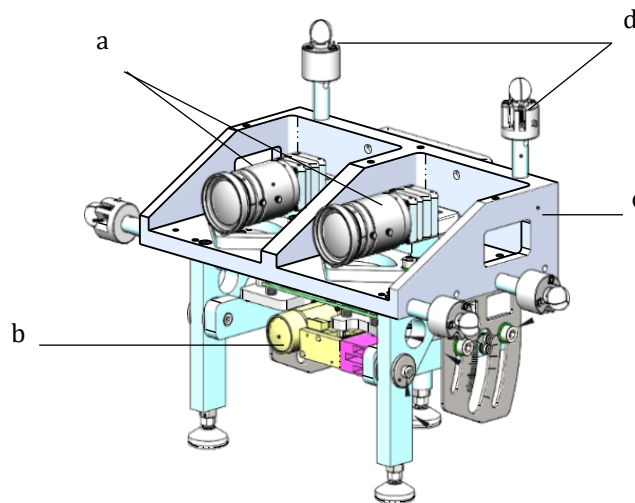


Figure 2 CAO du scanner 3D développé

Le robot industriel utilisé est un Kawasaki RS003N, dont l'espace opérationnel est de $967 \times 620 \times 620$ mm³. De plus, nous avons rajouté un 7^{ème} axe de déplacement afin d'effectuer des translations pour augmenter le volume de travail du robot dans l'optique de scanner des pièces avec un volume allant jusqu'à $2000 \times 600 \times 100$ mm³. Des sphères optiques peuvent être fixées sur la structure du scanner 3D pour pouvoir le suivre dans l'espace de mesure grâce aux 4 télémètres. Cela permet d'améliorer la connaissance du positionnement de l'effecteur dans l'espace de mesure (la répétabilité du Kawasaki est de 0,02 mm et l'incertitude sur la position et l'orientation de l'effecteur est de 2 mm [DaGD04, PłPi18b]).

Les télémètres laser appliquent le principe de la technique de temps de vol (ToF – Time of Flight) [HaDu14]. La distance est déterminée en mesurant la phase accumulée par une onde de radiofréquence qui se propage dans l'air à travers un faisceau laser. Cette propagation dans l'espace libre s'effectue au moyen d'un faisceau optique et se réfléchit ensuite sur une cible avant d'être convertie en signal électrique par un photodétecteur. Ainsi, la position et l'orientation des cibles dans l'espace des télémètres sont déterminées grâce au principe de multilatération [GuTW20a]. Les télémètres laser présentent une incertitude de $4,3 \mu\text{m}$ pour une distance de 7 m (figure 3).

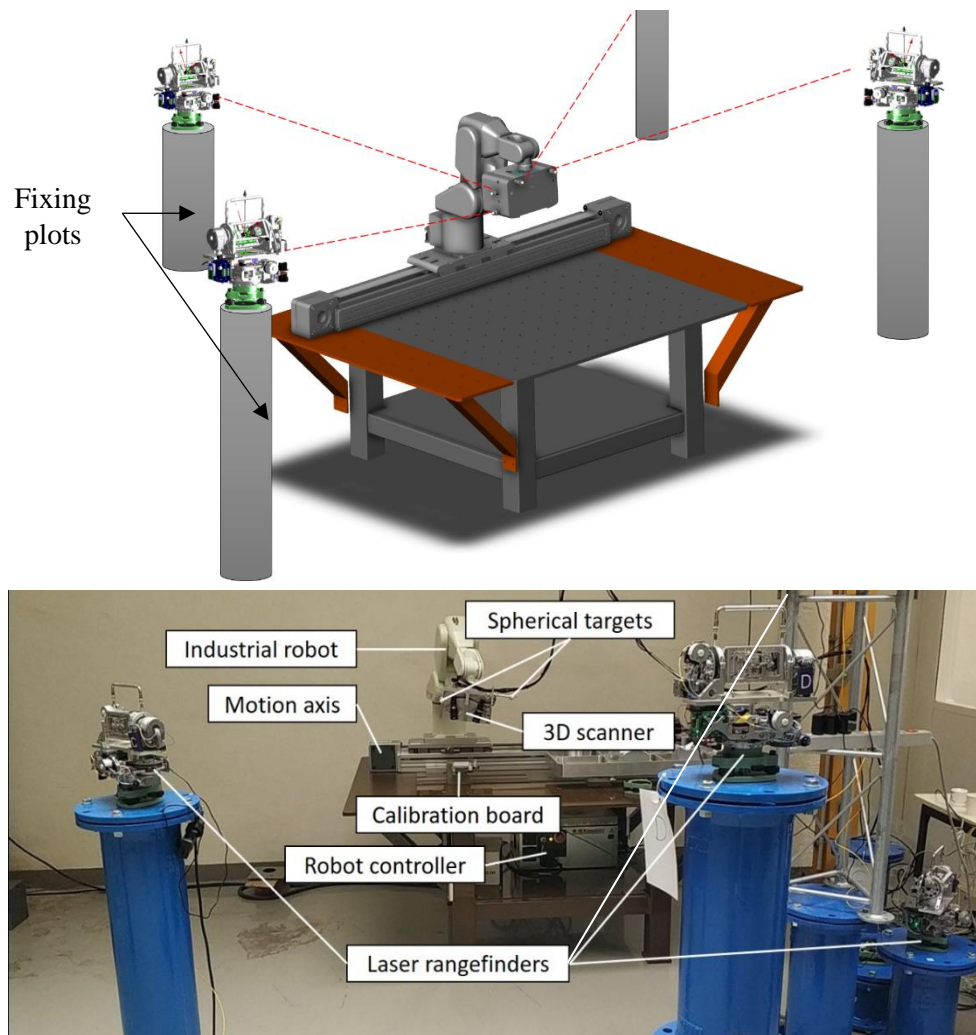


Figure 3 *Vue générale du système de mesure 3D*

3. Une nouvelle méthode d'optimisation de l'étalonnage

3.1. Vue d'ensemble sur les méthodes d'optimisation

De nombreuses études ont été proposées dans la littérature pour améliorer et automatiser le processus d'étalonnage [DKKP08], en particulier la méthode de Zhang, y compris l'optimisation de la détection des points caractéristiques [GhVN20, HEBA17, LWWP17] et l'optimisation du positionnement [GAPK19]. Rojtberg [RoKu18] a proposé une méthode d'optimisation [RoKu18] basée sur la sélection de poses, suite à une étude de l'influence du

nombre de poses de la grille d'étalonnage dans le champ de vue de la caméra. Il a aussi établi une corrélation entre les poses sélectionnées et l'incertitude d'étalonnage.

Peng et Strum [PeSt19] ont proposé une méthode d'étalonnage interactive, permettant de guider l'utilisateur dans le positionnement du motif appelée « Calibration Wizard » (CW). L'initialisation de cette méthode est basée sur une sélection de trois vues aléatoires. Une actualisation des vues est réalisée à chaque itération. Le calcul de la Jacobienne de l'erreur de reprojection lui permet d'identifier la nouvelle pose optimale à atteindre. Cette technique CW permet une meilleure estimation des paramètres intrinsèques de la caméra et donne des résultats plus exacts surtout dans des environnements non contrôlés. Néanmoins, l'inconvénient principal est le temps de traitement relativement élevé. De plus, les résultats obtenus par la technique CW dépendent de l'étape d'initialisation à 3 poses/images aléatoires, ce qui influence l'incertitude associée aux paramètres intrinsèques.

3.2. Principe de la nouvelle méthode d'étalonnage d'une camera

L'approche proposée est basée sur l'apprentissage automatique (ML – machine learning) des poses caméra par rapport à la grille d'étalonnage afin de minimiser l'erreur de reprojection. La Figure III.14 illustre l'évolution de l'erreur de reprojection en fonction de deux paramètres extrinsèques. Celle-ci peut être approchée par une fonction polynomiale.

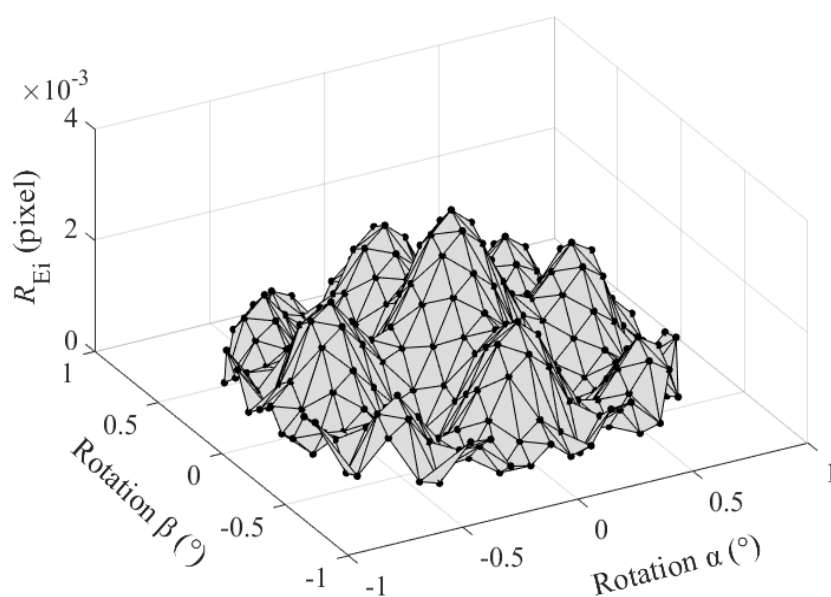


Figure 4 Evolution de l'erreur de reprojection R_{E_i} en fonction des orientations α et β

La relation entre le vecteur des paramètres extrinsèques $W_i = [\alpha_i, \beta_i, \gamma_i, t_{X_i}, t_{Y_i}, t_{Z_i}]$ et l'erreur de reprojection peut être modélisée par une régression polynomiale. Pour estimer les coefficients du polynôme, un grand nombre d'images de la grille d'étalonnage est collecté pour différentes poses. Ensuite, la méthode Zhang est appliquée tout en identifiant les vecteurs des paramètres extrinsèques W_i et les erreurs de reprojection associées R_{E_i} pour construire la base d'apprentissage de l'algorithme ML (Figure III.13). D'après Lu [Lu10], la base de données d'apprentissage est divisée en deux ensembles de données : 70 % des images sont utilisées comme ensemble d'entraînement, tandis que les 30 % restants constituent l'ensemble de test.

Cette étape est appelée découpage stratifié apprentissage/test (data split train/test). Il s'agit d'une technique utilisée dans les problèmes de régression et de classification afin d'évaluer les performances de l'algorithme. Comme la base d'apprentissage contient un nombre limité d'entrées et de sorties, l'application d'une seule stratégie de division stratifiée n'est pas appropriée pour obtenir une estimation exacte de la performance de l'algorithme. Dans ce contexte, Xu [XuGo18] souligne l'avantage de multiplier les ensembles d'entraînement et de test plutôt que d'utiliser une seule division. Par conséquent, la fiabilité du partitionnement stratifié apprentissage/test a été renforcée en adoptant la méthode de validation croisée décrite dans [Berr18]. Elle permet d'optimiser le degré D de la régression polynomiale entre $1 \leq D \leq 13$. Le critère sélectionné est l'erreur absolue moyenne (MAE). Selon la Figure III.35, les courbes d'entraînement et de test diminuent lorsque D augmente jusqu'à la valeur 10, puis la MAE test remonte à nouveau. Ceci est dû au sur-apprentissage (overfitting) [Ragh21] défini comme le modèle polynomial décrivant le bruit des données plutôt que le modèle sous-jacent.

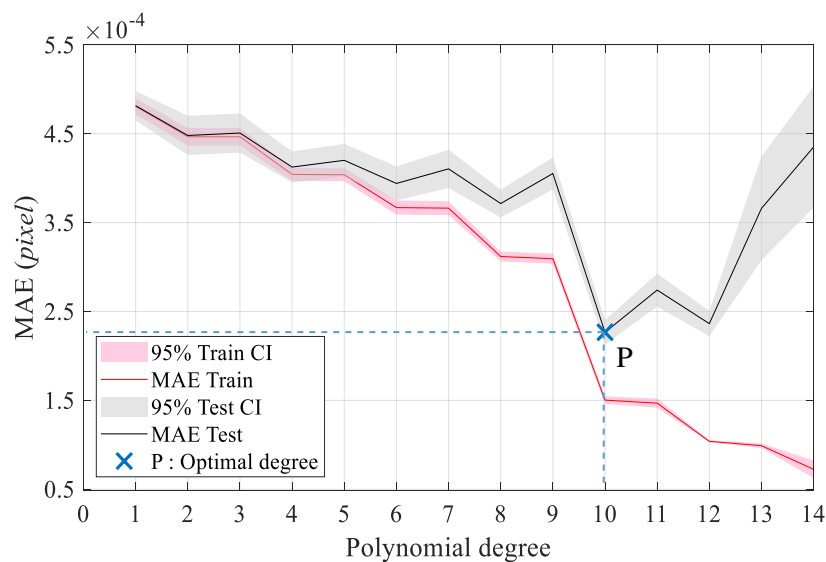


Figure 5 Évolution de MAE suivant le degré polynomial avec la validation croisée

Une fois le polynôme estimé, les poses optimales associées aux erreurs de reprojctions minimales sont extraites. La recherche des minimums requiert des contraintes linéaires et non linéaires, identifiées à partir de l'étude analytique proposée par Rojtberg [RoKu18]. D'après [CoHa03, YiAM20], l'optimisation par essaims de particules (PSO – Particle Swarm Optimization) représente une méthode appropriée pour ce problème d'optimisation. Elle vise à minimiser une fonction en effectuant une recherche de population dans un espace de recherche à D dimensions [Tamb19]. L'essaim est composé de plusieurs particules, et chaque particule est caractérisée par sa position dans le polynôme et par sa vitesse.

Pour résumer, 3 étapes peuvent être distinguées pour cette méthode : (1) l'étape d'acquisition où un ensemble d'images de la grille d'étalonnage est sélectionné pour construire la base d'apprentissage, (2) l'approche ML est appliquée pour extraire les données nécessaires pour effectuer la régression polynomiale. Cela inclut les erreurs de reprojction R_{E_i} et les paramètres extrinsèques associés, (3) l'application de la régression polynomiale sur ces données, combinée à l'optimisation PSO pour extraire les poses optimales associées.

3.3. Adaptation de la méthode d'optimisation aux systèmes stéréo actifs

D'après les simulations, l'approche ML semble être appropriée pour l'étalonnage d'une caméra. Cette méthode a été étendue pour le cas d'un scanner SL. En plus des paramètres intrinsèques, l'étalonnage stéréo inclut la transformation rigide entre la caméra et le projecteur. Rappelons qu'un scanner SL est basé sur la projection d'un motif pour établir la correspondance entre les pixels du projecteur et la grille d'étalonnage. La Figure III.56 illustre le processus d'étalonnage d'un système stéréo actif pour une pose donnée, où $[R_1 T_1]$ est la transformation du projecteur vers la grille d'étalonnage appelée matrice extrinsèque du projecteur et $[R_2 T_2]$ est la matrice extrinsèque de la caméra. Pour chaque pose de la grille d'étalonnage, une erreur de reprojection peut être associée à chaque élément du scanner.

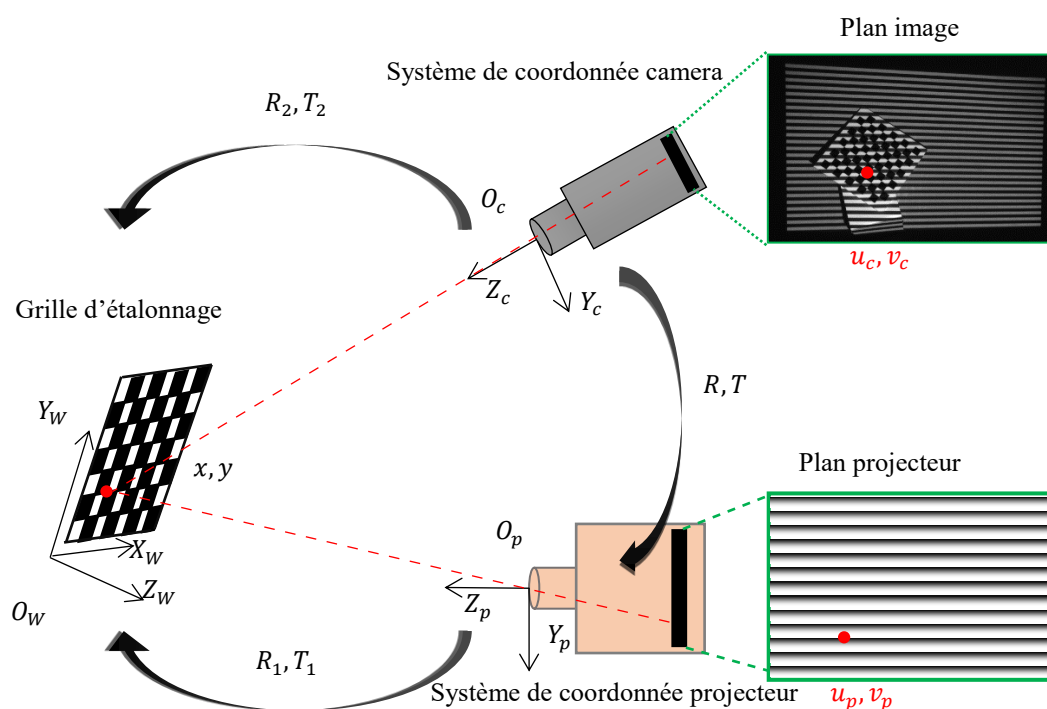


Figure 6 Illustration de l'étalonnage d'un système SL

N poses de la grille d'étalonnage sont adoptées et des images sont prises à l'aide du scanner 3D. Pour chaque pose, le code Gray est projeté et des images sont prises à l'aide de la caméra. Au moins 1000 poses sont adoptées puis la méthode de Zhang est appliquée pour extraire les paramètres extrinsèques et les erreurs de reprojection. Une fois l'ensemble de données créé, la régression polynomiale est appliquée pour estimer la fonction polynomiale qui modélise la relation entre les paramètres extrinsèques et les erreurs de reprojection.

Afin d'optimiser les poses du scanner SL, ce dernier est modélisé par une combinaison linéaire pondérée de deux polynômes $\widehat{R}_E^C(W_i)$ (polynôme caméra) et $\widehat{R}_E^P(W_i)$ (polynôme projecteur). Les poids w_i sélectionnés sont des entiers positifs tels que : $\sum_{i=0}^k w_i = 1, w_i \in [0,1]$. Etant donné que l'erreur de reprojection du projecteur est plus grande que celle de la caméra [WiOL14] (la caméra est un élément à part entière de la chaîne d'étalonnage du projecteur), les

pois sont répartis selon l'inégalité suivante : $w_{proj} > w_{cam}$. Par la suite, le PSO est appliqué pour extraire les poses associées aux minimums du polynôme.

4. Stratégie de recalage et évaluation des performances du scanner SL

4.1. Fabrication d'un étalon de mesure

Un étalon constitué par une pièce principale de grand volume a été conçu en s'inspirant des pièces utilisées dans l'aéronautique. Il s'agit d'une pièce en aluminium dont les dimensions sont $L = 1000$ mm, $l = 400$ mm, $H = 60$ mm et contenant des poches et des nervures. L'étalon principal peut être associé à 8 étalons secondaires, tels que le parabolöide et l'hyperboloïde. Il est conçu pour tester les performances du scanner SL sur diverses formes (Figure IV.37).

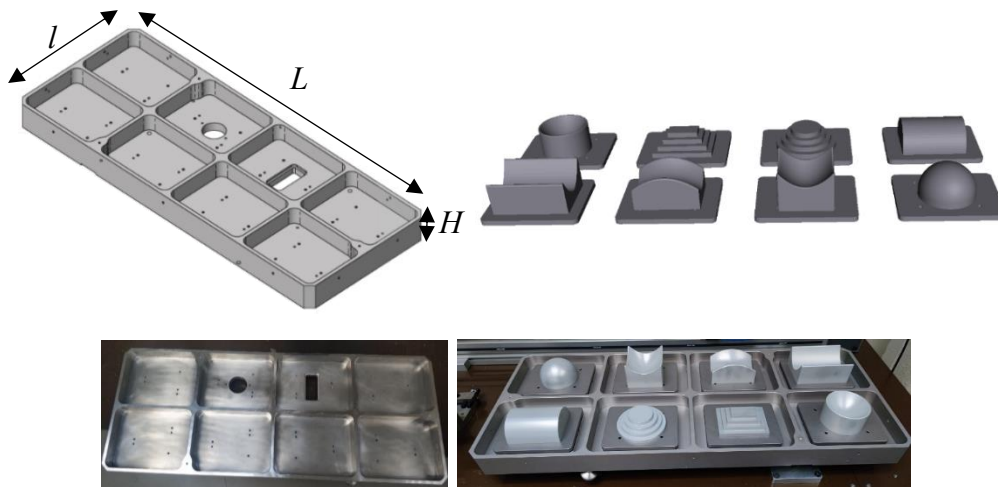


Figure 7 CAO de la pièce grand volume de forme complexe

4.2. Evaluation des performances du scanner

L'évaluation du scanner s'effectue en deux étapes : (i) **single shot** : le scanner est fixé par rapport à la pièce et seule la zone visible est numérisée. Ensuite, les écarts de forme sont calculés et la répétabilité est évaluée [Feng00, PrPo10] ; (ii) **multi shots** : le scanner balaye toute la surface de l'étalon. L'alignement des nuages de points enregistrés est étudié à l'aide de deux méthodes de recalage : (a) le recalage par paires où un maximum de deux nuages de points sont alignés et (b) le recalage par groupe qui implique plus de trois nuages de points. La métrique utilisée lors de l'analyse de l'ensemble des données scannées est le résidu entre les points scannés et le modèle CAO, ce qui permet de calculer les paramètres suivants : RMSE (Root mean square error) [URKG19], MAE (Mean absolute error) [BABB18] and PV (Peak to valley) [GoSe17].

4.2.1. Evaluation par single shot

La position et l'orientation du scanner sont fixés dans l'espace de mesure de telle sorte qu'une surface de 150×120 mm² est scannée. Le nuage de points de chaque surface scannée est généré par la projection d'un code Gray de 10 bits horizontalement et verticalement. La triangulation est réalisée en utilisant les paramètres résultant de la méthode Zhang optimisée. Les résidus obtenus sont estimés à 89 μ m, 142 μ m et 116 μ m pour les surfaces scannées (planéité, cylindricité et sphéricité). Afin d'évaluer la répétabilité du scanner SL, un test supplémentaire a été réalisé. Plusieurs nuages de points sont enregistrés pour chacune des pièces sélectionnées

puis un « fitting » par moindres carrés est appliqué à nouveau. Les répétabilités sont estimées à 2 µm, 5 µm et 8 µm respectivement pour la planéité, la cylindricité et la sphéricité.

4.2.2. Evaluation par multi-shots

La présence d'occlusions représente une limitation d'utilisation du scanner SL. Ainsi, les nuages de points doivent être générés le long de la surface scannée en numérisant partiellement plusieurs zones et en les fusionnant dans un système de coordonnées unique. Chaque scan génère un nuage de points dans le système de coordonnées de la caméra. En connaissant les positions et orientations du scanner, les nuages de points peuvent être transformés dans un système de coordonnées en identifiant les transformations relatives [Brow92].

Le recalage des nuages de points est nécessaire dans de nombreuses applications de vision industrielle, telles que la cartographie 3D et la reconstruction 3D d'objets. On distingue deux types de recalage : le recalage grossier et le recalage fin [RNAS15, Zhu19]. Le recalage grossier consiste à trouver la transformation initiale entre les nuages de points, sans nécessairement imposer des tolérances élevées pour les rotations et les translations (généralement quelques degrés pour les rotations et quelques millimètres pour les translations). Le recalage fin est appliqué afin d'obtenir un alignement 3D exact des données.

Selon la littérature, un nombre élevé de méthodes de recalage est proposé, toutes peuvent être classées en deux catégories: recalage basé sur le suivi d'un marqueur (tracking) et recalage basé sur l'exploitation d'éléments intrinsèques de la surface (features) [Bosc12]. Cette dernière est priorisée en raison de son exactitude, sa robustesse et son automatisation. Trois méthodes de recalage grossier ont été investiguées : ICP [DXWH17, LHZA22, YLCJ16, ZhYD21], CPD [MySo10] et NDT [BiSt03], puis comparées afin de sélectionner le meilleur algorithme en terme de performance. L'ICP semble être le meilleur en termes de temps de calcul et d'erreurs de recalage. Par ailleurs, l'ICP est un algorithme de recalage dit « pairwise » (ne permet de recaler que deux nuages de points). La succession de plusieurs recalages ICP peut propager des erreurs systématiques entre la première et la dernière mesure [EKHP14, EvHo18]. Afin de diminuer cette erreur, les algorithmes de recalage dit « groupwise » peuvent être utilisés. Choi [ChZK15] a proposé une méthode de pose de graphe “graph pose optimization” robuste qui ne repose pas sur le recalage pairwise, mais utilise plutôt l'optimisation “line process” [BIRa96].

Pour le recalage fin, l'ICP a été sélectionné pour le pairwise afin de recaler des scans 3D successifs avec une zone de chevauchement, suivi d'une optimisation pose de graphe. Ainsi, le nuage de points obtenu peut être recalé à la CAO pour analyser les résidus (Figure IV.207).

La traçabilité de la pièce étalon a été assurée par une MMT Zeiss UPMC carat traçable dont l'incertitude est estimée suivant l'expression « $0.7 + \frac{L}{1200} \mu\text{m}$ », où L est la longueur maximale de la pièce à mesurer. La résolution spatiale de la MMT est de 100 nm et le volume de mesure est de 1200×850×600 mm. La mesure de chaque pièce mécanique a été effectuée à l'intérieur de la salle blanche du LNE où la température est contrôlée à $20^{\pm 0.1} \text{ °C}$ et l'hygrométrie à 50%^{±5}. La comparaison de la mesure MMT, considérée comme la mesure de référence, et le scanner SL permet d'obtenir une information sur la performance du scanner SL.

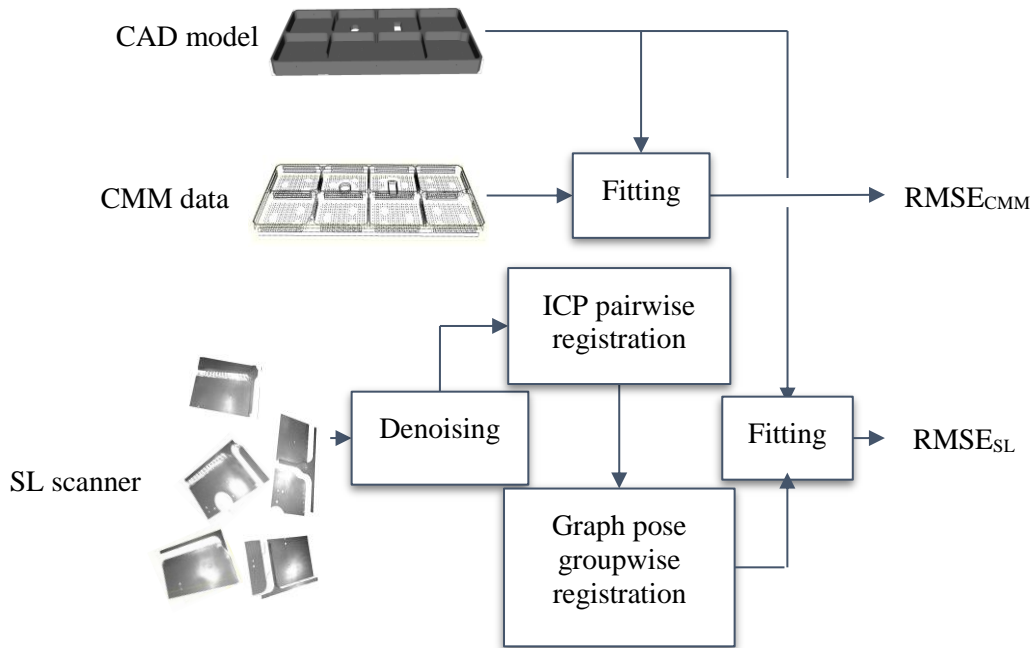


Figure 7 Organigramme stratégique de recalage proposée

4.2.3. Evaluation par simulation

Pour réaliser une simulation de la mesure par scanner, un nuage de points est construit à partir du modèle CAO. Les points sont échantillonnés le long du modèle CAO avec le pas correspondant à la résolution du scanner. Seules les zones accessibles de la pièce sont considérées dans la simulation (par exemple le dessous de la pièce ne sera pas traité).

La Figure IV.238 montre les valeurs obtenues pour les métriques RMSE, MAE et PV et les incertitudes associées. Pour obtenir les incertitudes avec un intervalle de confiance de 95 %, le processus a été répété 10 fois. Le résultat de la simulation montre une valeur négligeable de $RMSE_0$ (environ 3×10^{-12} mm) par rapport aux autres métriques $RMSE_{NT}$ et $RMSE_N$, respectivement estimées à 166 μm et 97 μm , où $RMSE_0$ est l'erreur numérique obtenue en appliquant un recalage entre la CAO et le nuage de points extrait de la CAO ; $RMSE_N$ est l'erreur de recalage entre la CAO et les nuages de points bruités ; enfin, $RMSE_{NT}$ est l'erreur entre la CAO et les nuages de points bruités et transformés.

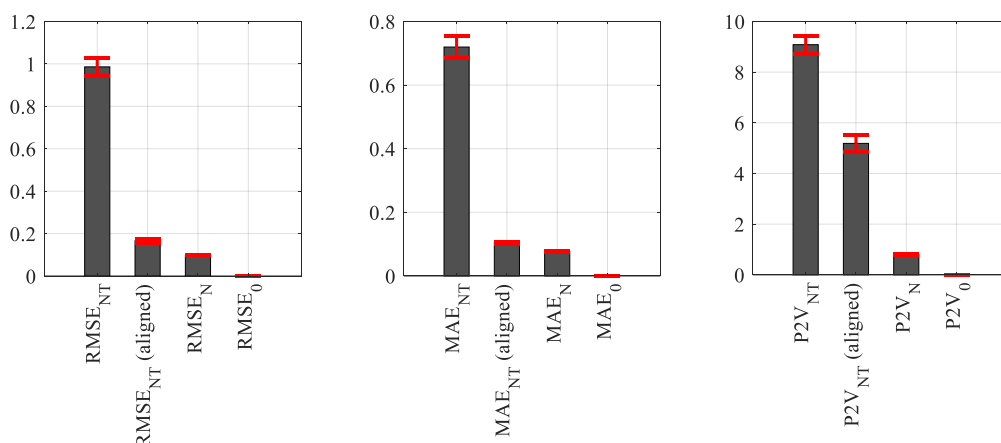


Figure 8 RMSE, MAE et PV obtenues (en mm) pour la simulation et leurs incertitudes

4.2.4. Evaluation expérimentale

Tout d'abord, les surfaces élémentaires de l'étalon sont scannées à l'aide du scanner SL. Plusieurs poses de l'effecteur du robot sont définies pour couvrir toute la surface, tout en assurant un chevauchement d'environ 60% entre les scans 3D successifs. Au total, 45 poses de l'effecteur du robot ont été définies, et à chaque pose, le nuage de points de la surface observée est reconstruit en 3D.

Pour effectuer le recalage grossier, les coordonnées de l'effecteur sont récupérées et utilisées pour passer du repère caméra (repère mobile dans lequel les nuages de points sont initialement enregistrés) au repère associé au robot (repère fixe correspondant à la base du robot). Cette stratégie est répétée autant de fois que le nombre de scans. Enfin, un ré-échantillonnage est utilisé pour obtenir une répartition uniforme de points, puisque les zones de chevauchement entre les acquisitions successives contiennent un plus grand nombre de points. La Figure IV.259 montre le résultat du recalage des nuages de points à l'aide de la stratégie proposée, où chaque couleur définit une reconstruction 3D unique à une pose spécifique.

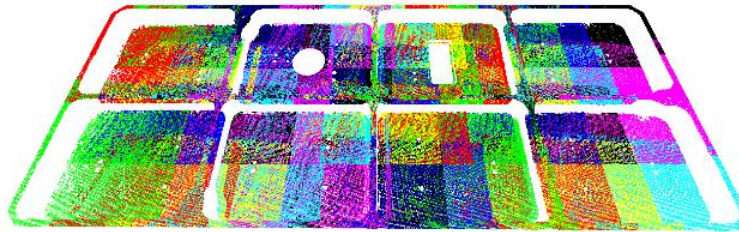


Figure 9 Reconstruction 3D de la pièce de grand volume

La RMSE converge à environ 0,05 mm après moins de 10 itérations pour l'étape de recalage avec ICP. Cependant, les minimums locaux limitent la convergence de l'ICP. Cela pourrait s'expliquer par une surestimation des distances point à point, car l'ICP adapterait le bruit plutôt que le modèle sous-jacent. Un recalage des mesures tactiles de la MMT Zeiss sur le modèle CAO est également effectué, ce qui permet d'évaluer le défaut de forme de l'étalon.

La MMT Zeiss tactile fournit 5×10^3 points alors que la densité de la SL est d'environ 3×10^6 points. En outre, l'erreur de recalage de la mesure par scanner SL est plus élevée que celle de la MMT. La valeur RMSE calculée sur les données mesurées par la MMT est égale à 65,92 μm alors que la RMSE est égale à 165,94 μm pour le scanner SL (Table IV.11 au 1). Pour le scanner SL, les erreurs sont principalement regroupées sur les bords du plan supérieur où la réflectivité est trop élevée, ce qui limite l'exactitude de la triangulation. Cependant, la distribution sur les nuages de points est globalement uniforme.

Tableau 1 Comparaison entre la MMT et SL

	RMSE (μm)	MAE (μm)	PV (mm)
MMT	65,92	56,08	0,29
SL	165,94	120,03	3,47

La différence d'exactitude entre les mesures MMT et le scanner SL est évidente. Cela était attendu car la MMT a une meilleure exactitude malgré la faible densité de points et le temps de mesure plus élevé. Cependant, pour le contrôle de qualité de pièces de grand volume, les scanners SL représentent le meilleur choix en raison du temps de mesure (quasiment en temps réel) et de la densité des données.

5. Conclusion

Les pièces de grand volume constituent un défi quant à leurs fabrications, assemblages et mesures. L'objectif de cette thèse est de contribuer au développement d'un système de scanning 3D permettant de contrôler la qualité des pièces mécaniques de grand volume et de formes complexes. Pour cela, les systèmes de numérisation 3D optiques ont été étudiés dans un premier temps afin de concevoir un scanner permettant de répondre aux besoins industriels en termes d'optimisation du cycle de fabrication. Plusieurs méthodes sont proposées dans la littérature, chacune répond à un besoin spécifique. Pour le contrôle-qualité des pièces, la méthode la plus appropriée est la lumière structurée car elle offre le meilleur compromis entre le temps de scan, l'exactitude et la densité de la numérisation. La lumière structurée est une technique active qui utilise le principe de triangulation entre une caméra et un projecteur. Un scanner 3D, basé sur le principe de la lumière structurée, a été conçu, développé, assemblé et étalonné afin de maîtriser la chaîne de traçabilité.

Pour effectuer la triangulation, un certain nombre de paramètres sont requis : les paramètres internes des caméras et du projecteur utilisé ainsi que la transformation rigide entre ces composants. L'identification de ces paramètres est appelée étalonnage. Différentes techniques ont été étudiées et proposées ; toutefois, la méthode de Zhang a été sélectionnée en raison de l'exactitude de cette méthode par rapport aux autres méthodes. La méthode de Zhang exploite une surface plane en 2D sur laquelle est imprimé un motif facilement détectable (appelé grille d'étalonnage). Elle comprend 5 étapes : acquisition d'images, détection de points caractéristiques, estimation de l'homographie, identification des paramètres intrinsèques et extrinsèques, raffinement global. Une étape supplémentaire de vérification peut être ajoutée pour satisfaire un seuil d'erreur prédéfini. Cette méthode est robuste mais présente encore quelques faiblesses. Des méthodes d'optimisation ont été mises au point pour réduire certaines sources d'incertitude, comme l'utilisation d'un algorithme de détection de points caractéristiques plus robuste ou l'optimisation du raffinement global. Dans la littérature, le composant le plus influent est le positionnement de la caméra par rapport à la grille d'étalonnage. Dans ce contexte, nous avons proposé une nouvelle méthode d'optimisation basée sur la régression polynomiale suivie d'une optimisation non linéaire par PSO. Celle-ci fournit un ensemble de poses optimales à adopter afin d'améliorer l'estimation des paramètres internes et externes. La méthode a été évaluée synthétiquement et expérimentalement et montre de meilleures performances comparées aux autres méthodes récemment publiées.

Ensuite, un étalon de grand volume ainsi que des étalons secondaires ont été conçus afin d'évaluer le scanner SL après l'avoir étalonné avec la méthode proposée. Dans un premier temps, le scanner SL a été évalué pour une prise de mesure unique sur des paramètres de forme simple (planéité, sphéricité et cylindricité). Le test montre une répétabilité globale d'environ $6 \mu\text{m}$ et des erreurs de forme d'environ $90 \mu\text{m}$. Ce test a été réalisé en fixant la position et l'orientation du scanner dans l'espace de mesure. En pratique, les objets de grand volume

nécessitent plus qu'un seul scan. Nous avons donc proposé une stratégie de recalage adaptée au scanner SL afin d'aligner les nuages de points et d'avoir un scan global des pièces de grand volume. La stratégie est divisée en deux phases : (1) les coordonnées de l'effecteur du robot sont utilisées pour un alignement grossier, de sorte que tous les nuages de points sont exprimés dans un repère lié à la base du robot. Puis (2) un recalage fin est effectué avec l'ICP, suivi d'une optimisation de la pose. Le résultat du recalage proposé a été évalué à la fois synthétiquement et expérimentalement. L'évaluation synthétique est basée sur le modèle CAO de la pièce de grand volume, sur lequel des nuages de points ont été générés avec du bruit. La simulation montre une erreur de recalage de l'ordre de 166 μm , 107 μm et 5 mm respectivement pour la RMSE, MAE et PV. Pour la validation expérimentale, les erreurs sont similaires à celles obtenues avec la simulation. Les métriques respectives ont été évaluées à 165,94 μm , 120,03 μm et 3,47 mm.

Ce travail de thèse traite à la fois la partie mécanique, optique et métrologique du scanner SL ainsi que les algorithmes et traitements d'image et de nuage de points associés, pour obtenir un résultat de numérisation 3D global dense et exact.

Appendix A: Overview of camera-based 3D scanners

Passive and active photogrammetry

A.1. Passive 3D scanning

A.1.1. Photogrammetry

Photogrammetry is based on projective geometry. It allows the digitization of large objects such as buildings and warehouses (Figure A.1). The principle of photogrammetry is to take multiple images of the object and manually or automatically locate common points (called features) in each image. The points allow a 3D digital reconstruction of the object by a triangulation [Rodi06]. Photogrammetric systems are capable of reconstructing scenes, in which the objects studied have simple geometries. This technique is less efficient for the 3D digitization of complex surfaces [Goul99].



Figure A.1 3D reconstruction using drone photogrammetry [Dron00]

Photogrammetry have been used to scan large objects such as building. However, it requires the detection of features to reconstruct a scene. Therefore, photogrammetry is useless for objects with uniform colour distribution and flat scenes.

A.1.2. Passive stereo vision

Passive stereovision is based on the acquisition of two images of the same scene [Hawi11]. In this case, a point $M(X, Y, Z)$ can be observed on the two images (left and right) with two different coordinates. The difference between the two coordinates is then used to compute the

3D coordinates of point M by triangulation [Rodi06]. Consequently, one of the essential phases of this method is the search for the stereo-corresponding points, which can be simplified if the shooting systems are separated only by translations. The principle of passive stereovision is to imitate human perception to the stereo disparity, which is the difference between the locations of the points in both cameras. It is used for example in the automotive field for smart car guidance or depth perception.

A.1.3. Shape-from-X

The Shape-from-X method uses 2D features of the surface to reconstruct the 3D shape. There are several 3D scanning techniques based on this method: “shape from silhouettes” [ChBK04], “shape from motion” [Alis11], “shape from texture” [BlAh89], “shape from focus / defocus” [NaNa94].

A.2. Active 3D scanning

A.2.1. Time-of-flight

The time-of-flight (ToF) technique uses a laser rangefinder to measure the time required to complete a round trip of a reflected laser beam pulse. Knowing the speed of light C , the return time t determines the distance D traveled by the light by solving the equation $D = \frac{C \cdot t}{2}$.

The accuracy of 3D scanning depends on the accuracy of the return time measurement. This technique is fast, but it provides a highly noised 3D reconstructions, which requires a post-processing step as proposed by Cui *et al.* [CSCT10].

A.2.2. Laser triangulation

Laser triangulation is a technique based on the principle of telemetry. A light is projected on the object. Part of the light reflected by the object is focused on the imaging sensor through a lens of focal length f . The optical system is adjusted to locate the surface to be analysed in the middle of the measurement field (Figure A.2).

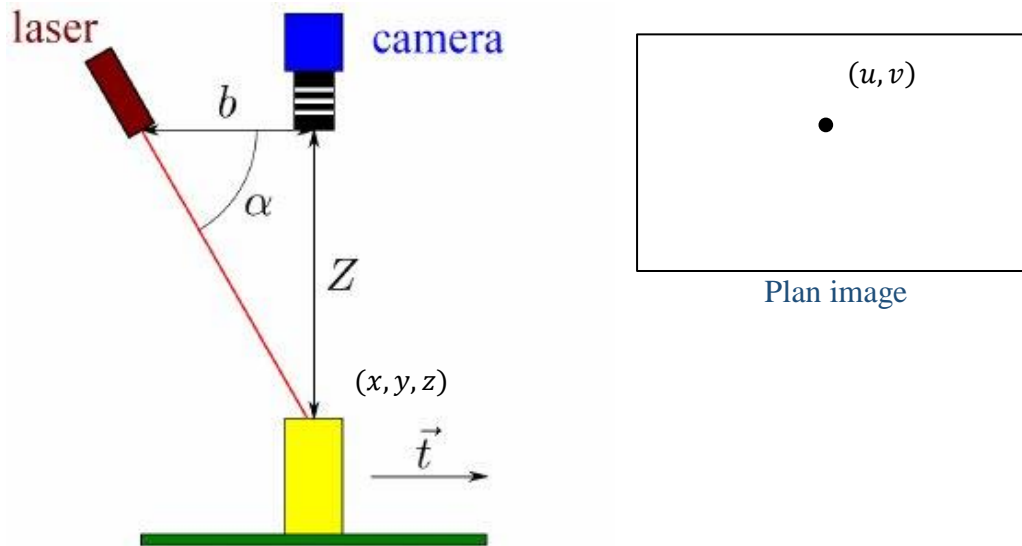


Figure A.2 Principal of laser triangulation [MSTM15]

The detector and the light source are separated by a distance b called baseline [MSTM15]. The projection of a point of coordinates (x, y, z) on the detector gives the point of coordinates (u, v) , according to the properties of geometric optics.

A.2.3. Structured lighting: Single-shot

Stripe indexing

Stripe indexing is a single shot 3D reconstruction based on the recognition of each projected stripe on the image plan by associating an index to the stripe, because the projected set of stripe does not necessarily correspond to the viewed ones. There are some encoding techniques based on stripe indexing that have been proposed in literature. Coloured stripe indexing proposed by Chen [CZLF07] consists of the analyse both the colour and the intensity of the projected fringes. The encoded pattern is composed in HSV colour space (Hue, Saturation, and Value). HSV is a model presented by [Smit78] such a non-linear transformation of RGB colour space from discrete values of colour to continuous. Not only is the colour considered but also the saturation and the brightness values. The objective of using HSV colour space is to provide enough colours on the projected pattern so they can be easily decoded later. To convert the RGB colour to HSV, Chen propose to separate the colour using the eq. A.1 [CZLF07].

$$H = \begin{cases} \frac{G - B}{\max(R, G, B) - \min(R, G, B)} \\ \frac{2 + (B - R)}{\max(R, G, B) - \min(R, G, B)} \\ \frac{4 + (G - B)}{\max(R, G, B) - \min(R, G, B)} \end{cases} \quad \text{A.1}$$

$$H = \begin{cases} H_t/6, & H_t > 0 \\ H_t/6 + 2, & H_t < 0 \end{cases} \quad S = \frac{(\max(R, G, B) - \min(R, G, B))}{\max(R, G, B)} \quad V = \max(R, G, B)$$

where R, G, B are red green and blue values in a range of $[0,1]$ and H, S, V are the hue, saturation, and brightness values also in range of $[0,1]$, $\max(R, G, B)$ and $\min(R, G, B)$ represent the maximum and minimum values in R, G and B channels, respectively, and H_t is a temporary variable in the algorithm. An example of the projected pattern is given in Figure A.3.



Figure A.3 Coloured stripe coding for 3D reconstruction using structured light systems

De Bruijn Sequences

De Bruijn sequences, used for one-shot 3D reconstruction, is based on colour stripe projection. The most effective way of encoding colour-based projections is by analysing the local neighbourhood of each pixels element. So the choice of colour combination must be well defined in order to have an accurate encoding strategy, such that the combinations of different colours is not repeated somewhere in the pattern. De Bruijn sequences are mathematical resources able to achieve this purpose.

To give an example of encoding strategy, let's consider a De Bruijn sequence of order m on an alphabet of n symbols. De Bruijn sequence is a string of n^m length that contains all m substrings of length m known as window properties. For a De Bruijn sequence with $n = 2$ (binary

De Bruijn sequence) and a window property of length $m = 4$, the form of De Bruijn equation is given in eq.A.2.

$$10000101111101001 \quad \text{A.2}$$

The De Bruijn sequences have been widely adopted of dynamic scene reconstruction. One of the first developed techniques based on this encoding was proposed by Zhang [ZhCS02]. Zhang proposed an 8 colours fringe pattern composed by 125 adjacent fringes. To generate the pattern, Zhang added a constraint such that two consecutive fringes in the De Bruijn sequence cannot have the same colour [HuMa89]. Figure A.4 shows the generated De Bruijn sequence and the result of its projection on a surface.

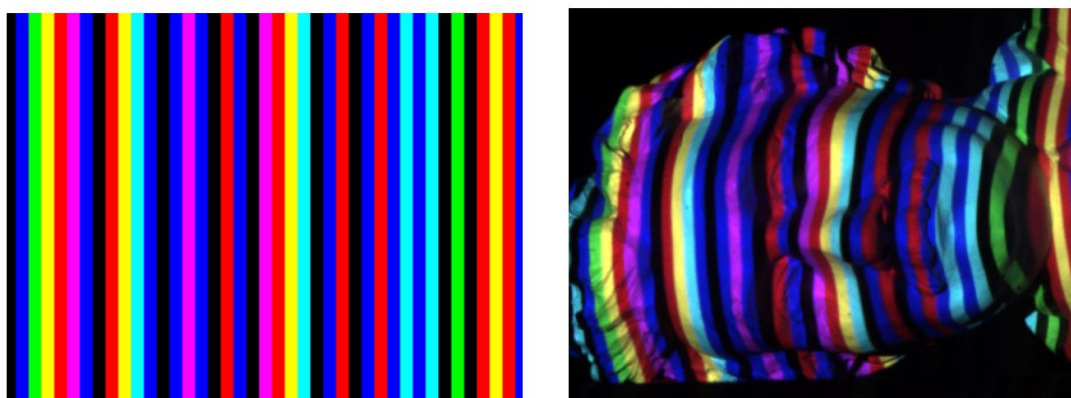


Figure A.4 Example of De Bruijn sequence projected on a freeform

A.2.4. Structured lighting: Multi-shot

Grid Indexing: 2D Spatial Grid Patterns

The principle of 2D grid pattern techniques is to provide a unique label for every sub window in the projected 2D pattern, such that the pattern in each area of the window is unique and can be easily identifiable with respect to its 2D position in the pattern. One grid indexing strategy consists of using pseudorandom binary array such that each part of the grid is marked by dots. The pseudorandom is defined by $n_1 \times n_2$ array encoded using pseudo random sequence. Figure shows the example of a pseudo-random grid.

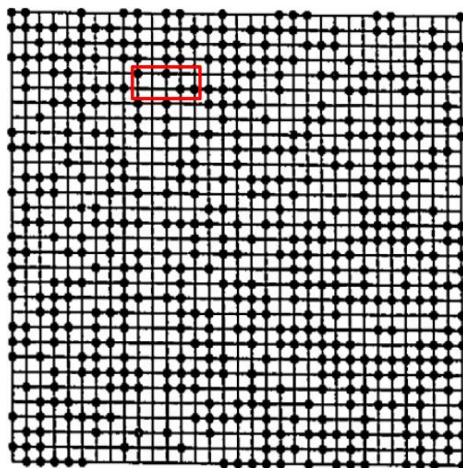


Figure A.5 Grid indexing codification strategy [Geng11]

Let's consider a sub window of $k_1 \times k_2$ size. It is noticeable that each position of the subwindow in the pseudo random grid is unique and fully defines the sub-window's absolute coordinate (i, j) [LeWS85, PaDe09]. To encode the pseudo-random array, the polynomial modulo 2^n method is used as described in the eq. A.3.

$$2^n - 1 = 2^{k_1 k_2} - 1 \quad n_1 = 2^{k_1} - 1, \quad n_2 = 2^n - \frac{1}{n_1} \quad \text{A.3}$$

Gray-code Patterns

Binary coding [IYDT07] uses two intensity values : black (intensity 0) and white (intensity 1) fringes to form a sequence of projection patterns, so that each point on the surface of the object has a unique binary code. In general, n patterns can encode 2^n bands. Figure A.6 shows an example of a simplified projection pattern of 4 bits. Once this pattern sequence is projected onto a static scene, there are 16 (2^4) unique areas encoded with unique bands. The 3D coordinates (X, Y, Z) can be calculated (based on a triangulation principle) for the 16 points along each horizontal line, forming a complete 3D image frame.

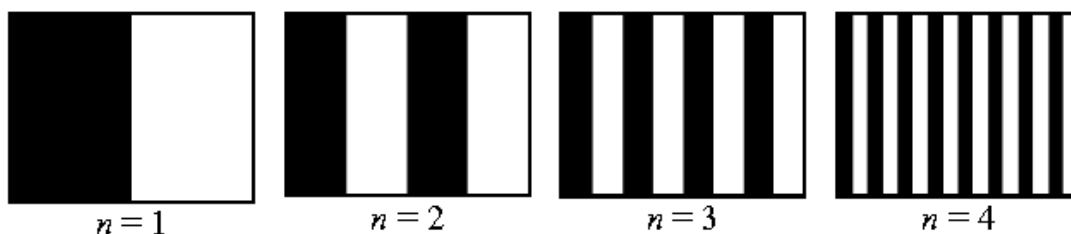


Figure A.6 Example of 4 bits binary coding [KiRL08]

Gray-Level Patterns

To reduce the number of patterns, Gray-level patterns are used. For example, it is possible to use M distinct levels of intensity, instead of two levels as applied in binary code (black and white), to produce a unique coding at each pixel. In this case, N patterns can encode M^N bands. Each fringe code can be visualized as a point in a N -dimensional space [CaKS98]. For example, for three $N = 3$ patterns, and $M = 4$ gray levels, the total number of unique code bands is 64 (4^3). Figure 1.7 shows an example of grayscale coding patterns.

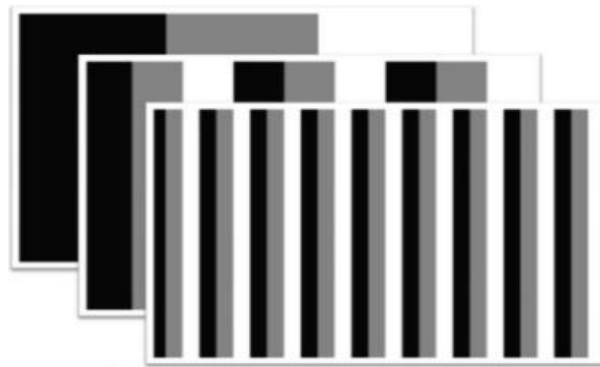


Figure A.7 3D reconstruction using Gray-coding strategy [Geng11]

Phase Shift

This technique has been studied in various 3D scanning applications due to its ability to achieve spatial resolution at the pixel level [BeLZ16]. The phase shift projection method consists of projecting bands with sinusoidal variation of light intensity, between 0 (black) and 255 (white), onto the part to be scanned. The pattern is then shifted by one phase. For a three-step phase shifting projection, the shift is done by $\frac{\pi}{3}$ phase. Figure A.8 shows an example of phase shifting projection technique.

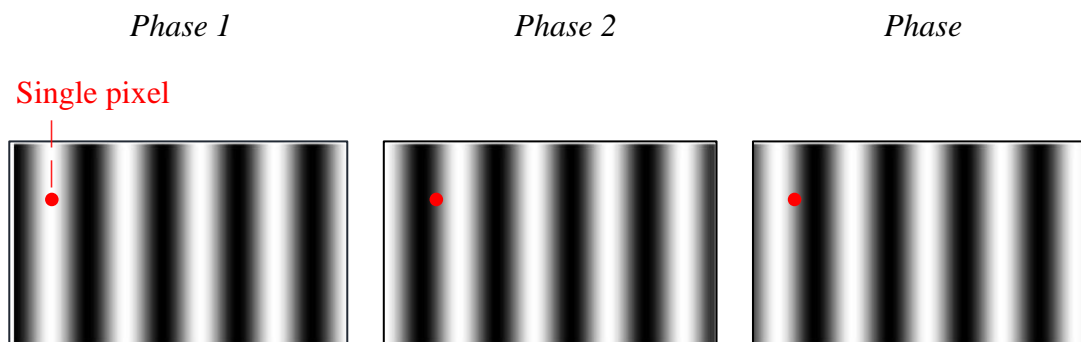


Figure A.8 3D reconstruction using phase shifting encoding strategy [BeLZ16]

This method uses the phase information calculated for each pixel, rather than the intensity values [YMMY21]. Each pixel of the projection pattern has its own phase, and can be located on the image plane.

Phase shift-based: calibration

This method works on the same principle as the Gray-code, the objective is to provide a sequence of projection that will allow identifying each single pixel of the projector. Then finding the correspondence between the pixels from the projector and the calibration grid. However, rather than using a binary code, a sinusoidal pattern is projected on the surface while shifting it, this allow obtaining unique identifiers of each pixel of the projector.

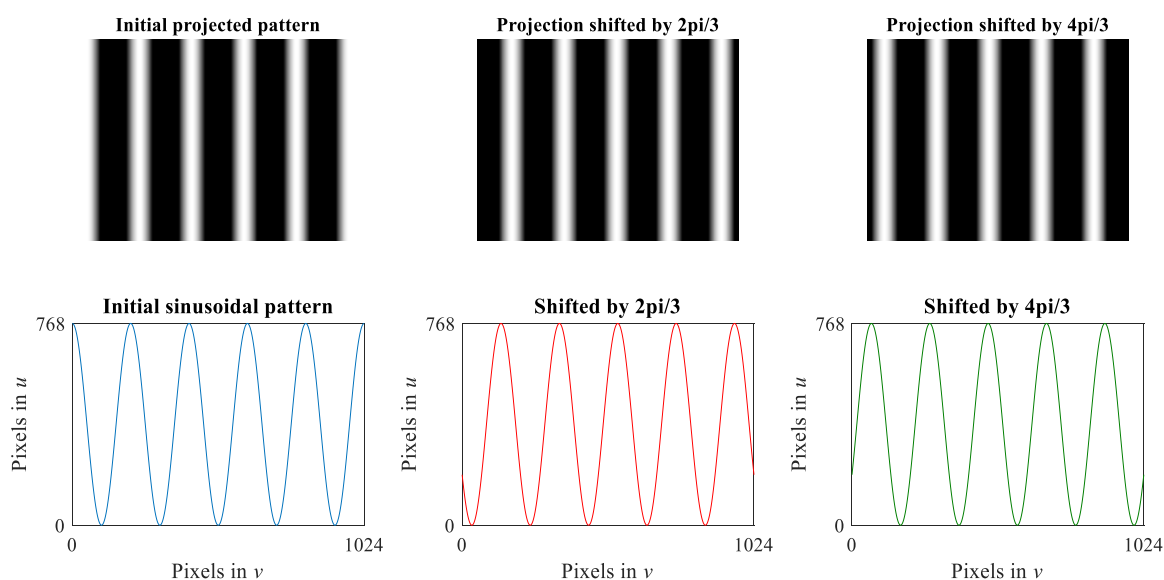


Figure A.9 Example of three-phase-shifting of a sinusoidal pattern for a projector with a resolution of 1024×768 pixels

Recently, Wilm [WiOL14] proposed an accurate and simple calibration of SL systems based on this method. Wilm projects a sinusoidal pattern as shown in Figure A.9. The projector pixels can be encoded by the mean of *Phase-shifting profilometry* to find the correspondence between the projector and the calibration grid. The major difference between the Gray-code and phase shifting is in the encoding of single pixel. The Gray-code results of only binary codes because only two colours are used (black and white). Whereas phase-shifting is based on gray-level to identify pixels. To encode projector pixels in both u_p and v_p direction, eq. A.4 is used.

$$\begin{cases} I_n^p(\mathbf{u}_p) = \frac{1}{2} + \frac{1}{2} \cos\left(\frac{2\pi n}{3} - \frac{2\pi \cdot \mathbf{u}_p}{3}\right) \\ I_n^p(\mathbf{v}_p) = \frac{1}{2} + \frac{1}{2} \cos\left(\frac{2\pi n}{3} - \frac{2\pi \cdot \mathbf{v}_p}{3}\right) \end{cases} \quad \text{A.4}$$

Where I_p^n is the projector normalized pattern intensity and n is the pattern index.

At the level of camera, the observed intensity can be expressed in eq. A.5, such that I_n^c is the camera observed n 'th pattern intensity.

$$\{I_n^c(\mathbf{u}_p, \mathbf{v}_p) = A + B \cos\left(\frac{2\pi n}{3} - \theta\right) \quad \text{A.5}$$

Where A is the intensity of the scene that includes ambient lighting, B is the projector intensity. By applying Fourier analysis, A can be considered as the magnitude of the constant components, B the magnitude of the principle frequency and θ the phase (Figure A.10).

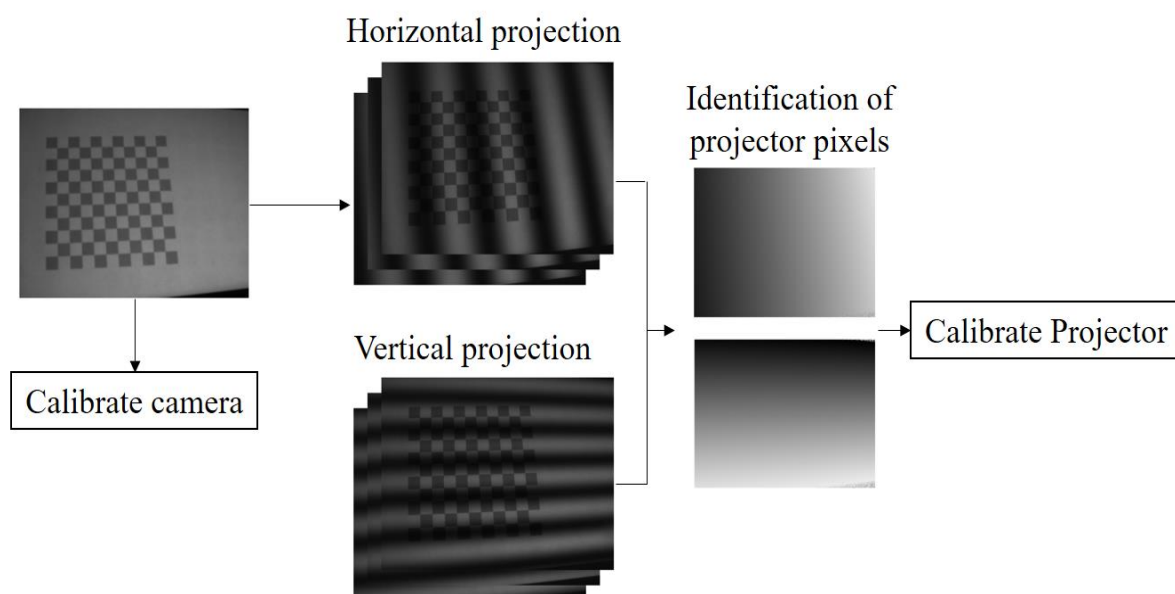


Figure A.10 Step of camera-projector calibration using phase-shifting projection

Appendix B: Non-linear optimisation using Levenberg-Marquardt

Levenberg-marquardt (LM) is one of the most used technique of minimization problems, usually non-linear problems [BeGR18]. The LM optimisation is based on Gauss-Newton and the gradient-descent algorithm. LM is more stable than the Gauss-Newton algorithm, it finds a solution even the initialisation is far from the global minimum.

B.1. Model establishing

Given a set of empirical data $\{x_i, y_i\}$, each composed of inputs $x_i \in R^P$ (is the dimensionality of the inputs) and their associated outputs $\tilde{y}_i \in R$. We assume that x_i and y_i are related by a single function f as expressed in eq. B.1. The predicted output values when applying the model $f()$ is denoted y_i (eq. B.2).

$$\tilde{y}_i \approx f(x_i, p) \quad \text{B.1}$$

$$y_i = f(x_i, p) \quad \text{B.2}$$

Usually, the observations \tilde{y}_i are different from y_i due to the empirical and computational errors. For a number of dimensions p , the error between the observations and the model is written as (eq. B.3).

$$\begin{aligned} e_i(p) &= |\tilde{y}_i - y_i|^2 \\ &= |\tilde{y}_i - f(x_i, p)|^2 \end{aligned} \quad \text{B.3}$$

The objective is to find the vector p that minimize the least square error $E(p)$ (eq. B.4).

$$\begin{aligned} E(p) &= \sum_{i=0}^{m-1} e_i(p) \\ &= \sum_{i=0}^{m-1} |\tilde{y}_i - f(x_i, p)|^2 \end{aligned} \quad \text{B.4}$$

Let's denote the vector $\tilde{Y} = (\tilde{y}_0, \dots, \tilde{y}_{m-1})^T$, $Y = (y_0, \dots, y_{m-1})$ and $X = (x_0, \dots, x_{m-1})$ respectively the observed values, the predicted values and the sample data. The least square error is written as (eq. B.5 where F is called the value function):

$$\begin{aligned} E(p) &= |\tilde{Y} - Y|^2 \\ &= |Y - F(X, p)|^2 \end{aligned} \quad \text{B.5}$$

B.2. Jacobian function

LM method requires the calculation of the Jacobian of the model. Let's define $J(X, p)$ as the $m \times n$ Jacobian matrix [Prof19] of the value function F for a specific input X (eq. B.6).

$$J(X, p) = \begin{pmatrix} \frac{\partial f_0(x_0, p)}{\partial p_0} & \frac{\partial f_0(x_0, p)}{\partial p_1} & \cdots & \frac{\partial f_0(x_0, p)}{\partial p_{n-1}} \\ \frac{\partial f_1(x_1, p)}{\partial p_0} & \frac{\partial f_1(x_1, p)}{\partial p_1} & \cdots & \frac{\partial f_1(x_1, p)}{\partial p_{n-1}} \\ \vdots & \vdots & \ddots & \vdots \\ \frac{\partial f_{m-1}(x_{m-1}, p)}{\partial p_0} & \frac{\partial f_{m-1}(x_{m-1}, p)}{\partial p_1} & \cdots & \frac{\partial f_{m-1}(x_{m-1}, p)}{\partial p_{n-1}} \end{pmatrix} \quad \text{B.6}$$

Each element of the matrix defined the partial derivative of the component of function $f_i(x, p)$ with respect to the parameter p_j . This derivative indicates the evolution of the output value at a specific position x_i . LM uses these parameters to optimise the exploration of the space.

Therefore, with the parameters X, \tilde{Y} and $J(X, p)$, the LM optimisation takes the following form (eq. B.7)

$$p_{opt} \leftarrow \text{Optimize}(F, J(X, p), X, \tilde{Y}, p_0) \quad \text{B.7}$$

With p_0 the initialization called also starting point. The result p_{opt} is a parameter vector that minimizes the least square deviation between the observations and the model F .

Appendix C: Representations of rotations

C.1. Euler rotation angles

In mechanics, the motion of an object in a reference could be expressed by six parameters: 3 translations (t_x, t_y, t_z) and 3 rotations (α, β, γ) called Euler angles. Euler angles were introduced to describe the orientation of an object or a coordinate frame with respect to a reference frame Figure C.1.

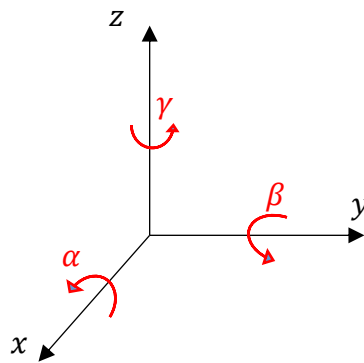


Figure C.1 rotation angles

C.2. Rotation matrix

The rotation of a rigid body around each axis could be expressed in eq. C.1. relation between Euler angles and rotation matrix is:

$$\begin{aligned}
 R_x &= \begin{bmatrix} 1 & 0 & 0 \\ 0 & \cos \alpha & -\sin \alpha \\ 0 & \sin \alpha & \cos \alpha \end{bmatrix} \\
 R_y &= \begin{bmatrix} \cos \beta & 0 & \sin \beta \\ 0 & 1 & 0 \\ -\sin \beta & 0 & \cos \beta \end{bmatrix} \\
 R_z &= \begin{bmatrix} \cos \gamma & -\sin \gamma & 0 \\ \sin \gamma & \cos \gamma & 0 \\ 0 & 0 & 1 \end{bmatrix}
 \end{aligned} \tag{C.1}$$

When 3 rotations are applied, the global rotation matrix is expressed as $R = R_x \times R_y \times R_z$, also written in (eq. C.2)

$$R = \begin{bmatrix} \cos \alpha & -\sin \alpha & 0 \\ \sin \alpha & \cos \alpha & 0 \\ 0 & 0 & 1 \end{bmatrix} \times \begin{bmatrix} \cos \beta & 0 & \sin \beta \\ 0 & 1 & 0 \\ -\sin \beta & 0 & \cos \beta \end{bmatrix} \times \begin{bmatrix} 1 & 0 & 0 \\ 0 & \cos \gamma & -\sin \gamma \\ 0 & \sin \gamma & \cos \gamma \end{bmatrix} \tag{C.2}$$

$$= \begin{bmatrix} r_{11} & r_{12} & r_{13} \\ r_{21} & r_{22} & r_{23} \\ r_{31} & r_{32} & r_{33} \end{bmatrix}$$

Where:

$$r_{11} = \cos(\beta) \cos(\gamma)$$

$$r_{21} = \sin(\alpha) \sin(\beta) \cos(\gamma) + \cos(\alpha) \sin(\gamma)$$

$$r_{31} = \sin(\alpha) \sin(\gamma) - \cos(\alpha) \sin(\beta) \cos(\gamma)$$

$$r_{12} = -\cos(\beta) \sin(\gamma)$$

$$r_{22} = \cos(\alpha) \cos(\gamma) - \sin(\alpha) \sin(\beta) \sin(\gamma)$$

$$r_{32} = \cos(\gamma) \sin(\alpha) + \cos(\alpha) \sin(\beta) \sin(\gamma)$$

$$r_{13} = \sin(\beta)$$

$$r_{23} = -\cos(\beta) \sin(\alpha)$$

$$r_{33} = \cos(\alpha) \cos(\beta)$$

C.3. Rodriguez rotations

Rodrigues is a vector representation of the rotations that assumes each rotation of a frame coordinate could be described as an angle of rotation around an axis with a unitary direction vector. In general, a rotation could be represented by four parameters a, b, c and d named Euler-Rodrigues parameters such that (eq. C.3):

$$a^2 + b^2 + c^2 + d^2 = 1$$

$$Rot = \begin{bmatrix} a^2 + b^2 - c^2 - d^2 & 2(bc - ad) & 2(bd + ac) \\ 2(bc + ad) & a^2 - b^2 + c^2 - d^2 & 2(cd - ab) \\ 2(bd - ac) & 2(cd + ab) & a^2 - b^2 - c^2 + d^2 \end{bmatrix} \quad \text{C.3}$$

Let's consider the vector \vec{V}' on which a rotation is applied and $\vec{\omega} = (b, c, d)$ is the vector parameter. The Rodrigues formulae used to transform a rotation angle to a vector is expressed in eq. C.4.

$$\vec{V}' = \vec{V} + 2a(\vec{\omega} \times \vec{V}) + 2(\vec{\omega} \times (\vec{\omega} \times \vec{V})) \quad \text{C.4}$$

Appendix D: Particle Swarm Optimisation (PSO)

Particle swarm optimisation (PSO) is a non-linear heuristic method based on the collective behaviour of several particles to converge to a solution [Part00]. PSO is inspired by the behaviour of bird flocks or the socio-psychology where individuals could influence each other's decisions.

In PSO, a particle is a single individual that moves in the space and memorizes its current position to share it with the other individuals. Thanks to simple motion rules in the space of solutions, the particles progressively converge towards a global minimum as all the particles positions are known (Figure D.1).

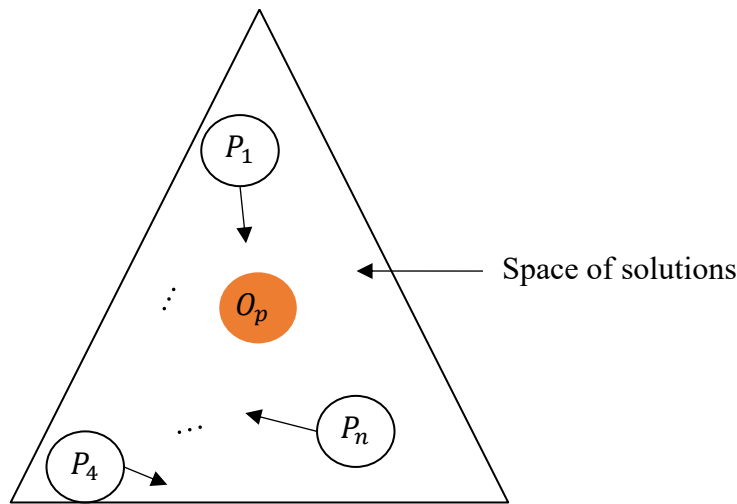


Figure D.1 Visualization of particles motion in PSO

Where O_p is the optimality and $P_i, i = \{1, \dots, n\}$ is the i^{th} particle.

D.1. Application of PSO on multivariate polynomial

Considering a multivariate polynomial of 6 dimensions, each particle p_i is expressed by its vector of position $(\alpha_i, \beta_i, \gamma_i, t_{xi}, t_{yi}, t_{zi})$ in the 6-dimensional space. Let's define the velocity (given in eq. D.1) as the speed of each particle in a specific direction. At each iteration, the particle p_i moves with respect to its velocity \vec{V}_i^k .

$$\vec{V}_i^{k+1} = w\vec{V}_i^k + c_1r_1(\vec{P}_i^k - \vec{X}_i^k) + c_2r_2(\vec{G}^k - \vec{X}_i^k) \quad \text{D.1}$$

Where: - \vec{V}_i^t : velocity vector of the particle at iteration k

- w : inertia weight
- c_1, c_2 : cognitive and social acceleration (positive constants)
- r_1, r_2 : random values in the interval $[0,1]$, sampled from a uniform distribution
- \vec{P}_i^k : best individual position associated with particle i
- \vec{G}^k : best position associated with the set of particles in the swarm

Given the dimensional complexity of our problem, the number of the particles in selected in the range $[20, 50]$ [PiNP20], this number doesn't influence the convergence time and efficient enough to find the optimality.

The particle's step is defined with a value that corresponds to the resolution of the robot used, because the optimal values define the camera-grid transformation. Therefore: $step = 20 \mu m$.

To ensure the convergence to the minimum, the inertia-weight value is chosen based of Bansal *et al* [BSSV11] and Maurya [MBPB19] where $w \in [0.4, 0.9]$. After testing empirically several values, the best one is $w = 0.7$.

Appendix E: Tsai calibration method

One of the most common camera calibration method is Tsai approach which is a two steps algorithm that allows to estimate separately intrinsic and extrinsic parameters [Tsai87b]. The calibration requires a known 3D calibration object that has a good accuracy. The Tsai model is based on pinhole perspective projection and the estimated parameters are as follow:

- f : Focal length of camera,
- k : Radial lens distortion coefficient,
- c_u, c_v : Coordinates of centre of radial lens distortion,
- s_x : Scale factor to account for any uncertainty due to imperfections in hardware timing for scanning and digitization,
- α, β, γ : Rotation angles between the world and camera coordinates respectively around x-, y-, and z- axis
- t_x, t_y, t_z : Translation components between the world and camera coordinates.

An object point in the world is projected into a pixel in the image coordinate system. However, it is not possible to recover the information of a real distance using the distance between two pixels, this is the reason why an equation that allows to link the two systems is established in order to evaluate the relationship between a real point and its projection in the image plane [SSBM11]. Tsai calibration method does not determine this relation directly, and thus an intermediate reference system is required.

Tsai method is based on perspective projection model. The transformation of the world coordinates system (X, Y, Z) to the image coordinates systems (u, v) is achieved following those steps [MaCM03]:

- Identification on camera coordinate system (X_c, Y_c, Z_c) using the eq. D.1.

$$\begin{pmatrix} X_c \\ Y_c \\ Z_c \end{pmatrix} = \begin{pmatrix} r_1 & r_2 & r_3 \\ r_4 & r_5 & r_6 \\ r_7 & r_8 & r_9 \end{pmatrix} * \begin{pmatrix} X \\ Y \\ Z \end{pmatrix} + \begin{pmatrix} t_x \\ t_y \\ t_z \end{pmatrix} \quad \text{D.1}$$

The parameters to be determined in this first step are r_i and T_i rotation and translation matrices.

- Estimation of focal distance f using the projection of the image plane onto the camera frame without considering lens distortions using eq. D.2:

$$x_p = f \frac{X_c}{Z_c} \quad \& \quad y_p = f \frac{Y_c}{Z_c} \quad \text{D.2}$$

- Estimation of distortion coefficients caused by camera lenses. Let's consider D_x and D_y the radial distortion function previously described, and (x_d, y_d) the distorted point, eq. D.3 allows to determine D_x and D_y [Tsai87b]:

$$\begin{cases} x_d + D_x = x_p \\ y_d + D_y = y_p \end{cases} \quad \text{where} \quad \begin{cases} D_x = x_d (1 + k_1 * r^2 + k_2 * r^4 + k_3 * r^6) \\ D_y = y_d (1 + k_1 * r^2 + k_2 * r^4 + k_3 * r^6) \end{cases} \quad \text{D.3}$$

Where $r = \sqrt{x^2 + y^2}$ is the distance from a point (x, y) to the optical centre (C_u, C_v) .

- The goal of this last step is to define the transition from distorted image coordinates (x_d, y_d) to the sensor coordinates (u, v) expressed in pixel. Eq. D.4 describes the relation between image system and the sensor:

$$\begin{cases} u = \frac{S_x}{d'_x} * x_d + C_u \\ v = \frac{S_y}{d'_y} * y_d + C_v \end{cases} \quad \text{with} \quad d'_x = d_x \frac{N_{cx}}{N_{fx}} \quad \text{D.4}$$

Where (d_x, d_y) is known as the pixel pitch. The pixel pitch refers to the density of pixels, it describes the physical distance between pixels on screen [Svil18], the smaller pixel pitch the higher pixel density and resolution. N_{cx} is the number of sensor elements in x direction and N_{fx} is the number of pixels of the computed image (or of the frame grabber) in x direction. The calculation of S_x parameter and the optical centre coordinates (C_u, C_v) are the objectives of this step, S_x is referred as the image scale uncertainty factor.

To establish the relationship between the world coordinate system and the image, eq. D.5 are used while taking account the first distortion coefficient k_1 :

$$\begin{aligned} \frac{d'_x}{S_x} x + \frac{d'_x}{S_x} x k_1 r^2 &= f \frac{r_1 X + r_2 Y + r_3 Z + T_x}{r_7 X + r_8 Y + r_9 Z + T_z} \\ d_y y + d_y y k_1 r^2 &= f \frac{r_4 X + r_5 Y + r_6 Z + T_y}{r_7 X + r_8 Y + r_9 Z + T_z} \end{aligned} \quad \text{D.5}$$

With $r = \sqrt{\left(\frac{d'_x}{S_x} x\right)^2 + (d_y y)^2}$

The calibration method proposed by Tsai can estimate intrinsic parameters such as focal length, the coordinates of the optical centre (C_u, C_v) and the image scale factor s_x , also the extrinsic parameters which defined the position of the camera in the world coordinate system (r_i, T_j) . These parameters minimize the error between the points of the calibration artefact and its projection in the image plane. Two stages allow the estimation of camera parameters: first is estimating of initial values for some parameters, and second is the estimation of all parameters with iterative non-linear simultaneous optimisation [Horn00][Will94].